

University of Alberta

Electrodeposition of Pb-free, Sn-based Alloy Solder Films

by

Chunfen Han

A thesis submitted to the Faculty of Graduate Studies and Research
in partial fulfillment of the requirements for the degree of

Doctor of Philosophy

in

Materials Engineering

Department of Chemical and Materials Engineering

©Chunfen Han

Fall 2009

Edmonton, Alberta

Permission is hereby granted to the University of Alberta Libraries to reproduce single copies of this thesis and to lend or sell such copies for private, scholarly or scientific research purposes only. Where the thesis is converted to, or otherwise made available in digital form, the University of Alberta will advise potential users of the thesis of these terms.

The author reserves all other publication and other rights in association with the copyright in the thesis and, except as herein before provided, neither the thesis nor any substantial portion thereof may be printed or otherwise reproduced in any material form whatsoever without the author's prior written permission.

Examining Committee

Douglas Ivey, Chemical and Materials Engineering

Qi Liu, Chemical and Materials Engineering

John Nychka, Chemical and Materials Engineering

Weixing Chen, Chemical and Materials Engineering

Jeremy Sit, Electrical and Computer Engineering

Dale Barkey, Chemical Engineering, University of New Hampshire

Abstract

The dominant materials used for solders in electronic assemblies over the past 60 years have been Pb-Sn alloys. Increasing pressure from environmental and health authorities has stimulated the development of various Pb-free solders. Two of the most promising replacements are eutectic Sn-Cu and Sn-Ag-Cu alloys that are produced primarily by electrodeposition. During soldering and solid state aging (storage or in service of the electronic assemblies), interactions take place at the solder/substrate metal interface and form intermetallic compounds (IMCs) which are crucial for the reliability of the solder joints.

Simple and "green" Sn-citrate and Sn-Cu-citrate solutions have been developed and optimized to electrodeposit eutectic and near eutectic Sn-Cu solder films. Sn-citrate suspensions with Cu particles and Sn-Cu-citrate suspensions with Ag nano-particles have also been developed and optimized to allow for electrochemical composite deposition of eutectic and near eutectic Sn-Cu and Sn-Ag-Cu solder films. Different plating and post-plating conditions, including solution concentration, current density, agitation, additives, and aging, have been investigated by evaluating their effects on plating rate, deposit composition and microstructure.

Tri-ammonium citrate is used as the only complexing agent for Sn, Sn-Cu, and Sn-Ag-Cu deposition. Speciation diagram calculations, reduction potential calculations, and polarization studies are conducted to study Sn-citrate solution chemistry and the kinetics of Sn electrodeposition. X-ray photoelectron

spectroscopy (XPS) analysis is used to identify the precipitates formed in Sn-citrate solutions at low pH. Current-controlled and potential-controlled electrochemical techniques, nucleation modeling, and surface morphology characterization techniques are applied to study the nucleation and film growth mechanism of Sn and Sn-Cu electrodeposition from Sn-citrate and Sn-Cu-citrate solutions.

Reflow and aging tests for deposited Sn-Cu and Sn-Ag-Cu solder films on Cu and Ni substrates are performed to study the interactions between the solder and the substrate and the formation and growth of IMCs at the solder/substrate interface, by characterizing the microstructure of the IMCs and calculating diffusion coefficients.

Acknowledgements

First and foremost, I wish to thank Dr. Douglas Ivey and Dr. Qi Liu for their guidance and their support throughout my graduate studies. I am very grateful for the opportunity they have given me to study under them and the trust they have placed in me.

I wish to thank my fellow group members and friends I made who have provided insight and friendship during my time with them. In particular, I wish to thank Brendan Crozier and Junfang Lu for helping me prepare TEM samples, and Nima Shaigan and Dr. Weifeng Wei for their assistance and input into my research.

I would also like to thank Tina Barker for help and training on the SEM, Shihong Xu for Auger analysis, Dr. Anqiang He for SEM and XPS analysis and help and training on the AFM, and Shiraz Merali for XRD training.

Special thanks to my husband Chris Repka, who gave me the support and encouragement to complete my Ph.D. degree.

Finally, I wish to thank the Natural Sciences and Engineering Research Council (NSERC) of Canada for providing the funding for this project, and Micralyne, Inc. for providing metallized Si wafers. I would also like to thank the Alberta Centre for Surface Engineering and Science (ACSES) for providing surface analysis services.

Table of Contents

1	Introduction	1
2	Literature review	5
2.1	<i>Electronic packaging</i>	5
2.1.1	Level 1 interconnections	5
2.1.2	Level 2 interconnections	7
2.2	<i>Soldering technologies for electronic packaging</i>	8
2.2.1	Solder materials	8
2.2.1.1	<i>Pb-Sn solder and its problems</i>	9
2.2.1.2	<i>Regulations for Pb-based solders</i>	11
2.2.1.3	<i>Pb-free solders</i>	12
2.2.2	Wetting and solderability	14
2.2.3	Reflow soldering	15
2.2.4	Soldering reactions	16
2.2.5	Intermetallic compound (IMC) formation	17
2.2.6	Interactions between solders and substrates	18
2.2.6.1	<i>Interactions between Sn and Cu</i>	18
2.2.6.2	<i>Interactions between Sn and Ni</i>	22
2.3	<i>Thin film deposition technologies for solders</i>	25
2.3.1	Evaporation	26
2.3.2	Sputter deposition	27
2.3.3	Electrodeposition	29
2.3.4	Electrodeposition of Sn and Sn alloys	29
2.3.4.1	<i>Alkaline baths</i>	30
2.3.4.2	<i>Sulfate baths</i>	31
2.3.4.3	<i>Methanesulfonate baths</i>	33
2.3.4.4	<i>Pyrophosphate-iodide baths</i>	34
2.4	<i>Theory of electrodeposition and electrochemical composite deposition</i>	35

2.4.1	Electrodeposition of a single metal	35
2.4.1.1	<i>Electrode reactions</i>	36
2.4.1.2	<i>Electrical double layer</i>	37
2.4.1.3	<i>Mass transfer mechanisms</i>	38
2.4.1.4	<i>Rate-determine steps in electrode reactions</i>	40
2.4.1.5	<i>Polarization and overpotential</i>	42
2.4.2	Electrodeposition of metal alloys	43
2.4.3	Pulsed current electrodeposition	44
2.4.4	Electrochemical composite deposition	48
2.4.5	Electrolyte additives	50
2.4.5.1	<i>Complexing agents</i>	51
2.4.5.2	<i>Leveling agents</i>	52
2.4.5.3	<i>Surfactants</i>	52
2.5	<i>Objectives of the current work</i>	53
3	Electrodeposition and electrochemical composite deposition of Sn-Cu alloys	56
3.1	<i>Introduction</i>	56
3.2	<i>Experimental materials and procedures</i>	58
3.3	<i>Results and discussion</i>	60
3.3.1	Optimization of Sn-citrate and Sn-Cu-citrate solutions for Sn and Sn-Cu electrodeposition	60
3.3.1.1	<i>Effect of tri-ammonium citrate concentration on Sn electrodeposition</i>	60
3.3.1.2	<i>Effect of current density on Sn electrodeposition</i>	63
3.3.1.3	<i>Effect of Cu²⁺ concentration on Sn-Cu electrodeposition</i>	65
3.3.2	Electrodeposition of Sn-Cu eutectic and near-eutectic alloys from Sn-Cu-citrate solutions	68
3.3.2.1	<i>Sn-Cu electrodeposition from the chloride-citrate solution</i>	68

3.3.2.2	<i>Effect of current density</i>	71
3.3.2.3	<i>Solution stability tests</i>	75
3.3.2.4	<i>Effect of agitation</i>	80
3.3.2.5	<i>Effect of gelatin+β-naphthol as additives</i>	86
3.3.3	Electrochemical composite deposition of Sn-Cu eutectic and near-eutectic alloys from Sn-citrate suspensions with Cu particles	89
3.4	<i>Conclusions</i>	94
4	Solution chemistry studies of Sn-citrate solutions for Sn electrodeposition	97
4.1	<i>Introduction</i>	97
4.2	<i>Experimental materials and procedures</i>	99
4.3	<i>Results and discussion</i>	100
4.3.1	Sn-citrate solution chemistry studies	100
4.3.2	Sn(II)-citrate precipitates identification	112
4.4	<i>Conclusions</i>	118
5	Nucleation and film growth of Sn and Sn-Cu solders during electrodeposition	120
5.1	<i>Introduction</i>	120
5.2	<i>Experimental materials and procedures</i>	122
5.3	<i>Results and discussion</i>	124
5.3.1	Current step (galvanostatic) method	124
5.3.2	Chronoamperometry and nucleation modeling	128
5.3.3	Microstructure characterization of Sn and Sn-Cu nucleation	134
5.3.4	Sn-Cu film growth mechanism	141
5.4	<i>Conclusions</i>	146
6	Electrochemical composite deposition of Sn-Ag-Cu alloys	148
6.1	<i>Introduction</i>	148

6.2	<i>Experimental materials and procedures</i>	151
6.3	<i>Results and discussion</i>	152
6.3.1	Effect of agitation	152
6.3.2	Effect of current density	156
6.3.3	Effect of SDS	166
6.3.4	DSC thermal analysis	172
6.4	<i>Conclusions</i>	174
7	Interfacial reactions between Pb-free Sn-based solders and substrates	175
7.1	<i>Introduction</i>	175
7.2	<i>Experimental materials and procedures</i>	177
7.3	<i>Results and discussion</i>	180
7.3.1	Interfacial reactions between Sn-Cu solder and Cu and Ni substrates during reflow and aging	180
7.3.1.1	<i>Sn-Cu solder and Cu substrate</i>	180
7.3.1.2	<i>Sn-Cu solder and Ni substrate</i>	187
7.3.2	Interfacial reactions between Sn-Ag-Cu solder and Cu and Ni substrates during reflow and aging	195
7.3.2.1	<i>Sn-Ag-Cu solder and Cu substrate</i>	195
7.3.2.2	<i>Sn-Ag-Cu solder and Ni substrate</i>	200
7.4	<i>Conclusions</i>	207
8	Conclusions and recommendations	209
8.1	<i>Conclusions of the current work</i>	209
8.1.1	Solution chemistry studies for Sn-citrate solutions	209
8.1.2	Nucleation and film growth mechanism studies for Sn and Sn-Cu from citrate solutions	210
8.1.3	Deposition of Sn, Sn-Cu and Sn-Ag-Cu solder films from citrate plating baths	212
8.1.3.1	<i>Sn electrodeposition</i>	212

8.1.3.2	<i>Sn-Cu deposition</i>	213
8.1.3.3	<i>Sn-Ag-Cu deposition</i>	214
8.1.4	Interfacial reactions between Sn-Cu and Sn-Ag-Cu solders and Cu and Ni substrates during reflow and aging	215
8.1.4.1	<i>Interfacial reactions between solders and Cu substrate</i>	215
8.1.4.2	<i>Interfacial reactions between solders and Ni substrate</i>	215
8.2	<i>Original contribution highlights</i>	216
8.3	<i>Recommendations for future work</i>	217
8.3.1	Other plating parameters	217
8.3.1.1	<i>Pulse plating conditions</i>	217
8.3.1.2	<i>SnCl₂·2H₂O concentration</i>	217
8.3.2	Speciation calculation for Cu-citrate solution	217
8.3.3	Reactions between Ag nano-particles and other species in suspensions	218
8.3.4	Sn-Ag deposition using AgNO ₃ as Ag source	218
8.3.5	Mechanical properties of Pb-free solder joints	221
	References	222

List of Tables

Table 2-1	Important properties of solder alloys.	9
Table 3-1	Volume of precipitates formed in different Sn-citrate solutions.	60
Table 3-2	Composition of Sn-citrate solutions studied by polarization measurements.	61
Table 3-3	Composition of Sn-Cu-citrate solutions studied.	65
Table 4-1	Stability constants for Sn(II)-citrate complex ions and Sn(II)-hydroxyl species.	101
Table 4-2	Selected free energy data for the Sn(II)-citrate system at 298K.	101
Table 4-3	Composition of Sn-citrate solutions used in this study.	101
Table 4-4	Binding energies for main components of XPS C 1s, O 1s and Sn 3d _{5/2} peaks for citric acid, tri-ammonium citrate and Precipitates obtained from solution S1 at pH 2.5.	115
Table 4-5	Composition results for citric acid, tri-ammonium citrate and precipitates obtained from solution S1 at pH 2.5.	117
Table 5-1	Calculated diffusion coefficients for reducing ionic species from Sn-citrate and Sn-Cu-citrate solutions on Pt.	128
Table 5-2	Diffusion coefficients for reducing ionic species in Sn-citrate and Sn-Cu-citrate solutions on Pt.	133
Table 7-1	EDX point analysis results for Sn, Cu, Ni at positions marked in Fig. 7-9c.	189

List of Figures

Fig. 2-1	Schematic drawings showing the cross sections of a BGA joint and a flip-chip joint in a electronic packaging.	6
Fig. 2-2	Schematic diagram of three phase contact angle θ .	14
Fig. 2-3	Reflow profile for Pb-free soldering packages.	16
Fig. 2-4	Sn-Cu phase diagram.	19
Fig. 2-5	Sn-Ni phase diagram.	23
Fig. 2-6	Schematic illustration for an electrolytic cell.	35
Fig. 2-7	Proposed model of the electrical double layer region under conditions where anions are specifically adsorbed and the according potential profile across the double layer region.	38
Fig. 2-8	Metal ion concentration profile as a function of distance from the electrode surface.	39
Fig. 2-9	Pathway of a general electrode reaction.	41
Fig. 2-10	Processes in an electrode reaction represented as resistances and overpotentials.	43
Fig. 2-11	Typical direct current and pulsed current waveform.	45
Fig. 2-12	Metal ion concentration profile as a function of distance from the electrode surface during PC plating (δ , the thickness of the diffuse layer; δ_s , the thickness of the steady state diffuse layer; δ_p , the thickness of the pulse diffuse layer in a quasi-steady state).	46
Fig. 2-13	The variation of metal ion concentration ($C_{M^{n+}}$), and reduction produce concentration (C_R) with time during PC and DC plating.	47
Fig. 3-1	pH values for Sn-citrate solutions. In all five solutions, the concentration of $\text{SnCl}_2 \cdot 2\text{H}_2\text{O}$ was kept at 0.22 mol/L, while the concentration of tri-ammonium citrate was varied from	

- 0.30 mol/L to 0.82 mol/L. 61
- Fig. 3-2 Polarization curves for Sn-citrate solutions. In all five solutions, the concentration of $\text{SnCl}_2 \cdot 2\text{H}_2\text{O}$ was kept at 0.22 mol/L, while the concentration of tri-ammonium citrate was varied as follows: S1: 0.30 mol/L; S2: 0.41 mol/L; S3: 0.51 mol/L, S4: 0.62 mol/L and S5: 0.82 mol/L. 62
- Fig. 3-3 SEM secondary electron (SE) plan view (left) and cross section (right) images of Sn films electrodeposited onto Au seed layers from Sn-citrate solutions containing 0.22 mol/L $\text{SnCl}_2 \cdot 2\text{H}_2\text{O}$ and different tri-ammonium citrate concentrations: (a) 0.30 mol/L; (b) 0.33 mol/L; (c) 0.44 mol/L and (d) 0.66 mol/L. The current density is 5 mA/cm^2 and samples were plated for 30 min. 63
- Fig. 3-4 SEM SE (a) plan view and (b) cross section images of Sn films electrodeposited onto Au seed layers from Sn-citrate solutions containing 0.22 mol/L $\text{SnCl}_2 \cdot 2\text{H}_2\text{O}$ and 0.4 mol/L tri-ammonium citrate at different current densities: 5 mA/cm^2 , 10 mA/cm^2 and 15 mA/cm^2 . The plating time was 1 hour. 64
- Fig. 3-5 Cu content in Sn-Cu deposits and in Sn-Cu-citrate solutions as a function of Cu concentration in solutions. The concentration of $\text{SnCl}_2 \cdot 2\text{H}_2\text{O}$ and tri-ammonium citrate was kept at 0.22 mol/L and 0.30 mol/L, respectively. 66
- Fig. 3-6 SEM SE plan view images of Sn-Cu films electrodeposited onto Au seed layers from Sn-Cu-citrate solutions with different Cu^{2+} concentrations: (a) 0.003 mol/L, (b) 0.006 mol/L, (c) 0.009 mol/L, (d) 0.012 mol/L, (e) 0.015 mol/L and (f) 0.018 mol/L. The concentration of $\text{SnCl}_2 \cdot 2\text{H}_2\text{O}$ and tri-ammonium citrate was kept at 0.22 mol/L and 0.30 mol/L, respectively. The current density was 10 mA/cm^2 and plating time was 30 min. 66
- Fig. 3-7 SEM SE cross section images of Sn-Cu films electrodeposited onto Au seed layers from Sn-Cu-citrate solutions with different

- Cu²⁺ concentrations: (a) 0.003 mol/L, (b) 0.006 mol/L, (c) 0.009 mol/L, (d) 0.012 mol/L, (e) 0.015 mol/L and (f) 0.018 mol/L. The concentration of SnCl₂·2H₂O and tri-ammonium citrate was kept at 0.22 mol/L and 0.30 mol/L, respectively. The current density was 10mA/cm² and plating time was 30min. 67
- Fig. 3-8 Cyclic voltammetry measurements for various solutions: (a) 0.30 mol/L tri-ammonium citrate and 0.22 mol/L CuCl₂·2H₂O; (b) 0.30 mol/L tri-ammonium citrate and 0.22 mol/L SnCl₂·2H₂O; (c) 0.30 mol/L tri-ammonium citrate, 0.22 mol/L SnCl₂·2H₂O and 0.003 mol/L CuCl₂·2H₂O. 68
- Fig. 3-9 SEM SE plan view images of Sn-Cu films electrodeposited onto Au seed layers from Sn-Cu-citrate solutions containing 0.22 mol/L SnCl₂·2H₂O, 0.003 mol/L CuCl₂·2H₂O, and 0.30 mol/L tri-ammonium citrate. 70
- Fig. 3-10 SEM SE cross section images of Sn-Cu films electrodeposited onto Au seed layers from a Sn-Cu-citrate solution containing 0.22 mol/L SnCl₂·2H₂O, 0.003 mol/L CuCl₂·2H₂O + 0.30 mol/L tri-ammonium citrate. 70
- Fig. 3-11 XRD patterns from (a) PC and (b) DC plated Sn-Cu films onto Au seed layers from a Sn-Cu-citrate solution containing 0.22 mol/L SnCl₂·2H₂O, 0.003 mol/L CuCl₂·2H₂O and 0.30 mol/L tri-ammonium citrate. The current density was 10 mA/cm². 71
- Fig. 3-12 Deposit Cu content as a function of average current density. The solution contained 0.22 mol/L SnCl₂·2H₂O, 0.003 mol/L CuCl₂·2H₂O, and 0.30 mol/L tri-ammonium citrate. 72
- Fig. 3-13 Plating rate as a function of average current density for both PC and DC plating. The solution contained 0.22 mol/L SnCl₂·2H₂O, 0.003 mol/L CuCl₂·2H₂O, and 0.30 mol/L tri-ammonium citrate. 73
- Fig. 3-14 XRD patterns from PC plated Sn-Cu films onto Au seed

- layers from a Sn-Cu-citrate solution containing 0.22 mol/L $\text{SnCl}_2 \cdot 2\text{H}_2\text{O}$, 0.003 mol/L $\text{CuCl}_2 \cdot 2\text{H}_2\text{O}$, and 0.30 mol/L tri-ammonium citrate. a) 5 mA/cm²; b) 10 mA/cm²; c) 15 mA/cm². 74
- Fig. 3-15 Deposit Cu content as a function of the distance from the solder/substrate interface for both PC and DC Sn-Cu films electrodeposited from a Sn-Cu-citrate solution containing 0.22 mol/L $\text{SnCl}_2 \cdot 2\text{H}_2\text{O}$, 0.003 mol/L $\text{CuCl}_2 \cdot 2\text{H}_2\text{O}$, and 0.30 mol/L tri-ammonium citrate (+). Plating was done at 10 mA/cm² on Ni coated Cu substrates. 75
- Fig. 3-16 Deposit Cu content as a function of solution aging time for both PC and DC: (a) Test 1, (b) Test 2. The solution contained 0.22 mol/L $\text{SnCl}_2 \cdot 2\text{H}_2\text{O}$, 0.003 mol/L $\text{CuCl}_2 \cdot 2\text{H}_2\text{O}$, and 0.30 mol/L tri-ammonium citrate. The average current density was 5 mA/cm². 76
- Fig. 3-17 SEM SE images (plan view and cross section) for Sn-Cu films PC plated in a solution aged for: (a) 36 days, Test 1, (b) 36 days, Test 2 and (c) 77 days, Test 2. The solution contained 0.22 mol/L $\text{SnCl}_2 \cdot 2\text{H}_2\text{O}$, 0.003 mol/L $\text{CuCl}_2 \cdot 2\text{H}_2\text{O}$, and 0.30 mol/L tri-ammonium citrate. Plating was done at 5 mA/cm². 77
- Fig. 3-18 Polarization curves for (a) Cu-citrate solution containing 0.22 mol/L $\text{CuCl}_2 \cdot 2\text{H}_2\text{O}$ and 0.30 mol/L tri-ammonium citrate, (b) Sn-citrate solution containing 0.22 mol/L $\text{SnCl}_2 \cdot 2\text{H}_2\text{O}$ and 0.30 mol/L tri-ammonium citrate, after different aging times. 79
- Fig. 3-19 Polarization curves for Sn-Cu-citrate solutions containing 0.22 mol/L $\text{SnCl}_2 \cdot 2\text{H}_2\text{O}$, 0.003 mol/L $\text{CuCl}_2 \cdot 2\text{H}_2\text{O}$ and 0.30 mol/L tri-ammonium citrate (a) without agitation, (b) With agitation, stir speed = 600 rpm. 81
- Fig. 3-20 SEM SE plan view images of Sn-Cu films electrodeposited onto Au seed layers from Sn-Cu-citrate solutions under

- current densities of 10 and 40 mA/cm² and at different stir speeds. The solution contained 0.22 mol/L SnCl₂·2H₂O, 0.003 mol/L CuCl₂·2H₂O, and 0.30 mol/L tri-ammonium citrate. 82
- Fig. 3-21 Deposit Cu content as a function of current density plated from Sn-Cu-citrate solutions at different agitation rates. The solution contained 0.22 mol/L SnCl₂·2H₂O, 0.003 mol/L CuCl₂·2H₂O and 0.30 mol/L tri-ammonium citrate. 83
- Fig. 3-22 SEM SE images: (a) plan view images, (b) cross section images of Sn-Cu films electrodeposited onto Au seed layers from Sn-Cu-citrate solutions with different CuCl₂·2H₂ concentrations under different current densities. The concentrations of SnCl₂·2H₂O and tri-ammonium citrate were fixed at 0.22 mol/L and 0.30 mol/L. The stirring speed was 600 rpm. 84
- Fig. 3-23 Deposit Cu content as a function of current density from Sn-Cu-citrate solutions with different CuCl₂·2H₂O concentrations. The concentrations of SnCl₂·2H₂O and tri-ammonium citrate were fixed at 0.22 mol/L and 0.30 mol/L, respectively. The stirring speed was 600 rpm. 85
- Fig. 3-24 Sn-Cu deposit plating rate as a function of current density from solutions containing different CuCl₂·2H₂O concentrations. The concentrations of SnCl₂·2H₂O and tri-ammonium citrate were fixed at 0.22 mol/L and 0.30 mol/L, respectively. The stirring speed was 600 rpm. 85
- Fig. 3-25 SEM SE plan view images of Sn-Cu films electrodeposited onto Au seed layers from Sn-Cu-citrate solutions with the addition of different amounts of gelatin + naphthol and a constant total solution volume (40 mL): (a) 20 mL, 2 g/L gelatin + 1 g/L naphthol; (b) 10 mL, 1 g/L gelatin + 0.5 g/L naphthol; (c) 5 mL, 0.5 g/L gelatin + 0.25 g/L naphthol; (d) 2.5 mL, 0.2 g/L gelatin + 0.125 g/L naphthol. The

concentrations of $\text{SnCl}_2 \cdot 2\text{H}_2\text{O}$, $\text{CuCl}_2 \cdot 2\text{H}_2\text{O}$, and tri-ammonium citrate were fixed at 0.22 mol/L, 0.003 mol/L and 0.30 mol/L, respectively. The current density was 15 mA/cm². 86

Fig. 3-26 SEM SE plan view images of Sn-Cu films electrodeposited onto Au seed layers from Sn-Cu-citrate solutions with the addition of different amounts of gelatin + β -naphthol and a constant total solution volume (40 mL) : (a) 20 mL, 2 g/L gelatin + 1 g/L naphthol; (b) 10 mL, 1 g/L gelatin + 0.5 g/L naphthol; (c) 5 mL, 0.5 g/L gelatin + 0.25 g/L naphthol. The concentrations of $\text{SnCl}_2 \cdot 2\text{H}_2\text{O}$, $\text{CuCl}_2 \cdot 2\text{H}_2\text{O}$ and tri-ammonium citrate were fixed at 0.22 mol/L, 0.003 mol/L and 0.30 mol/L, respectively. The current density was 25 mA/cm². 87

Fig. 3-27 SEM SE cross section images of Sn-Cu films electrodeposited onto Au seed layers from Sn-Cu-citrate solutions with the addition of 10 mL gelatin + naphthol (1 g/L gelatin + 0.5 g/L naphthol) and a constant total solution volume (40 mL) at two different current densities: (a) 25 mA/cm²; (b) 15 mA/cm². The concentrations of $\text{SnCl}_2 \cdot 2\text{H}_2\text{O}$, $\text{CuCl}_2 \cdot 2\text{H}_2\text{O}$, and tri-ammonium citrate were fixed at 0.22 mol/L, 0.003 mol/L and 0.30 mol/L, respectively. 88

Fig. 3-28 Deposit Cu content as a function of volume percent of gelatine + naphthol addition which was calculated by dividing the volume of gelatin + naphthol addition with the constant total solution volume (40 mL). The concentrations of $\text{SnCl}_2 \cdot 2\text{H}_2\text{O}$, $\text{CuCl}_2 \cdot 2\text{H}_2\text{O}$ and tri-ammonium citrate were fixed at 0.22 mol/L, 0.003 mol/L and 0.30 mol/L, respectively. 88

Fig. 3-29 (a) SEM SE images of Cu particles. (b) Schematic illustration of experimental set-up for Sn-Cu electrochemical composite deposition: A: horizontal plating; B: vertical plating. 90

Fig. 3-30 SEM SE plan view images (left) and cross section images (right) of Sn-Cu films deposited onto Au seed layers from

Sn-citrate suspensions with Cu particles (0.22 mol/L $\text{SnCl}_2 \cdot 2\text{H}_2\text{O}$ + 0.4 mol/L tri-ammonium citrate + 0.5 g/L Cu) with different experimental set-ups: (a) horizontal plating; (b) vertical plating. The current density used was 10 mA/cm^2 , the plating time was 1 hour and stirring speed was 80 rpm.

91

Fig. 3-31 SEM BSE plan view images of Sn-Cu films after polishing. The films were plated onto Au seed layers from suspensions containing 0.22 mol/L $\text{SnCl}_2 \cdot 2\text{H}_2\text{O}$, 0.4 mol/L tri-ammonium citrate, and 0.2 g/L Cu. (a) Without ultrasonic dispersion; (b) with ultrasonic dispersion. The current density used was 10 mA/cm^2 and the stirring speed was 80 rpm.

91

Fig. 3-32 Particle size measurements of Sn-citrate suspensions with Cu particles, without and with the addition of sodium metaphosphate (S.M.) as a dispersant. The solution contains 0.22 mol/L $\text{SnCl}_2 \cdot 2\text{H}_2\text{O}$, 0.30 mol/L tri-ammonium citrate, and 0.2 g/L copper particles.

92

Fig. 3-33 SEM SE plan view images (left) and cross section images (right) of Sn-Cu films plated onto Au seed layers from suspensions containing two different Cu concentrations: (a) PC plating, 0.5 g/L Cu, (b) PC plating, 0.2 g/L Cu. The concentrations of $\text{SnCl}_2 \cdot 2\text{H}_2\text{O}$, tri-ammonium citrate and sodium metaphosphate were kept at 0.22 mol/L, 0.30 mol/L and 0.48 g/L, respectively. The current density used was 10 mA/cm^2 , the plating time was 30 min and the stirring speed was 80 rpm.

93

Fig. 4-1 Polarization curves for Sn-citrate solutions. In all solutions, the concentration of $\text{SnCl}_2 \cdot 2\text{H}_2\text{O}$ was kept at 0.22 mol/L, while the concentration of tri-ammonium citrate was varied as follows: S1, 0.30 mol/L; S2, 0.33 mol/L; S3, 0.44 mol/L; S4, 0.66 mol/L.

102

Fig. 4-2	Sn(II)-citrate speciation diagram as a function of pH for solution S1 (0.22 mol/L Sn ²⁺ and 0.30 mol/L tri-ammonium citrate). γ is the molar percentage of Sn(II)-citrate complexes.	104
Fig. 4-3	Speciation diagrams as a function of pH for solutions S1 (a), S2 (b), S3 (c) and S4 (d). Note that all solutions contain 0.22 mol/L Sn ²⁺ , but different concentrations of tri-ammonium citrate: (a) 0.30 mol/L, (b) 0.33 mol/L, (c) 0.44 mol/L, and (d) 0.66 mol/L.	106
Fig. 4-4	(a) Calculated reduction potentials for SnHL ⁻ , SnH ₂ L and SnH ₃ L ⁺ for solutions S1, S2, S3 and S4 at natural pH. (b) Comparison of calculated and experimental reduction potentials as a function of tri-ammonium citrate concentration.	107
Fig. 4-5	(a) Calculated reduction potentials for SnHL ⁻ , SnH ₂ L and SnH ₃ L ⁺ for solution S1 (0.22 mol/L Sn ²⁺ and 0.30 mol/L tri-ammonium citrate) at pH 1.1, 2.5 and 4.1. (b) Polarization curves for solution S1 at pH 1.1, 2.5 and 4.1. (c) Comparison of calculated and experimental reduction potentials for solution S1 as a function of pH.	108
Fig. 4-6	SEM SE images (plan view and cross section) of Sn films electrodeposited from solution S1 (0.22 mol/L Sn ²⁺ and 0.30 mol/L tri-ammonium citrate) at pH 1.1 (a), 2.5 (b) and 4.1 (c).	109
Fig. 4-7	EDX point analysis for Sn plated from solution S1 at pH 1.1 (a-1, a-2) and 2.5 (b-1, b-2).	111
Fig. 4-8	XRD pattern for precipitates obtained from solution S1 at pH 2.5.	113
Fig. 4-9	XPS survey spectrum for precipitates obtained from solution S1 at pH 2.5.	113
Fig. 4-10	XPS C 1s spectrum from: a) citric acid, b) tri-ammonium citrate and c) precipitates obtained from solution S1 at	

	pH 2.5.	114
Fig. 4-11	XPS O 1s spectrum from: (a) citric acid, (b) tri-ammonium citrate and (c) precipitates obtained from solution S1 at pH 2.5.	115
Fig. 4-12	XPS Sn3d core level spectrum for precipitates obtained from solution S1 at pH 2.5. The thick solid line is the experimental spectrum; the thin line is the fitted spectrum.	117
Fig. 4-13	Proposed structure of Sn(II)-citrate precipitate with a formula of Sn ₂ L (where L represents the tetravalent citrate ligand).	118
Fig. 5-1	Potential-time transients for plating from Sn-citrate solution (0.22 mol/L SnCl ₂ ·2H ₂ O and 0.30 mol/L tri-ammonium citrate) on Pt at different current densities: (a) 5 mA/cm ² ; (b) 10 mA/cm ² ; (c) 15 mA/cm ² ; (d) 25 mA/cm ² ; (e) 35 mA/cm ² ; (f) 50 mA/cm ² ; (g) 75 mA/cm ² .	124
Fig. 5-2	Potential-time transients for plating from Sn-Cu-citrate solution (0.30 mol/L tri-ammonium citrate + 0.22 mol/L SnCl ₂ ·2H ₂ O + 0.003 mol/L CuCl ₂ ·2H ₂ O) on Pt at different current densities: (a) 5 mA/cm ² ; (b) 10 mA/cm ² ; (c) 15 mA/cm ² ; (d) 25 mA/cm ² ; (e) 35 mA/cm ² ; (f) 50 mA/cm ² ; (g) 75 mA/cm ² .	126
Fig. 5-3	Current-time transient curves for Sn electrodeposition on Pt at potentials ranging between -0.72 and -1.5 V.	129
Fig. 5-4	Normalised $(j/j_{max})^2$ vs. t/t_{max} plots obtained from current-time transient curves in Fig. 3 at -0.72, -1.1 and -1.5 V. The thick and thin solid lines represent the theoretical models for instantaneous and progressive nucleation, respectively.	131
Fig. 5-5	Current-time transient curves for Sn-Cu alloy electrodeposition on Pt at potentials ranging between -0.72 and -1.5 V.	132
Fig. 5-6	Normalised $(j/j_{max})^2$ vs. t/t_{max} plots obtained from current-time transient curves in Fig. 5 at -0.72, -1.1 and -1.5 V. The thick and thin solid lines represent the theoretical models for	

	instantaneous and progressive nucleation, respectively.	132
Fig. 5-7	Auger SE images for (a) Pt seed layer and Sn deposited under potentiostatic conditions of (b) -0.72 V, (c) -1.1 V and (d) -1.5 V for 0.2 seconds.	134
Fig. 5-8	Auger SE images for (a) Pt seed layer and Sn-Cu deposited under potentiostatic conditions of (b) -0.72 V, (c) -1.1 V and (d) -1.5 V for 0.2 seconds.	135
Fig. 5-9	AFM images for (a) Pt seed layer and Sn deposited under potentiostatic conditions of (b) -0.72 V, (c) -1.1 V and (d) -1.5 V for 0.2 seconds.	136
Fig. 5-10	(a) Auger spectra for Sn deposit on Pt at an applied potential of -0.72 V for 0.2 seconds. (b) Auger SE image for Sn nuclei deposited on Pt under potentiostatic conditions at -0.72 V for 0.2 seconds; the area in the square is the tested area for the imaging analysis. (c) Pt and (d) Sn Auger imaging analysis for Sn nuclei deposited on Pt under potentiostatic conditions at -0.72 V for 0.2 seconds.	137
Fig. 5-11	AFM images for (a) Pt and Sn-Cu alloys deposited under potentiostatic conditions of (b) -0.72 V, (c) -1.1 V and (d) -1.5 V for 0.2 seconds.	138
Fig. 5-12	(a) Auger spectra for Sn-Cu deposit on Pt at an applied potential of -0.72 V for 0.2 seconds. (b) Auger SE image for Sn-Cu nuclei deposited on Pt under potentiostatic conditions at -0.72 V for 0.2 seconds; the area in the square is the tested area for the imaging analysis. (c) Pt, (d) Sn and (e) Cu Auger imaging analysis for Sn-Cu alloys deposited on Pt under potentiostatic conditions at -0.72 V for 0.2 seconds.	139
Fig. 5-13	XRD patterns of Sn electrodeposited on Pt at different potentials: (a) -0.72 V, (b) -1.1 V, (c) -1.5 V plated for 0.2 seconds.	140

- Fig. 5-14 XRD patterns of Sn-Cu alloys electrodeposited on Pt at different potentials: (a) -0.72 V, (b) -1.1 V, (c) -1.5 V plated for 0.2 seconds; (d) -0.72 V plated for 0.8 seconds. 140
- Fig. 5-15 SEM SE plan view (a) and cross section (b) images of Sn-Cu electrodeposited on Ni or Au seed layer for different lengths of time in solution containing 0.22 mol/L $\text{SnCl}_2 \cdot 2\text{H}_2\text{O}$, 0.003 mol/L $\text{CuCl}_2 \cdot 2\text{H}_2\text{O}$ and 0.30 mol/L tri-ammonium citrate. The current density is 10 mA/cm². 142
- Fig. 5-16 XRD patterns for Sn-Cu electrodeposited onto Ni substrate for 1s, 4s and 7s. 144
- Fig. 5-17 Schematic illustration of three different film growth mechanisms: (a) island (Volmer-Weber) growth mechanism, (b) layer growth (Frank-van der Merwe) mechanism and (c) mixed growth mechanism. 144
- Fig. 5-18 Auger SE images (left) and Auger spectra point analysis (right) of Sn-Cu electrodeposited onto Ni substrates for: (a) 1 s, (b) 4 s and (c) 7 s. 145
- Fig. 6-1 Schematic illustration of plating set up for Sn-Ag-Cu electrochemical composite deposition: (a) magnetic agitation, 40mL suspension; (b) agitation from top, 80mL suspension. 153
- Fig. 6-2 Deposit Ag and Cu content as a function of Ag concentration in 40mL suspension. The concentrations of $\text{SnCl}_2 \cdot 2\text{H}_2\text{O}$, tri-ammonium citrate, and $\text{CuCl}_2 \cdot 2\text{H}_2\text{O}$ were fixed at 0.22 mol/L, 0.30 mol/L, and 0.001 mol/L. The current density was 10 mA/cm². The suspension was agitated with a magnetic stir bar during electroplating. 154
- Fig. 6-3 SEM SE plan view images of Sn-Ag-Cu films deposited onto Au seed layers from 40mL Sn-Cu-citrate suspensions with different Ag additions: (a) 0.8 g/L, (b) 1 g/L and (c) 3 g/L. The concentrations of $\text{SnCl}_2 \cdot 2\text{H}_2\text{O}$, tri-ammonium citrate, and

- CuCl₂·2H₂O were fixed at 0.22 mol/L, 0.30 mol/L, and 0.001 mol/L. The current density was 10 mA/cm². The suspensions were agitated with a magnetic stir bar during electroplating. 154
- Fig. 6-4 Deposit Ag and Cu content as a function of Ag concentration in 80 mL suspension. The concentrations of SnCl₂·2H₂O, tri-ammonium citrate and CuCl₂·2H₂O were fixed at 0.22 mol/L, 0.30 mol/L and mol/L, respectively. The current density was 10 mA/cm². The suspensions were agitated by an overhead mechanical stirrer during electroplating. 155
- Fig. 6-5 SEM SE plan view images of Sn-Ag-Cu films deposited onto Au seed layers from 80mL Sn-Cu-citrate suspensions with different Ag additions: (a) 0.6 g/L, (b) 0.8 g/L and (c) 1 g/L. The concentrations of SnCl₂·2H₂O, tri-ammonium citrate, and CuCl₂·2H₂O were fixed at 0.22 mol/L, 0.30 mol/L and 0.001 mol/L, respectively. The current density was 10 mA/cm². The suspensions were agitated with an overhead mechanical stirrer during electroplating. 155
- Fig. 6-6 XRD pattern of Sn-Cu-Ag film deposited onto Au seed layer from suspension containing 0.22 mol/L SnCl₂·2H₂O, 0.30 mol/L tri-ammonium citrate, 0.001 mol/L CuCl₂·2H₂O and 0.8g/L Ag nano-particles. The current density was 10 mA/cm². 156
- Fig. 6-7 Deposit Ag content as a function of current density in 80mL Sn-Cu-citrate + Ag suspension. The concentrations of SnCl₂·2H₂O, tri-ammonium citrate and Ag were fixed at 0.22 mol/L, 0.30 mol/L and 0.8 g/L, respectively. Ag content in the area between the two solid horizontal lines are acceptable for Sn-Ag-Cu solder based on literature. 158
- Fig. 6-8 Deposit Cu content as a function of current density in 80mL Sn-Cu-citrate + Ag suspension. The concentrations of SnCl₂·2H₂O, tri-ammonium citrate and Ag were fixed at

0.22 mol/L, 0.30 mol/L and 0.8 g/L, respectively. The solid horizontal line represents the eutectic composition of Sn-Cu solder.

158

- Fig. 6-9 SEM SE images of Sn-Ag-Cu films deposited onto Au seed layers from 80mL Sn-Cu-citrate + Ag suspensions under different current densities: (a) low magnification plan view images, (b) high magnification plan view images and (c) cross section images. The concentrations of $\text{SnCl}_2 \cdot 2\text{H}_2\text{O}$, tri-ammonium citrate and Ag were fixed at 0.22 mol/L, 0.30 mol/L and 0.8 g/L, respectively. 160
- Fig. 6-10 Sn-Ag-Cu film plating rate as a function of current density from suspensions containing different $\text{CuCl}_2 \cdot 2\text{H}_2\text{O}$ concentrations. The concentrations of $\text{SnCl}_2 \cdot 2\text{H}_2\text{O}$, tri-ammonium citrate and Ag were fixed at 0.22 mol/L, 0.30 mol/L, and 0.8 g/L, respectively. 161
- Fig. 6-11 (a) Deposit Cu content as a function of current density for both Sn-Ag-Cu films and Sn-Cu films plated under the same conditions. The concentrations of $\text{SnCl}_2 \cdot 2\text{H}_2\text{O}$, tri-ammonium citrate and Ag were fixed at 0.22 mol/L, 0.30 mol/L and 0.8 g/L, respectively. (b) Differences in Cu content between Sn-Ag-Cu films and Sn-Cu films as a function of current density. 162
- Fig. 6-12 Polarization curves for (a) Sn-Cu-citrate solution (0.22 mol/L $\text{SnCl}_2 \cdot 2\text{H}_2\text{O}$ + 0.003 mol/L $\text{CuCl}_2 \cdot 2\text{H}_2\text{O}$ + 0.30 mol/L tri-ammonium citrate) and (b) Sn-Cu-citrate suspension with Ag nano-particles (0.22 mol/L $\text{SnCl}_2 \cdot 2\text{H}_2\text{O}$ 0.003 mol/L $\text{CuCl}_2 \cdot 2\text{H}_2\text{O}$ + 0.30 mol/L tri-ammonium citrate + 0.8 g/L Ag. The stirring speed was 600 rpm. 163
- Fig. 6-13 Sn-Ag-Cu and Sn-Cu film plating rate as a function of current density from baths containing different $\text{CuCl}_2 \cdot 2\text{H}_2\text{O}$ concentrations. The concentrations of $\text{SnCl}_2 \cdot 2\text{H}_2\text{O}$, tri-

- ammonium citrate and Ag were fixed at 0.22 mol/L, 0.30 mol/L and 0.8 g/L, respectively. 163
- Fig. 6-14 SEM SE plan view images of films deposited onto Au seed layers from (a) Sn-citrate solution + Ag particles and (b) Cu-citrate solution + Ag particles. The concentrations of tri-ammonium citrate and Ag were fixed at 0.30 mol/L and 0.8 g/L, respectively. The concentrations of $\text{SnCl}_2 \cdot 2\text{H}_2\text{O}$ and $\text{CuCl}_2 \cdot 2\text{H}_2\text{O}$ were 0.22 mol/L. 165
- Fig. 6-15 Deposit Ag and Cu content from suspensions without and with SDS and with different stirring times. The concentrations of $\text{SnCl}_2 \cdot 2\text{H}_2\text{O}$, tri-ammonium citrate, $\text{CuCl}_2 \cdot 2\text{H}_2\text{O}$, Ag and SDS were fixed at 0.22 mol/L, 0.30 mol/L, 0.001 mol/L, 0.8 g/L and 0.1 g/L, respectively. The current density was 10 mA/cm^2 . 167
- Fig. 6-16 Solutions after stirring for different times: (a) Sn-Cu-citrate + Ag, stirred for 1 hour, (b) Sn-Cu-citrate + Ag + SDS, stirred for 1 hour, (c) Sn-Cu-citrate + Ag + SDS, stirred for 4 hrs, (d) Sn-Cu-citrate + Ag + SDS, stirred for 24 hrs. 167
- Fig. 6-17 SEM SE plan view images of Sn-Ag-Cu films deposited onto Au seed layers from 80mL suspensions: (a) Sn-Cu-citrate + Ag, stirred for 1 hour, (b) Sn-Cu-citrate + Ag + SDS, stirred for 4 hrs, (c) Sn-Cu-citrate + Ag + SDS, stirred for 24 hrs. The concentrations of $\text{SnCl}_2 \cdot 2\text{H}_2\text{O}$, tri-ammonium citrate, $\text{CuCl}_2 \cdot 2\text{H}_2\text{O}$, Ag and SDS were fixed at 0.22 mol/L, 0.30 mol/L, 0.001 mol/L, 0.8 g/L and 0.1g/L, respectively. The current density was 10 mA/cm^2 . 169
- Fig. 6-18 Deposit Ag and Cu content as a function of Ag concentration in 80 mL Sn-Cu-citrate + Ag + SDS suspensions. The concentrations of $\text{SnCl}_2 \cdot 2\text{H}_2\text{O}$, tri-ammonium citrate, and SDS were fixed at 0.22 mol/L, 0.30 mol/L and 0.1g/L, respectively. The suspensions were stirred for 24hrs. The current

- density was 10 mA/cm². 169
- Fig. 6-19 SEM SE plan view images of Sn-Ag-Cu films deposited onto Au seed layers from 80 mL Sn-Cu-citrate + Ag + SDS suspensions: (a) 0.001 mol/L CuCl₂·2H₂O + 0.6 g/L Ag, (b) 0.001 mol/L CuCl₂·2H₂O + 1 g/L Ag, (c) 0.003 mol/L CuCl₂·2H₂O + 0.6 g/L Ag and (d) 0.003 mol/L CuCl₂·2H₂O + 0.8 g/L Ag. The concentrations of SnCl₂·2H₂O, tri-ammonium citrate and SDS were fixed at 0.22 mol/L, 0.30 mol/L and 0.1g/L, respectively. The suspensions were stirred for 24hrs. The current density was 10 mA/cm². 170
- Fig. 6-20 Deposit Ag and Cu content as a function of CuCl₂·2H₂O concentration in 80 mL Sn-Cu-citrate + Ag + SDS suspensions. The concentrations of SnCl₂·2H₂O, tri-ammonium citrate, Ag and SDS were fixed at 0.22 mol/L, 0.30mol/L, 0.6 g/L and 0.1g/L, respectively. The suspensions were stirred for 24hrs. The current density was 10 mA/cm². 170
- Fig. 6-21 SEM SE plan view images of Sn-Ag-Cu films electrodeposited onto Au seed layers from 80 mL Sn-Cu-citrate + Ag + SDS suspensions with different CuCl₂·2H₂O concentrations: (a) 0.001 mol/L, (b) 0.003 mol/L and (c) 0.005 mol/L. The concentrations of SnCl₂·2H₂O, tri-ammonium citrate, Ag and SDS were fixed at 0.22 mol/L, 0.30 mol/L, 0.8 g/L and 0.1g/L, respectively. The solutions were stirred for 24hrs. The current density was 10 mA/cm². 171
- Fig. 6-22 Comparison of DSC curves of as-deposited Sn-Ag-Cu films on Au seed layers and as-deposited Sn-Cu alloys on Au seed layers and Ni substrates. (a) Sn-4.9 wt% Ag-1.1 wt% Cu/Au; (b) Sn-1.1 wt% Cu/Au, (c) Sn-1.1 wt% Cu/Ni. 172
- Fig. 6-23 DSC curves of as-deposited Sn-Ag-Cu films on Au seed layers with various compositions. (a) Sn-3.3 wt% Ag-1.1

	wt% Cu, (b) Sn-3.6 wt% Ag-1.4 wt% Cu, (c) Sn-4.9 wt% Ag-1.4 wt% Cu.	173
Fig. 7-1	SEM BSE cross section images of Sn-Cu films electrodeposited onto Cu substrate (from sectioned Cu sheet) after reflow at 260°C for 90s: (a) Sn-Cu/Cu, low magnification, (b) Sn-Cu/Cu, higher magnification, (c) Sn-Cu/Cu after etching most of the solder layer.	180
Fig. 7-2	XRD patterns of Sn-Cu films electrodeposited onto Cu substrate (from sectioned Cu sheet): (a) as-deposit, (b) after reflow at 260°C for 90s.	181
Fig. 7-3	Deposit Cu distribution in Sn-Cu films electrodeposited onto Cu substrate (from sectioned Cu sheet) along the cross section before and after reflow at 260°C for 90s.	182
Fig. 7-4	(a) Schematic illustration of sample structure for Sn-Cu/Cu reflow analysis; (b) SEM BSE image of Sn-Cu/Cu after reflow at 260°C for 30s at spot I in Fig. 7-4a with a carbon barrier layer; (c) SEM BSE image of Sn-0.7wt%Cu/Cu after reflow at 260°C for 30s at spot II as in Fig. 7-4a without a carbon barrier layer.	183
Fig. 7-5	Schematic illustration of the formation of Cu ₃ Sn and Cu ₆ Sn ₅ bilayer at the interface of Sn-Cu/Cu during reflow.	184
Fig. 7-6	SEM BSE cross section images of Sn-0.7wt%Cu films electrodeposited onto Cu substrate after reflow and aging: (a) reflowed at 260°C for 30 s, no aging; (b) reflowed at 260°C for 30 s and aged at 125°C for 24hrs; (c) reflowed at 260°C for 30s and aged at 125°C for 48 hrs; (d) reflowed at 260°C for 30 s and aged at 125°C for 72 hrs.	185
Fig. 7-7	Schematic illustration of the diffusion mechanism for the growth of IMCs layers in reflowed Sn-Cu/Cu during aging.	186
Fig. 7-8	Plot of Cu ₃ Sn thickness in Sn-Cu/Cu as a function of square root of aging time at 125°C.	187

Fig. 7-9	SEM BSE cross section images of Sn-Cu films electrodeposited onto Ni substrate, after reflow at 260°C for 90s: (a) at low magnification; (b) at higher magnification; (c) etched.	188
Fig. 7-10	(a) Auger SE plan view image of Sn-Cu films electrodeposited onto Ni substrate after reflow at 260°C for 30s and etching; (b) Auger point analysis at points 1 to 5 in (a).	189
Fig. 7-11	XRD patterns of Sn-Cu films electrodeposited onto Ni substrate: (a) as-deposited, (b) as-deposited and etched, (c) after reflow at 260°C for 30 s, (d) after reflow at 260°C for 30 s and etched.	191
Fig. 7-12	(a) Auger SE plan view image of Sn-Cu film electrodeposited onto Ni substrate after etching; (b) Auger point analysis of points 1 and 2 in (a) after etching.	192
Fig. 7-13	Deposit Cu distribution in Sn-Cu films electrodeposited onto Ni substrate along the cross section before and after reflow at 260°C for 30s.	193
Fig. 7-14	Ni distribution in Sn-Cu films electrodeposited onto Ni substrate along the cross section after reflow at 260°C for 30s.	193
Fig. 7-15	SEM BSE cross section images of Sn-Cu films electrodeposited onto Ni substrate after reflow and aging: (a) reflowed at 260°C for 30s; (b) reflowed at 260°C for 30s and aged at 125°C for 24hrs; (c) reflowed at 260°C for 30s and aged at 125°C for 48hrs; (d) reflowed at 260°C for 30s and aged at 125°C for 72hrs.	194
Fig. 7-16	SEM BSE images of Sn-Ag-Cu films deposited onto Cu substrate: (a) plan view, after etching; (b) cross section, (c) plan view, after reflow at 260°C for 30s and etching; (d) cross section, after reflow at 260°C for 30s and before etching.	195
Fig. 7-17	XRD pattern of Sn-Ag-Cu film after reflow at 260°C	

	for 30s.	196
Fig. 7-18	Deposit Cu distribution through thickness for Sn-Ag-Cu films deposited onto Cu substrate before and after reflow at 260°C for 30s. The analysis points are indicated in Figure 7-16b.	197
Fig. 7-19	Deposit Ag distribution through thickness for Sn-Ag-Cu films deposited onto Cu substrate before and after reflow at 260°C for 30s. The analysis points are indicated in Figure 7-16d.	198
Fig. 7-20	SEM BSE cross section image of Sn-Ag-Cu film deposited onto Cu substrate after reflow at 260°C for 30s and etching.	198
Fig. 7-21	SEM BSE cross section images of Sn-Ag-Cu films deposited onto Cu substrate after reflow and aging: (a) reflowed at 260°C for 30s; (b) reflowed at 260°C for 30s and aged at 125°C for 24hrs; (c) reflowed at 260°C for 30s and aged at 125°C for 48hrs; (d) reflowed at 260°C for 30s and aged at 125°C for 72hrs. (e)-(f) are SEM BSE images of samples (a)-(d) after etching.	199
Fig. 7-22	Plot of Cu ₃ Sn layer diffusion distance in Sn-Ag-Cu/Cu as a function of the square root of aging time at 125°C.	200
Fig. 7-23	SEM SE plan view images of Sn-Ag-Cu films deposited onto Ni substrate: (a) after reflowing at 230°C for 30s and etching; (b) higher magnification at location I in (a); (c) higher magnification image at location II in (a); (d) after reflowing at 260°C for 30s and etching.	201
Fig. 7-24	(a), (c) TEM image of Sn-Ag-Cu/Ni sample after reflow at 260°C for 30s; (b) TEM selected area diffraction (SAD) pattern from region 1 in (a); (d) TEM SAD pattern from region 1 in (c).	202
Fig. 7-25	(a) TEM image of Sn-Ag-Cu/Ni sample after reflow at 260°C for 30s (b) TEM SAD pattern from region 1 in (a).	203
Fig. 7-26	SEM BSE cross section images of Sn-Ag-Cu film deposited onto Ni substrate: a) after reflow at 260°C for 30s, without	

	etching; b) after etching in for 5s.	204
Fig. 7-27	(a) TEM cross section image at Sn-Ag-Cu/Ni interface after reflow at 260°C for 30s; (b) TEM SAD pattern from regions 1 and 2 in (a); (c) TEM SAD pattern from region 3 in (a).	205
Fig. 7-28	(a) TEM image of Sn-Ag-Cu/Ni sample after reflow at 260°C for 30s; (b) TEM SAD pattern from region 1 in (a); (c) TEM image of (Ni,Cu) ₃ Sn ₄ particle in Sn-Ag-Cu/Ni sample after reflow at 260°C for 30s.	206
Fig. 7-29	SEM BSE cross section images of Sn-Ag-Cu films deposited onto Ni substrate after reflow and aging: (a) reflowed at 260°C for 30s; (b) reflowed at 260°C for 30s and aged at 125°C for 24hrs; (c) reflowed at 260°C for 30s and aged at 125°C for 48hrs; (d) reflowed at 260°C for 30s and aged at 125°C for 72hrs. (e)-(f) are SEM BSE images of sample (a)-(d) after etching.	206
Fig. 8-1	SEM SE plan view (left) and cross section (right) images of Sn-Ag films deposited onto Au seed layer from plating baths containing 0.22 mol/L SnCl ₂ ·2H ₂ O, 0.01 mol/L AgNO ₃ , and 0.30 mol/L tri-ammonium citrate. The current density is 10 mA/cm ² and the plating time is 30 min.	220
Fig. 8-2	EDX point analysis for Sn-Ag deposits at (a) position 1 in Fig. 8-1a and (b) position 2 in Fig. 8-1b.	220

Abbreviations

AFM	Atomic force microscopy
ANPR	Advanced notice of proposal rule
BGA	Ball grid arrays
BSE	Backscattered electron
CV	Cyclic voltammetric measurement
DC	Direct current
DSC	Differential scanning calorimetry
EDX	Energy dispersive x-ray
EMS	Electronic manufacturing services
EPA	Environmental protection agency
EPMA	Electron probe microanalysis
G+N	Gelatin + naphthol
HT	Heliotropin
IC	Integrated circuit
IHP	Inner Helmholtz plane
IMC	Intermetallic compound
I/O	Input/output
IPC	International printed circuit association
JEITA	Japan Electronics and Information Technology Industries Association
MSA	Methanesulfonate acid
NEMI	National Electronics Manufacturing Initiative
OHP	Out Helmholtz plane
OPPE	Iso-octyl phenoxy polyethoxy ethanol
PBB	Polybrominated biphenyls
PBDE	Polybrominated diphenyl ether
PC	Pulsed current
PCB	Printed circuit board

POELE	Polyoxyethylene lauryl ether
RF	Radio frequency
RoHS	Restriction of hazardous substances
SAD	Selected area diffraction
SCE	Saturated calomel electrode
SDS	Sodium lauryl sulfate
SE	Secondary electron
SEM	Scanning electron microscopy
S.M.	Sodium metaphosphate
SMT	Surface mount technology
TEA	Triethanolamine
TEM	Transmission electron microscopy
TSCA	Toxic substance control act
UBM	Under bump metallurgy
UV	Ultraviolet
WEEE	Waste electrical and electronic equipment directive
XPS	X-ray photoelectron spectroscopy
XRD	X-ray diffraction

Symbols

A	Electrode surface area
C_0	Concentration of the metal ions in bulk solution
$C_{M^{n+}}, C'_{M^{n+}}, C''_{M^{n+}}$	Concentration of the metal ions at the cathode surface
C_R, C'_R, C''_R	Concentration of the reduction products at the cathode surface
D	Diffusion coefficient
E^0	Standard electrode potential
F	Faraday's constant
ΔG^0	Standard Gibbs free energy
i	Applied current
j_a	Average current density
j_p	Peak current density
j_{max}	Current coordinate at the peak of the current-time transient curve
n	Number of electrons consumed in the reaction
R	Universal gas constant
t_{max}	Time coordinate at the peak of the current-time transient curve
T_{OFF}	Off-time
T_{ON}	On-time
τ	Transition time
$\gamma_{ls}, \gamma_{vl}, \gamma_{sv}$	Interfacial tension
δ	Thickness of the diffuse layer
θ	Contact angle
$\eta, \eta_{mt}, \eta_{rxt}, \eta_{ct}$	Overpotential
$R, R_{mt}, R_{rxn}, R_{ct}$	Resistance
φ	Potential

Chapter 1 Introduction

Solders are the most important joining materials in electronic packages and assemblies (Evans et al., 2007). During the past 60 years, eutectic and near-eutectic Pb-Sn solders have been used as the principal joining materials because of their low cost, low melting point (183°C), outstanding solderability and good mechanical properties (Suganuma, 2001; Puttlitz and Stalter, 2004). Pb-Sn solders are also highly compatible with electronics assembly processes and materials and can form stable joints that are usable under a wide variety of service environments (Suganuma, 2001; Puttlitz and Stalter, 2004). However, increasing health and environmental concerns worldwide regarding the toxicity of Pb have prompted countries such as Japan and those from the European Union to pass legislation prohibiting or restricting the use of Pb-Sn solders (Abteu and Selvaduray, 2000). These restrictions have stimulated the development of a large number of Pb-free alternative solders (Abteu and Selvaduray, 2000; Suganuma, 2001; Kang et al., 2005), most of which are Sn-rich solders.

Among all the Pb-free solders, eutectic Sn-Cu solder is relatively cheap and it is mainly used in wave soldering. In addition, eutectic and near eutectic Sn-Ag-Cu solder is considered as one of the most promising candidates to replace Pb-Sn solders because of its relatively low melting temperature, enhanced mechanical properties, and relatively good wetting properties (Zeng and Tu, 2002; Suganuma, 2004; Anderson, 2007). It has been used in both reflow and wave soldering (Shangguan, 2005). Solders used in electronic assemblies can be fabricated by thin film deposition techniques such as evaporation, sputtering and electrodeposition. Electrodeposition has many advantages over the other two techniques, including low cost, low operating temperature, easy and precise control of thickness and film composition, and versatility with respect to substrate size and shape, and have been widely used to deposit solder alloys in electronic packaging. During soldering, chemical reactions between the solder and substrate

metal occur and intermetallic compounds (IMCs) form, which affect the performance of solder joints as well as the entire electronic product. The objective of this thesis is to investigate the deposition of eutectic and near eutectic Sn-Cu and Sn-Ag-Cu solders for electronic packaging applications, and to study the interactions between electrodeposited near eutectic Sn-Cu and Sn-Ag-Cu solders and substrate metals during reflow and aging.

The thesis contains eight chapters. After a brief introduction in Chapter 1, Chapter 2 provides a comprehensive literature review on electronic packaging, soldering technologies, and thin film deposition. Chapter 3 details the development of plating baths for Sn-Cu alloy deposition. Two different methods, electrodeposition and electrochemical composite deposition, are applied. Accordingly, two types of plating baths, which are simple and environmentally green, are developed. For the *electrodeposition* of Sn-Cu solder films, the plating solution contains Sn and Cu chloride salts and tri-ammonium citrate as a complexing agent. Both pulsed current (PC) plating and direct current (DC) plating are performed and compared according to their effects on deposit composition and microstructures. The effects of several plating parameters, e.g., tri-ammonium citrate concentration, $\text{CuCl}_2 \cdot 2\text{H}_2\text{O}$ concentration, current density, agitation, and additives, on deposit composition, microstructures, and phase structures are investigated in detail. In order to test solution stability, solution performance upon aging is studied. For the *electrochemical composite deposition* of Sn-Cu alloys, the plating bath contains Sn chloride salt, and tri-ammonium citrate with suspended Cu particles, along with sodium metaphosphate as a dispersant. The effects of dispersant on Cu particle size distribution, deposit composition, and morphology are studied.

Chapter 4 presents the results of a study on the solution chemistry of the investigated Sn-citrate systems. Citrate is a complexing agent for many metal ions during electrodeposition and is used as the only complexing agent in this research work for both Sn-Cu and Sn-Ag-Cu alloy deposition. Since Sn is the main ingredient in most of the Pb-free solders, it is beneficial to study Sn-citrate solution chemistry, as well as the role of Sn(II)-citrate complexes during Sn

electrodeposition. The distribution of various Sn(II)-citrate complexes and citrate ligands is calculated and the results are presented as speciation diagrams. Polarization studies and reduction potential calculations are performed for solutions with different citrate concentrations and at different pH values. Tin deposits from solutions at different pH are analyzed to understand the effect of different Sn(II)-citrate complexes on Sn electrodeposition. Precipitates are observed from Sn-citrate solutions at low pH and are identified using compositional and structural analyses.

Chapter 5 presents the results of a kinetic study on the initial stages of Sn and Sn-Cu electrodeposition from Sn-citrate and Sn-Cu-citrate solutions on Pt, using both current-controlled and potential-controlled electrochemical techniques. The diffusion coefficients for both Sn-citrate and Sn-Cu-citrate solutions are calculated from both the current-time transient plots and the Sand Equation. The analysis of the electrochemical and surface morphology results are carried out to determine the nucleation mechanism. To understand the mechanism of film growth, Sn-Cu films are electrodeposited from developed Sn-Cu-citrate solutions under controlled current densities for different lengths of time.

Chapter 6 describes the results of electrochemical composite deposition for Sn-Ag-Cu solder films, from Sn-Cu-citrate suspensions with Ag nanoparticles. Plating parameters such as current density, $\text{CuCl}_2 \cdot 2\text{H}_2\text{O}$ concentration, Ag particle concentration, and agitation are studied to obtain eutectic and near eutectic Sn-Ag-Cu solders. Sodium lauryl sulfate (SDS) is added to help disperse Ag nano-particles so that they can be evenly incorporated into cathode deposits. Chapter 6 also includes a study on the melting behavior of as-deposited Sn-Cu and Sn-Ag-Cu alloys using differential scanning calorimetry thermal analysis.

Chapter 7 presents results on the interfacial reactions between the as-deposited Sn-Cu or Sn-Ag-Cu solder films and Cu and Ni substrates. Intermetallic compounds (IMCs) form at the solder/substrate interface during soldering, and grow in thickness or increase in number during storage or in the use of the assemblies, especially if the operation temperature is relatively high. The challenge with respect to the formation of IMCs at the solder/substrate interface is

that a thin, continuous IMC layer is an essential requirement for good bonding, but too thick an IMC layer at the solder/substrate interface may decrease the reliability of the solder joints. Therefore, it is important to study the formation and growth of IMCs at the solder/substrate interface during reflow and aging. In Chapter 7, interfacial reactions between near eutectic Sn-Cu and Sn-Ag-Cu solders deposited from solutions developed in Chapter 3 and Chapter 6 and two common substrate materials, Cu and Ni, during reflow and aging are investigated, by characterizing the microstructure of the IMCs formed at the interface.

Finally, Chapter 8 summarizes the results of this thesis work and points out future research work that can be undertaken to move Sn-Cu and Sn-Ag-Cu solder research forward.

Chapter 2 Literature review

2.1 Electronic packaging

Electronic packaging refers to the processes to establish interconnections between electrical components such as transistors, capacitors, and resistors to form circuits, functionalize these integrated circuits (ICs, also called chips) through interconnections, and support and protect the ICs from the external environment. Individual ICs are not really useful and must be interconnected to other components such as input/output (I/O) devices and power supplies. The electronic packages thus serve four functions (Datta et al., 2005): provide electrical or photonic contact to and from the ICs; distribute the signals to and from the ICs; dissipate the heat and stress generated between ICs and the printed circuit board (PCB) during operation; provide mechanical support and environmental isolation to the components and interconnections.

There are many different types of packages in use today. Based on the types of components to be packaged together, interconnections can be separated into three levels. Level 1 interconnections involve joining of ICs to a substrate, Level 2 interconnections involve joining of Level 1 packages to a PCB, and Level 3 interconnections include cable-connector assemblies used to transmit signals between PCBs and the hard wired solder joints (Puttlitz and Stalter, 2004; Datta et al., 2005). In this thesis, only Level 1 and Level 2 interconnections are of interest.

2.1.1 Level 1 interconnections

Level 1 interconnections refer to the connections made between an IC die and a substrate. Techniques include wire bonding, tape automated bonding and flip-chip packaging. Both wire bonding and tape automated bonding are bonding through wires, which means the bonding pads on the IC are connected to the leads

on the substrate using gold or aluminum wires. The difference is that for wire bonding technology, the bonds are formed sequentially, while for tape automated bonding all the wires are flat circuit traces and all the bonds are formed in a single step. In flip-chip packaging, wires are replaced by solder balls or solder bumps. An array of solder balls is deposited on wettable metal layers on the IC die and a matching footprint of solder-wettable metal layers are deposited on the substrate. The IC die is then flipped over to join to the substrate. Most solder balls used in flip-chip packaging are made from Pb-rich, Pb-Sn alloys such as Pb-3Sn and Pb-5Sn¹. They are typically deposited by evaporation or electrodeposition on the IC bond pads. Normally, three different seed layers, an adhesion layer, a solderable layer, and a diffusion barrier layer, are deposited on the IC bond pads (Al or Cu) to help the solder wet and join to the pads. These seed layers are also referred to as the under bump metallurgy (UBM). Copper is the most popular choice for the adhesion layer and the solderable layer, mainly due to its good wetting property with solders. Nickel often serves as the diffusion barrier layer. A schematic drawing of a flip-chip joint is shown in Fig. 2-1. During soldering or normal

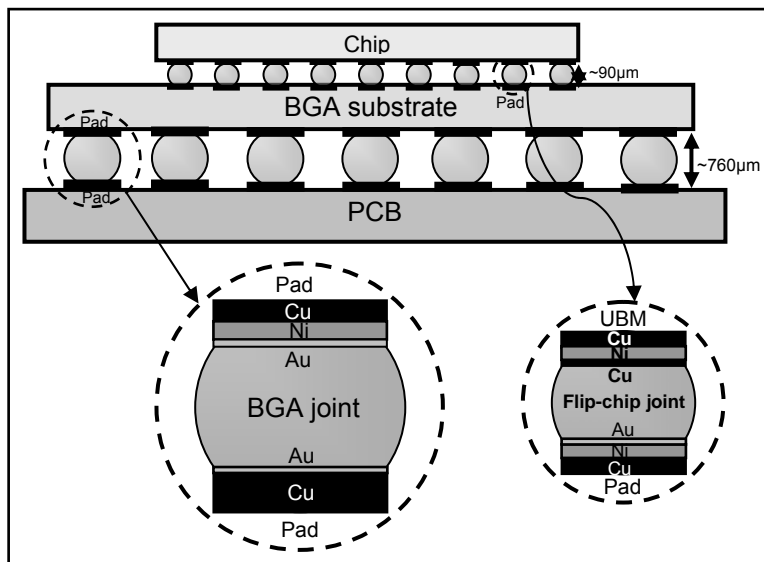


Fig. 2-1 Schematic drawings showing cross sections of a BGA joint and a flip-chip joint in an electronic package (Ho et al., 2007).

¹ All the alloy compositions in this thesis are expressed as weight percent, unless otherwise specified.

service of the device, the Cu layer will be consumed completely, exposing the Ni layer to the solder eventually. The top layer of the Ni metallization is covered with a noble metal, such as Au, to prevent oxidation that inhibits solder wetting. The Au layer will be rapidly dissolved into the solder during soldering.

2.1.2 Level 2 interconnections

Level 2 interconnections are solder joints that attach Level 1 packages to the PCBs, which provide both mechanical support and electrical interconnection for the devices. The most common PCB is made from epoxy resin with glass reinforcement. Plated through-hole and surface mount technology (SMT) are the two most popular Level 2 packaging styles. In the plated through-hole technique, component leads are placed through holes on the PCB, and the board is then moved over a stationary solder wave. The solder is drawn upwards and forms a bond between the IC package leads and the PCB pads. This process is called wave soldering. It is a low cost and simple technology. However, it is not amenable to mounting large numbers of components in a small PCB area. Surface-mount technology is a method in which IC packages are soldered directly onto the surface of PCB. There is normally no lead or small leads with various styles, which makes the SMT components smaller than the plated through-hole counterpart. For both the wave soldering and the surface mount technology, those leads are typically made from Cu or Fe-Ni alloy with a Cu or Ni solderable finish and an electroplated Sn or Pb-Sn protective layer. Leadless chip devices use a thick Ag film as a conductor which is covered by a Ni or Cu solderable coating and then an electroplated Pb-Sn protective finish. Ball grid arrays (BGA) are one type of surface mount technology, with solder balls covering one side of the package and Cu pads deposited on the PCB in a pattern matching that of the solder balls. Once the device package is placed on the PCB, the assembly is heated either in a reflow oven or by an infrared heater to melt the solder balls which hold the package in alignment with the PCB. A schematic drawing of the BGA joint is shown in Fig. 2-1.

Summarizing all the popular material choices for the UBM and the surface finishes in both Level 1 and Level 2 interconnections, one can expect that the most common material sequences across a solder joints are Cu/solder/Cu, Cu/solder/Ni, and Ni/solder/Ni.

2.2 Soldering technologies for electronic packaging

Soldering is a well-known metallurgical joining method and has been the key assembly and interconnection technology for electronic packaging. Solder forms electrical interconnections between packaging levels, facilitates heat dissipation from active devices, provides mechanical/physical support, and serves as a solderable surface finish layer on PCBs and lead frames. The performance and quality of solders are crucial to the integrity of a solder joint, which in turn controls the overall lifespan of the electronic product.

2.2.1 Solder materials

Solders are generally described as fusible alloys with a liquidus temperature below 400°C. The elements commonly used in solder alloys are Sn, Pb, Cu, Ag, Au, Bi, In, Sb, and Cd. Details on Pb-Sn solders and other Pb-free solders used in electronic packaging will be discussed later.

Solders are applied in different physical forms, such as bar, ingot, wire, powder, ball, and paste. Among them, solder paste is the primary material used in electronic packaging (Harper, 2004). Solder paste is a mixture of solder alloy powder, flux, and other additives, which forms metallurgical bonds during soldering and can be adapted to automated production in making reliable and consistent solder joints.

Solder bumps are another form of solders used in electronic packaging (flip-chip technique and BGA). Because the temperature tolerance level of PCB materials is low, solders used in the Level 2 interconnections are limited to eutectic and near eutectic solders having a relatively low melting point, or with

other components such as Bi or In. In a two-level packaging, solder bumps with high melting point such as Pb-5Sn or Pb-10Sn are used in flip-chip technology to join the IC dies to a ceramic substrate, and then a second set of eutectic and near eutectic alloys such as Pb-62Sn are used to join the ceramic substrate to a PCB. Eutectic Pb-62Sn solder is used in the second set because it has a much lower melting point (183°C) than the Pb-rich solder (320°C), so that the Pb-rich solder bumps used in the first level packaging will not melt during second level packaging.

There are strict performance requirements for solders used in electronic packaging, as shown in Table 2-1. In general, solders must have the desired melting temperature and meet the expected levels of electrical, thermal, and mechanical performance. The solders must have good wettability to form solder joints, allow high volume soldering, and provide reliable solder joints under service conditions. The cost must not be too high.

Table 2-1 Important properties of solder alloys (Abteu and Selvaduray, 2000)

Properties relevant to manufacturing	Properties relevant to reliability and performance
Melting/liquidus temperature	Electrical conductivity
wettability	Thermal conductivity
Cost	Coefficient of thermal expansion
Environmental friendliness	Shear properties
Availability and number of suppliers	Tensile properties
Manufacturability using current processes	Creep properties
Recyclability	Fatigue properties
	Corrosion and oxidation resistance
	Intermetallic compound formation

Solders used in electronic packaging, including Pb-Sn and Pb-free solders, are discussed in the next sections.

2.2.1.1 Pb-Sn solder and its problems

Lead (Pb) and tin (Sn) as well as their alloys have been used as solders for several thousand years (Puttlitz and Stalter, 2004). In the past 60 years, eutectic

and near-eutectic Pb-Sn alloys have played a critical role in Level 1, Level 2 and Level 3 interconnections for commercial and military electronics assemblies. Much of this is because of their low cost, low eutectic melting point of 183°C, outstanding solderability, and ability to form stable solder joints that are capable of operating in a wide variety of service environments (Suganuma, 2001).

Despite the many attributes of Pb-Sn solders in electronics applications, legislations have been proposed and some of them have been passed in Japan and those countries from the European Union to prohibit or restrict the use of Pb-Sn solders, primarily because of the potential impact of Pb on human health and environment. Lead and Pb compounds have been cited by the Environmental Protection Agency (EPA) as one of the top 17 chemicals posing the greatest threat to human life and the environment (Abtew and Selvaduray, 2000). It has been reported that when Pb accumulates in the body over time, it binds strongly to proteins and inhibits normal processes and functions of human body. Therefore, Pb has various adverse health effects, such as nervous and reproductive system disorders, delays in neurological and physical development, cognitive and behavioral changes, and reduced production of hemoglobin resulting in anemia and hypertension (Abtew and Selvaduray, 2000). When the Pb level in the blood exceeds 50 mg/dL (2.78 mmol/L) of blood, symptoms of lead poisoning occur. Recent studies have found that a Pb level even well below the established official threshold could be hazardous to a child's neurological and physical development.

In the electronics industry, Pb pollution is believed to be the result of disposal of electronic assemblies in solid waste landfills. The Pb is leached off, flows into the ground water stream, and enters the animal and human food chain, although there are no scientific data or studies that clearly describe the mechanism.

2.2.1.2 Regulations for Pb-based solders (Suganuma, 2004; Abteu and Selvaduray, 2000)

Legislations to limit the use of Pb were first introduced in the U.S. with the Lead Exposure Reduction Act of 1991 and the Lead Exposure Act of 1992, banning Pb in some applications and limiting Pb content in others to less than 0.1%. These bills have not passed yet, but the proposals in these bills have stimulated great interest worldwide in developing Pb-free solders. The EPA (Environmental Protection Agency) has released an Advanced Notice of Proposal Rule (ANPR) entitled “Comprehensive Review of Lead in the Environment” under the Toxic Substance Control Act (TSCA) that has significant regulatory implications.

In Europe, the European Union included the adoption of Pb-free solder in the movement to legislate disposal of all electronic products in its proposal for the Waste Electrical and Electronic Equipment directive (WEEE). The final draft of the WEEE directive (in June 2000) deals separately with the recycling of hazardous elements, dividing recycling into two parts: WEEE and the RoHS (Restriction of Hazardous Substances) and it came into effect on July 1, 2006. There are 10 categories of electronics equipment that have been targeted in the directives, i.e., (1) large household appliances, (2) small household appliances, (3) IT and telecommunication equipment, (4) consumer equipment, (5) lighting equipment, (6) electrical and electronic tools, (7) toys, leisure, and sports equipment, (8) medical devices, (9) monitoring and control instruments, and (10) automatic dispensers. It can be noticed that almost all electronics products are involved, except for space and military uses. In RoHS, the prohibited hazardous substances include: lead, cadmium, mercury, hexavalent chromium, polybrominated biphenyls (PBB), and polybrominated diphenyl ether (PBDE).

In Japan, the use of Pb is not banned yet. However, it is controlled strictly in such ways as Water Quality Standards Concerning Lead, the Disposal Laws, and the Home Appliance Recycling Law enacted in April 2001. This leaves manufacturers with the options of either attaining 100% recycling of Pb, or using Pb-free solder alloys. Most companies, including Sony, Toshiba, NEC, Hitachi,

and Panasonic have their own programs for developing or selecting suitable Pb-free solders.

2.2.1.3 Pb-free solders

Extensive research has been carried out to find alternative Pb-free solders, and a large number of Pb-free solders have been proposed. The ability of Sn to alloy with other metals and to wet and spread on a wide range of substrates, together with its low melting points (231.9°C), makes it an essential ingredient in solder alloys. The Pb-free solders developed so far have been Sn-rich, typically containing more than 90% Sn, with alloying elements such as Bi, Ag, Cu, In, Zn, and Sb. They can be binary, ternary, and even quaternary alloys with variations in compositions. Some examples include Sn-0.7Cu, Sn-9Zn, Sn-58Bi, Sn-3.5Ag, Sn-3.8Ag-0.7Cu, and Sn-3.5Ag-4.8Bi (Kang et al., 2005). It has been reported that 69 Pb-free alloys have been identified (Abtey and Selvaduray, 2000), and only the ones of interest for this research work will be discussed here.

The Sn-Cu alloy has a eutectic composition of Sn-0.7Cu and a eutectic temperature of 227°C. Among all the Pb-free solders, Sn-0.7Cu eutectic alloy solder is particularly attractive (Suganuma, 2001; Tu et al., 2003; Puttlitz and Stalter, 2004). Sn-Cu solders are only about 1.3 times more expensive than Sn-Pb solders, whereas other Pb-free solders typically cost 2 to 3 times more. The relatively low cost makes the Sn-Cu alloy a good candidate for wave soldering in the mass production of commercial electronics. Although Cu is not an abundant element in the Earth's crust, the extraction technology for Cu is relatively straightforward so that its supply is secure. Furthermore, Cu has been widely used in electronic devices and can be recycled from scrap electronic equipment. Therefore, the use of Sn-0.7Cu alloy solders will not introduce a new element into these recycling processes. One concern about Sn-0.7Cu solder is excessive IMC growth, which can be controlled by using Ni as a barrier layer since Ni has relatively low reaction rates with most solders (Wang and Chen, 2006; Ho et al., 2007). Another concern about Sn-0.7Cu solder is low thermal reliability. By

adding a third element such as Ag into the Sn-0.7Cu system, the melting temperature will be reduced from 227°C to about 217°C and the reliability can be improved (Puttlitz and Stalter, 2004).

Sn-Ag-Cu alloys are believed to be the most promising replacement for Pb-Sn solders. The melting point of the Sn-Ag-Cu eutectic alloy is 216°C. Research indicates that Sn-Ag-Cu alloy is extremely stable and, accordingly, is considered able to meet the globally acknowledged standards. Sn-Ag-Cu alloys with Ag contents of 3.0-4.0 wt% are all acceptable (Shangguan, 2005). Recent studies by the International Printed Circuit (IPC) association and Electronic Manufacturing Services (EMS) companies (IPC, 2003), in an effort to standardize the Sn-Ag-Cu alloy composition, have concluded that there is no significant difference in the process performance and thermo-mechanical reliability among different alloy compositions (Shangguan, 2005). One challenge about Sn-Ag-Cu solder is Ag₃Sn precipitates, which can grow into large plates. If such an Ag₃Sn crystal has formed in a stress concentration region, e.g., the corner region between a solder bump and the UBM, cracks can initiate and propagate along the Ag₃Sn/solder interface.

One issue about Pb-free solder is that the melting point of most Pb-free commercial solders is within the range of 208-227°C, which is about 30°C higher than the melting point of eutectic Pb-Sn solders. This increase in melting temperature requires higher soldering temperatures, which would require better thermal resistance for the materials used in packaging (such as PCBs) and affect the reliability of electronic assemblies. Another issue about Pb-free solders is related to multi-level packaging as discussed in Section 2.2.1. The melting point of the Pb-rich solder bumps (320°C) used in the first level of packaging is more than 100°C higher than that of the eutectic Pb-Sn solder bumps (183°C) used in the second level of packaging. Therefore the solder joints formed in the first level of assembly at a higher temperature (350°C) do not become molten during the subsequent reflow operation (215°C). For Pb-free solders, there is only a maximum possible separation of less than 30°C between the melting points of any two solders. Hence, process control, during successive multiple soldering

processes with Pb-free solders, becomes more challenging and requires higher precision in mounting temperature control (Kang et al., 2005).

2.2.2 Wetting and solderability

To form a proper metallurgical bond between two metals, a specific interaction must take place between the solid surface of the parts to be soldered and the liquid solder. This is called wetting. The wetting phenomenon follows the basic principle that liquid will spread over a solid surface until the three interfacial tensions, i.e., the interfacial tension between the liquid solder and solid substrate, between liquid solder and atmosphere, and between substrate and atmosphere, are in balance (Harper, 2004; Humpston and Jacobson, 2004), as shown in Fig. 2-2.

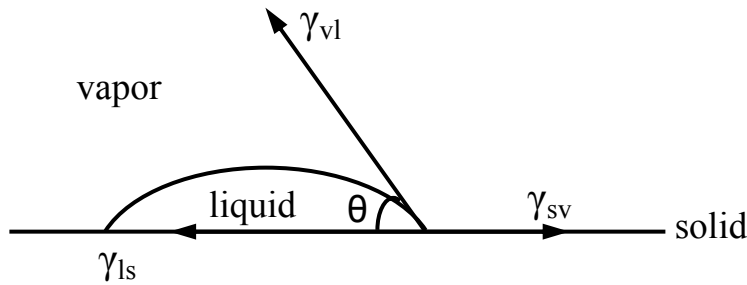


Fig. 2-2 Schematic diagram of a three-phase contact angle θ (Harper, 2004; Humpston and Jacobson, 2004).

For spreading to occur,

$$\gamma_{sv} > \gamma_{ls} + \gamma_{vl} \cos \theta \quad (2-1)$$

where γ_{ls} is the liquid-solid interfacial tension, γ_{vl} is the liquid-vapor interfacial tension, and γ_{sv} is the solid-vapor interfacial tension. θ is the contact angle between the solid and the liquid.

Wetting can be measured by the contact angle (θ), at the juncture of a solid and liquid, as shown in Fig. 2-2. A system will be considered to be wetting when the contact angle is between 0° and 90° , and non-wetting when the contact angle

lies between 90° and 180°. Good wetting is visualized as the formation of a smooth, uniform, and continuous solder coating on the surface of the solder pads.

Solderability is the ability to achieve a clean metallic surface on the substrates to be joined during a dynamic heating process so that good wetting of molten solder on the substrate surface can be formed.

2.2.3 Reflow soldering

To form a solder joint, solders need to be heated above their melting point. Reflow soldering in a furnace is a dynamic heating process in that the condition of the packages is constantly changing as it travels through the furnace in a relatively short reflow time. Fig. 2-3 shows a typical reflow profile used in industry. There are three stages of heating during reflow: natural warm up, preheating, and spike and reflow. In the natural heating stage, the heating rate used in industry is about 2-4°C/s. In the preheating stage, the heating rate is less than 1°C/s, and the recommended conditions are 120-150°C for a duration of 45-150 s. During this stage, the flux is concentrated and activated when solder paste is used. The temperature distribution across the board is homogenized and voiding in the solder joints is minimized. After preheating, the temperature spikes quickly to the peak reflow temperature at a rate of 1-4°C/s to minimize the exposure time of the organic system to high temperature. The peak temperature is the key parameter for the reflow profiles. Adequate reflow temperature is needed for a solder to melt, flow and wet, interact with the substrate metal, and form a good intermetallic bond during cooling and solidification. The peak temperature is normally set at 20-50°C above the solder melting temperature. For Pb-free soldering, because of concerns about the thermal stability of the components, efforts are needed to minimize the soldering temperature. The dwell time or time above liquidus temperature is typically 5-10 s. Higher peak temperatures and longer dwell times allow more wetting to occur, which also allows more IMCs to form. More discussion about the formation of IMCs will be given later in this chapter.

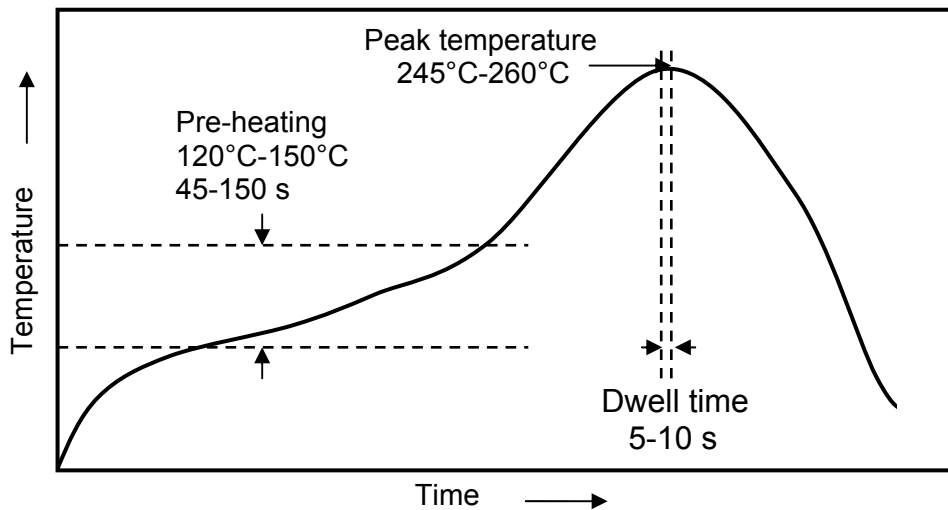


Fig. 2-3 Reflow profile for Pb-free soldering packages (Harper, 2004).

2.2.4 Soldering reactions

During soldering, a series of reactions and interactions occur between the solder and the two surfaces to be joined. Immediately after the solder makes contacts with the substrate metal, the contacted metal starts to dissolve into the molten solder, with a very high dissolution rate initially which is due to the very high local concentration of substrate metal before alloying starts. The dissolution rate of the substrate into the molten solder depends on the substrate material and temperature. After a short period of time, the layer of molten solder that is adjacent to the contacted substrate metal becomes saturated with the dissolved metal along the interface. Thermodynamically, for local equilibrium solubility, solid IMCs start to form in this part of the solder (Kivilahti, 2002). The formation of an IMC takes dissolved metal out of the saturated liquid solder and causes further dissolution of the contacted metal, especially if the intermetallic layer is not uniform along the surface of the substrate. Generally, after this stage, the reaction structure consists of two parts. Next to the substrate metal there is a relatively thin “uniphase” layer and on top of this there is sometimes a thick irregular two phase layer.

2.2.5 Intermetallic compound (IMC) formation

An IMC forms when two metal elements have limited mutual solubility. It is a type of intermediate phase (or solid solution) with an intermediate range of composition. The crystal structure of the IMC is different from those of the elemental components, as are the properties. In many cases, the IMC has reduced ductility, density, and conductivity. As the major ingredient in most Pb-free solders, tin is metallurgically active with most metals that are commonly used in electronic packaging, and various IMCs have been identified under equilibrium conditions between Sn and other alloying elements, as well as substrate metals. Such information can be found in phase diagrams.

When solder comes in contact with a substrate metal for a sufficient amount of time and/or at a high enough temperature, IMCs may form. Some IMCs even form at room temperature, such as AuSn_4 for Sn/Au couples, Cu_6Sn_5 for Sn/Cu couples, and Ni_3Sn_4 for Sn/Ni couples (Marinkovic and Simic, 1982). Below the liquidus temperature, the formation of IMCs is primarily a solid state diffusion process, and the temperature and time play very important roles. When solder is in a molten state, as discussed in the previous section, the solubility of the substrate metal into the molten solder accelerates IMC formation. The rate and extent of IMC growth is determined by the peak temperature and the dwell time during reflow.

Intermetallic compounds formed in the interior of the solder (away from the interface) and at the solder/substrate interface can be beneficial or detrimental to the performance of the solder joint. For IMCs in the interior of the solder, their morphology, size, and distribution in the solder affect the solder joint in two different ways. If they possess the correct properties, the IMCs in the interior of the solder act as a strengthening phase. In contrast, large and needle-shaped IMCs generally weaken the mechanical properties of a solder joint. For the IMCs at the solder/substrate interface, their presence usually reduces the interfacial energy between the liquid solder and the substrate and improves the wettability of liquid solder (Sun et al., 2006). Wetting on the substrate followed by the formation of a thin layer of IMCs is necessary to make permanent solder bonds. However, solder

joint failure may occur if the IMCs layer becomes too thick. Cracks are often initiated around the interfacial area under stressful conditions when excessive IMCs develop along the solder/substrate interface. The adverse effect of IMCs on solder joints is due to their brittle nature, tendency to generate structural defects because of the microstructural mismatch between the solder and substrate, and their different thermal expansion properties from the interior solder. The difference in thermal expansion may contribute to internal stress development for the solder joint. In addition, excessive IMC formation may deplete some elements at the interface and, in turn, may impair the solderability of the system.

2.2.6 Interactions between solders and substrates

Many research efforts have been carried out to study interactions between solders and substrates. The interactions can be divided in two classes: liquid solder/substrate reactions during soldering and solid solder/substrate reactions during subsequent aging.

Most Pb-free solders developed so far are Sn-rich solders. Sn is the major constituent, with a small amount of other alloying elements. Among all the common base materials, board surface finishes and underlying conductors such as Cu, Ni, Ag, and Au, Cu is the most commonly used solderable surface finish in PCBs (Kang et al., 1996). Nickel is often used as a diffusion barrier layer between Cu and Sn to prevent excessive formation of IMCs, since the reaction rate of Ni with liquid Sn is typically slower than that of Cu (Tu and Zeng, 2001; Laurila et al., 2005; Luo et al., 2005) and the growth rate of IMCs is slower in the solder/Ni system than in the solder/Cu system (Kim et al., 1999). The discussion in the following sections will be focused primarily on the interactions between Sn and substrate metals, which are limited to Cu and Ni.

2.2.6.1 Interactions between Sn and Cu

The phase diagram for the Sn-Cu system is shown in Fig. 2-4. The intermetallic phases stable below 300°C are the ϵ and η phases. The ϵ phase

contains 25.7-27.1 at% Sn, which corresponds to the composition of Cu_3Sn . The η phase contains 44.8-45.5 at% Sn and corresponds to the composition of Cu_6Sn_5 . Interaction between Sn and Cu occurs at room temperature to form Cu_6Sn_5 and at temperatures above 100°C to form Cu_3Sn at the expense of Cu_6Sn_5 (Tu, 1973; Tu and Thompson, 1982; Hwang et al., 2003).

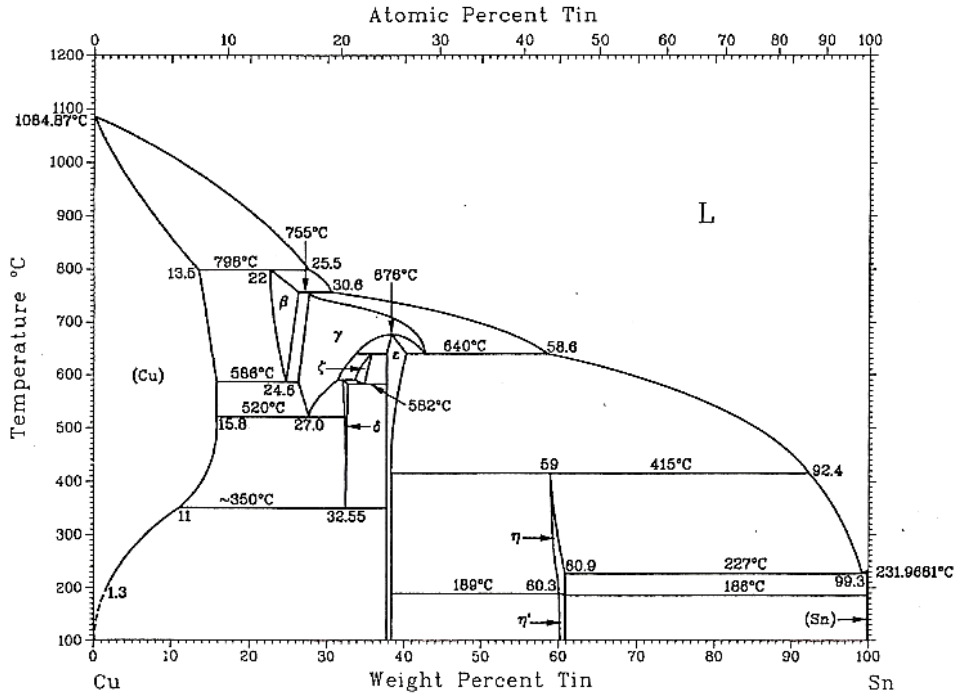


Fig. 2-4 Sn-Cu phase diagram (Baker, 1992).

As soon as molten Sn solder contacts the Cu substrate, Cu dissolves into the molten solder rapidly. Meanwhile, Sn and Cu atoms interdiffuse at the molten solder/substrate interface in a direction driven by the chemical potential gradient of the elements existing between substrate and solder, to minimize the Gibbs free energy of the solder/substrate system. Initially, Cu dissolution is almost linear with the reflow time and slows down as the concentration of substrate metal in the molten joint approaches its solubility limit. The overall kinetics appears parabolic with reaction time (Kang et al., 1996; Shanguan, 2005). The local equilibrium solubility causes IMCs to form at the solder/substrate interface. Cu_6Sn_5 was reported as the first phase to form at the liquid Sn/Cu interface (Laurila et al.,

2005; Shangguan, 2005) and the Cu_3Sn phase was also detected for reflow temperatures higher than 235°C (Hwang et al., 2003; Dariavach et al., 2006; Yen et al., 2008; Yu and Wang, 2008).

The dissolution rate of Cu is different in different molten solders. Yen et al. (2008) investigated the dissolution behavior of a Cu substrate in molten Sn, Sn-3.0Ag-0.5Cu, Sn-58Bi, and Sn-9Zn solders at temperatures of $240\text{--}300^\circ\text{C}$ and found out that the dissolution rate followed the order of $\text{Sn} > \text{Sn-3.0Ag-0.5Cu} > \text{Sn-58Bi} > \text{Sn-9Zn}$. Similar results were obtained by Yeh et al. (2006), with the Cu dissolution rate in the molten solders decreasing in the order of Sn, Sn-3.5Ag, Sn-4.0Ag-0.5Cu, Sn-37Pb, and Sn-8.6Zn at temperatures between 300°C and 400°C . The differences in dissolution rate may be due to the difference in the morphologies of interfacial IMCs and the solubility of substrate in the molten solders (Yen et al., 2008). Alam et al. (2003) investigated the dissolution behavior of Cu metallizations in Sn-3.5Ag and Sn-3.5Ag-0.5Cu, and found that the dissolution rate of Cu in molten Sn-3.5Ag-0.5Cu slowed down dramatically relative to Sn-3.5Ag. They attributed the decrease in dissolution rate to the addition of 0.5 wt% Cu which reduced the concentration gradient at the Cu/molten solder interface and thus reduced the driving force for dissolution (Alam et al., 2003).

The solubility of Cu in molten Sn was measured and calculated in the temperature range of $232\text{--}260^\circ\text{C}$ in the Sn-rich portion of the Sn-Cu binary phase diagram (Moon et al., 2000) and it increased from 1.75 at% to 2.5 at% as the temperature increased from 232°C to 260°C . Chada et al. (2000) determined the Cu solubility in molten Sn-3.5Ag solders under non-isothermal conditions by both experimental measurements and calculations, and found that the solubility increased from 2.2 at% to 3.4 at% when the temperature was increased from 232°C to 260°C . Comparison of Cu solubility in molten Sn and molten Sn-3.5Ag solders showed that the addition of Ag in the molten Sn enhanced the solubility of Cu, which is also demonstrated in the 240°C isothermal section of the Sn-Ag-Cu ternary phase diagram proposed by Chen et al. (1999). Kang et al. (1996) studied the interfacial reactions between Cu and different solders (38Pb-62Sn, Sn-57Bi,

Sn-3.5Ag, Sn-5Sb, and pure Sn) and found that the amount of Cu dissolved in the solder increased as the Sn content of a solder alloy increased, and as the reflow temperature increased.

Sn-Cu IMCs with a thicker layer of scallop-shaped Cu_6Sn_5 and a thinner planar layer of Cu_3Sn are commonly found in reactions between eutectic Pb-Sn solder and Cu (Kim et al., 1995; Tu et al., 2001; Tu and Zeng, 2001; Lee et al., 2002). These phases and morphologies have also been observed in reactions between eutectic Sn-Cu (Dariavach et al., 2006), eutectic Sn-Ag (Dariavach et al., 2006; Yu et al., 2008), and eutectic Sn-Ag-Cu solders (Dariavach et al., 2006; Yu and Wang, 2008) and Cu substrates. The scallop-shaped IMC has many deep grooves or channels where the distance between the liquid Sn and Cu substrate are minimal. Therefore, at the base of these grooves, copper atoms diffuse rapidly and dissolve into the molten solder. The dissolution model is dominated by grain boundary diffusion (Schaefer et al., 1998; Yen et al., 2008). The grooves are the main channels through which Cu atoms dissolve into molten solders giving the Cu substrate a very high dissolution rate. Since the channels are short paths for Cu atoms to reach the molten solder, the neighboring scallops will not join together and form grain boundaries. Scallops can grow both vertically and laterally, but the lateral growth will slow down since the number of channels per unit area at the interface will reduce over time. This is why Cu_6Sn_5 grows into whiskers rather than large scallops over a long period of reflow time (Gagliano and Fine, 2001). As the immersion time increases, the grooves get wider and their density is reduced. Diffusion slows down, not only by the increase in path length and reduction in concentration gradient, but also by the reduction of transport capacity of the grooves at the solder/substrate interface. The growth of the scallop-shaped Cu_6Sn_5 particles during aging has also been examined and the results showed that the scallops increased in size but decreased in number (Tu, 1996).

Tu et al. (2003) investigated the IMCs between Pb-Sn solder and a thick Cu substrate after reflow at 200°C and aging at 170°C for 1000 h, and observed that the morphology of Cu_6Sn_5 changed from scallop-type to layer-type during solid state aging. After reflowing an aged Pb-Sn/Cu sample at 200°C again, the

scallop-shaped morphology of Cu_6Sn_5 showed up again. The authors concluded that the scallop-shaped grains are stable when in contact with molten solder, but the layer-shaped grains are stable when in contact with solid solder. The interfacial energy between a molten solder and Cu_6Sn_5 is less than that between a solid solder and Cu_6Sn_5 , so the scallop-shaped morphology of grains persists in wetting reactions and the layer-shaped morphology persists in solid state aging. The authors also concluded that the wetting reaction is a very low activation energy process and that solid state aging is a much slower kinetic process. The rate of free energy gain is much faster in scallop-shaped growth than in layer-shaped growth, which determines the scallop-shaped IMC growth during reflowing. The morphology of the reaction product in the form of scallops has enabled a high rate of reaction to take place in wetting reactions (Tu et al., 2003).

2.2.6.2 Interactions between Sn and Ni

The phase diagram for the Sn-Ni system is shown in Fig. 2-5. There are three stable intermetallic phases at temperatures below 300°C, i.e., Ni_3Sn , Ni_3Sn_2 , and Ni_3Sn_4 (Laurila et al., 2005). Nickel can react with Sn at room temperature and forms Ni_3Sn_4 (Marinkovic and Simic, 1982). Ni_3Sn_4 is frequently found at the Sn/Ni interface (Tomlinson and Rhodes, 1987; Bader et al., 1995; Chen et al., 1998; Chen et al., 2003; Shangguan, 2005). Sometimes, a thin layer of Ni_3Sn or Ni_3Sn_2 is observed between Ni and Ni_3Sn_4 . Ni_3Sn_2 has been reported to form after reflow at 240°C for 1000 hrs or reflow at 300°C for 86 hrs, and both Ni_3Sn_2 and Ni_3Sn were detected after reflow at 400°C (Bader et al., 1995).

At temperatures below 260°C, Ni_3Sn_4 is the first phase formed at the liquid Sn/Ni interface (Laurila et al., 2005). Similar to the Sn/Cu system, the first stage of the reaction is the dissolution of Ni into liquid Sn. Once Sn has been saturated with Ni at the liquid Sn/Ni interface, Ni_3Sn_4 nucleates at the interface and starts to grow. Three different morphologies of Ni_3Sn_4 phase have been found at the Sn/Ni interface after reflow at 240°C for short times: a planar layer at the Ni interface; long, thin needles; and large, polygonal crystals (Bader et al., 1995).

After reflow for only 7 s, a high density of Ni_3Sn_4 needles is present and no large crystals are found. The density and thickness of the needles reach maximum after 2 min and decrease afterwards. After reflow for 30 s, the first large crystal appears and the number increases rapidly from the first to the fifth minute of annealing. Recrystallization of the needles into the large crystals takes place. The driving force for this recrystallization is the reduction of the surface area and energy of the Ni_3Sn_4 phase. The solubility limit of Ni in molten Sn is extremely small at temperatures below 400°C , as shown in the Ni-Sn binary phase diagram (Baker, 1992). It has been estimated that the Ni solubility limit in molten eutectic Pb-Sn is approximately 10^{-5} at% (Shangguan, 2005). The Ni_3Sn_4 phase was believed to have a special lattice direction in which the crystallization speed is high (Bader et al., 1995). Grains with the appropriate orientation grow out of the planar layer above the Ni substrate and form needles. As the density of the needles and large crystals increase at the liquid Sn/Ni interface, the transport capacity of the diffusion paths through the liquid Sn decreases, and the reactions between Sn and Ni slow down.

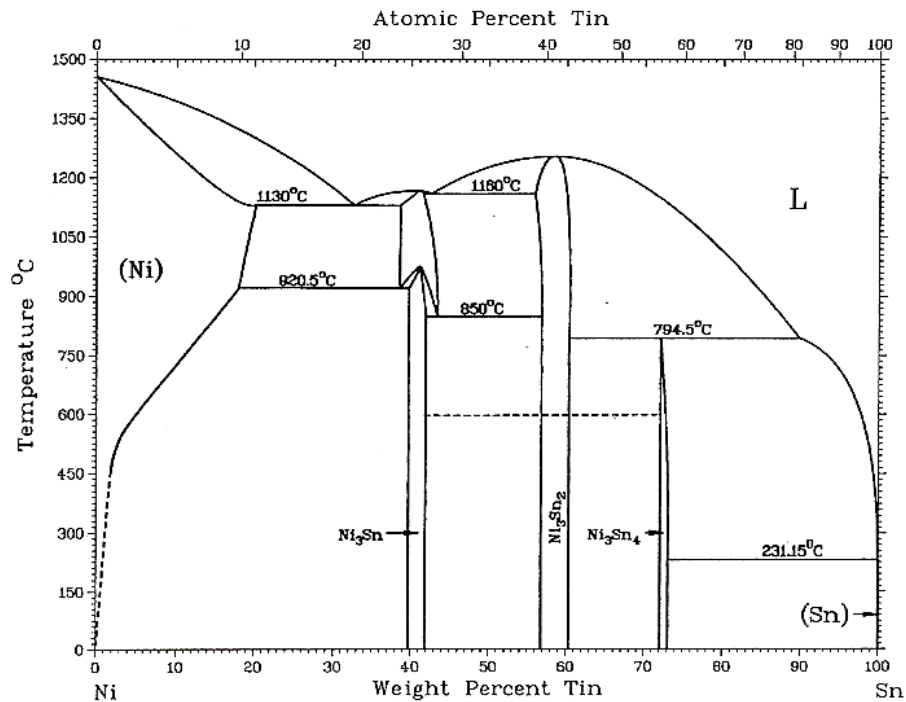


Fig. 2-5 Sn-Ni phase diagram (Baker, 1992).

The dissolution rate of Ni into liquid Sn is much lower than that of Cu, which results in thinner IMC layers at the Sn/Ni interface than at the Sn-Cu interface (Kim et al., 1999). Nickel, therefore, is often used as a diffusion barrier layer between Cu and Sn. Kang et al. (1996) studied the interfacial reactions between different solders and Ni metallizations and found that for Pb-Sn and Sn-Bi eutectic solders (Sn-38Pb, Sn-57Bi), a thin layer of Ni (0.5-1.0 μm) on the Cu base metal is a good reaction barrier to control the interfacial reactions. For Sn-rich solders (Sn-5Sb, Sn-3.5Ag, and pure Sn), a Ni layer up to 2.0 μm is not a good reaction barrier for an extended reaction time of 20 min. Islam et al. (2005) found that for Sn-0.7Cu solder, a Ni layer less than 3 μm thick was consumed after reflow at 250°C for 180 min or after aging at 175°C for 16 days.

For solders with Cu addition, such as Sn-Cu and Sn-Ag-Cu solders, the interactions between solders and Ni substrates lead to the formation of ternary IMCs consisting of Sn, Cu, and Ni, with compositions which depend on the solder composition (especially Cu concentration) and reflow conditions. It has been reported in the literature that Ni_3Sn_4 compounds dissolve as much as 8.5 at% Cu and the metastable solubility of Ni in Cu_6Sn_5 can be over 20 at% (Sun et al., 2006). When the amount of solder is large so that the supply of Cu is not an issue, the types of the reaction products formed are very sensitive to the Cu concentration (Chen et al., 2002; Ho et al., 2002; Luo et al., 2005; Ho et al., 2007). When the Cu concentration is low (≤ 0.2 wt%), a continuous layer of $(\text{Ni,Cu})_3\text{Sn}_4$ forms at the interface. When the Cu concentration increases to 0.4 wt%, a continuous layer of $(\text{Ni,Cu})_3\text{Sn}_4$ and a small amount of discontinuous $(\text{Cu,Ni})_6\text{Sn}_5$ particles form at the interface. When the Cu concentration increases to 0.5 wt%, the amount of $(\text{Cu,Ni})_6\text{Sn}_5$ increases and become a continuous layer, with a continuous but very thin layer of $(\text{Ni,Cu})_3\text{Sn}_4$ underneath the $(\text{Cu,Ni})_6\text{Sn}_5$ layer. At higher Cu concentrations (0.6-3.0 wt%), $(\text{Ni,Cu})_3\text{Sn}_4$ disappears and only $(\text{Cu,Ni})_6\text{Sn}_5$ is present. Yoon et al. investigated the interfacial reactions between eutectic Sn-0.7Cu solder and Ni substrate during reflow and aging, and reported the formation of a layer of $(\text{Cu,Ni})_6\text{Sn}_5$ IMC after reflow at 250°C (Yoon et al., 2005; Yoon and Jung, 2006; Yoon et al., 2006). They also detected the

formation of an additional $(\text{Ni,Cu})_3\text{Sn}_4$ IMC layer between the Ni substrate and the $(\text{Cu,Ni})_6\text{Sn}_5$ layer after aging at 170°C for 50 days, at 185°C for 3 days, or at 200°C for 1 day through the consumption of the $(\text{Cu,Ni})_6\text{Sn}_5$ layer.

Some research has shown that the sensitivity of IMC formation to Cu concentration disappears when the solder joints are subjected to aging at high temperatures for sufficient amounts of time. Luo et al. (2005) studied the reactions between five Sn-3.9Ag- x Cu solders ($x = 0.2, 0.4, 0.5, 0.6,$ and 0.8) and Ni substrate by reflowing at 250°C for 120 s and then aging at 180°C for 5000 h. They found that the same type of IMCs, a layer of $(\text{Cu,Ni})_6\text{Sn}_5$ over a layer of $(\text{Ni,Cu})_3\text{Sn}_4$, formed at the interface. It was proposed that the $(\text{Ni,Cu})_3\text{Sn}_4$ layer grew by the reaction of the Ni substrate with the $(\text{Cu,Ni})_6\text{Sn}_5$ layer.

Yoon et al. (2006) studied the effect of reflow and cooling conditions on the morphologies of IMCs formed at the Sn-0.7Cu/Ni interface and found that at low temperatures ($\leq 255^\circ\text{C}$), only a needle-type $(\text{Cu,Ni})_6\text{Sn}_5$ IMC with a hexagonal cross section was formed. As the reflow temperature and time was increased, the IMC morphology changed to a dodecahedron-type with similar chemical composition.

2.3 Thin film deposition technologies for solders

Many thin film deposition techniques are available today (Maissel and Glang, 1970; Bunshah, 1994; Pauleau, 1999). They are either purely physical, such as evaporative methods, or purely chemical, such as gas-phase and liquid-phase chemical processes, or a combination of physical and chemical processes, such as glow discharge and sputtering processes. Among all these technologies, evaporation (Pittroff et al., 1995; Dohle et al., 1996), sputtering (Lugscheider et al., 2001; Lugscheider et al., 2003), and electrodeposition methods have been reported to deposit solders for electronic packaging (Maissel and Glang, 1970; Ohring, 1992; Bunshah, 1994; Pauleau, 1999; Seshan, 2002).

2.3.1 Evaporation

Evaporation is one of the oldest techniques used for depositing thin films and is still widely used today for depositing metals and metal alloys. It consists of the following steps: (1) a vapor is generated by boiling or subliming a source material (solid or liquid); (2) the vapor is transported from the source to the substrate at reduced gas pressure; and (3) the vapor is condensed to a solid film on the surface of the substrate, followed by film nucleation and growth. The process is usually carried out in vacuum (typically 10^{-5} - 10^{-6} Torr, or 10^{-3} - 10^{-4} Pa) so that the vapor travels from the source to the substrate with minimal collisions with gas molecules and the oxidation of the source, vapor, and deposit is greatly reduced.

The evaporation of materials in a vacuum system requires a vapor source to supply the vapor and a heat source to supply the heat of evaporation, while maintaining the temperature sufficiently high to produce the desired vapor pressure. The vapors are produced from a material located in a container which can be heated by direct resistance, radiation, an electron beam, a laser beam, or an arc discharge. Resistance-heated wires and metal foils of various types such as W, Mo, and Ta are the simplest vapor sources. For electron beam evaporation, the evaporation of the source material is accomplished by electron bombardment instead. A stream of electrons is accelerated through electrostatic fields of typically 5-10 kV and focused onto the surface of the vapor source. Upon impingement, most of the kinetic particle energy is converted into heat and surface temperatures can reach 3000°C or higher. Since the energy is imparted by charged particles, it can be concentrated on the vapor source surface while other portions are maintained at low temperature. Hence, interactions between the vapor source and support material are greatly reduced.

A variety of metals, alloys, and compounds have been deposited using evaporation by varying the way in which the source is heated. Alloy films, such as Pb-Sn, Sn-Cu, Sn-Ag, Ag-Al, Ag-Cu, Ni-Cr, and Cr-Ge, can be deposited by melting two materials together or in separate containers. Relatively few inorganic compounds and alloys evaporate congruently because the constituents which are present in solid or liquid state usually differ in their vapor pressures. The vapor

pressure of each element must be carefully controlled to obtain the desired composition. Evaporation can also be used to deposit multilayer films.

In the electronics industry, evaporation is used to selectively deposit both UBM layers and solders through a mask in the flip-chip technique. The limitations of the evaporation method include the following (Datta et al., 2005): (1) High cost. The equipment is expensive and operation cost is high, so is the cost for the low life mask and waste disposal. (2) Low efficiency. The efficiency of evaporative deposition is typically less than 5%, and more than 95% of the evaporated materials is deposited on the evaporator walls and on the metal mask which need to be cleaned; (3) Evaporation cannot be used for finer bump pitch due to the inability to fabricate masks with finer pitch and diameter while maintaining the mask thickness; (4) Evaporation cannot deposit Sn-rich solders with low melting points. The relatively low vapor pressure of Sn limits the effective evaporation rate, leading to very long deposition times or solder melting on the wafer because of excessive tin source power levels.

2.3.2 Sputter deposition

Sputtering is a process that occurs at the surface of a solid target, which is exposed to an ion beam. Ejection of the target surface atoms occurs by momentum transfer from bombarding ions to the target surface atoms, leading to the transformation of the target material being sputtered into a gas-like phase. Sputtering is, therefore, an etching process and has been used for surface cleaning and pattern delineation in the microelectronics industry. Sputter deposition involves the condensation of atoms ejected from the target onto a substrate surface. Sputter deposition operates in a chamber filled with a working gas and the pressure is about 1-100 mTorr (or 0.1-10 Pa). This limits the technology to materials which are compatible with high vacuums, because volatile or organic materials are frequently unable to withstand ion bombardment.

Based on the source of ions, sputtering can be separated into ion beam sputtering and plasma sputtering. Ion beam sputtering uses an autonomous, noble

gas ion beam source. Ion beam sputtering has several advantages, such as high purity of deposits due to the absence of a working gas in the processing chamber and precise and easy control of the ion beam parameters, such as density and energy. The main disadvantage is the fact that the deposition rates are relatively low. Typical deposition rates are in the range of 5 to 300 nm/min.

For plasma sputtering, initially the process chamber is filled with a noble working gas under low pressure. Then a direct current (DC) or radio frequency (RF) glows at high discharge voltage of 0.5-5 kV and creates working gas ions, which are the plasma. The plasma is accelerated to sufficiently high energy for the sputtering of the target materials before sputter deposition takes place. The plasma can be confined with magnetic fields to achieve higher efficiency and greater film thickness uniformity. The process is called magnetron sputtering. The magnetic fields keep the target-generated secondary electrons away from the substrate, which reduces substrate heating and radiation damage, and thus allows the use of substrates that are temperature sensitive (such as polymers) and surface sensitive (such as metal oxides in semiconductor devices) with minimal adverse effects. In addition, magnetron sputtering has higher deposition rates than conventional systems.

During sputtering, the target material is transformed into a gas-like phase by a physical momentum exchange process, rather than a chemical or thermal process, which means any material can be used as a target material. This makes it possible to sputter thin films of different kinds of materials, such as conducting materials, insulating materials, elemental materials, alloys, and compounds. When sputtering alloys or compounds, the gas phase transport of all the components is the same, so that the composition of the deposited film tends to be the same as that of the target material. Therefore, the target can be maintained sufficiently cool to avoid bulk diffusion and decomposition of the constituents. Compared to evaporation deposition, there are many advantages for sputter deposition. It is a good technique for multilayer deposition, because the deposition rates for different materials are not much different. Film thickness control is simple through the adjustment of deposition time. Sputtering can be accomplished from

large-area targets, which can reduce the shadowing effects from dust particles and improve the film thickness uniformity. The surface of the substrate can be cleaned easily by ion bombardment before sputtering deposition.

2.3.3 Electrodeposition

Both evaporation and sputter deposition techniques require high vacuum and/or high temperature processing, which increases operation cost, and may limit patterning or other process options in electronic packaging and cause interdiffusion problems. Compared to these fabrication processes, electrodeposition offers significant advantages. Electrodeposition is performed at much lower temperatures and it is a low cost technique. It can be used to plate either a single layer or multilayer deposits, with easy and precise control of the thickness and composition of each layer. Electrodeposition can be performed on substrates with varying sizes and complex shapes and the deposit can be very thin or very thick (Hodes, 2001). There are, however, safety and environmental concerns associated with the electrodeposition process with regard to chemical treatment and safe disposal of wastes to prevent pollution. The theories of electrodeposition will be covered in Section 2.4.

Numerous metals and metal alloys have been successfully electrodeposited from aqueous solutions. The most useful electrodeposited metals include Sn, Cr, Cu, Ni, Ag, Au, Zn, and alloys such as Cr-Ni, Fe-Co and various Sn alloys.

2.3.4 Electrodeposition of Sn and Sn alloys

Sn electrodeposition has been used for a long time as a surface treatment on different metals, such as steel, to protect them from corrosion or to improve their appearance (Igarashi et al., 1979; Opaskar and Capper, 2002; Torrent-Burgues et al., 2002). Both acidic and alkaline baths have conventionally been used for Sn electrodeposition (Tan, 1993). In acidic baths, Sn usually exists as Sn^{2+} ions, while in alkaline baths, Sn^{4+} is the more stable species. For Sn alloy

electrodeposition, plating baths have to be capable of co-depositing the alloying metals with the desired composition and necessary properties. Different types of plating baths have been developed to electrodeposit Sn and Sn alloys, such as alkaline baths, sulfate, methanesulfonate, pyrophosphate, and fluoroborate acid baths, and others. Only cyanide-free baths will be discussed here. Simple acidic baths tend to produce loosely adhering and dendritic deposits with poor covering power. In addition, Sn^{2+} ions are subject to both hydrolysis and oxidation in solution. Additives are required to stabilize Sn^{2+} ions and help produce uniform deposits.

2.3.4.1 Alkaline baths

One major disadvantage of alkaline plating baths is that highly alkaline baths may dissolve the photoresists used to define areas on semiconductor wafers. Alkaline plating baths also usually require higher plating temperatures (60-70°C).

Some research work has been conducted to develop weakly alkaline plating baths. Toben et al. (2001) proposed different kinds of alkaline baths for Sn-rich, Sn-Ag alloy electrodeposition. The solution pH was adjusted to about 8 and the plating temperature was 50°C. The plating bath contained a soluble Sn salt (SnSO_4 , $(\text{CH}_3\text{SO}_3)_2\text{Sn}$, or $\text{SnCl}_2 \cdot 2\text{H}_2\text{O}$), a soluble Ag salt (AgNO_3 or $\text{CH}_3\text{SO}_3\text{Ag}$), a Sn chelating agent (polyhydroxy compound) in an amount sufficient to complex all the Sn ions, and a Ag chelating agent (heterocyclic compound) in an amount sufficient to complex all the Ag ions. In addition, grain refining additives such as jeffamine T-403, triton RW, triton QS-15, and gelatin or gelatin derivatives were added to improve deposit appearance. Pure Sn was used as the anode. Sn-Ag alloys with Ag content in the range of 0.2-9.6 wt% were obtainable. One of the proposed Sn-Ag plating baths contained 75.5 g/L $\text{SnCl}_2 \cdot 2\text{H}_2\text{O}$, 11 g/L AgNO_3 , 175 g/L sodium gluconate, 60 g/L dimethylhydantoin, 0.4 g/L jeffamine T-403, and 0.1 g/L triton QS-15 (Toben et al., 2001).

2.3.4.2 Sulfate baths

Sulfate baths are primarily used for bright Sn plating and are very inexpensive to operate, especially where large tank volumes are required. $\text{H}_2\text{SO}_4/\text{SnSO}_4$ systems operate at 100% cathode efficiency with high throwing power. The major drawback of this system is oxidation. At high current density, soluble Sn anodes become passivated due to the formation of SnO_2 . When an insoluble anode is used, Sn(II) is oxidized to Sn(IV) at the anode in addition to natural oxidation from exposure to air. Another disadvantage of sulfate baths is that both Ag and Bi form insoluble compounds and cannot be used to deposit pure Ag and Bi and alloys containing Ag or Bi.

Sulfate baths have been successfully used to plate pure Sn and various Sn alloys (Galdkiene and Mockus, 1994; Rehim et al., 1996; Carlos et al., 2000; Fukuda et al., 2001; Fukuda et al., 2003; Ozga, 2006). In the steel industry, Sn has been plated from $\text{H}_2\text{SO}_4/\text{SnSO}_4$ baths for many years, with phenol sulfonic acid as additive to inhibit Sn(II) oxidation as well as to increase the current density (Gillman et al., 2003). The problem is that phenol derivatives are harmful to the environment.

Gillman et al. (2003) found that by adding alkali metals, alkaline earth metals, ammonium, and substituted ammonium salts of alkyl and alkanol sulfonic acid into the basic sulfate electroplating baths, the performance of the Sn and Sn alloy plating baths was improved, so that much higher current densities could be used which gave higher plating rates. The Sn oxidative stability was also improved.

Different additives have been added into basic $\text{H}_2\text{SO}_4/\text{SnSO}_4$ electroplating baths, as well as commercial $\text{H}_2\text{SO}_4/\text{SnSO}_4$ plating baths, to try to produce smooth and bright Sn deposit (Commander and Panecasio, 1991). Acidic plating baths contained SnSO_4 and H_2SO_4 as the main components and an effective amount of a quaternized derivative of vinyl-pyridine or vinyl-quinoline as a brightener additive. In addition, at least one aldehyde was added into the plating bath to improve the deposit brightness. One or more wetting or surface active agents were added to improve leveling and brightness, as well as bath

stability. The electroplating was carried out at the conventional temperatures used in Sn plating baths, usually from room temperature to 40°C and the pH of the bath was generally less than about 1. It was found that by adding pyridine and quinoline derivative additives into commercial plating baths which contained brighteners, the brightening effect was enhanced with a longer operating life over a wider operating temperature range. One example of the additive package in a proposed Sn plating bath included trion X-100, acrylic acid, and 1-naphthaldehyde (Commander and Paneccasio, 1991).

Igarashi et al. (1979) proposed sulfate plating baths for Sn, Sn-Cu, and Sn-Zn electroplating. The plating baths contained one or two metal sulfate salts (SnSO_4 , CuSO_4 , and ZnSO_4) and different kinds of additives. The additives included a citric acid (or its salt), an ammonium salt, at least one saturated hydroxycarboxylic acid (or its salt) other than citric acid (or its salt), and/or at least one saturated dibasic carboxylic acid (or its salt), as stabilizers. The saturated hydroxycarboxylic acid (or its salt) other than citric acid (or its salt) was selected from tartaric acid, malic acid, glycollic acid, glyceric acid, lactic acid, and β -hydroxypropionic acid or their sodium, potassium, and ammonium salts. The saturated dibasic carboxylic acid (or its salt) was selected from oxalic acid, malonic acid, succinic acid, glutaric acid, adipic acid, or their sodium, potassium, and ammonium salts. To obtain bright Sn and Sn alloys, a conventional brightener was added in addition to the stabilizer. The pH of the bath was set at 6, and Sn plate or Sn alloy plate was used as the anode. One of the proposed Sn plating baths contained 50 g/L SnSO_4 , 90 g/L citric acid, 70g/L $(\text{NH}_4)_2\text{SO}_4$, 9 g/L ammonium tartrate, 120 g/L 30% aqueous solution of ammonia, and 8 ml/L brightener. One of the Sn-Cu plating baths contained 22 g/L SnSO_4 , 25g/L $\text{CuSO}_4 \cdot 5\text{H}_2\text{O}$, 100 g/L ammonium hydrogen citrate, 80 g/L $(\text{NH}_4)_2\text{SO}_4$, 20g/L glycollic acid, 75 g/L 30% aqueous solution of ammonia, and 8 ml/L brightener (Igarashi et al., 1979).

2.3.4.3 Methanesulfonate baths

As mentioned previously, one difficulty for Sn and Sn alloy deposition in acidic baths is preventing the oxidation of Sn(II) to Sn(IV). Methanesulfonate acid (MSA, $\text{CH}_3\text{SO}_3\text{H}$) is a reducing acid and, thus, can minimize the oxidation of Sn(II). MSA is much less corrosive to electronic materials than either fluoborate or sulfate baths. It has a high solubility for salts of all Pb-free candidate metals except for Sb. A basic methanesulfonate plating bath contains metal methanesulfonate(s) and methanesulfonic acid. Different kinds of methanesulfonate baths have been developed to electrodeposit both pure Sn and various Sn alloys by adding different additives (Cavallotti et al., 1998).

Martyak and Seefeldt (2004) studied Sn deposition from a plating bath containing $(\text{CH}_3\text{SO}_3)_2\text{Sn}$, $\text{CH}_3\text{SO}_3\text{H}$, hydroquinone and other additives. The addition of polyethylene glycol suppressed hydrogen evolution but had little effect on the mechanism of Sn reduction and the structures of the deposit. Polypropylene glycol enhanced Sn reduction and produced a slightly smoother Sn deposit. The addition of phenolphthalein and the glycol additives changed the Sn reduction process from diffusion controlled to charge transfer controlled and produced a smooth matte Sn deposit.

A systematic investigation of the electrodeposition of Sn-Cu, Sn-Ag-Cu, and Sn-Cu-Bi alloys from methanesulfonate baths has been reported by Tsuji et al. (2003). The study focused on selecting suitable additives and examining the deposits plated at two different current densities (5 mA/cm^2 and 30 mA/cm^2). Pure Sn plate was used as the anode and the plating temperature was 25°C . The additives studied included 2,2'-dipyridyl disulfide, thiodiglycolic acid, polyoxyethylene nonylphenyl ether (EO 15 moles), hydroquinone, thiobis, polypropoxylate (PO 3 moles), 1,3-dimethylthiourea, and others. It was found that by adding additives in certain combinations, the composition of the deposits was similar to the metal composition in the plating baths and had very low dependency on the current density. This means that any desired deposit composition can be obtained by adjusting the concentration of the baths. The additives also helped in obtaining uniform deposits and to improve the bath

stability. One combination of additives added in a Sn-Cu electroplating bath contained $(\text{CH}_3\text{SO}_3)_2\text{Sn}$, $(\text{CH}_3\text{SO}_3)_2\text{Cu}$, $\text{CH}_3\text{SO}_3\text{H}$, 1,5-dimercapto-3-thiapentane-bis (hexadecaethylene glycol), 2,2'-bipyridyl, 1-naphthaldehyde, methacrylic acid, β -naphthol polyethoxylate (EO 13 moles), tristyrenated phenol polyethoxylate (EO 20 moles), laurylamine polyethoxylate (EO 15 moles), catechol, and hydroquinone (Tsuji et al., 2003).

2.3.4.4 Pyrophosphate-iodide baths

The pyrophosphate-iodide system, which contains both $\text{P}_2\text{O}_7^{2-}$ and I^- ions, is considered as one of the most stable systems and is widely used for plating Sn and Sn alloys. One disadvantage is that it requires more control and maintenance than the other plating baths. The operational temperature should not exceed 43-60°C, because the pyrophosphate complex hydrolyzes to orthophosphate at temperatures higher than 60°C, which degrades the solution.

A pyrophosphate-iodide plating bath containing $\text{K}_4\text{P}_2\text{O}_7$, KI, $\text{Sn}_2\text{P}_4\text{O}_7$, AgI, and $\text{Cu}_2\text{P}_4\text{O}_7$ was developed for Sn-Ag-Cu alloy deposition (Arai and Kaneko, 1997). No precipitation was observed after the plating bath stood for more than one year. Both the pyrophosphate and the iodide acted as complexing agents for Sn, Ag, and Cu. Sn-Ag-Cu alloys, containing 1.7-8.7 at% Ag and 2.0-11.1 at% Cu, were formed at room temperature without agitation and with a current density of 2-20 mA/cm².

Some researchers also showed that the pyrophosphate-iodide system could not sufficiently stabilize Ag ions in the Sn-Ag plating bath, and different kinds of additives were added to help deposit Sn-Ag alloys. Chen et al. (2008) studied the effect of polyethylene glycol (PEG) with different molecular weights on the electrodeposition of Sn-Ag alloys. Eutectic Sn-3.5Ag alloy films were readily obtained with a homogenous composition and smooth surface morphology. Polarization tests showed that PEG additives inhibited the preferential deposition of Ag^+ ions and PEG with a molecular weight of 4000 had the highest inhibition capability, while PEG with a molecular weight of 200 exhibited the lowest

inhibition. Other additives such as triethanolamine, sortitol, sodium gluconate, 1,4-hydroxybenzene, and trion X100 were added as chelating agents for Ag^+ ions for Sn-Ag deposition (Neveu et al., 2006). The results showed that the addition of the organic additives decreased the plating rate and suppressed dendritic Sn-Ag growth by adsorbing on the deposited surface. Sn-Ag bumps of controlled shape were successfully obtained from a plating bath containing triethanolamine.

2.4 Theory of electrodeposition and electrochemical composite deposition

2.4.1 Electrodeposition of a single metal

Fig. 2-6 shows the basic set up for an electrolytic cell used in electrodeposition.

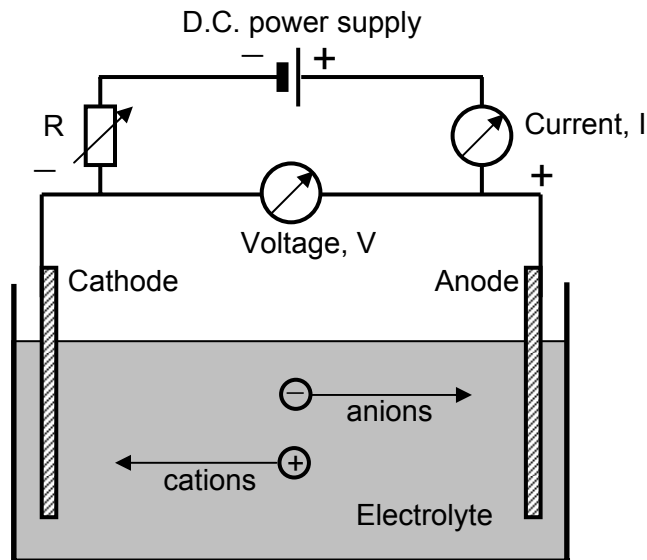


Fig. 2-6 Schematic illustration of an electrolytic cell (Raub and Muller, 1967).

Two electrodes are immersed in solution and are connected to the external DC power supply. The electrode on which the reduction reactions occur is called the cathode and the one where oxidation reactions occur is called the anode. When a voltage is applied between the two electrodes (cathode is negative with

respect to the anode), a current consisting of electrons starts flowing from anode, through the external circuit, and back to the cathode. Ionic current flows through the solution by the movement of cations towards the cathode and anions towards the anode. The quantitative aspects of the process are governed by the Faraday's Law.

2.4.1.1 Electrode reactions

During electrodeposition, reduction reactions occur on the cathode and oxidation reactions occur on the anode. One general cathodic reaction equation during the electrodeposition of a single metal M is:



where n is the number of electrons a metal ion obtains to be reduced to an atom. During metal electrodeposition, M^{n+} can be simple metal ions such as Sn^{2+} , or it can be a metal complex.

Reaction (2-2) is often accompanied by hydrogen evolution. In acid solutions, hydrogen evolution follows the equation:



In neutral and basic solutions, hydrogen evolution follows the equation:



Other reactions may also take place at the cathode, for example:



At the anode, when an insoluble anode is used, the main anode reaction is oxygen evolution. In an acidic solution, the anode reaction is:



In an alkaline solution, the anode reaction is:



When the anode is a soluble metal, oxidation reactions, which will dissolve the anode into solution, occur.



The equilibrium electrode potential between a metal and a solution of its ions ($M^{n+} + ne^- \rightarrow M$) is given by the Nernst Equation:

$$E_{M/M^{n+}} = E^{\circ} + \frac{RT}{nF} \ln C_{M^{n+}} \quad (2-9)$$

where E° is the standard electrode potential, R is the gas constant, F is the Faradaic constant, and C is the metal ion concentration. It can be noticed that the value of E depends on the concentration of metal ions to be plated. Addition of complexing agents can significantly change the concentration of metal ions, which will be discussed later in the thesis.

2.4.1.2 Electrical double layer

When a metal electrode is immersed in an aqueous solution, an electrically charged double layer forms in the immediate vicinity of the electrode. This layer is called the electrical double layer. Different models have been proposed to describe the features of the electrical double layer and a model that considers solvent molecules and specifically adsorbed anions is shown in Fig. 2-7.

The electrical double layer is defined by an inner Helmholtz plane (IHP) and an outer Helmholtz plane (OHP). The IHP is at a distance X_1 and contains solvent molecules and other ions or molecules, which are specifically adsorbed on the electrode surface. The OHP is at a distance X_2 , which is the closest point that nonspecifically adsorbed species can approach the cathode surface. The region extending from the OHP into the bulk solution, where the nonspecifically adsorbed ions are distributed due to the thermal agitation in the solution, is called the diffuse layer. The thickness of the diffuse layer is represented by δ which depends on the total ionic concentration in the solution. Fig. 2-7 also shows the potential-distance profile across the double layer region. The electrical double layer acts like a capacitor during the electrode reaction and produces a charging current. In some cases, if the concentrations of the electroactive species are very low, the charging current can be much larger than the Faradaic current for the electrode reaction. When a pulsed current is applied, the electrical double layer repeatedly charges and discharges during the on-time and the off-time period.

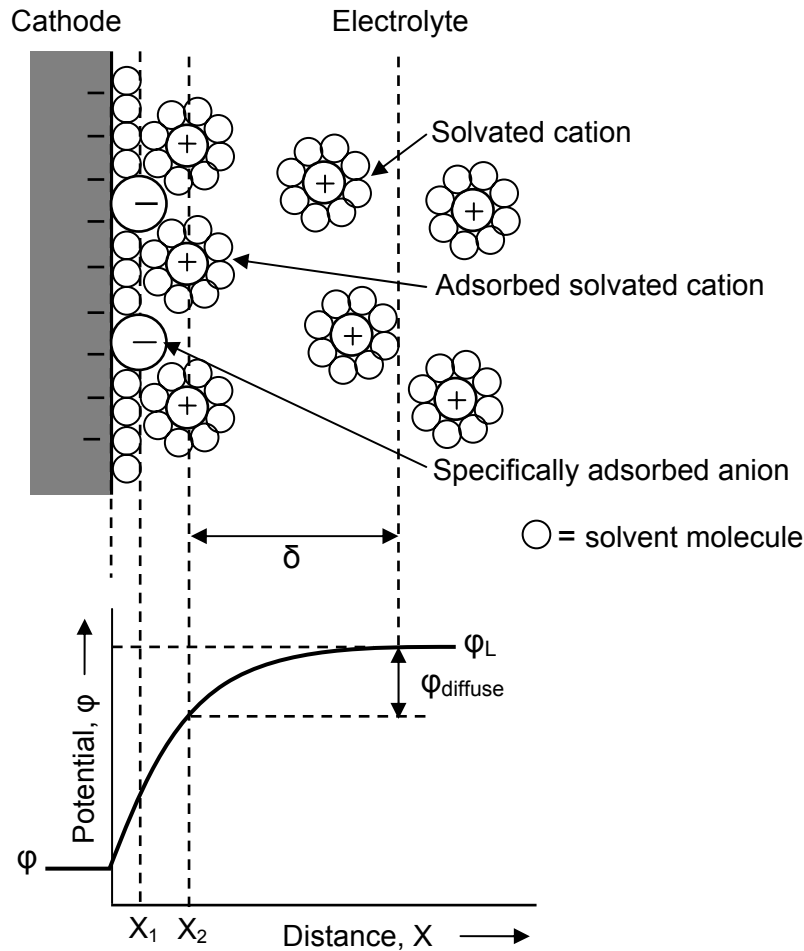


Fig. 2-7 Proposed model for the electrical double layer region under conditions where anions are specifically adsorbed and the corresponding potential profile across the double layer region (Bard and Faulkner, 2001).

2.4.1.3 Mass transfer mechanisms

During electrodeposition, electroactive species have to move from the bulk solution to the electrode surface continuously to support the reactions as well as to be part of the solution current flow. There are 3 main mechanisms for species in solution to move from one location to another, namely migration (under a potential gradient), diffusion (under a concentration gradient), and convection (movement of the solution) (Raub and Muller, 1967; Bard and Faulkner, 2001; Kanani, 2004).

When a voltage is applied across the two electrodes, an electrical field between the anode and cathode is set up. Assuming the solution has uniform conductivity, the potential gradient is given simply by dividing the voltage by the distance between the two electrodes. The magnitude of this potential gradient determines the rate at which ions move towards the two electrodes. However, the overall contribution to the supply of ions resulting from the migration process is very small during electrodeposition and can generally be neglected.

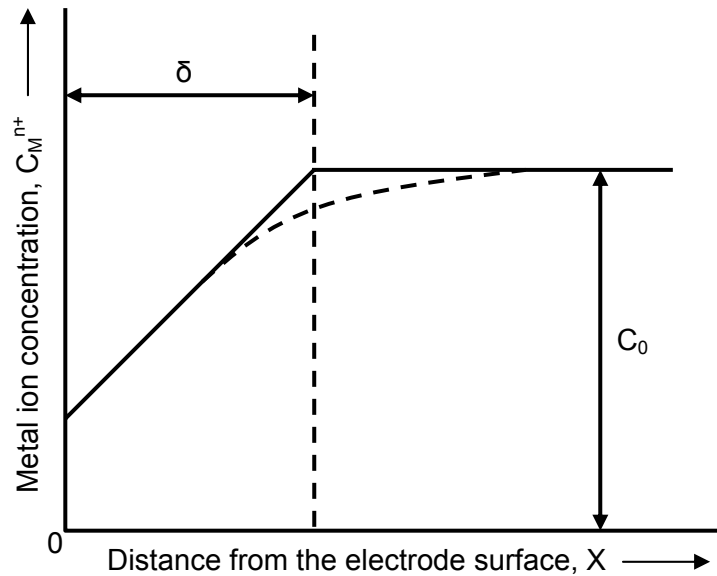


Fig. 2-8 Metal ion concentration profile as a function of distance from the electrode surface (Kanani, 2004).

Before charge transfer takes place at the electrode surface, the electroactive species, both charged and uncharged, have to move across the diffuse layer. The driving force for this movement is the concentration gradient. Under open circuit conditions, the concentration of species at the electrode surface is the same as that in the bulk solution. However, once current flow starts, metal ions are reduced onto the cathode and a concentration gradient is established. The metal ion concentration profile as a function of distance from the electrode surface is shown in Fig. 2-8. C_0 represents the bulk concentration of metal ions, and δ represents the thickness of the diffuse layer. The electrode surface is shown as the Y axis and the vertical dashed line indicates the outer edge

of the diffuse layer. The solid line shows the concentration profile predicted by the Nernst Equation and the curved dashed line shows a typical experimental result. When the diffusion rate of metal ions is not sufficient for the reduction, the metal ions will be depleted at the electrode surface, which means that the concentration on Y axis drops to zero.

In contrast to both the migration and diffusion mechanisms, which involve the movement of species in solution, convection results from fluid flow by stirring (forced convection) or by the natural circulation of a solution which is caused by a density gradient. Convection is responsible for the formation of the diffuse layer. Movement of ions across this diffuse layer takes place by diffusion. Convection may not operate within the diffuse layer, but it determines the thickness of the diffuse layer. The stronger the agitation, the thinner the diffuse layer and the higher the concentration gradient.

2.4.1.4 Rate-determining steps in electrode reactions

An overall electrode reaction begins with a metal ion dissolved in bulk solution and ends with its incorporation as a metal atom onto the cathode surface. The process can be divided into a series of steps, as shown in Fig. 2-9. The first step is for the ions to move from the bulk solution to the electrode surface region. This is mainly achieved by means of mass transfer processes or, more precisely, convection and migration, as discussed in the previous section. The ions then reach the outer layer of the diffuse layer, and diffuse across this layer driven by the concentration gradient. Once immediately adjacent to the cathode, the ions must move through the electrical double layer, after which they become adsorbed adatoms. These adatoms diffuse laterally across the cathode surface and transfer electrons, eventually coming together to form actual metal atoms. These metal atoms then incorporate themselves into the cathode surface and form the deposit layer through nucleation and growth of the deposit layer, which is referred to as electrocrystallization.

The electrode reaction rate is generally controlled by the following four processes (Bard and Faulkner, 2001): (1) mass transfer; (2) chemical reactions proceeding or following the mass transfer; (3) other surface reactions, such as adsorption, desorption, or crystallization; (4) electron transfer at the electrode surface.

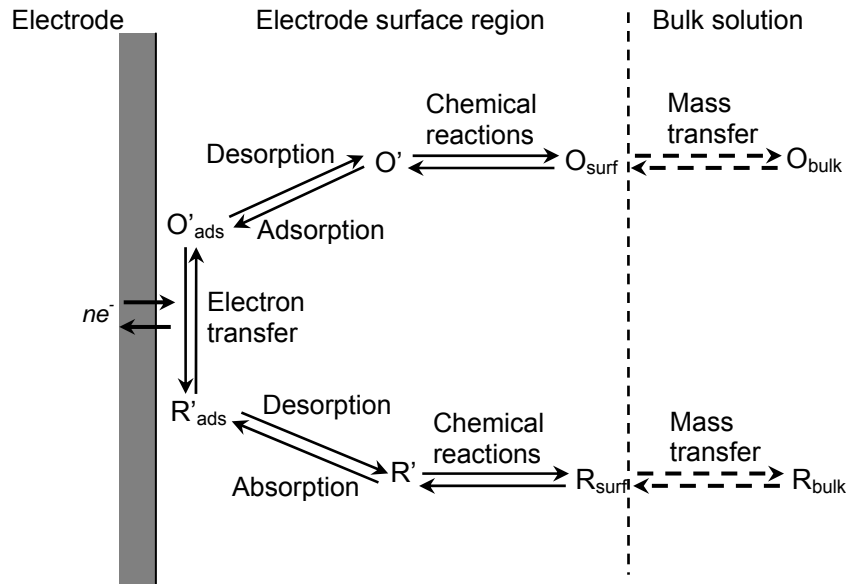


Fig. 2-9 Pathway for a general electrode reaction (Bard and Faulkner, 2001).

The electrode reaction rate is determined by the slowest process of these four, which is the rate-determining step. Under certain conditions, any one of these four processes can be the rate-determining step. In cathodic metal deposition, the process is initiated by discharge of metal ions which are already very close to the electrode. Thus, at the onset of the process, the rate-determining step is the movement of the charged species through the electrical double layer to the electrode surface. This leads to a depletion of the dischargeable metal ions in the near electrode region and metal electrodeposition can only continue if the metal ions are replenished from the bulk solution. The deposition process is increasingly mass-transfer controlled, except in the case of low current densities and higher metal ion concentrations.

2.4.1.5 Polarization and overpotential

The electrochemical equilibrium at an electrode surface is a dynamic equilibrium, during which ions in solution move in both directions at an equal rate and no net current flows. The departure of the electrode potential from the equilibrium value upon passage of a Faradaic current is termed polarization. The extent of polarization is measured by the overpotential, η . The overpotential is produced by inhibiting factors of various kinds, which affect the reaction at the electrodes. Depending on the kind and sites of the inhibition factors, different kinds of overpotentials, such as charge transfer overpotential, reaction overpotential, and mass-transfer overpotential, may be distinguished (Raub and Muller, 1967; Bard and Faulkner, 2001; Kanani, 2004).

The charge transfer overpotential is also called activation overpotential and is caused by inhibition of the charge transfer reaction which takes place across the electrical double layer. It is the energy required to overcome the reaction activation energy barrier. In metal deposition, the inhibition is in the discharge mechanism. A large overpotential is observed sometimes even at low current densities which is mainly due to the activation overpotential. The presence of a certain activation overpotential must always be assumed in metal deposition.

The reaction overpotential is caused by the inhibition of reactions, which precede or follow the electrode reactions. These are mainly hydration, dehydration, complex formation, and complex decomposition reactions.

The mass-transfer overpotential (also called concentration overpotential) is caused by inhibition of the transfer processes of the potential-determining ions or complexes towards the electrical double layer. As mentioned earlier, during cathodic metal deposition, the metal ions are consumed at the cathode, so that a diffusion layer is formed in the immediate vicinity of the cathode and the metal ion concentration in this layer is different from that in the bulk solution. More pronounced differences in concentration will cause greater inhibition of ion diffusion at the electrodes.

The total overpotential occurring at an electrode can be considered as a sum of the above overpotentials, as shown in Fig. 2-10. η_{mt} represents the mass-

transfer overpotential, η_{ct} represents the charge transfer overpotential, and η_{rxn} represents the reaction overpotential. The electrode reaction can then be represented by a resistance, R , composed of a series of resistances (or more precisely, impedance) which represent the different steps: R_{mt} , R_{ct} , and R_{rxn} . A fast reaction step is characterized by a small resistance, while a slow reaction step is represented by a high resistance. Although different reactions at an electrode may be complex and differ in certain aspects, all systems have a common feature in that the reacting species must pass through the metal-solution interface and these species must either be transferred away from the electrode or towards the electrode. The site of the inhibition is thus either at the electrical double layer or is concerned with the transport processes; both cases can occur simultaneously.

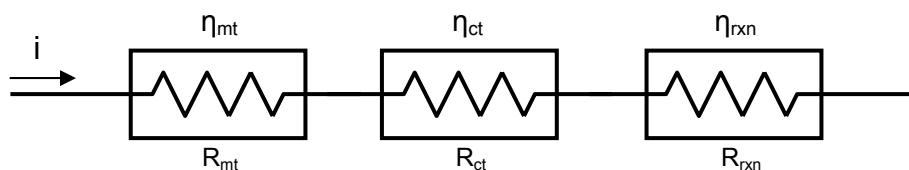


Fig. 2-10 Processes in an electrode reaction represented as resistances and overpotentials (Bard and Faulkner, 2001).

2.4.2 Electrodeposition of metal alloys

Metal alloys can be electrodeposited through two ways: (1) by sequential plating where the metals are individually deposited in layers and then are alloyed during reflow, which is also called "sandwiched layers deposition"; (2) by co-deposition where all metals are electrodeposited in a single step. Here the co-deposition method is of interest.

The feasibility of co-deposition of metal alloys can be determined using the Nernst Equation. The reduction potential of each metal ion in solution can be calculated. The smaller the difference in potential between the two metals, the more likely they can be co-deposited. As pointed out by Kanani (2004), for a solution containing two or more different metal ions, at low overpotential, the metal with the most noble reduction potential will deposit at a faster rate. As

overpotential increases, the overall reaction will shift from charge transfer control to the mixed control and then to mass-transfer control. At higher overpotentials, where the electrodeposition reaction is under mass-transfer control, the relative deposition rates of two or more metals will depend on their concentrations and the diffusion coefficients of the metal containing ions. There are two common ways to adjust the reduction potential for metal ions. One way is by adjusting the concentration of one or more metals. The Nernst Equation (Equation 2-9) shows that the concentration term is a logarithmic function of the reduction potential and only has minimal effect if differences of the standard potentials between different metals are large. Therefore, simple adjustments of metal concentrations may not give the desired deposit composition. The other way is by using complexing agents. The formation of complexes by bonding the metal ions with complexing agents will decrease the concentration of the free metal ions in solution significantly and modify the reduction potential of the metal ions. For individual metals, the chemistry between metal ions and different complexing agents is fairly well known. When many ions are present in the solution, it is difficult to determine a suitable complexing agent and this requires extensive study. More details about complexing agents will be given later.

2.4.3 Pulsed current electrodeposition

In direct current (DC) electrodeposition, the potential or current density is kept constant all the time. In other words, there is only one parameter, current density, that can be changed. In pulsed current (PC) plating, the potential or current density alternates rapidly between two different values (Ghaemi and Binder, 2002; Chandrasekar and Pushpavanam, 2008). This is accomplished with a series of pulses of equal amplitude, duration, and polarity, separated by period of zero current as shown in Fig. 2-11. Each pulse consists of an on-time (T_{ON}) during which potential and current is applied, and an off-time (T_{OFF}), during

which open circuit potential and zero current is applied. j_a is the average current density and j_p is the peak current density.

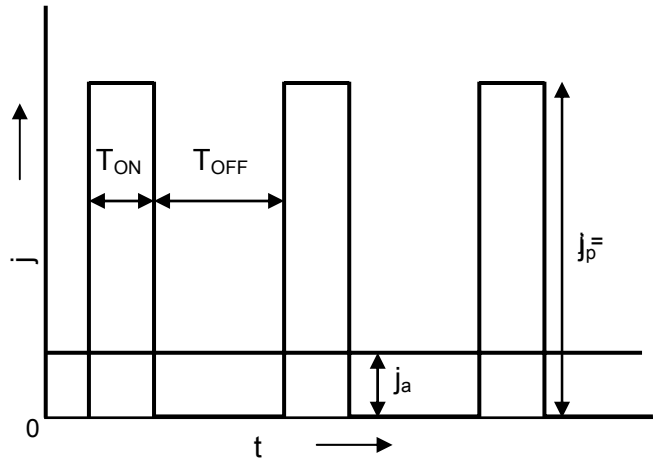


Fig. 2-11 Typical direct current and pulsed current waveform.

The duty cycle corresponds to the fraction of on time of a cycle and is given by the equation below:

$$\text{Duty cycle} = \frac{T_{ON}}{T_{ON} + T_{OFF}} \quad (2-10)$$

The average current density (j_a) is defined as:

$$j_a = \text{peak current density } (j_p) \times \text{duty cycle} \quad (2-11)$$

The average current density in PC plating is similar to the current density used in DC plating. Duty cycles may vary from 1 to 100% with on-off times from microseconds to milliseconds depending on the power supply limitation. In PC plating, there are three variables, namely peak current density, current on-time, and current off-time, that can be changed over a very broad range. For a given average current density, a number of combinations of different peak current densities and on-off times are available. This gives PC plating two important features (Ibl, 1980). Firstly, a very high instantaneous current density, one to two orders in magnitude greater than the steady-state limiting current density as reported, can be used without depleting the metal ions at the electrode surface. This favors the initiation of the nucleation process and greatly increases the

number of grains per unit area, resulting in a finer grained deposit with better properties than conventional DC plating (Ibl, 1980; Chin and Zhang, 1986). Secondly, during the off-time period, adsorption and desorption, as well as recrystallization of the deposit occurs, which can change the microstructure of the deposits. In addition, more time is provided for the ions to diffuse from the bulk solution to the electrode surface (Chin and Zhang, 1986; Ghaemi and L. Binder, 2002), resulting in a different diffuse layer structure as well as a different ion concentration profile as a function of time, as shown in Fig. 2-12 and Fig. 2-13.

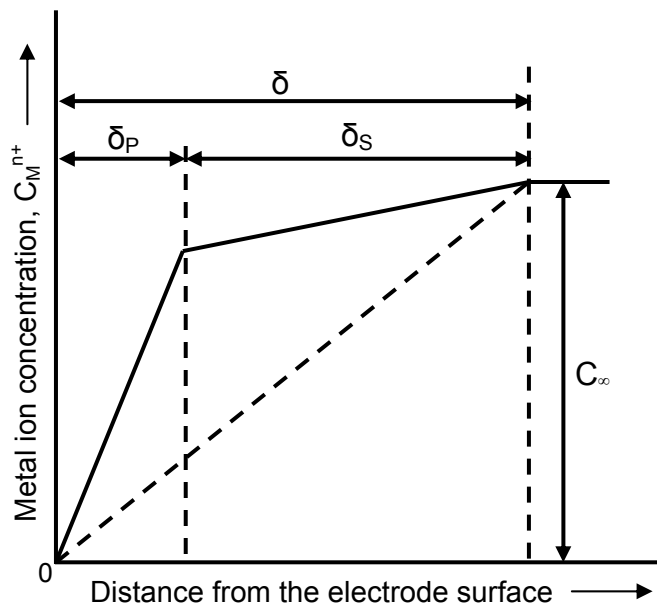


Fig. 2-12 Metal ion concentration profile as a function of distance from the electrode surface during PC plating (δ is the thickness of the diffuse layer, δ_s is the thickness of the steady state diffuse layer and δ_p is the thickness of the pulsed diffuse layer in a quasi-steady state) (Kanani, 2004).

An additional pulsed-diffuse layer immediately adjacent to the cathode surface forms during PC plating. The metal ions migrate from the bulk solution to the outer edge of the steady-state diffuse layer, which is analogous to the diffuse layer formed in DC plating. After passing through this layer, the metal ions move closer to the cathode, entering the pulsed-diffuse layer. This layer builds up and collapses in synch with the pulse frequency, which causes a variation in the metal ion concentration within the diffuse layer. Repetition of the formation and

collapse of this layer with the corresponding change in metal ion concentration is known as quasi-steady-state. The thinner the pulsed-diffuse layer, the better it can follow the contours of the surface, so that all areas of the cathode surface are equally accessible. The total thickness of the diffuse layer, δ , denotes an expansion of the diffuse layer formed in DC plating.

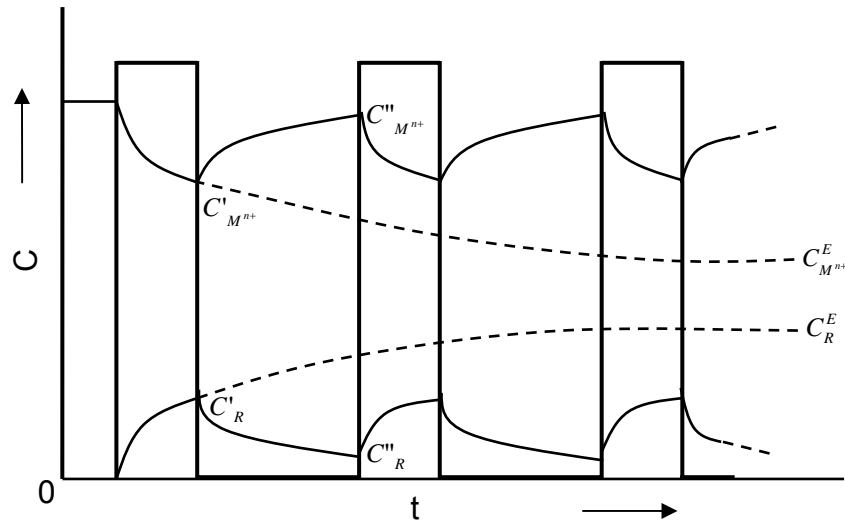


Fig. 2-13 The variation of metal ion concentration $C_{M^{n+}}$ and reduction product concentration C_R with time during PC and DC plating (Kanani, 2004).

Fig. 2-13 shows the pulsed current, the metal ion concentration, and the concentration of the reduction product at the cathode surface during PC and DC plating as a function of time. During the on-time in the first pulse, the metal ion concentration at the cathode surface falls from $C_{M^{n+}}$ to $C'_{M^{n+}}$. It then increases during the off-time to $C''_{M^{n+}}$ and once again decreases during the on-time in the second pulse, followed by an increase again in the second off-time period, and so on. In this quasi-steady-state, the metal ion concentration at the cathode surface is significantly higher than that in DC plating, which is expressed as $C_{M^{n+}}^E$. The concentration of the reduction product at the cathode surface increases to C'_R at the end of the first on-time period, and then falls to C''_R at the end of the first off-

time period. This progressive decrease continues until quasi-steady-state is reached and the reduction product concentration is significantly lower than that in DC plating, which is expressed as C_R^E .

The pulsed current not only changes the structure of the diffuse layer, but also affects the structure of the electrical double layer. As soon as a current is applied to the plating cell, a negatively charged layer is formed around the cathode. When using DC plating, this layer charges to a defined thickness and obstructs ions from reaching the cathode. In PC plating, the output of the current is periodically turned off, during which the layer is discharged. This allows easier passage of the ions through the double layer and onto the electrode surface.

Compared to DC plating, PC plating has many advantages. It offers better control over the properties of deposits because more parameters can be varied independently. It is possible to achieve higher instantaneous current densities and higher overpotentials which results in higher nucleation rate and yields a finer grain size (Kim and Weil, 1989; Devaraj et al., 1990; Marlot et al., 2002). PC plating has proved to be an important technology for improving the mechanical and physical properties of deposits, as well as the corrosion resistance (Cherkaoui et al., 1988; Devaraj et al., 1990; Ghosh et al., 2000). It can also be used to produce alloy compositions and microstructures which are not attainable with DC plating, such as smoother surfaces, higher purity and uniformity, lower porosity, and inhibited dendrite growth (Popov et al., 1988; Chin and Balamurugan, 1992; Honma, 2001; Nakanishi et al., 2001; Richoux et al., 2007). It has been reported that PC plating can reduce additive requirements by 50-60% (Chandrasekar and Pushpavanam, 2008).

2.4.4 Electrochemical composite deposition

Electrochemical composite deposition was initially developed to improve the properties of deposited metals, such as wear resistance, micro-hardness, and corrosion resistance, by co-depositing fine particles ($< 30 \mu\text{m}$) into the deposited layers (Hovestad and Janssen, 1995; Talbot 2004; Hou et al., 2006). The

incorporation of the particles into the growing metallic deposits is usually accomplished by suspending the particles in suspension and then settling them onto a horizontal cathode. The particles used should be inert to the solution, which means that they do not dissolve into the solution. Different types of particles such as metals (Cr, Ti, W), inorganic compounds (Al_2O_3 , SiO_2 , SiC, diamond), or organic compounds (PTFE) particles, have been used. These particles can be different shapes, such as powders, fibers, or encapsulated particles. Recently, more attention has been placed on the incorporation of nanoparticles, 100 nm or less in size, to obtain improved properties. By using metallic particles, this method can be used to deposit alloys which could not have been formed by simple electrodeposition of metal ions. The problem is that these conductive particles tend to agglomerate on the deposit surface, and as soon as they are adsorbed on the deposit surface, both metal deposition and hydrogen evolution occurs on them, resulting in rough and porous deposits.

The properties of the composite deposits are largely influenced by the amount of particles incorporated into the metallic matrix. Numerous process parameters have been found to affect the particle incorporation in composite deposits directly or indirectly. The plating parameters include: (1) Particle properties, such as particle materials, particle size, and particle shape; (2) Suspension properties, such as pH, constituents, additives, aging; (3) Deposition variables, such as particle concentration in suspension, current density, agitation, and temperature. The influence of some of the parameters is interrelated.

The properties of composite deposits also depend on the particle distribution in the deposits. In order to achieve a uniform distribution of particles through the deposit, the particles must be uniformly suspended in the suspension, preventing the settling of particles under gravity. This can be achieved by agitation, such as stirring, air bubbling, recirculation, and ultrasonic agitation. The rate of agitation affects particle co-deposition in two opposite ways (Lee and Wan, 1988). Increased agitation results in higher particle incorporation, because agitation enhances the transfer of particles from the bulk of the suspension to the cathode. However, excessive agitation decreases particle incorporation by ejecting

the particles from the cathode surface before being incorporated. When very fine particles are used, e.g., nano-particles, a suitable surfactant is often added to help disperse the particles.

Particle incorporation in a metal matrix is a three step process, involving particle mass transfer from the bulk of the suspension to the electrode surface, adsorption of the particles at the electrode surface, and mechanical inclusion of the particles into the deposit layer (Kanani, 2004). The transfer of the particles toward the electrode and the adsorption of the particles onto the electrode surface is a complicated process. After particles are added into solution, chemical and physical adsorption of electrolyte ions onto the particles occurs (Conway, 2005). This adsorption and the initial particle surface composition determine the particle surface charge, which induces a double layer of electrolyte ions around the particle. These double layers surrounding the particles play a major role in the interactions between particles and between particles and the electrodes. Surfaces in electrolytes interact through the competitive action of attractive and repulsive forces. Overlap of double layers results in the electro-osmotic force, which is repulsive for surfaces of like charge and attractive for surfaces of unlike charge. The applied electrical field also places an electrophoretic force on the particle double layer. Particles with a positive charge codeposit onto the cathode more easily, because they are attracted to the negatively charged cathode.

2.4.5 Electrolyte additives

Different kinds of additives have been used in aqueous deposition processes (electrodeposition, electroless deposition, and electrochemical composite deposition), due to their effects on electrolyte characteristics and the growth and structure of the deposits. The additives can be organic or inorganic, ionic or nonionic, and are added into plating baths for specific purposes, such as increasing solution conductivity or stability, improving leveling or metal distribution, optimizing chemical, physical, or mechanical properties of the deposits including corrosion resistance, brightness, hardness, mechanical strength,

ductility, internal stress, and wear resistance. One concern about additives used in deposition is that they can be environmentally harmful and the spent electroplating bath may have to be subjected to special treatment to destroy the harmful chemicals. In the following sections, three different kinds of additives are discussed in detail.

2.4.5.1 Complexing agents

As discussed in Section 2.4.2, one way to bring the reduction potentials of different metal ions closer together in alloy electrodeposition is to use complexing agents. Complexing agents are species that are able to form ionic compounds with metal ions without forming any precipitates. These ionic complexes often behave quite differently from the metal ions themselves. By forming complexes, the metal ions become more stable and are less readily available for any form of reactions. To become available again, the complex has to decompose. If the metal ion is too strongly bonded in such a complex, it will not be released for reduction and no metal deposition will take place. The strength with which the metal is locked up in a complex is represented by its stability constant. Certain complexing agents can only form complexes with certain metal ions, and for each complexing agent and metal ion, different kinds of complexes can form with different numbers of each species or different bonding configurations. Each complex has its own stability constant.

Although the total amount of metal ions in a system cannot be changed by forming complexes, the concentration of free metal ions that are not complexed will decrease. The greater the stability constant, the more the metal ions will be complexed and the lower the concentration of the free metal ions in solution. Complexing agents can help dissolve metal ions, affect the bath stability, make deposition initiation easier, and in some cases increase the deposition rate.

2.4.5.2 Leveling agents

A leveling agent is a chemical that helps smooth preexisting irregularities on the substrate surface, such as pits or scratches, to form a smoother deposit surface than that of the original substrate. In normal electrodeposition, the surface of the deposit is not always smooth, i.e., there are peaks and valleys within the substrate surface. At the peak regions, the distance to the anode is the shortest, so the electrical field strength is the highest. Therefore, the current density at the peak regions will be the highest, causing more metal reduction at the peak regions than in the valleys, which will accentuate the roughness of the deposits. In order to obtain a smooth and reflective surface, more metal needs to be deposited in the valleys than at the peaks, which is the opposite of normal deposition behavior. The function of the leveling agent used in electrodeposition is to produce this leveling in plating solutions. The agents are adsorbed preferentially on the peaks and edges of the substrate and restrict metal deposition at such positions. The leveling effect increases as the deposit thickness grows. After sufficient time, the peaks and valleys will be effectively leveled.

2.4.5.3 Surfactants

Surfactants are also known as wetting agents. A surfactant is a kind of surface active species, which can improve surface wetting by accumulating at a surface or interface. A surfactant has an asymmetric or dipolar nature, normally with a hydrophilic head and a hydrophobic tail. Surfactants can be anionic, cationic, or non-ionic, depending on the hydrophilic functional groups. The ionic hydrophilic heads are typically -COO^- or -SO_3^- groups, and the hydrophobic tail may be a non-polar aliphatic long-chain hydrocarbon. Non-ionic surfactants themselves are uncharged; they acquire charge from ions present in solution.

At an air-water interface, surfactants are oriented with the hydrophilic head into the aqueous solution, and the hydrophobic tail to the air side. In this way, they can reduce the interfacial tension of the air/water interface. At a water-solid interface, the hydrophilic groups are hydrated and drawn towards the

aqueous phase, with the hydrophobic end weakly adsorbed onto the solid surface, which can be the electrode surface in electrodeposition. With this degree of ordering imposed at the interface, the interfacial tension is reduced, which means the electrode surface becomes more easily wetted by the electrolyte. This reduced surface tension at the electrode and solution interface can be beneficial to the electrodeposition process by facilitating the release of gas bubbles (hydrogen or trapped air) adhering to the electrodes (cathode or anode). The adhesion of such bubbles on the electrodes shields the reactions that occur in the area leading to pitting or porosity in the deposits.

Other than suppressing hydrogen evolution, surfactants can also be used to alter the electrode polarization, induce leveling and grain refining to obtain uniform and smooth deposits, enhance surface brightness, assist the suspension and incorporation of inert particles into the metallic matrix to produce composite deposits, help clean solutions by precipitating out suspended contaminations in solid matter, and help dissolve insoluble or poorly soluble organic compounds in water and improve their distribution in solution.

2.5 Objectives of the current work

Pb-Sn solders have many excellent properties and have been used as the principal joining materials in electronic packages over the past 60 years. The main purpose for the Sn, Sn-Cu and Sn-Ag-Cu solder film deposition work presented in this thesis is to obtain alternative Pb-free solders from an environmental and health prospective. Previous research on Sn, Sn-Cu and Sn-Ag-Cu electrodeposition has focused on investigating different additives in alkaline baths, sulfate, methanesulfonate, pyrophosphate and fluoroborate acid baths to stabilize plating solutions and improve deposit morphologies. One concern about these additives is that many of them are not safe to work with and can be environmentally harmful. Therefore, before waste disposal, special treatments are required to make them harmless.

The objectives of the current work are to develop simple and environmentally friendly plating baths for Sn, Sn-Cu and Sn-Ag-Cu deposition, by using as few additives as possible. Two techniques, electrodeposition from dissolved metal salts solution and electrochemical composite deposition from dissolved metal salts and particle suspensions, have been studied. Appropriate dispersants were added to suspensions with Cu or Ag particles. Different plating parameters, including chemical concentration, current density, agitation, aging and additives were evaluated and optimized to obtain eutectic and near eutectic solder films. Tri-ammonium citrate was used as the only complexing agent for Sn, Sn-Cu and Sn-Ag-Cu deposition. It was of interest to determine the distribution of Sn(II)-citrate complexes and their effects on Sn electrodeposition. For this purpose, speciation diagram calculations, reduction potential calculations, and polarization studies were performed. To study the nucleation and film growth mechanism of Sn and Sn-Cu electrodeposition from Sn-citrate and Sn-Cu-citrate solutions, current-controlled and potential-controlled electrochemical analysis, nucleation modeling and surface morphology characterization using atomic force microscopy (AFM), Auger electron spectroscopy (AES) and scanning electron microscopy (SEM) were employed.

Another objective of the current work was to study the interfacial reactions between the as-deposited Sn-Cu and Sn-Ag-Cu solders and common substrate metals Cu and Ni. As mentioned in previous sections, solders play very important roles in electronic packaging by forming electrical interconnections, facilitating heat dissipation, providing mechanical/physical support and serving as a solderable surface finish layer. The performance and quality of solders are crucial to the integrity of a solder joint, which in turn control the reliability of the whole electronic product. During soldering, solders are heated above their melting point and become molten. Two processes occur simultaneously: the substrate metal dissolves into the molten solder and the active constituents in the solder combine with the substrate metal to form IMCs at the solder/substrate interface. During subsequent storage or service of the assemblies, the IMCs generated during soldering grow further in thickness or increase in number. The formation

of excessive IMCs may lead to poor joint strength and eventual failure of the solder joint. Much research work has been carried out to study the interfacial reactions between liquid and/or solid Sn and Cu and Ni which have been summarized in previous sections. However, most solders used in the research are from commercial solder pastes and solder balls, or pure metals assembled with specified compositions. In this work, Sn-Cu and Sn-Ag-Cu solders were deposited onto Cu and Ni substrate from self-developed solutions. To study the formation and growth of the IMCs at the solder/substrate interface during reflow and aging, microstructure characterization and diffusion coefficient calculations of the IMCs were performed.

Chapter 3 Electrodeposition and electrochemical composite deposition of Sn-Cu alloys¹

3.1 Introduction

Electrodeposition is a useful technique to deposit different metals and alloys. A number of baths and additives have been developed to electrodeposit Sn and Sn-based alloys as discussed in the previous chapter. The standard electrode potential for Cu^{2+}/Cu is 0.34 V vs SHE (standard hydrogen electrode), which is much higher than that of Sn^{2+}/Sn (-0.14 V vs SHE). Complexing reagents are often used to bring the standard reduction potentials of the two pairs closer.

Typical Sn-Cu plating solutions are strongly alkaline with alkali cyanide or alkali pyrophosphate as a complexing agent (Yanada et al., 2003). These solutions are not compatible with photoresists when plating on patterned substrates. Some solutions such as pyrophosphate baths and borofluorate baths are also used to co-deposit both the Sn and Cu. The purpose of these baths, however, is not to obtain a Sn-Cu eutectic alloy but rather to obtain an alloy with a much higher Cu content. Other Sn-Cu plating solutions are based on sulfuric acid or methanesulfonic acid (MSA) with additives such as polyoxyethylene laurylether, sodium alkyl sulfate ester, thiourea, dimethylthiourea, polyoxyethylene β -naphthol ether, 1-naphthaldehyde and tri-ammonium citrate, among others (Fukuda et al., 2003; Yanada et al., 2003; Martyak and Seefeldt, 2004). These additives are believed to be helpful in forming smooth and homogeneous deposits, minimizing hydrogen gas evolution, improving solution stability and refining grain structures. In spite of these benefits, the application of many of these additives is undesirable from a safety and environmental perspective. The additives also create difficulty in the treatment of the wastewater streams. It is,

¹ Some of the results in this chapter have been published. Han, C., Liu, Q. and D. G. Ivey, Electrodeposition of Sn-0.7wt%Cu eutectic alloys from chloride-citrate solutions, *Journal of Applied Surface Finishing*, 3 (2008) 119-127.

therefore, desirable to develop new Sn-Cu solder plating processes where the deposition potential is controlled without using too many additives (Survila et al., 2001).

Tri-ammonium citrate is an ammonium salt of citric acid and can be used as an emulsifier in dairy products, such as processed cheeses, and as an acidity regulator. Tin-citrate complexes have been reported to form in solutions containing both stannous chloride and ammonium citrate (Hess and Taft, 1938). The formation of the Sn-citrate complexes was deduced from the observation that the addition of sodium carbonate to the solution did not result in the precipitation of Sn carbonate (Hess and Taft, 1938). Ammonium citrate has been used as a complexing agent in both acidic and alkaline solutions for Sn, Sn-Co, Sn-Au, Co-Mo, Co-W and Cu electrodeposition (Makino and Maeda, 1992; Aravinda et al., 2000; Survila et al., 2001; Kim and Duquette, 2006b; Subramania et al., 2007). Yanada et al. (2003) have used tri-ammonium citrate and Sn/Cu methanesulfonate to electrodeposit Sn-Cu alloys, with many other additives.

Alloys can also be deposited using electrochemical composite deposition when metallic particles are used. During deposition, suspended metallic particles incorporate into the growing metallic deposits to form alloys. No report has been found focusing on the electrodeposition of Sn-Cu alloys from simple chloride-citrate solutions, nor from Sn-citrate suspensions with Cu particles.

The objective of this part of the research is to develop simple plating baths to electroplate Sn-Cu eutectic and near-eutectic solder films. A key target is to minimize the number of additives, thereby making the plating bath as “green” as possible. To achieve this goal, tri-ammonium citrate will be the primary additive and Cu and Sn chloride will be the salts. Two approaches are being pursued: one involves a single solution with dissolved metal salts (Sn-Cu-citrate solution) and the other involves a Sn suspension with Cu particles (Sn-citrate solution + Cu particles). Both PC plating and DC plating are utilized for comparison purposes. Solutions with fixed $\text{SnCl}_2 \cdot 2\text{H}_2\text{O}$ concentration and various tri-ammonium citrate concentrations are tested, both in terms of solution stability and Sn and Sn-Cu films electrodeposition, to optimize the Sn-citrate solution. Sn and Cu co-

deposition behavior from chloride-citrate baths and the electrodeposition conditions to obtain eutectic and near-eutectic Sn-Cu solder films by both PC and DC plating are studied. Work is also conducted to study the effect of current densities on the plating rate and Cu content in the deposits, solution stability and the effect of agitation and the addition of gelatin and naphthol on Sn-Cu electrodeposition. For Sn-Cu deposition from a Sn-citrate suspension with Cu particles, the electrodes are arranged in both horizontal and vertical orientations, and a dispersant is tested to help disperse the Cu particles.

3.2 Experimental materials and procedures

The Sn-citrate solution initially developed contains tri-ammonium citrate ((NH₄)₃C₆H₅O₇, Alfa Aesar, 98%) and SnCl₂·2H₂O (Fisher Scientific). The Sn-citrate solutions were prepared by dissolving tri-ammonium citrate in deionized water and then dissolving SnCl₂·2H₂O in the citrate solution. To obtain Sn-Cu-citrate plating solutions, either CuCl₂·2H₂O (Fisher Scientific) or Cu particles (200-300 nm in size) were added into the Sn-citrate solution. The chlorides were added as the source of Sn²⁺ and Cu²⁺ ions and the citrate was added as a stabilizer (complexing agent). The volume of the plating solution was kept at 40 mL.

The prepared solutions were characterized using a Gamry electrochemical system, with silicon wafer pieces, metalized with a 25 nm TiW layer and a 200 nm Pt layer (provided by Micralyne, Inc.) as both the working and the counter electrodes, and a saturated calomel electrode (SCE) as the reference electrode. All potentials are specified relative to SCE. Before testing, the Pt electrodes were cleaned in an ultrasonic bath for 2 minutes in acetone followed by ethanol and then rinsed with deionized water. Polarization measurements were carried out at a scanning rate of 1 mVs⁻¹. Cyclic voltammetric (CV) measurements were carried out from 0.9 V to -1.1 V (vs SCE) at a scanning rate of 50 mVs⁻¹.

Two types of substrates were used for electrodeposition. Silicon wafer pieces, metallized with a 25 nm TiW layer and a 200 nm Au layer through sputtering, were used for electrodeposition on Au. TiW acts as an adhesion and

barrier layer and Au as a seed layer for electroplating. Sectioned Cu sheets with a Ni layer (~12 μm thick) electroplated on one side were utilized for electrodeposition on Ni. A standard Watts Ni plating solution was used for Ni electrodeposition on Cu. Before plating, the Cu pieces were cleaned and any surface oxide layers removed by treating in a $\text{CuCl}_2 + \text{H}_2\text{SO}_4$ solution for about 20 seconds, followed by rinsing with deionized water. The plating surface area of all the samples was maintained at around 0.8 cm^2 . A Dynatronix DuPR 10-0.1-0.3 pulse plating power supply was used for both PC and DC plating, with a 2 ms forward on-time and 8 ms forward off-time during PC plating based on previous work (Sun and Ivey, 1999; Olsen, 2005). For both PC and DC plating, current densities were varied from 2.5 mA/cm^2 to 15 mA/cm^2 and all deposition was done at room temperature.

The microstructure and composition of the Sn-Cu films were characterized using a Hitachi H2700 scanning electron microscope (SEM) equipped with an ultrathin window energy dispersive x-ray (EDX) spectrometer. Deposit compositions were found by averaging measurements taken from at least three regions, each $400 \times 400 \mu\text{m}^2$ in size. Analysis was done at 20 kV with a working distance of 17 mm and a count rate of 2500-4000 counts/s. Two different methods were used to make cross section samples. One way was by cleaving the samples along Si {110} planes using a diamond pen. The other way was by cleaving and polishing. The samples were cleaved into the desired size first, mounted with epoxy resin, ground with SiC papers (240, 320, 400, 600, 1200 and 4000 grit in sequence) in cold water and finally polished with a $0.05 \mu\text{m}$ diameter Al_2O_3 particle suspension. Phase analysis was performed using thin film X-ray diffraction (XRD) with a Rigaku rotating Co anode system, operating in continuous scanning mode at a voltage of 40 kV and a current of 160 mA.

The thickness of the Sn-Cu films was measured using an Alpha-step 200 profilometer. The thickness was taken as the average (A) of at least seven measurements (A_i). The error (R) was calculated using the following equation:

$$R = \sum |A - A_i| / 7 \quad (3-1)$$

Brookhaven ZetaPALS was used to measure particle size in the suspensions using its 90Plus module.

3.3 Results and discussion

3.3.1 Optimization of Sn-citrate and Sn-Cu-citrate solutions for Sn and Sn-Cu electrodeposition

3.3.1.1 Effect of tri-ammonium citrate concentration on Sn electrodeposition

Previous work by He et al. (2008) showed that solutions containing 0.31-0.41 mol/L (75-100 g/L) tri-ammonium citrate and 0.22 mol/L (50 g/L) $\text{SnCl}_2 \cdot 2\text{H}_2\text{O}$ can be used to electrodeposit tin films. To determine the optimum ratio of tri-ammonium citrate to Sn salt, both in terms of solution stability and electrodeposition of Sn and Sn-Cu films, initial work focused on solutions containing 0.22 mol/L (50 g/L) $\text{SnCl}_2 \cdot 2\text{H}_2\text{O}$ and different amounts of tri-ammonium citrate. The concentrations of tri-ammonium citrate were varied from 0.22 mol/L (54 g/L) to 0.82 mol/L (200 g/L), i.e., the molar ratio of Sn^{2+} :citrate varied from 1:1 to 1:3.6. At a molar ratio of 1:1 (Solution A in Table 3-1), a white precipitate was formed after mixing $\text{SnCl}_2 \cdot 2\text{H}_2\text{O}$ with the tri-ammonium citrate solution. The precipitate occupied about 25% of the solution volume. The minimum concentration of tri-ammonium citrate required to completely dissolve 0.22 mol/L $\text{SnCl}_2 \cdot 2\text{H}_2\text{O}$, without forming precipitates, was found to be 0.30 mol/L (Table 3-1).

Table 3-1 Volume of precipitates formed in different Sn-citrate solutions

	A	B	C	D	E	F
$\text{SnCl}_2 \cdot 2\text{H}_2\text{O}$ (mol/L)	0.22	0.22	0.22	0.22	0.22	0.22
Tri-ammonium citrate (mol/L)	0.22	0.28	0.29	0.30	0.31	0.33
Volume of precipitates (%)	25%	17%	2%	0	0	0

Table 3-2 Composition of Sn-citrate solutions studied by polarization measurements

	S1	S2	S3	S4	S5
SnCl ₂ •2H ₂ O (mol/L)	0.22	0.22	0.22	0.22	0.22
Tri-ammonium citrate (mol/L)	0.30	0.41	0.51	0.62	0.82

The work that follows is, therefore, focused on solutions with tri-ammonium citrate concentrations ranging from 0.30 mol/L to 0.82 mol/L, which are identified as S1, S2, S3, S4 and S5 in Table 3-2. The pH values of these five solutions are shown in Fig. 3-1 with values ranging between 4.1 and 5.8, which are slightly acidic. As the tri-ammonium citrate concentration increases, solution pH increases, which is due to the hydrolysis of HL³⁻ ions to form H₂L²⁻, H₃L⁻ and H₄L (where L represents the tetravalent citrate ligand, e.g., C₆H₄O₇⁴⁻, and citric acid can be represented as H₄L). More details about the Sn(II)-citrate solution chemistry are discussed in Chapter 4.

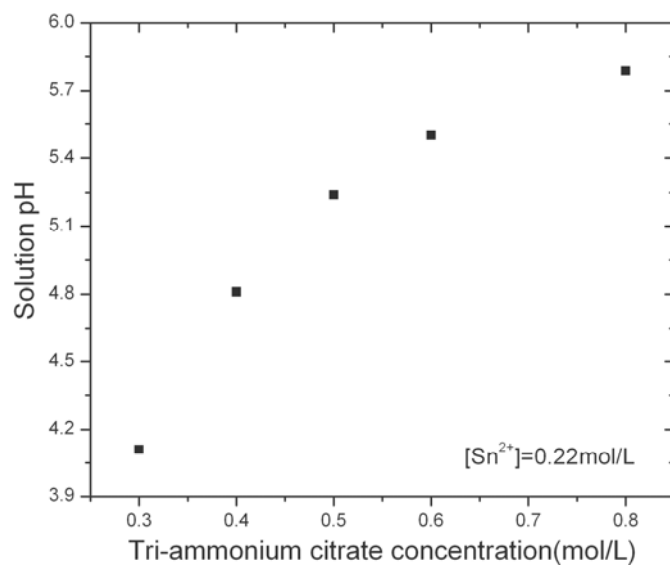


Fig. 3-1 pH values for Sn-citrate solutions. In all five solutions, the concentration of SnCl₂•2H₂O was kept at 0.22 mol/L, while the concentration of tri-ammonium citrate was varied from 0.30 mol/L to 0.82 mol/L.

Polarization measurements for the five solutions are shown in Fig. 3-2. Both the electrodes were placed vertically during the measurements. All five solutions showed similar polarization behavior. The reduction of stannous ions starts where the current density rises from zero. After this point, the current density increases rapidly as the potential is swept to more negative values, reaches a plateau at a potential between about -0.8 and -0.9 V (vs SCE), and then increases again at more negative potentials. Clearly, the plateau shows the limiting current density for the reduction of the stannous ions and the subsequent increase in current density is due to stannous reduction and hydrogen evolution. As the amount of tri-ammonium citrate in the solution was increased from 0.30 to 0.82 mol/L, the onset potential for the reduction of Sn(II)-citrate complexes decreased from about -0.64 V to about -0.73 V. Sn(II)-citrate solution chemistry studies (Chapter 4) showed that as tri-ammonium citrate concentration increases, the distribution of different Sn(II)-citrate complexes stays the same, while citrate species in solution increases, which makes the Sn(II)-citrate complexes more difficult to reduce. This gives a more negative onset potential.

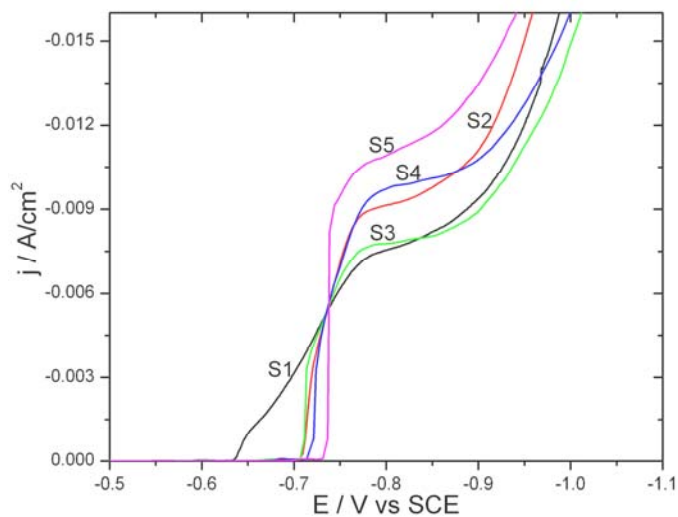


Fig. 3-2 Polarization curves for Sn-citrate solutions. In all five solutions, the concentration of $\text{SnCl}_2 \cdot 2\text{H}_2\text{O}$ was kept at 0.22 mol/L, while the concentration of tri-ammonium citrate was varied as follows: S1: 0.30 mol/L; S2: 0.41 mol/L; S3: 0.51 mol/L, S4: 0.62 mol/L and S5: 0.82 mol/L.

The SEM plan view and cross section images of the Sn deposits obtained from solutions containing 0.22 mol/L $\text{SnCl}_2 \cdot 2\text{H}_2\text{O}$ and 0.30, 0.33, 0.44 and 0.66 mol/L tri-ammonium citrate are shown in Fig. 3-3. The average current density utilized was 5 mA/cm^2 , and all deposits were dense and fairly uniform with similar morphologies. The plating rate was about 8-10 $\mu\text{m/hr}$.

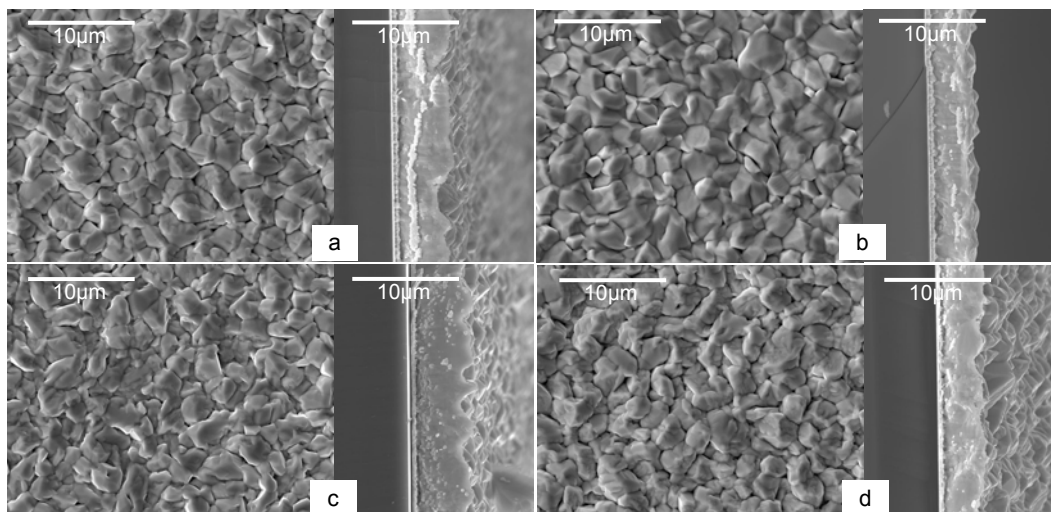


Fig. 3-3 SEM secondary electron (SE) plan view (left) and cross section (right) images of Sn films electrodeposited onto Au seed layers from Sn-citrate solutions containing 0.22 mol/L $\text{SnCl}_2 \cdot 2\text{H}_2\text{O}$ and different tri-ammonium citrate concentrations: (a) 0.30 mol/L; (b) 0.33 mol/L; (c) 0.44 mol/L and (d) 0.66 mol/L. The current density is 5 mA/cm^2 and samples were plated for 30 min.

3.3.1.2 Effect of current density on Sn electrodeposition

Fig. 3-4a shows SEM plan view images of Sn films plated at average current densities of 5, 10 and 15 mA/cm^2 , respectively, by both PC and DC plating, from a solution containing 0.22 mol/L of $\text{SnCl}_2 \cdot 2\text{H}_2\text{O}$ and 0.40 mol/L of tri-ammonium citrate. The corresponding cross section images are shown in Fig. 3-4b. The plan view images show that for both PC and DC plating, Sn films plated at 5 mA/cm^2 are slightly smoother than the ones plated at 10 mA/cm^2 . When the current density is as high as 15 mA/cm^2 , the Sn film becomes very rough, which can be easily noticed from the cross section image in Fig. 3-4b.

Cross section images in Fig. 3-4b also show that the plating rate for the Sn films increases as current density increases and DC plating gives slightly smoother Sn films than PC plating does. This may be due to the lower peak current density for DC plating compared with PC plating, so that hydrogen evolution during DC plating is not as significant as during PC plating.

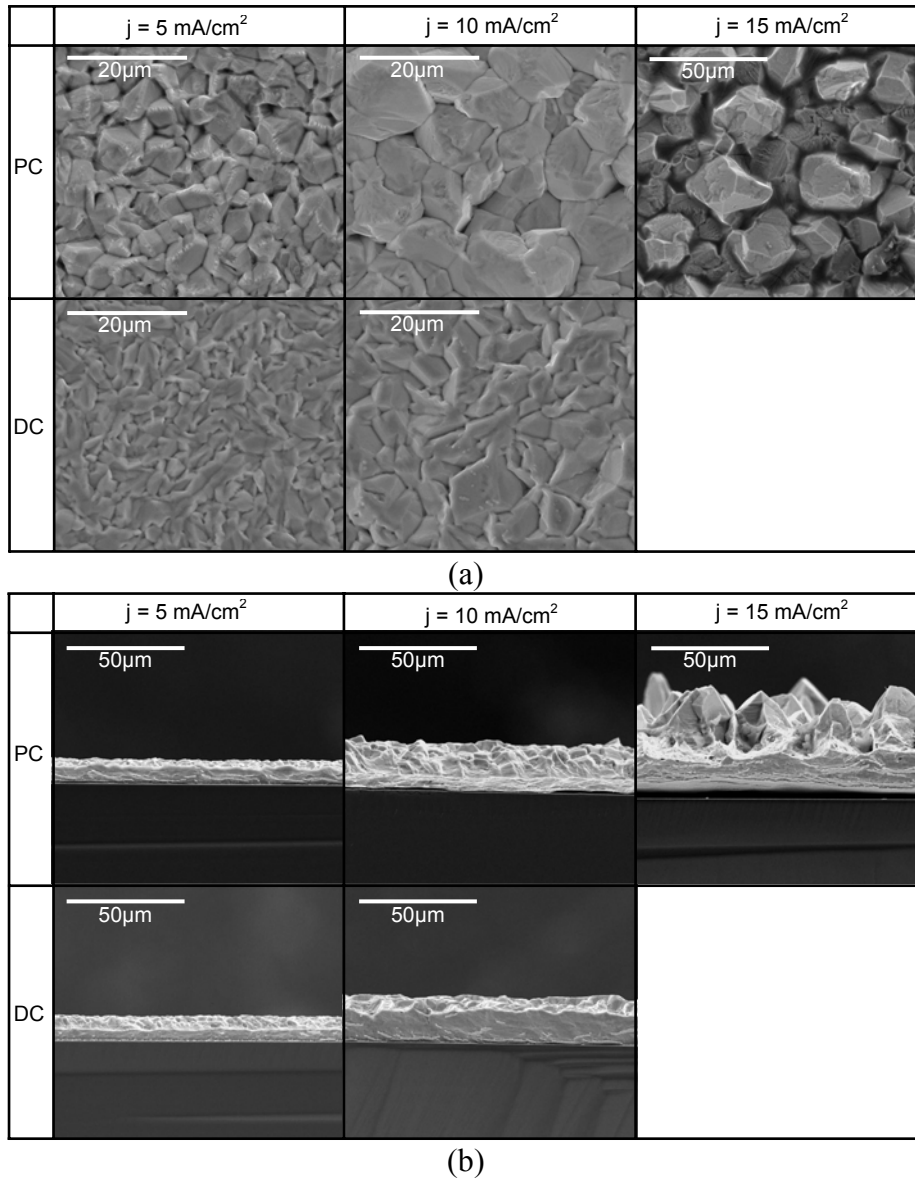


Fig. 3-4 SEM SE (a) plan view and (b) cross section images of Sn films deposited onto Au seed layers from Sn-citrate solutions containing 0.22 mol/L $\text{SnCl}_2 \cdot 2\text{H}_2\text{O}$ and 0.41 mol/L tri-ammonium citrate at different current densities: 5 mA/cm^2 , 10 mA/cm^2 and 15 mA/cm^2 . The plating time was 1 hour.

The Sn-citrate solutions remained transparent and colorless for more than 3 months. After adding $\text{CuCl}_2 \cdot 2\text{H}_2\text{O}$, however, the color changed upon aging, and electroplating from the aged solution gave rough and discontinuous films. The higher the tri-ammonium citrate concentration, the sooner the color changed. Therefore, in all subsequent work, only the lowest tri-ammonium citrate concentration needed to completely dissolve the tin salt, i.e., 0.30 mol/L, was utilized, while the $\text{SnCl}_2 \cdot 2\text{H}_2\text{O}$ concentration was maintained at 0.22 mol/L.

3.3.1.3 Effect of Cu^{2+} concentration on Sn-Cu electrodeposition

Assuming that Cu content ($\text{Cu}/(\text{Sn}+\text{Cu})$, wt%) in as-deposited Sn-Cu films will be the same as Cu content in Sn-Cu-citrate solutions ($\text{Cu}/(\text{Sn}+\text{Cu})$, wt%), to obtain Sn-Cu eutectic solder films with 0.7wt% Cu, the $\text{CuCl}_2 \cdot 2\text{H}_2\text{O}$ concentration in the solution should be 0.003 mol/L. Other Sn-Cu-citrate solutions with different $\text{CuCl}_2 \cdot 2\text{H}_2\text{O}$ concentrations are listed in Table 3-3. Copper content in Sn-Cu deposits (measured) and in Sn-Cu-citrate solutions (calculated) as a function of $\text{CuCl}_2 \cdot 2\text{H}_2\text{O}$ molar concentration in solution are shown in Fig. 3-5. It can be noticed that the Cu content in the deposits is higher than Cu content in the solution, which means Cu reduction is more favorable than Sn reduction in Sn-Cu-citrate solutions. The addition of 0.003 mol/L $\text{CuCl}_2 \cdot 2\text{H}_2\text{O}$ gives near eutectic Sn-Cu solder films.

Table 3-3 Composition of Sn-Cu-citrate solutions studied

	1	2	3	4	5	6
$\text{SnCl}_2 \cdot 2\text{H}_2\text{O}$ (mol/L)	0.22	0.22	0.22	0.22	0.22	0.22
$\text{CuCl}_2 \cdot 2\text{H}_2\text{O}$ (mol/L)	0.003	0.006	0.009	0.012	0.015	0.018
Tri-ammonium citrate (mol/L)	0.30	0.30	0.30	0.30	0.30	0.30

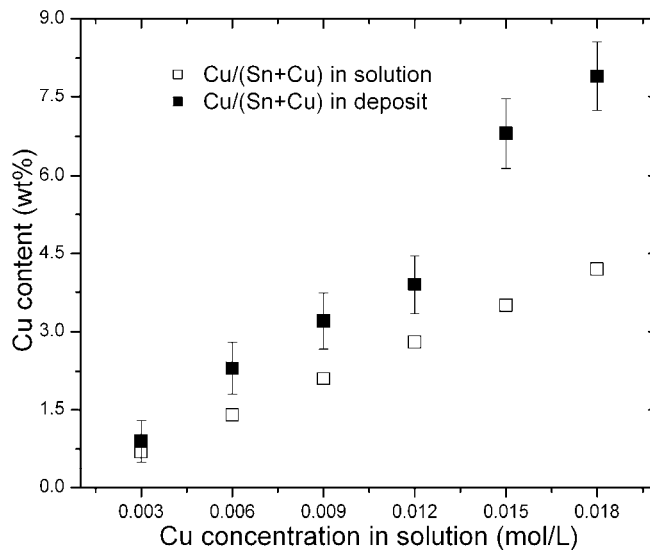


Fig. 3-5 Cu content in Sn-Cu deposits and in Sn-Cu-citrate solutions as a function of Cu concentration in solutions. The concentration of $\text{SnCl}_2 \cdot 2\text{H}_2\text{O}$ and tri-ammonium citrate was kept at 0.22 mol/L and 0.30 mol/L, respectively.

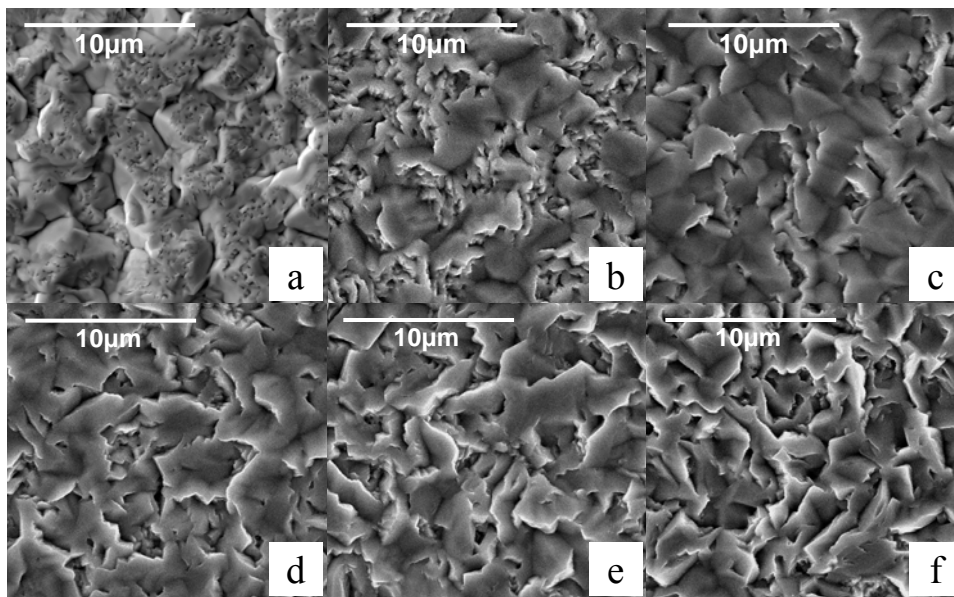


Fig. 3-6 SEM SE plan view images of Sn-Cu films electrodeposited onto Au seed layers from Sn-Cu-citrate solutions with different Cu^{2+} concentrations: (a) 0.003 mol/L, (b) 0.006 mol/L, (c) 0.009 mol/L, (d) 0.012 mol/L, (e) 0.015 mol/L and (f) 0.018 mol/L. The concentration of $\text{SnCl}_2 \cdot 2\text{H}_2\text{O}$ and tri-ammonium citrate was kept at 0.22 mol/L and 0.30 mol/L, respectively. The current density was 10 mA/cm^2 and plating time was 30 min.

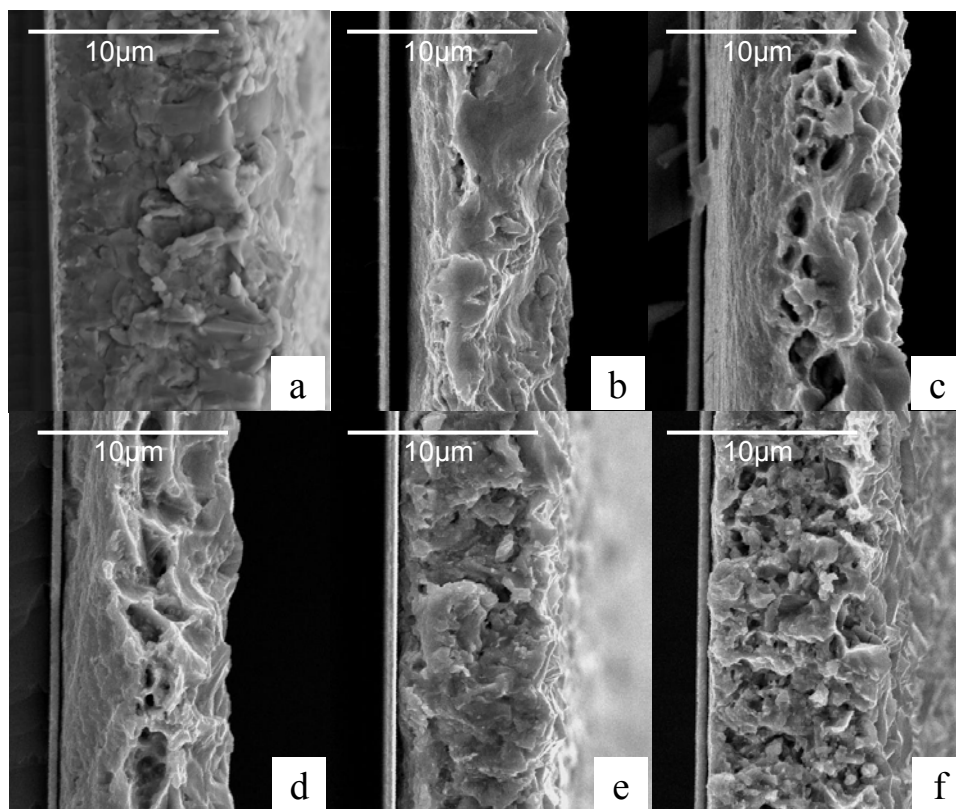


Fig. 3-7 SEM SE cross section images of Sn-Cu films electrodeposited onto Au seed layers from Sn-Cu-citrate solutions with different Cu^{2+} concentrations: (a) 0.003 mol/L, (b) 0.006 mol/L, (c) 0.009 mol/L, (d) 0.012 mol/L, (e) 0.015 mol/L and (f) 0.018 mol/L. The concentration of $\text{SnCl}_2 \cdot 2\text{H}_2\text{O}$ and tri-ammonium citrate was kept at 0.22 mol/L and 0.30 mol/L, respectively. The current density was $10\text{mA}/\text{cm}^2$ and plating time was 30min.

SEM plan view and cross section images of Sn-Cu films PC electrodeposited from solutions listed in Table 3-3 are shown in Fig. 3-6 and Fig. 3-7. Previous results showed that average current densities of both 5 and $10\text{mA}/\text{cm}^2$ gave smooth Sn films and the plating rate for the Sn films increased as current density was increased. In order to obtain Sn-Cu films with higher plating rate, an average current density of $10\text{mA}/\text{cm}^2$ was applied. The surfaces of all 6 samples in Fig. 3-6 are smooth and look very similar. However, the corresponding cross section images show differences (Fig. 3-7). The pores in Fig. 3-7c-f indicate that the Sn-Cu films become less dense as $\text{CuCl}_2 \cdot 2\text{H}_2\text{O}$

concentration increases. The plating rate does not change much as the concentration of $\text{CuCl}_2 \cdot 2\text{H}_2\text{O}$ increases.

3.3.2 Electrodeposition of Sn-Cu eutectic and near-eutectic alloys from Sn-Cu-citrate solutions

3.3.2.1 Sn-Cu electrodeposition from the chloride-citrate solution

To electrodeposit Sn-Cu solder films with the eutectic composition (0.7wt% Cu) at a current density of 10 mA/cm^2 , 0.003 mol/L (0.53 g/L) of $\text{CuCl}_2 \cdot 2\text{H}_2\text{O}$ was added into a Sn-citrate solution containing 0.22 mol/L (50 g/L) $\text{SnCl}_2 \cdot 2\text{H}_2\text{O}$ and 0.30 mol/L (72.4 g/L) tri-ammonium citrate. This Sn-Cu solution was stable for at least 36 days, with the pH stabilizing at around 4.

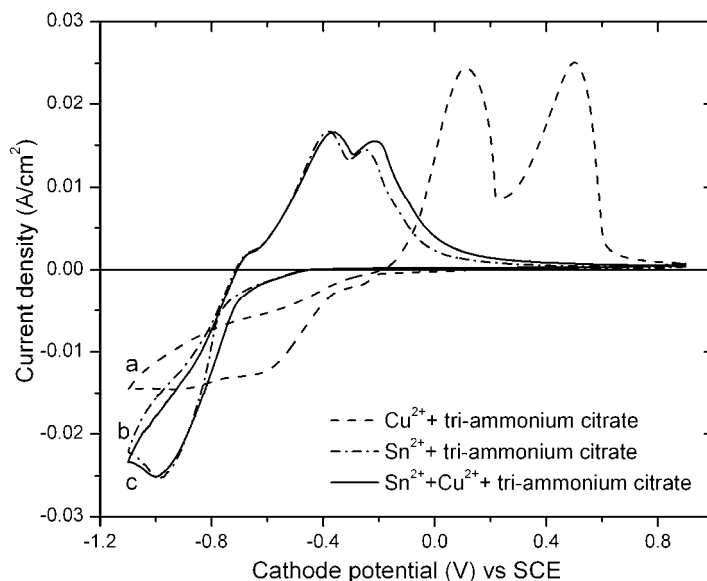


Fig. 3-8 Cyclic voltammetry measurements for various solutions: (a) 0.30 mol/L tri-ammonium citrate and 0.22 mol/L $\text{CuCl}_2 \cdot 2\text{H}_2\text{O}$; (b) 0.30 mol/L tri-ammonium citrate and 0.22 mol/L $\text{SnCl}_2 \cdot 2\text{H}_2\text{O}$; (c) 0.30 mol/L tri-ammonium citrate, 0.22 mol/L $\text{SnCl}_2 \cdot 2\text{H}_2\text{O}$, and 0.003 mol/L $\text{CuCl}_2 \cdot 2\text{H}_2\text{O}$.

Cyclic voltammetric studies were carried out to identify the contributions to the cathodic current from either metal ion reduction or hydrogen gas evolution,

and to understand the stages of the reduction and oxidation reactions for different metal ions in the tri-ammonium citrate solutions. Fig. 3-8 shows the voltagrams for a Sn-citrate solution, a Cu-citrate solution and a combined Sn-Cu-citrate solution. The concentration of the tri-ammonium citrate was kept the same (0.30 mol/L) for all three solutions. For the Cu-citrate solution, a concentration of 0.22 mol/L was chosen for the Cu salt to be consistent with the Sn-citrate solution. All the tests were conducted without stirring. The two peaks at -0.26 V and -0.6 V for the Cu-citrate solution appear to indicate the two Cu reduction reactions; Cu(I)-citrate \rightarrow Cu (at -0.26 V) and Cu(II)-citrate \rightarrow Cu (at -0.6 V). The peak at about -0.98 V for the Sn-citrate solution indicates the Sn(II)-citrate \rightarrow Sn reaction. There are two steps for Cu oxidation and three steps for Sn oxidation in the citrate solutions. Under these conditions, the onset of the voltammetric reduction current for the Sn-Cu-citrate solution appeared at an intermediate potential value between those corresponding to tin and copper reduction, but very close to that of tin. The same behaviour was observed during oxidation. Both the reduction and oxidation potentials of Cu were higher than those for Sn in the tri-ammonium citrate solution, which indicates that Cu remained more noble than Sn with tri-ammonium citrate as a complexing agent. Therefore, by adding Cu to the Sn-citrate solution, both the main reduction and oxidation peaks shifted to more positive potentials. Since the concentration of Cu salt in the Sn-Cu-citrate solution is very low, i.e., almost two orders of magnitude lower than that of the Sn salt, the addition of the Cu salt only caused a slight shift of the Sn-citrate curve towards the Cu-citrate curve. It is envisaged that Cu electrodeposition from the Sn-Cu-citrate solution would dominate initially, but Cu ions would be depleted quickly at the cathode surface, so that Sn electrodeposition would become dominant afterwards.

Smooth and dense Sn-0.7Cu films were obtained by both PC and DC plating from the above Sn-Cu-citrate solution with an average current density of 10 mA/cm². Plan view and cross section images of the plated films are shown in Fig. 3-9 and Fig. 3-10. Both deposits were uniform with very similar surface morphologies, except that the DC deposit was slightly rougher. XRD analysis

(Fig. 3-11) showed that for both deposits, two phases were detected. The major phase was tetragonal Sn, with a small amount of the Cu_6Sn_5 intermetallic.

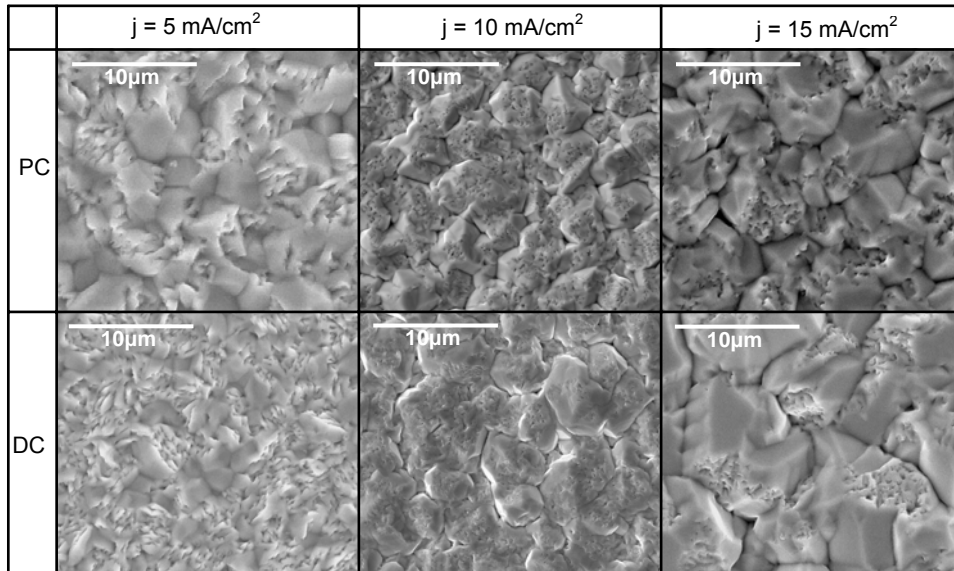


Fig. 3-9 SEM SE plan view images of Sn-Cu films electrodeposited onto Au seed layers from Sn-Cu-citrate solutions containing 0.22 mol/L $\text{SnCl}_2 \cdot 2\text{H}_2\text{O}$, 0.003 mol/L $\text{CuCl}_2 \cdot 2\text{H}_2\text{O}$, and 0.30 mol/L tri-ammonium citrate.

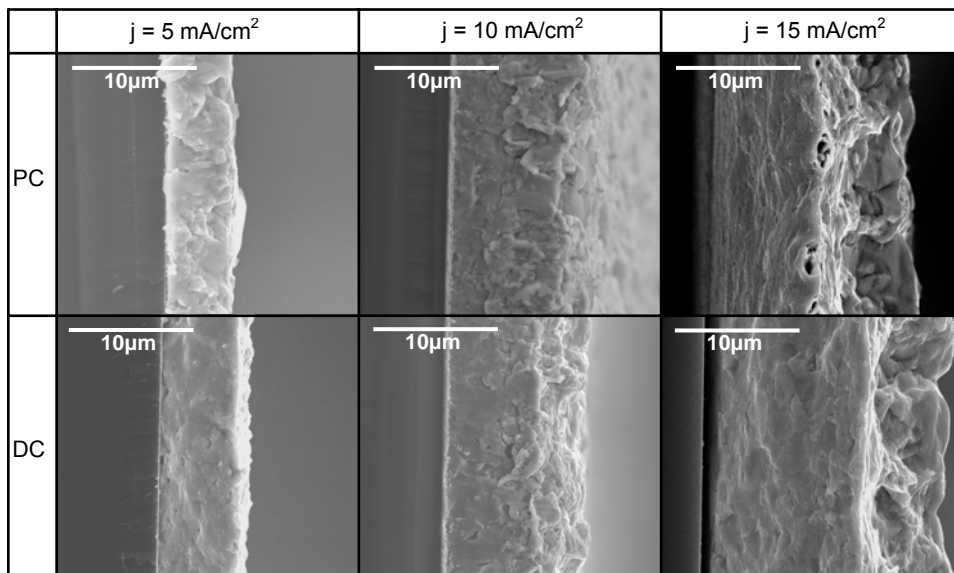


Fig. 3-10 SEM SE cross section images of Sn-Cu films electrodeposited onto Au seed layers from a Sn-Cu-citrate solution containing 0.22 mol/L $\text{SnCl}_2 \cdot 2\text{H}_2\text{O}$, 0.003 mol/L $\text{CuCl}_2 \cdot 2\text{H}_2\text{O}$, and 0.30 mol/L tri-ammonium citrate.

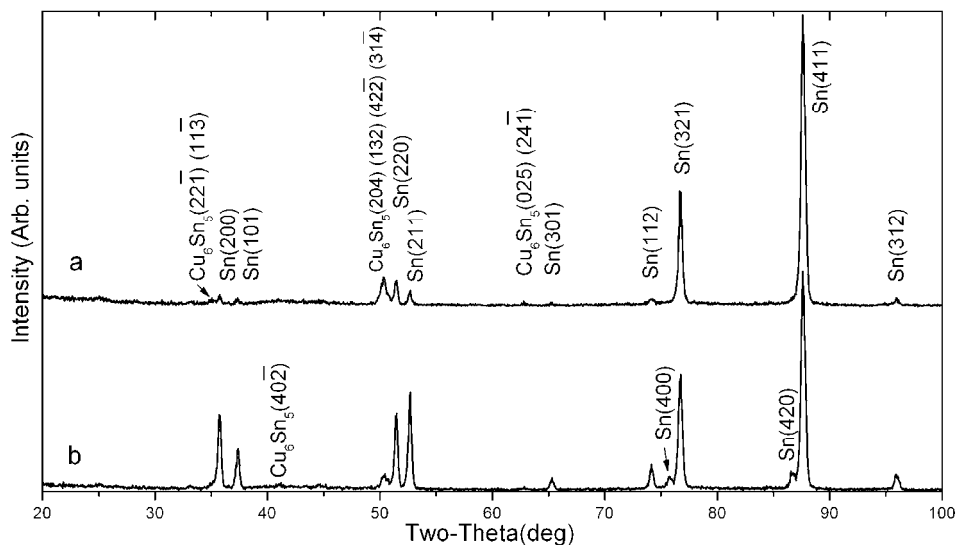


Fig. 3-11 XRD patterns from (a) PC and (b) DC plated Sn-Cu films onto Au seed layers from a Sn-Cu-citrate solution containing 0.22 mol/L $\text{SnCl}_2 \cdot 2\text{H}_2\text{O}$, 0.003 mol/L $\text{CuCl}_2 \cdot 2\text{H}_2\text{O}$, and 0.30 mol/L tri-ammonium citrate. The current density was 10 mA/cm^2 .

3.3.2.2 Effect of current density

Current density is an important parameter in electrodeposition. The effect of average current density on the Cu content in PC and DC deposits was studied and the results are shown in Fig. 3-12. Copper content decreased with increasing current density, which was as expected since the limiting current density for Cu electrodeposition would be significantly lower than that for Sn given the disparity in solution concentration. PC plating produced deposits with higher Cu content, although at higher current densities the differences were small, or even insignificant, particularly given the magnitude of the error bars. For both PC and DC plating, current densities higher than 10 mA/cm^2 gave near eutectic Sn-Cu deposits. Dendrites formed on the wafer edges when the average current density exceeded 15 mA/cm^2 .

The effect of average current density on plating rate at a fixed plating time of 30 minutes is shown in Fig. 3-13. As expected, the plating rate increased with increasing current density but leveled off when current density reached 13-15 mA/cm^2 . The magnitude of the error bars increases with increasing current

density, due to increased deposit roughness. An average current density of 10-12.5 mA/cm² was considered optimal, as the deposit Cu concentration was near the eutectic composition (without dendrites) and plating rates were 20-27.5 μm/hr. PC plating gave lower plating rates than DC plating. One possible reason is that the peak current density for PC plating was 5 times the value for DC plating for the duty cycle utilized, i.e., 2 ms on and 8 ms off and hydrogen evolution was more significant under these high current densities. Chang et al. (2007) studied both PC and DC chromium electrodeposition and reported that during PC plating, the applied cathodic current charged the interface between the electrode and the electrolyte before any reduction happened. This charging current only had a capacitance effect for the electrical double layer and was not involved in any reduction reaction. This interfacial charging current was required for each PC cycle, thereby reducing the current efficiency for PC plating relative to DC plating for the same average current density.

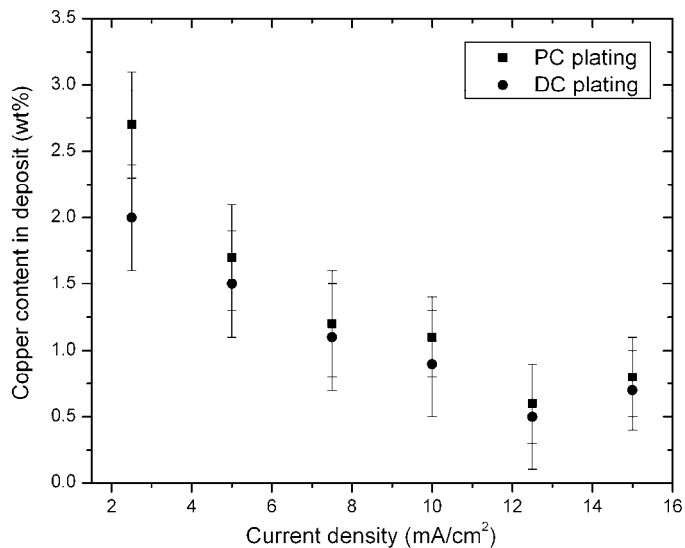


Fig. 3-12 Deposit Cu content as a function of average current density. The solution contained 0.22 mol/L SnCl₂·2H₂O, 0.003 mol/L CuCl₂·2H₂O, and 0.30 mol/L tri-ammonium citrate.

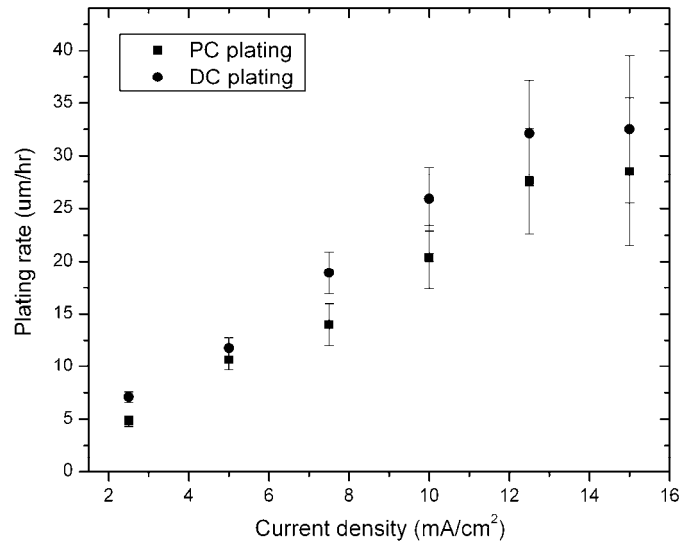


Fig. 3-13 Plating rate as a function of average current density for both PC and DC plating. The solution contained 0.22 mol/L $\text{SnCl}_2 \cdot 2\text{H}_2\text{O}$, 0.003 mol/L $\text{CuCl}_2 \cdot 2\text{H}_2\text{O}$, and 0.30 mol/L tri-ammonium citrate.

It is generally believed that the surface roughness of plated films changes with current density (Watanabe, 2004). Fig. 3-9 shows SEM plan view images of Sn-Cu films plated at average current densities of 5, 10 and 15 mA/cm², respectively, by both PC and DC plating, from a solution with 0.22 mol/L of $\text{SnCl}_2 \cdot 2\text{H}_2\text{O}$, 0.003 mol/L of $\text{CuCl}_2 \cdot 2\text{H}_2\text{O}$ and 0.30 mol/L of tri-ammonium citrate. The corresponding cross section images are shown in Fig. 3-10. The plan view images show that for both PC and DC plating, Sn-Cu films plated at low current densities had a smoother surface morphology than the ones plated at higher current densities. The difference in surface morphology between PC deposits and DC deposits becomes more significant at the highest current densities, because the difference in peak current densities between PC plating and DC plating is larger. Cross section images in Fig. 3-10 show that the Sn-Cu films became less dense as the current density was increased. Pores appear at average current densities of 15 mA/cm², and can be attributed to hydrogen evolution.

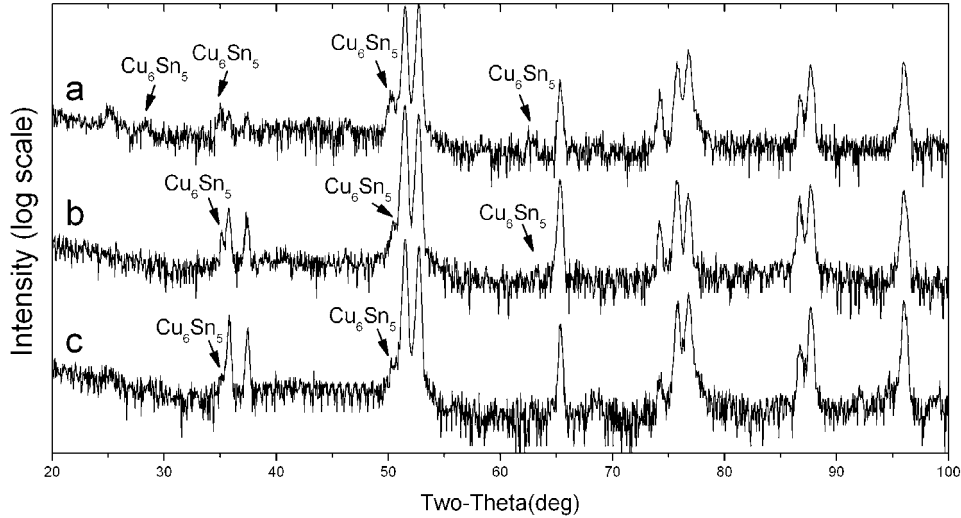


Fig. 3-14 XRD patterns from PC plated Sn-Cu films onto Au seed layers from a Sn-Cu-citrate solution containing 0.22 mol/L SnCl₂·2H₂O, 0.003 mol/L CuCl₂·2H₂O, and 0.30 mol/L tri-ammonium citrate. (a) 5 mA/cm²; (b) 10 mA/cm²; (c) 15 mA/cm².

X-ray diffraction patterns for PC plated Sn-Cu deposits on Au seed layers at different current densities are shown in Fig. 3-14. In this figure, the vertical axis is plotted on a log scale in order to better show the intensity of the minority Cu₆Sn₅ phase. The structures of the three films are similar. As current density is increased from 5 mA/cm² to 10 mA/cm², the Cu₆Sn₅ peak at 25° disappears and the ones at 50.7° and 63.1° become weaker. As the current density is increased further to 15 mA/cm², additional Cu₆Sn₅ peaks at 63.1° disappear and the ones at 35.0° and 50.7° become even weaker. This is because at higher current densities, the deposits contained less Cu so that less Cu₆Sn₅ formed.

To determine the through thickness Cu distribution in Sn-Cu deposits, EDX analysis at 2 μm intervals across the thickness was carried out and the results are shown in Fig. 3-15 for both PC and DC plating. It has been reported that interdiffusion between Au and Sn occurs even at room temperature (Buene et al., 1980; Tang et al., 2008b). To avoid the effects of Sn-Au interdiffusion at room temperature, as well as the effect of Cu from the Cu substrate on any composition measurements, Ni coated Cu substrates were used. As can be seen from Fig. 3-15, for both PC and DC plating, the Cu concentration was uniform

across the thickness, except at the Sn-Cu solder/Ni interface where the Cu content was much higher. As discussed previously, Cu^{2+} ions are more noble than Sn^{2+} ions in citrate solutions, so that Cu^{2+} reduction dominates initially, giving a higher Cu composition in the initial deposits. This initial enrichment disappears quickly, due to the low concentration of Cu in the electrolytes.

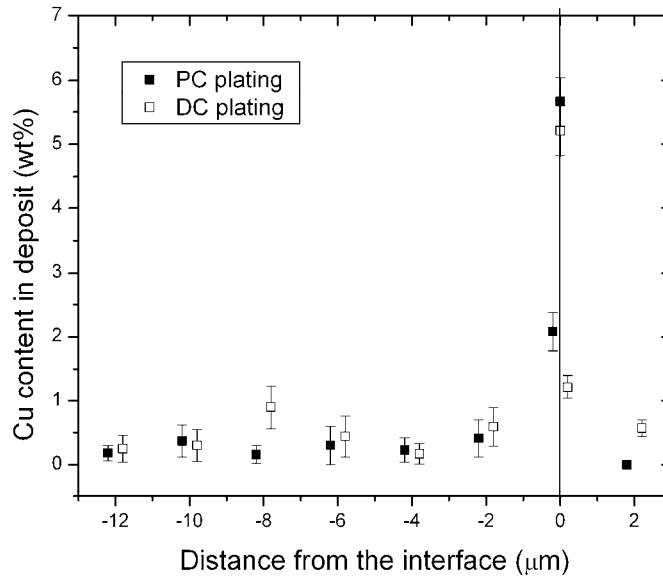


Fig. 3-15 Deposit Cu content as a function of the distance from the solder/substrate interface for both PC and DC Sn-Cu films electrodeposited from a Sn-Cu-citrate solution containing 0.22 mol/L $\text{SnCl}_2 \cdot 2\text{H}_2\text{O}$, 0.003 mol/L $\text{CuCl}_2 \cdot 2\text{H}_2\text{O}$, and 0.30 mol/L tri-ammonium citrate. Plating was done at 10 mA/cm^2 on Ni coated Cu substrates.

3.3.2.3 Solution stability tests

Solution stability is another key consideration when developing new plating solutions. Two series of aging tests were conducted, one in which the solution was repeatedly used for electrodeposition over a given length of time (Test 1), and the other in which the solution was aged for a given length of time and then used for electrodeposition (Test 2). All the solutions were stored in sealed bottles when not use for electrodeposition. To ensure that there would be sufficient Cu in the deposit to be detected by EDX analysis, a current density of 5 mA/cm^2 was applied in all the tests. Deposit Cu content remained approximately

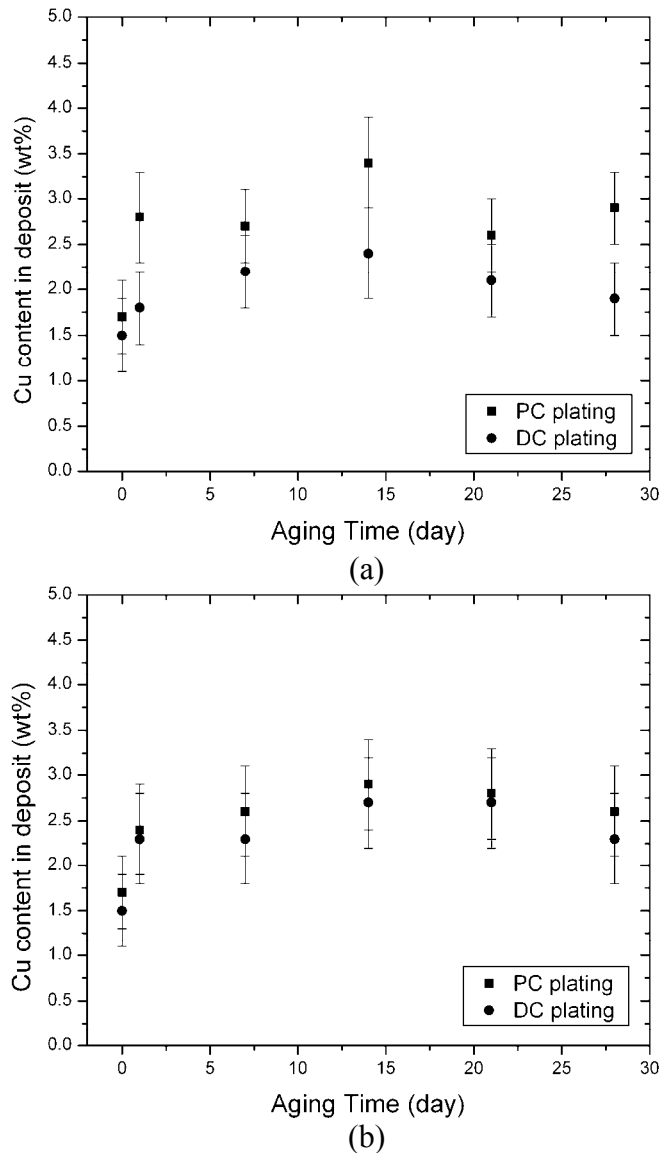


Fig. 3-16 Deposit Cu content as a function of solution aging time for both PC and DC: (a) Test 1, (b) Test 2. The solution contained 0.22 mol/L $\text{SnCl}_2 \cdot 2\text{H}_2\text{O}$, 0.003 mol/L $\text{CuCl}_2 \cdot 2\text{H}_2\text{O}$, and 0.30 mol/L tri-ammonium citrate. The average current density was 5 mA/cm^2 .

constant throughout the ageing tests for both Test 1 (Fig. 3-16a) and Test 2 (Fig. 3-16b). In Test 1, the Cu content was in the 1.5-3.5 wt% range for PC plating and in the 1.5-2.5 wt% range for DC plating. In Test 2, the Cu contents for both PC and DC plating were close to each other, and were in the range of 1.5-3.0 wt%. SEM images for the PC deposits from a 36 day old solution from Test 1 and Test 2 are shown in Fig. 3-17a and 3-17b. Fig. 3-17c shows a PC deposit from a 77 day

old solution from Test 2. All the surfaces are fairly smooth and the plating rate was about $11 \mu\text{m/hr}$ at a current density of 5 mA/cm^2 , which was almost the same as that for a fresh solution.

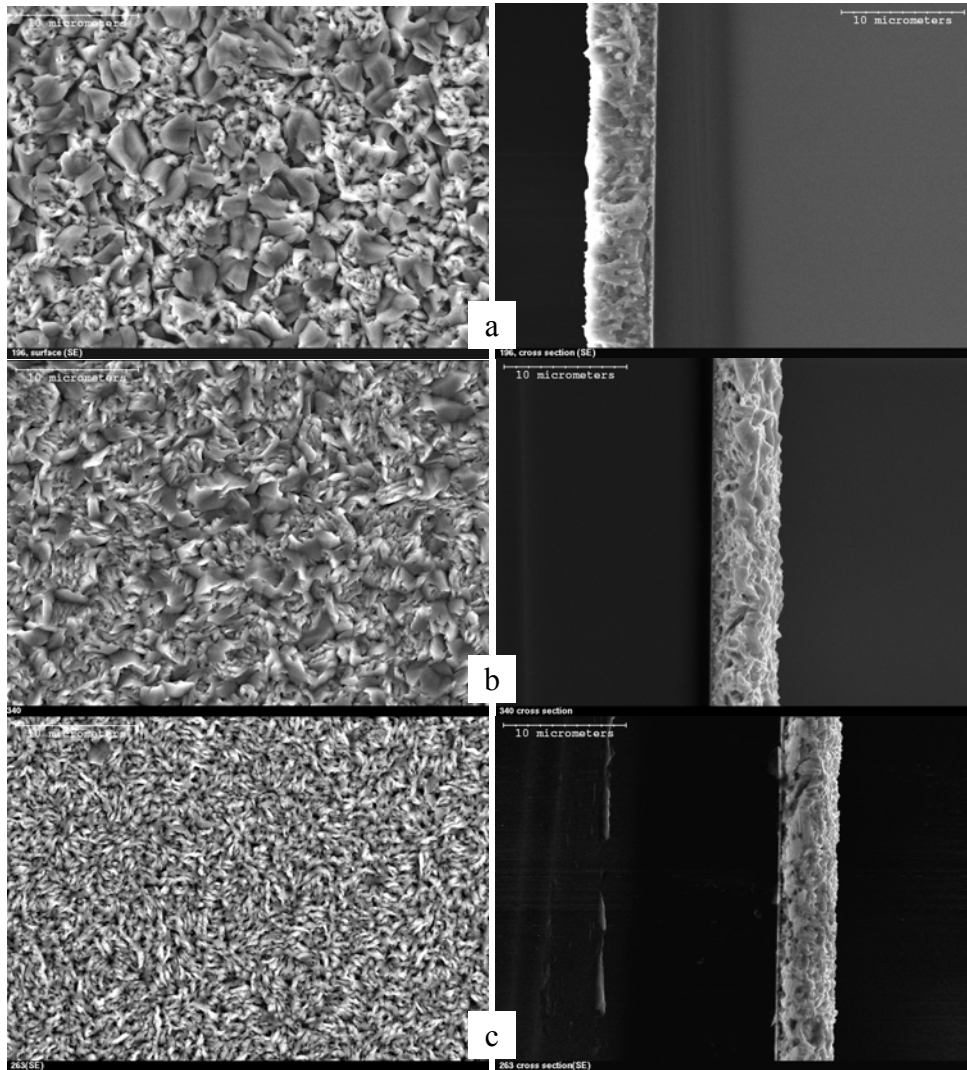
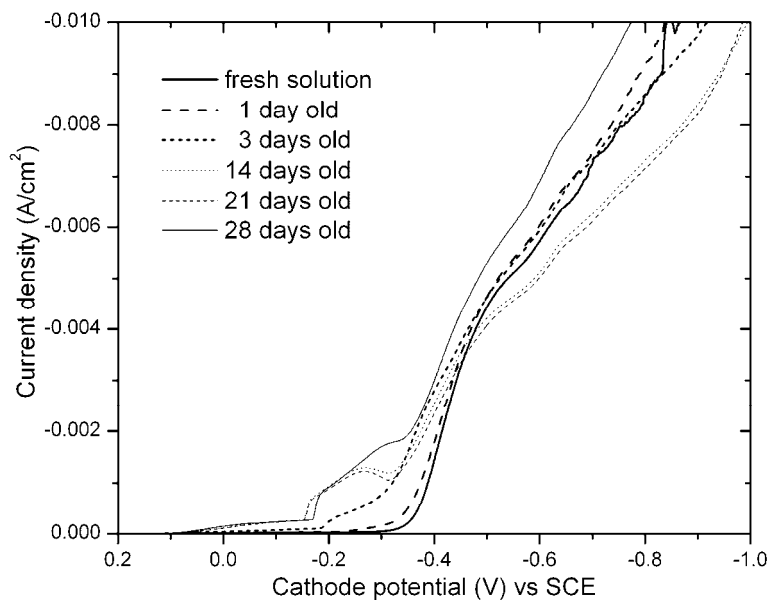


Fig. 3-17 SEM SE images (plan view and cross section) for Sn-Cu films PC plated in a solution aged for: (a) 36 days, Test 1, (b) 36 days, Test 2 and (c) 77days, Test 2. The solution contained 0.22 mol/L $\text{SnCl}_2 \cdot 2\text{H}_2\text{O}$, 0.003 mol/L $\text{CuCl}_2 \cdot 2\text{H}_2\text{O}$, and 0.30 mol/L tri-ammonium citrate. Plating was done at 5 mA/cm^2 for 30 min.

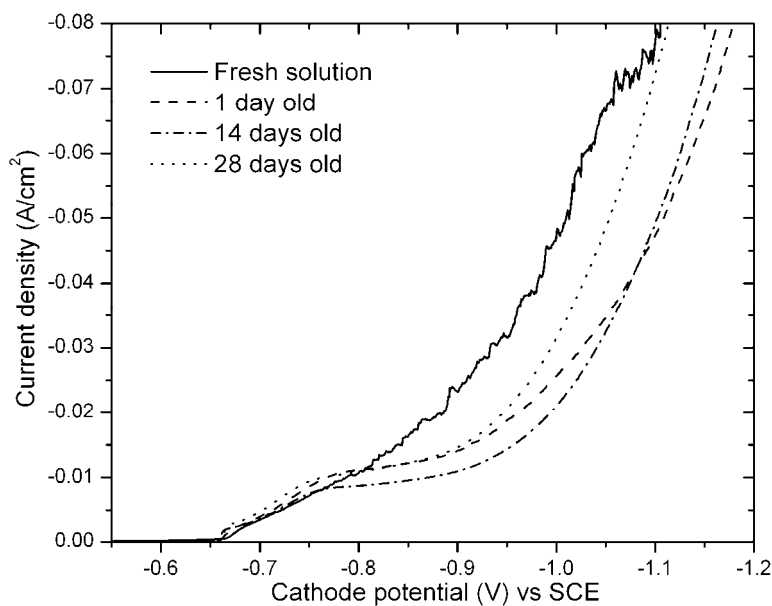
A simple, approximate calculation can be done to determine whether the metal ion consumption over time would have any effect on the electrodeposition

process. The Sn deposits are assumed to have densities corresponding to the bulk value for Sn (7.3 g/cm^3), the plating rates are assumed to be the same for aged and fresh solutions and the plated area is taken to be the maximum sample area utilized (0.8 cm^2). The amount of Sn consumed during each electrodeposition process is about 3.2 mg or 0.03% of the Sn in solution. For Test 1, where the same solution is used for each deposition after ageing, the total amount of Sn consumed after 12 electroplating cycles is about 38.5 mg or about 0.37 wt% of the Sn in solution. Both of these values are essentially negligible, so that the Sn concentration in the solution remains approximately constant and should have no effect on electrodeposition. Copper is assumed to be evenly distributed inside the deposits and Cu content in deposit is taken to be 3.4 wt% which is the highest amount among all the EDX results for both Test 1 and Test 2. The amount of Cu consumed during each electrodeposition process is about 0.1 mg or 1.4 wt% of the Cu in solution. For Test 1, after 12 electrodeposition cycles, the total amount of Cu consumed is about 1.35 mg or about 17% of the Cu in solution. As such, the deposit Cu content might be expected to drop, particularly after the longer aging times (e.g., 21 and 28 days), as shown in Fig. 3-16a. However, Cu consumption from the electrolyte does not account for the initial increase in deposit Cu content for both Test 1 and 2 when the ageing times were less than 15 days (Fig. 3-16a and 3-16b).

To determine whether any changes occurred to Cu(II)-citrate and Sn(II)-citrate solutions during aging, polarization tests were done for Cu(II)-citrate solutions containing 0.22 mol/L $\text{CuCl}_2 \cdot 2\text{H}_2\text{O}$ and 0.30 mol/L tri-ammonium citrate and Sn(II)-citrate solutions containing 0.22 mol/L $\text{SnCl}_2 \cdot 2\text{H}_2\text{O}$ and 0.30 mol/L tri-ammonium citrate after different aging times. The results are shown in Fig. 3-18a and 3-18b, respectively. After the Cu(II)-citrate solutions were aged for 1 day, 3 days and as long as 28 days, the onset reduction potential moved from -0.33 V to less negative values, i.e., -0.26 V after aging for 1 day, -0.05V after aging for 3 days and as long as 28 days (Fig. 3-18a). The Cu-citrate complexes became easier to reduce upon ageing. One possible reason is that some of the Cu^{2+} ions were reduced to Cu^+ in the citrate solution and formed Cu(I)-citrate



(a)



(b)

Fig. 3-18 Polarization curves for (a) Cu-citrate solution containing 0.22 mol/L $\text{CuCl}_2 \cdot 2\text{H}_2\text{O}$ and 0.30 mol/L tri-ammonium citrate, (b) Sn-citrate solution containing 0.22 mol/L $\text{SnCl}_2 \cdot 2\text{H}_2\text{O}$ and 0.30 mol/L tri-ammonium citrate, after different aging times.

complexes. It also can be noticed that after the solution was aged for 3 days, an additional small plateau appears right after the onset of reduction reactions and becomes more prominent with longer aging times. This plateau may be due to the

reduction of Cu(I)-citrate ions. For the Sn(II)-citrate solution, the onset reduction potential remained essentially constant even after aging for 28 days, which is an indication that the Sn(II)-citrate solution is quite stable. Since Cu-citrate became easier to reduce and the Sn-citrate did not change, the deposit Cu content would be expected to increase upon aging, as shown in Fig. 3-16a and Fig. 3-16b. After 14 days, the reaction between Cu^{2+} ions and Cu^+ ions probably reached equilibrium, while the solution became increasingly depleted of the copper ions with each plating cycle, leading to decreasing deposit Cu contents, as shown in Fig. 3-16a. No Cu was consumed for Test 2 prior to each plating, so that deposit Cu content stayed almost the same after aging for more than 14 days.

3.3.2.4 Effect of agitation

Many electroplating processes also require constant agitation during plating, which is believed to be helpful to ensure a uniform concentration of additives in the plating bath that is directly adjacent to the cathode and thus provide uniform deposits at various current densities (Chen et al., 2001; Tan and Lim, 2003). Mechanical agitation from the top was applied in this work to ensure continuous contact between the electrode and fresh plating solutions.

To better understand the effect of agitation on Sn-Cu electrodeposition, polarization tests were carried out first for the same Sn-Cu-citrate solutions without and with agitation, and the results are shown in Fig. 3-19. With agitation at a stirring speed of 600 rpm, no limiting current was found in the polarization curve as the cathode potential was scanned towards negative values, and the current densities reached much higher values than without agitation. This means that mass transfer from the bulk solution to the electrode surface is sufficiently fast to maintain the reduction reactions on the cathode.

Sn-Cu deposits plated without and with agitation at different stirring speeds and average current densities of 10 mA/cm^2 and 40 mA/cm^2 are shown in Fig. 3-20. At a current density of 10 mA/cm^2 , the Sn-Cu deposit has a smoother morphology without agitation. Dendrites were found (as indicated in Fig. 3-20) on

the entire surface (no agitation) when the current density was as high as 40 mA/cm²; however, no dendrites were found for plating at 40 mA/cm² with agitation. Sn-Cu deposits plated with different stirring speeds have very similar surface morphology when the current density is 10 mA/cm². At a current density of 40 mA/cm², the surface morphology becomes slightly smoother with higher stirring speed.

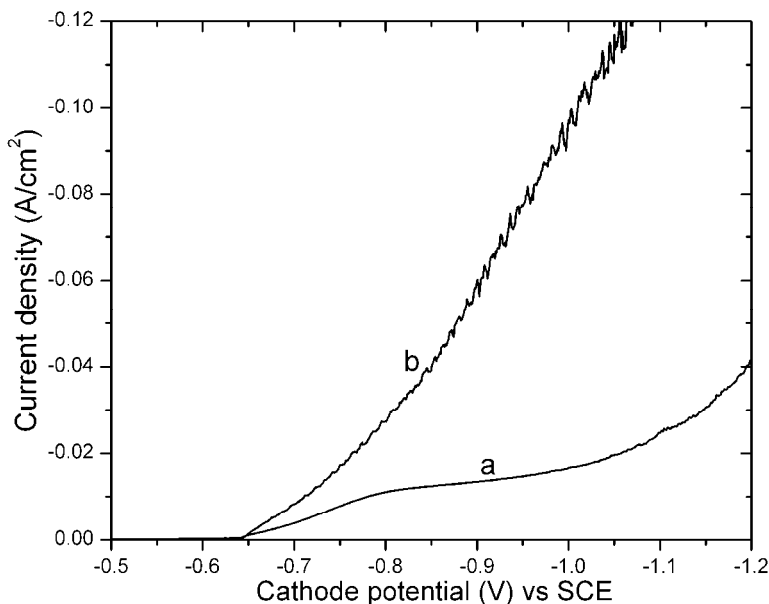


Fig. 3-19 Polarization curves for Sn-Cu-citrate solutions containing 0.22 mol/L SnCl₂·2H₂O, 0.003 mol/L CuCl₂·2H₂O and 0.30 mol/L tri-ammonium citrate (a) without agitation and (b) with agitation. An overhead mechanical stirrer was used for stirring at a speed of 600 rpm.

The effect of agitation on Cu content in Sn-Cu deposits at different current densities is shown in Fig. 3-21. Earlier results showed that without agitation, dendrites started growing on the wafer edges when the current density was higher than 15 mA/cm², so only current densities lower than 15 mA/cm² were applied for Sn-Cu plating without agitation. For Sn-Cu deposits plated both with and without agitation, Cu content decreases as current density increases and Cu content decreases much faster without agitation. At a current density of 10 mA/cm², agitation gives a higher Cu content which can be attributed to the increase in mass transfer rate caused by agitation. With agitation, current densities higher than 20

mA/cm^2 only have minor effects on Cu content in deposits. A stirring speed of 600 rpm gives a more constant Cu content at different current densities.

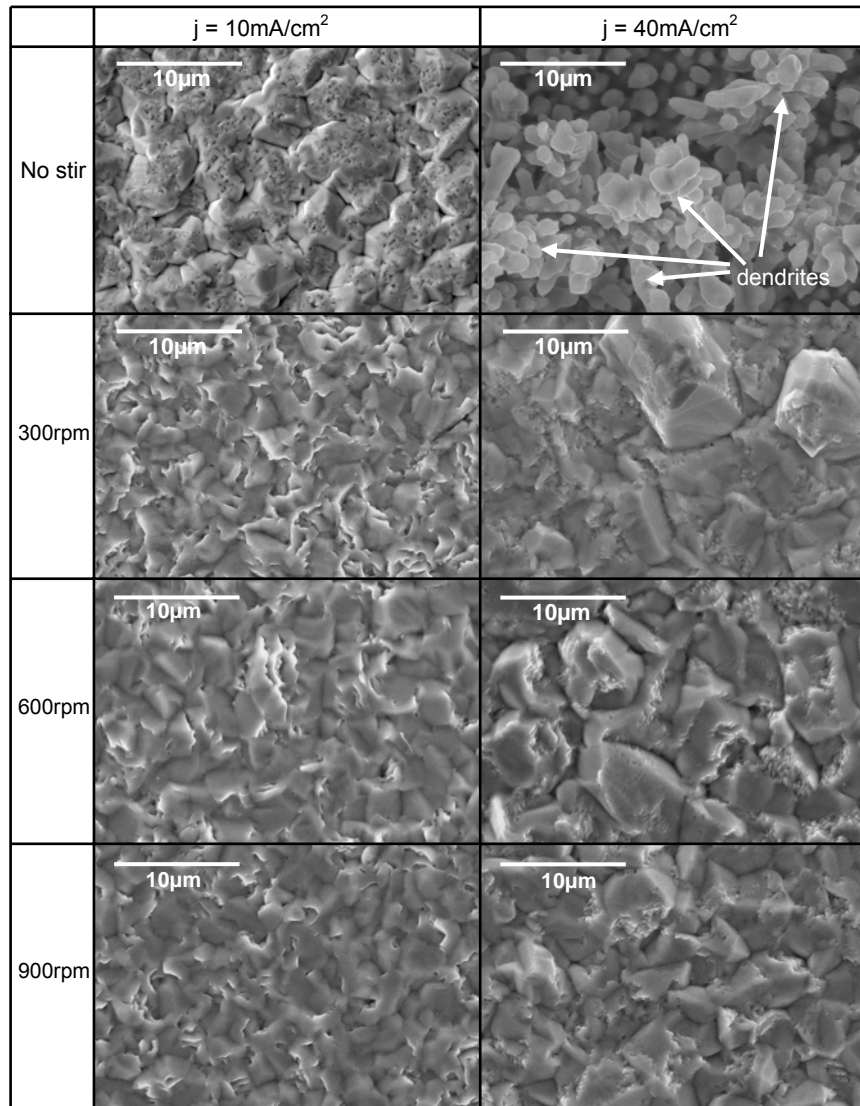


Fig. 3-20 SEM SE plan view images of Sn-Cu films electrodeposited onto Au seed layers from Sn-Cu-citrate solutions under current densities of 10 and 40 mA/cm^2 and at different stir speeds. The solution contained 0.22 mol/L $\text{SnCl}_2 \cdot 2\text{H}_2\text{O}$, 0.003 mol/L $\text{CuCl}_2 \cdot 2\text{H}_2\text{O}$, and 0.30 mol/L tri-ammonium citrate.

The effect of $\text{CuCl}_2 \cdot 2\text{H}_2\text{O}$ concentrations on Sn-Cu electrodeposition at current densities of 10 mA/cm^2 and 40 mA/cm^2 and a stirring speed of 600 rpm was studied. SEM SE plan view and cross section images of as-deposited Sn-Cu

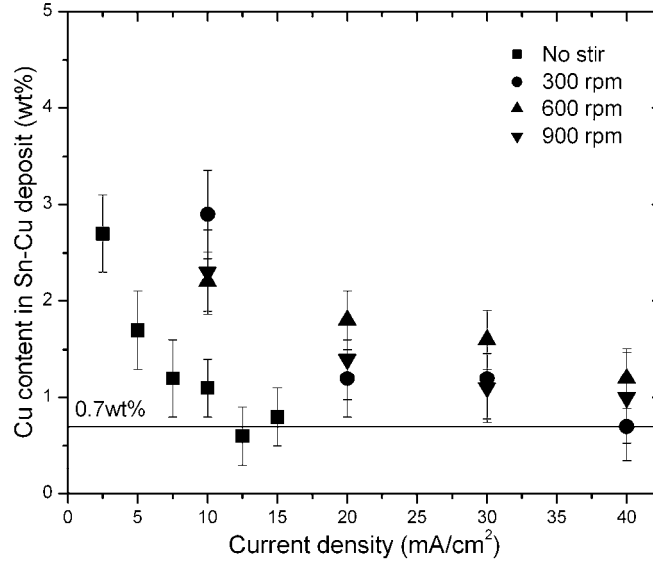
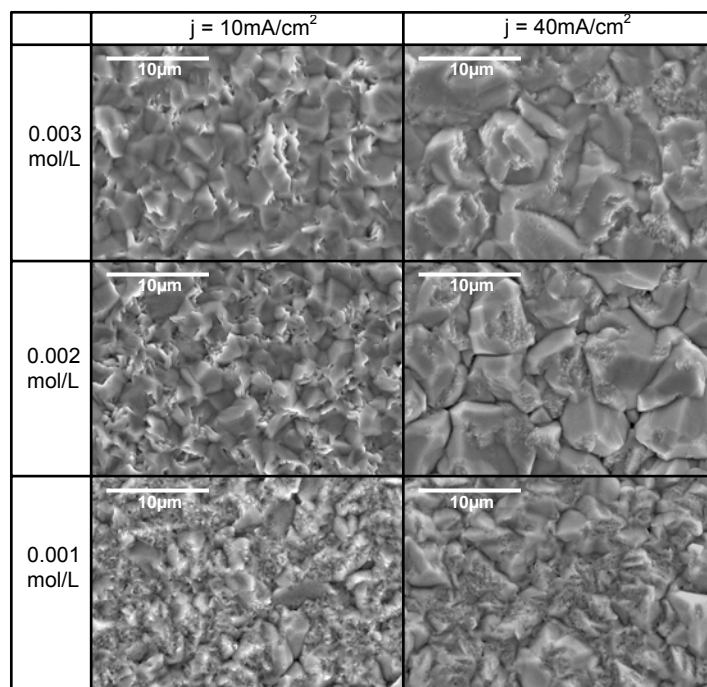
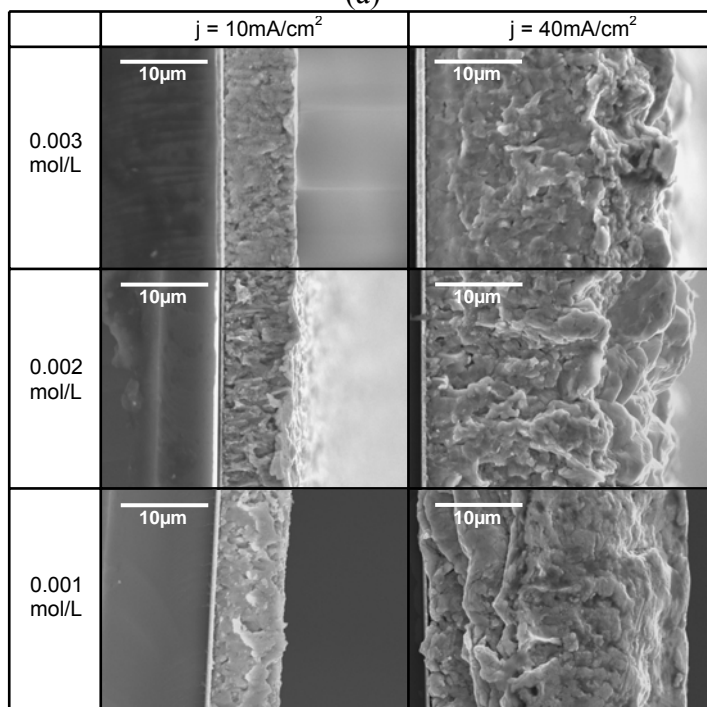


Fig. 3-21 Deposit Cu content as a function of current density plated from Sn-Cu-citrate solutions at different agitation rates. The solution contained 0.22 mol/L $\text{SnCl}_2 \cdot 2\text{H}_2\text{O}$, 0.003 mol/L $\text{CuCl}_2 \cdot 2\text{H}_2\text{O}$ and 0.30 mol/L tri-ammonium citrate.

films are shown in Fig. 3-22. All the films obtained were dense and uniform. It can be noticed that higher $\text{CuCl}_2 \cdot 2\text{H}_2\text{O}$ concentrations and lower current densities give smoother Sn-Cu films. Cu content in the deposits as a function of current density for solutions with different $\text{CuCl}_2 \cdot 2\text{H}_2\text{O}$ concentrations is shown in Fig. 3-23. The higher the $\text{CuCl}_2 \cdot 2\text{H}_2\text{O}$ concentration in solution, the higher the Cu content in deposit. The Sn-Cu eutectic composition is attainable from Sn-Cu-citrate solutions containing 0.001 mol/L (0.27 g/L) $\text{CuCl}_2 \cdot 2\text{H}_2\text{O}$ at current densities from 20 mA/cm² to 40 mA/cm² and a stirring speed of 600 rpm. Fig. 3-24 shows the effect of current density on Sn-Cu plating rate with and without agitation. The plating rate increases as current density increases both with and without agitation. It increases at a faster rate without agitation, as the current density is increased from 2.5 to 15 mA/cm², than with agitation as current density is increased from 10 to 40 mA/cm². At each current density, plating rates for solutions containing different amounts of $\text{CuCl}_2 \cdot 2\text{H}_2\text{O}$ are similar. The plating rate for eutectic Sn-Cu films at 20-40 mA/cm² with agitation is about 36-60 $\mu\text{m/hr}$.



(a)



(b)

Fig. 3-22 SEM SE images: (a) plan view images, (b) cross section images of Sn-Cu films electrodeposited onto Au seed layers from Sn-Cu-citrate solutions with different $\text{CuCl}_2 \cdot 2\text{H}_2\text{O}$ concentrations under different current densities. The concentrations of $\text{SnCl}_2 \cdot 2\text{H}_2\text{O}$ and triammonium citrate were fixed at 0.22 mol/L and 0.30 mol/L. The stirring speed was 600 rpm.

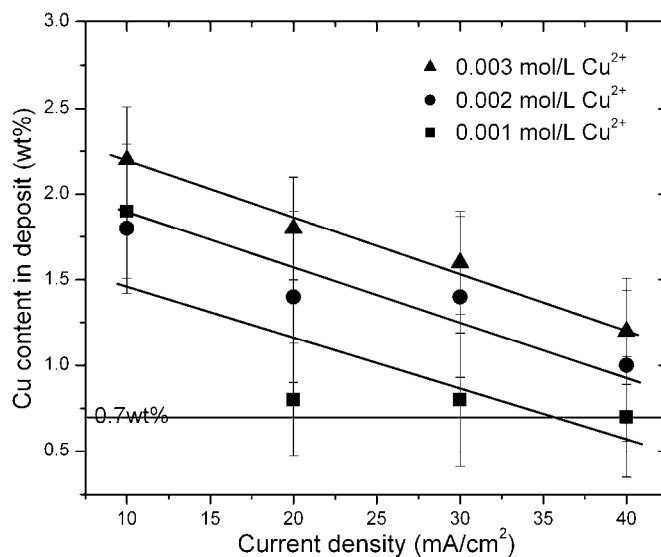


Fig. 3-23 Deposit Cu content as a function of current density from Sn-Cu-citrate solutions with different $\text{CuCl}_2 \cdot 2\text{H}_2\text{O}$ concentrations. The concentrations of $\text{SnCl}_2 \cdot 2\text{H}_2\text{O}$ and tri-ammonium citrate were fixed at 0.22 mol/L and 0.30 mol/L, respectively. The stirring speed was 600 rpm.

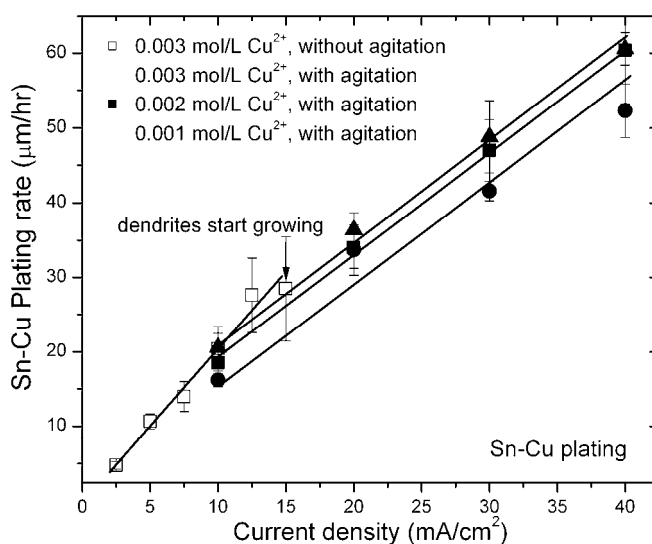


Fig. 3-24 Sn-Cu deposit plating rate as a function of current density from solutions containing different $\text{CuCl}_2 \cdot 2\text{H}_2\text{O}$ concentrations. The concentrations of $\text{SnCl}_2 \cdot 2\text{H}_2\text{O}$ and tri-ammonium citrate were fixed at 0.22 mol/L and 0.30 mol/L, respectively. The stirring speed was 600 rpm.

3.3.2.5 Effect of gelatin+ β -naphthol as additives

Additives (inorganic and organic) are commonly used in electrodeposition to produce smooth deposits, enhance corrosion protection or mechanical properties of the electroplated coating or to provide some other desirable properties (Lowenheim, 1974; Martyak and Seefeldt, 2004; Watanabe, 2004), which has been discussed in Chapter 2. Gelatin and β -naphthol are generally used in bright tin acid baths, such as fluoboric, sulphate, chloride or methanesulfonic baths, as leveling agents (Jawitz, 1997; Kuwako, 2000; Broggi et al., 2006) and have been observed to be useful in smoothening Sn films in Sn-citrate plating baths (Tang et al., 2008a). To examine their effect on Sn-Cu electrodeposition, Sn-Cu-citrate solutions with different amounts of gelatin and β -naphthol additions were tested. 4 g/L gelatin and 2 g/L β -naphthol were dissolved in water at 100°C and stored in sealed bottles. The concentrations selected were based on previous

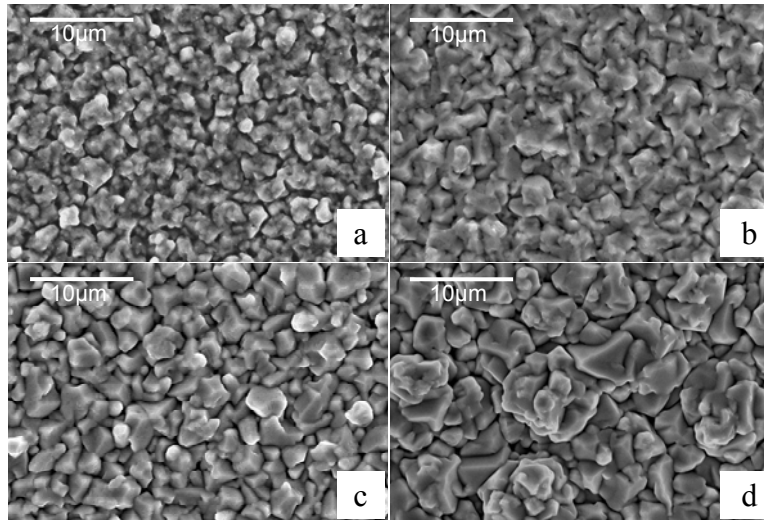


Fig. 3-25 SEM SE plan view images of Sn-Cu films electrodeposited onto Au seed layers from Sn-Cu-citrate solutions with the addition of different amounts of gelatin + naphthol and a constant total solution volume (40 mL): (a) 20 mL, 2 g/L gelatin + 1 g/L naphthol; (b) 10 mL, 1 g/L gelatin + 0.5 g/L naphthol; (c) 5 mL, 0.5 g/L gelatin + 0.25 g/L naphthol; (d) 2.5 mL, 0.25 g/L gelatin + 0.125 g/L naphthol. The concentrations of $\text{SnCl}_2 \cdot 2\text{H}_2\text{O}$, $\text{CuCl}_2 \cdot 2\text{H}_2\text{O}$, and tri-ammonium citrate were fixed at 0.22 mol/L, 0.003 mol/L and 0.30 mol/L, respectively. The current density was 15 mA/cm².

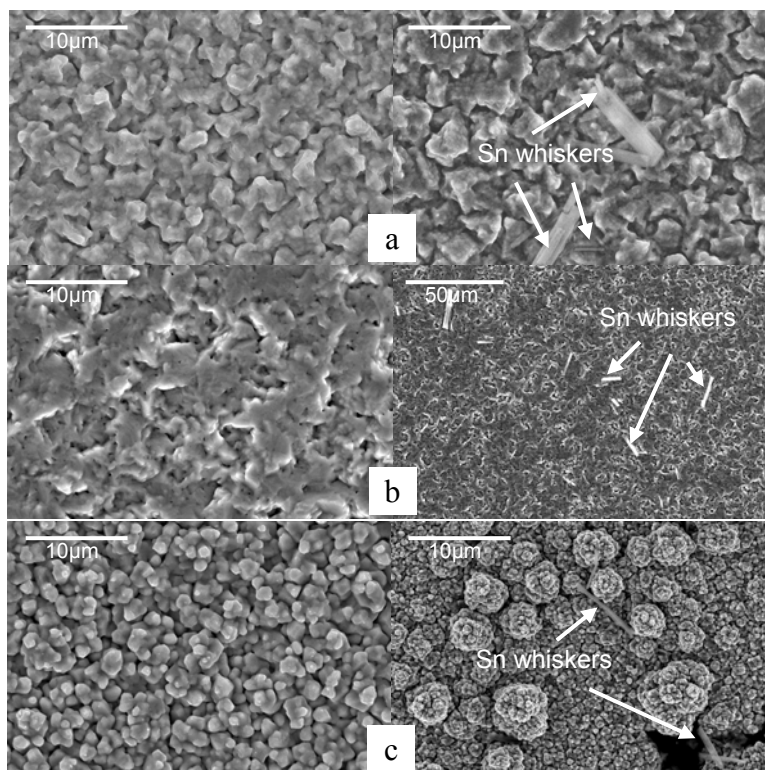


Fig. 3-26 SEM SE plan view images of Sn-Cu films electrodeposited onto Au seed layers from Sn-Cu-citrate solutions with the addition of different amounts of gelatin + β -naphthol and a constant total solution volume (40 mL): (a) 20 mL, 2 g/L gelatin + 1 g/L naphthol; (b) 10 mL, 1 g/L gelatin + 0.5 g/L naphthol; (c) 5 mL, 0.5 g/L gelatin + 0.25 g/L naphthol. The concentrations of $\text{SnCl}_2 \cdot 2\text{H}_2\text{O}$, $\text{CuCl}_2 \cdot 2\text{H}_2\text{O}$ and triammonium citrate were fixed at 0.22 mol/L, 0.003 mol/L and 0.30 mol/L, respectively. The current density was 25 mA/cm².

work in the literature (Jawitz, 1997; Kuwako, 2000; Broggi et al., 2006; Tang et al., 2008a). Specific amounts of the gelatin and β -naphthol solutions were added to Sn-Cu-citrate solutions. The final volume of the mixed solution was kept constant at 40 mL.

SEM plan view images of Sn-Cu films plated from solutions with different amounts of the gelatin and β -naphthol solution at current densities of 15 mA/cm² and 25 mA/cm² are shown in Fig. 3-25 and Fig. 3-26, respectively. Cross section images of Sn-Cu films electrodeposited (at 15 and 25 mA/cm²) from the solution with 1 g/L gelatin and 0.5g/L β -naphthol additions (10 mL) are shown in Fig. 3-27. At a current density of 15 mA/cm², the addition of gelatin and β -naphthol

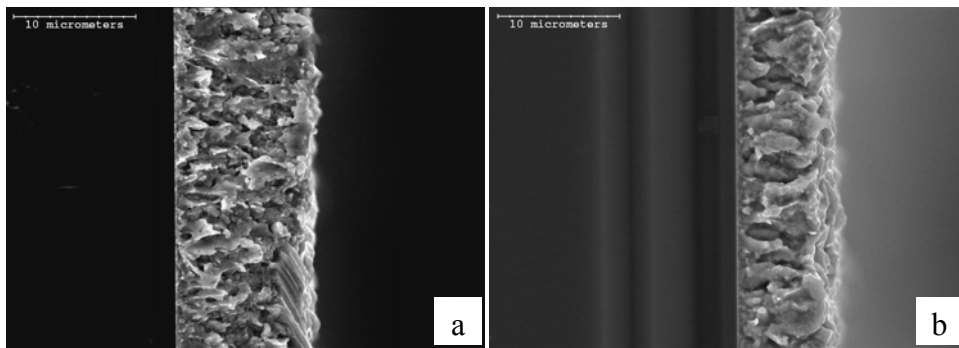


Fig. 3-27 SEM SE cross section images of Sn-Cu films electrodeposited onto Au seed layers from Sn-Cu-citrate solutions with the addition of 10 mL gelatin + naphthol (1 g/L gelatin + 0.5 g/L naphthol) and a constant total solution volume (40 mL) at two different current densities: (a) 25 mA/cm²; (b) 15 mA/cm². The concentrations of SnCl₂·2H₂O, CuCl₂·2H₂O, and tri-ammonium citrate were fixed at 0.22 mol/L, 0.003 mol/L and 0.30 mol/L, respectively.

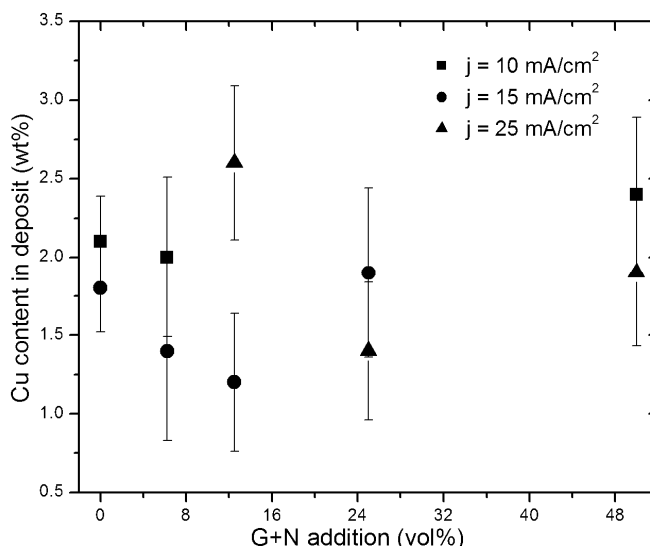


Fig. 3-28 Deposit Cu content as a function of volume percent of gelatin + naphthol addition which was calculated by dividing the volume of gelatin + naphthol addition with the constant total solution volume (40 mL). The concentrations of SnCl₂·2H₂O, CuCl₂·2H₂O and tri-ammonium citrate were fixed at 0.22 mol/L, 0.003 mol/L and 0.30 mol/L, respectively.

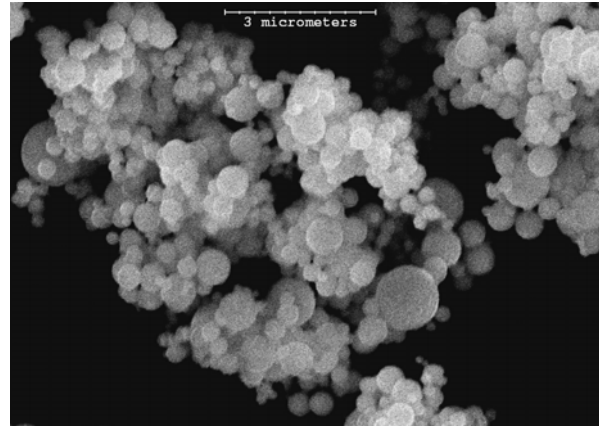
changed the morphology of the Sn-Cu films. Comparing with the images in Fig. 3-22, Sn-Cu films became rougher and less dense. Porous structures are evident from the cross section images in Fig. 3-27. At a current density of 25 mA/cm²,

with the addition of 1 g/L gelatin and 0.5 g/L β -naphthol, a smoother Sn-Cu film was obtained, with small pores on the surface. In addition, Sn whiskers as marked in Fig. 3-26 were found. Similar Sn whiskers were also found on samples with the addition of 2 g/L gelatin and 1 g/L β -naphthol, or 0.5 g/L gelatin and 0.25 g/L β -naphthol at a current density of 25 mA/cm². Fig. 3-28 shows the Cu content in deposits as a function of the volume percentage of gelatin and β -naphthol of the total solution volume at different current densities. The effect of the addition of gelatin (0-2 g/L) and β -naphthol (0-1 g/L) on Cu content in Sn-Cu deposits is not significant, especially considering the error bars.

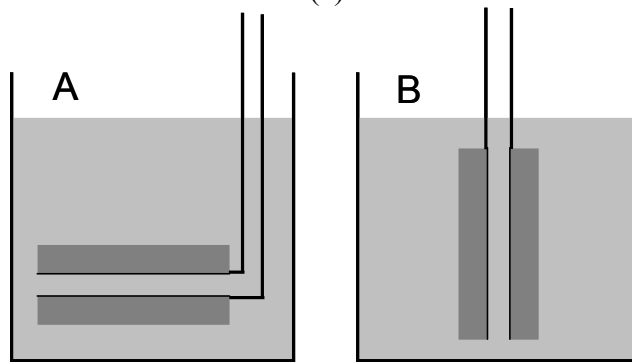
3.3.3 Electrochemical composite deposition of Sn-Cu eutectic and near eutectic alloys from Sn-citrate suspensions with Cu particles

In the second approach, instead of CuCl₂·2H₂O, Cu is supplied through suspended copper particles which are 200 nm to 300 nm in diameter, as shown in Fig. 3-29a. Both horizontal and vertical plating set-ups were applied, as shown in Fig. 3-29b. In configuration A, both electrodes are kept horizontal, making it easier to trap Cu particles as they settle by gravity. In configuration B, the two electrodes are kept vertical, which is normally used in electroplating processes. Fig. 3-30 shows plan view and cross section images of Sn-Cu films plated with horizontal and vertical plating configurations. Sn-Cu films plated with the horizontal configuration showed very rough morphologies, with large agglomerates of Cu particles settled on the surface. Vertical plating gave much smoother Sn-Cu films. As such, only vertical plating is used in the following work. Ultrasonic treatment is commonly used to help disperse particles in suspension. However, under certain conditions, ultrasonic treatment can cause particle agglomeration. SEM backscattered electron (BSE) plan view images of Sn-Cu films (after polishing) without and with ultrasonic dispersion during plating bath preparation are shown in Fig. 3-31. Small bright particles in both samples were identified as Cu₆Sn₅ and the remaining areas were the Sn matrix. With ultrasonic dispersion, the Cu₆Sn₅ particles are finer and more evenly

distributed in the deposits. Therefore, ultrasonic dispersion was continuously applied to help disperse Cu particles during plating bath preparation in the following experiments.



(a)



(b)

Fig. 3-29 (a) SEM SE images of Cu particles. (b) Schematic illustration of experimental set-up for Sn-Cu electrochemical composite deposition: A: horizontal plating; B: vertical plating.

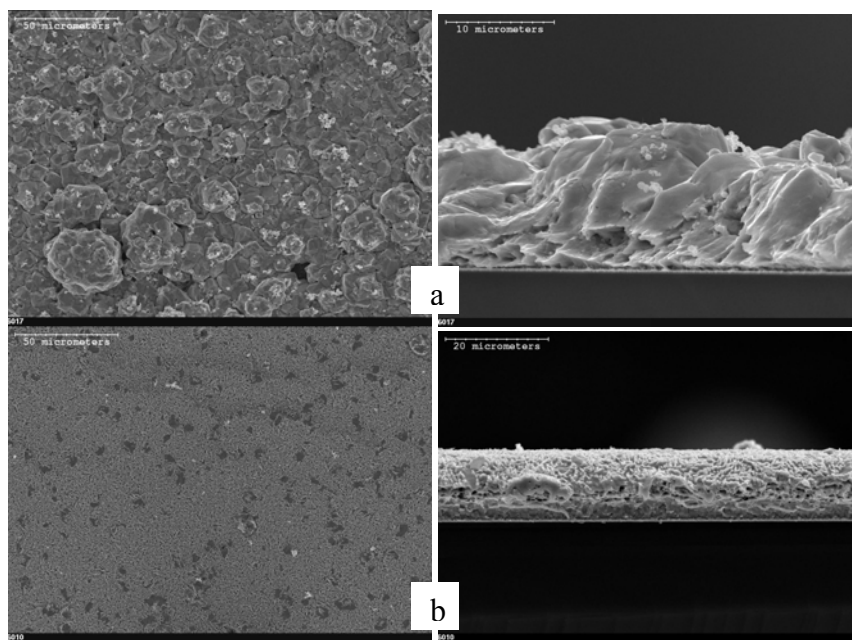


Fig. 3-30 SEM SE plan view images (left) and cross section images (right) of Sn-Cu films deposited onto Au seed layers from Sn-citrate suspensions with Cu particles (0.22 mol/L $\text{SnCl}_2 \cdot 2\text{H}_2\text{O}$ + 0.4 mol/L tri-ammonium citrate + 0.5 g/L Cu) with different experimental set-ups: (a) horizontal plating; (b) vertical plating. The current density used was 10 mA/cm^2 , the plating time was 1 hour and stirring speed was 80 rpm.

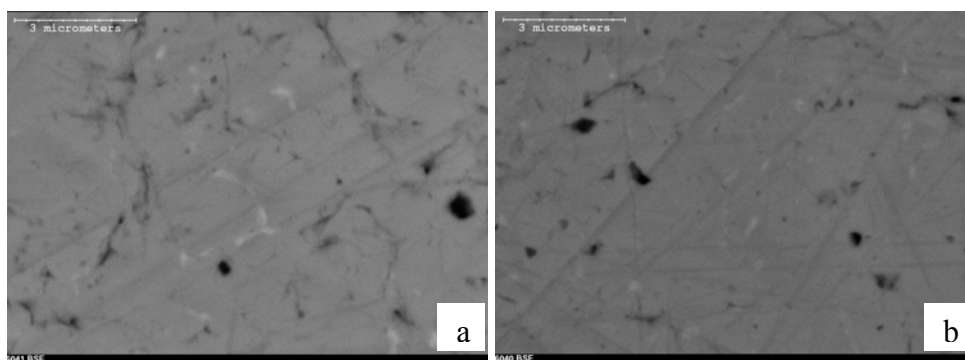


Fig. 3-31 SEM BSE plan view images of Sn-Cu films after polishing. The films were plated onto Au seed layers from suspensions containing 0.22 mol/L $\text{SnCl}_2 \cdot 2\text{H}_2\text{O}$, 0.4 mol/L tri-ammonium citrate, and 0.2 g/L Cu. (a) Without ultrasonic dispersion; (b) with ultrasonic dispersion. The current density used was 10 mA/cm^2 and the stirring speed was 80 rpm.

The Cu particles easily agglomerate and settle, even with agitation and ultrasonic dispersion. To better disperse the copper particles and allow them to

stabilize in the suspension, sodium metaphosphate was utilized as a dispersant. The suspension was stirred at a rate of 80 rpm by magnetic agitation during deposition.

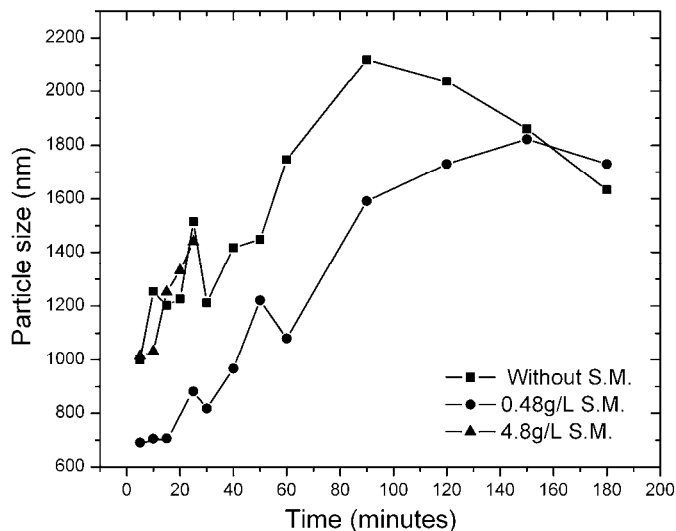


Fig. 3-32 Particle size measurements of Sn-citrate suspension with Cu particles, without and with the addition of sodium metaphosphate (S.M.) as a dispersant. The suspension contains 0.22 mol/L $\text{SnCl}_2 \cdot 2\text{H}_2\text{O}$, 0.30 mol/L tri-ammonium citrate, and 0.2 g/L copper particles.

One way to determine whether the dispersant is effective is to measure the particle size. Suspensions without and with different amounts of sodium metaphosphate were tested and the results are shown in Fig. 3-32. Without sodium metaphosphate, the initial size of copper particles after ultrasonic dispersion is about 1 μm . The nominal particle size of the Cu powder particles specified by the supplier is 200-300 nm. Clearly, the particles are agglomerated even after the ultrasonic treatment and they agglomerate continuously with time (Figure 3.32). The drop in particle size after about 100 minutes is probably because the large agglomerates have settled out. With the addition of 0.48 g/L sodium metaphosphate, the initial particle size is reduced to about 700 nm and smaller particle sizes were detected over most of the tested time period. When the addition of sodium metaphosphate was increased to 4.8 g/L, the measured particle size did not change significantly relative to the case with no dispersants.

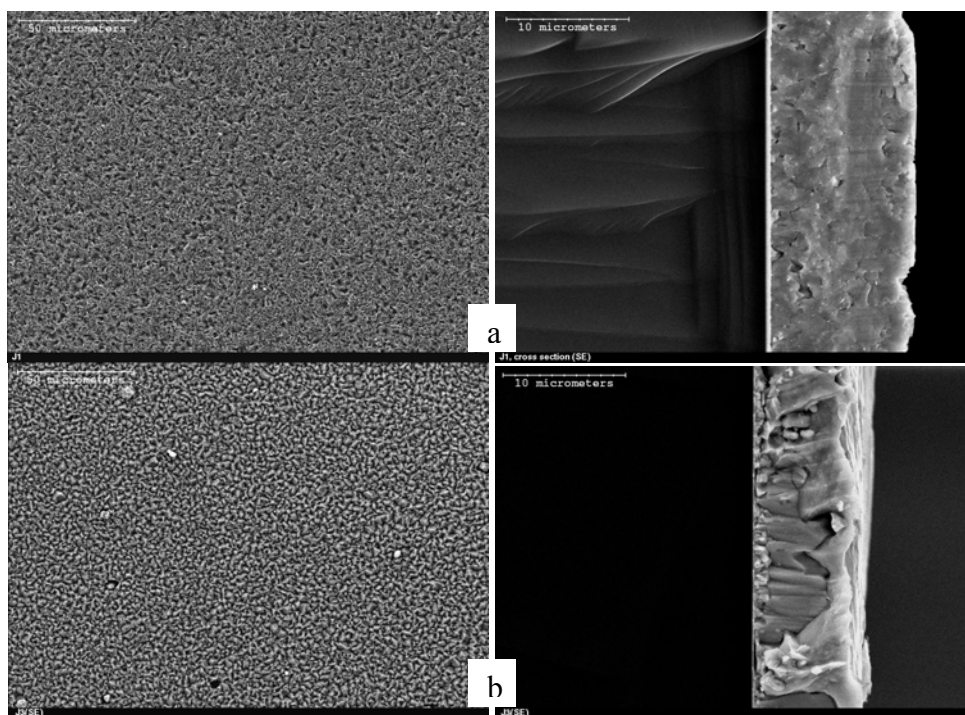


Fig. 3-33 SEM SE plan view images (left) and cross section images (right) of Sn-Cu films plated onto Au seed layers from suspensions containing two different Cu concentrations: (a) PC plating, 0.5 g/L Cu, (b) PC plating, 0.2 g/L Cu. The concentrations of $\text{SnCl}_2 \cdot 2\text{H}_2\text{O}$, tri-ammonium citrate and sodium metaphosphate were kept at 0.22 mol/L, 0.30 mol/L and 0.48 g/L, respectively. The current density used was 10 mA/cm^2 , the plating time was 30 min and the stirring speed was 80 rpm.

Fig. 3-33 shows SE images of Sn-Cu films plated from the suspensions with 0.48 g/L sodium metaphosphate as the dispersant. The deposit obtained from the suspension without the dispersant (Fig. 3-30b) was plated for 1 hour, while the deposits obtained from the suspension with the dispersant were plated for 30 minutes. Both were plated at 10 mA/cm^2 . Without the dispersant, the plating rate was about $13 \text{ }\mu\text{m/hr}$, and the copper content in the deposit was $11.3 \pm 0.4 \text{ wt}\%$. After adding the dispersant (Fig. 3-33a), the plating rate increased to about $23.5 \text{ }\mu\text{m/hr}$ and the Cu content in the deposit decreased to $2.3 \pm 0.4 \text{ wt}\%$. The deposit from the suspension containing the dispersant had a higher plating rate, improved surface morphology and a more uniform Cu distribution. A particle concentration of 0.2 g/L was required to give a deposit composition of $1.1 \pm 0.3 \text{ wt}\%$ Cu at a

plating current density of 10 mA/cm². Plan view and cross section images are shown in Fig. 3-33b.

Initially, research on both Sn-Cu electrodeposition and Sn-Cu electrochemical composite deposition was performed at the same time. However, due to the success of Sn-Cu electrodeposition from Sn-Cu-citrate solutions, as well as the more complicated experimental set-up (with ultrasonic dispersion and agitation) and solution chemistry (with dispersant) for Sn-Cu electrochemical composite deposition from the Sn-citrate + Cu particle suspensions, no further research was carried out for the latter method.

3.4 Conclusions

Sn-citrate solutions containing 0.22 mol/L (50 g/L) SnCl₂·2H₂O and different concentrations of tri-ammonium citrate (0.22-0.82 mol/L, 54-200 g/L) were studied. It was found that 0.30 mol/L (72.4 g/L) is the minimum concentration of tri-ammonium citrate needed to completely dissolve 0.22 mol/L (50 g/L) SnCl₂·2H₂O without forming precipitates. Dense and uniform Sn films were attainable from solutions containing 0.22 mol/L (50 g/L) SnCl₂·2H₂O and tri-ammonium citrate concentrations ranging from 0.30 mol/L (72.4 g/L) to 0.82mol/L (200 g/L) at an average current density of 5 mA/cm², with a plating rate of 8-10 μm/hr. As current density increases, the Sn deposit surface becomes rougher. Higher current densities give higher plating rates. Polarization studies, combined with Sn(II)-citrate solution chemistry studies in Chapter 4 show that as the tri-ammonium citrate concentration increases, Sn(II)-citrate complexes become more difficult to reduce.

The Sn-citrate solutions remained transparent and colorless for more than 3 months. The addition of CuCl₂·2H₂O causes the solution to change color upon aging, with rough and discontinuous films produced. The higher the tri-ammonium citrate concentration, the sooner the color changed. Therefore, the optimal concentration of tri-ammonium citrate for 0.22 mol/L (50 g/L)

$\text{SnCl}_2 \cdot 2\text{H}_2\text{O}$ is 0.30 mol/L (72.4 g/L), which is the lowest tri-ammonium citrate concentration needed to completely dissolve the 0.22 mol/L (50 g/L) tin salt.

Two different types of simple Sn-Cu plating baths have been developed and optimized. One solution contains $\text{SnCl}_2 \cdot 2\text{H}_2\text{O}$ and $\text{CuCl}_2 \cdot 2\text{H}_2\text{O}$ with tri-ammonium citrate as the only additive. Cu content in deposits increases as $\text{CuCl}_2 \cdot 2\text{H}_2\text{O}$ concentration increases. Cu reduction is more favorable than Sn reduction in all the Sn-Cu-citrate solutions. Solutions with higher $\text{CuCl}_2 \cdot 2\text{H}_2\text{O}$ concentration give rougher and less dense Sn-Cu deposits. The Sn-Cu-citrate solutions developed for electrodepositing eutectic and near eutectic Sn-Cu films contain 0.22 mol/L (50 g/L) $\text{SnCl}_2 \cdot 2\text{H}_2\text{O}$, 0.30 mol/L (72.4g/L) tri-ammonium citrate and 0.003 mol/L (0.533g/L) $\text{CuCl}_2 \cdot 2\text{H}_2\text{O}$. The pH of the solutions is around 4. Copper remains more noble than Sn in the tri-ammonium citrate solution so that Cu reduction dominates initially. This causes Cu enrichment at the Sn-Cu solder/substrate interface. Since the Cu concentration in the solutions is almost two orders of magnitude lower than that of Sn, Cu levels deplete rapidly and Sn reduction soon becomes dominant. For both PC and DC plating, the average deposit Cu content decreases and plating rate increases as the current density increases. PC plating gives slightly higher Cu contents in the deposits but lower plating rates than DC plating. A current density between 10 and 12.5 mA/cm^2 gives near-eutectic Sn-Cu compositions with a plating rate between 20 and 27.5 $\mu\text{m}/\text{hr}$.

The co-deposition of Sn and Cu from the Sn-Cu-citrate solutions leads to the formation of two phases, i.e., Sn as the major phase with small amounts of Cu_6Sn_5 .

The developed Sn-Cu-citrate solutions are stable for at least 77 days, with similar plating rates as for fresh solutions. The copper ions in the Cu-citrate complexes become easier to reduce with aging while Sn-citrate is stable; therefore, the Cu content in the deposited Sn-Cu films increases slightly when the solutions, aged for up to 14 days, are used to plate these films.

Agitation increases the limiting current density and allows higher current densities to be utilized, resulting in higher plating rates. Smooth and uniform Sn-

Cu films were attainable at a current density of 40 mA/cm² with agitation. Copper content in deposits decreases as current density increases and it decreases much more slowly with agitation. Eutectic Sn-Cu deposits are attainable from Sn-Cu-citrate solutions containing 0.001 mol/L (0.27 g/L) CuCl₂·2H₂O at current densities from 20 mA/cm² to 40 mA/cm² and stirring speeds of 600 rpm. The plating rate is 36-60 μm/hr.

Gelatin and β-naphthol were added to Sn-Cu-citrate solutions to study their effect on Sn-Cu electrodeposition. At a current density of 15 mA/cm², the addition of gelatin and β-naphthol gave rougher and less dense Sn-Cu films. When the current density was as high as 25 mA/cm², Sn whiskers were detected. In addition, small pores were found on the surface of Sn-Cu films plated from solutions with 10 mL gelatin and β-naphthol additions (1 g/L gelatin + 0.5 g/L naphthol). The change in Cu content in deposits with the addition of gelatin (0-2 g/L) and β-naphthol (0-1 g/L) was insignificant.

An alternative suspension was made up of SnCl₂·2H₂O and tri-ammonium citrate with suspended Cu particles, along with sodium metaphosphate as a dispersant. A dosage of 0.48 g/L dispersant helps improve deposit surface morphology, uniformity and plating rate. With 0.2 g/L Cu particles, a composition of 1.1±0.3 wt% Cu is attainable at a plating current density of 10 mA/cm². The plating rate is about 15.6 μm/hr.

Chapter 4 Solution chemistry studies of Sn-citrate solutions for Sn electrodeposition¹

4.1 Introduction

A large number of Sn-rich alloys have been developed as alternative Pb-free solders in electronic assemblies (Abtey and Selvaduray, 2000; Suganuma, 2001; Kang et al., 2005). Since Sn is the main ingredient in these alloys, studies on Sn solution chemistry and, in particular, on the role of complexing agents in Sn electrodeposition are beneficial.

Different complexing agents for metals and alloys electrodepositions have been investigated and citrate is one of the most extensively studied ones, particularly in the electrodeposition of pure Cu (Rode et al., 2004; Kim and Duquette, 2006b) and Cu and Co alloys, such as Cu-Ni (Cherkaoui et al., 1988; Bonhote and Landolt, 1997; Green et al., 1998), Cu-Co (Gomez et al., 2000), Co-Mo (Subramania et al., 2007) and Co-W (Aravinda et al., 2000). Citrate has also been used in Sn, Sn-Au, Sn-Cu and Sn-Co electrodeposition (Sun and Ivey, 1999; Survila et al., 2001; Yanada et al., 2003; He et al., 2008). Citrate has been shown to be a suitable complexing agent, because good quality Sn and Sn-rich alloys have been obtained and more importantly because of its inherent low toxicity. Moreover, citrate can function as a brightening, leveling and buffering agent, thus eliminating the need for other plating bath additives (Green et al., 1998; Rode et al., 2004).

The formation of Sn(II)-citrate complexes in solutions containing both stannous chloride and ammonium citrate was confirmed by Hess and Taft (1938) in 1938 from the observation that the addition of sodium carbonate to the solution did not result in any precipitation. A kinetic model for Sn electrodeposition from

¹ A version of this chapter has been published. Han, C., Liu, Q. and Ivey, D. G., Kinetics of Sn electrodeposition from Sn(II)-citrate solutions, *Electrochimica Acta*, 53 (2008) 8332-8340.

citrate solutions was proposed by Survila et al. (2000) for the codeposition of Sn and Co. SnL^{2-} and SnHL^- (where L represents the tetravalent citrate ligand, i.e., $\text{C}_6\text{H}_4\text{O}_7^{4-}$, and citric acid can be represented as H_4L) were considered as the most likely complexes formed in acidic solutions. A stability constant of 3.2×10^{19} for SnHL^- was determined experimentally by Survila et al. (2000). Their distribution diagrams of Sn(II)-citrate complexes showed that at a Sn^{2+} concentration of 0.05 mol/L and a citrate concentration of either 0.1 or 0.3 mol/L, SnHL^- was the main species between pH 2 and 4, SnL^{2-} was the main species at pH > 4 and Sn^{2+} was the dominant species below pH 2. Several other researchers have also studied the Sn(II)-citrate system (Tikhonov and Kurolap, 1956; Elbourne and Buchanan, 1970; Jean and Sinicki, 1981; Tselesh, 2008), and proposed different Sn(II)-citrate complexes and stability constants. Jean and Sinicki (1981) proposed three mono-nuclear complexes, SnH_3L^+ , SnH_2L and SnHL^- , and calculated their stability constants, which were 3.2×10^5 , 2.5×10^7 and 2.0×10^{10} , respectively. Tikhonov and Kurolap (1956) used potentiometric methods to study the complexes formed between citric acid and stannous ions and showed that SnHL^- formed when the pH was below 7 and $\text{SnH}(\text{OH})\text{L}^{2-}$ formed when the pH was greater than or equal to 7. Elbourne and Buchanan (1970) proposed the formation of two different Sn(II)-citrate complexes in solutions containing 0.4 mol/L citrate and different concentrations of stannous ions. They proposed that in a solution containing 1×10^{-3} - 2×10^{-3} mol/L stannous ions a bi-nuclear structure ($\text{Sn}_2(\text{H}_2\text{L})_2$) was formed, where two citrate groups chelated with two stannous ions. However, in solutions containing higher concentrations of stannous ions (2.5×10^{-3} mol/L), a mono-nuclear structure ($\text{Sn}(\text{H}_3\text{L})_2$) was formed, where two citrate groups chelated with one stannous ion. The stability constants for the complexes were not determined.

One concern about a citrate electroplating solution is its instability. Although precipitation has occurred in the Sn-citrate solution, the precipitates have never been characterized. The principal objective of this chapter was to study Sn-citrate solution chemistry, to study the reduction behavior of Sn(II) from the Sn-citrate solution and to identify precipitates formed in the Sn-citrate

solutions to better understand the kinetics of Sn electrodeposition from Sn-citrate solutions.

4.2 Experimental materials and procedures

The Sn-citrate solutions were prepared by dissolving tri-ammonium citrate ((NH₄)₃C₆H₅O₇, Alfa Aesar, 98%) in deionized water, followed by the dissolution of SnCl₂·2H₂O (Fisher Scientific) in the citrate solution. The deionized water was obtained from an Aqua MAX™-ultra purification system. An Accumet Basic AB15/15⁺ pH meter was utilized to measure the solution pH. Before each test, the pH meter and electrode were calibrated to compensate for electrode variation by using a buffer solution (Fisher Scientific) with pH values of 4, 7 and 10. During each test, the solution was stirred at 80 rpm using a laboratory magnetic stir bar. Solution pH was adjusted by the addition of HCl.

Polarization measurements were performed using a Gamry electrochemical system operating at a scanning rate of 1 mVs⁻¹. Silicon wafer pieces, metalized with a 25 nm TiW layer and a 200 nm Pt layer, which were provided by Micralyne, Inc., were used as both the working and the counter electrodes, and a saturated calomel electrode (SCE) was used as the reference electrode. Before testing, the Pt electrodes were cleaned ultrasonically for 2 minutes in acetone followed by ethanol and then rinsed with deionized water.

All electrodeposition was done on Si wafer pieces, metallized with a 25 nm TiW adhesion layer and a 200 nm Au seed layer. TiW acts as an adhesion and barrier layer and Au as a seed layer for electroplating. A Dynatronix DuPR 10-0.1-0.3 pulse plating power supply was used for electrodeposition, with a 2 ms forward on-time and 8 ms forward off-time based on previous work (Sun and Ivey, 1999; Olsen, 2005). All electrodeposition was done with a current density of 5 mA/cm² at room temperature for 30 minutes.

The microstructure and composition of the Sn films plated under different conditions were characterized using a Hitachi H2700 scanning electron microscope (SEM), equipped with an ultra thin window energy dispersive X-ray

(EDX) spectrometer. Analysis was done at 20 kV with a working distance of 17 mm and a count rate of 2500-4000 counts/s. Cross section samples were made by cleaving the samples with a diamond pen. Precipitates were formed in the Sn-citrate solutions when the pH was decreased and these were filtered out from the aqueous solutions using filter paper and rinsed with deionized water. The collected precipitates were dried under vacuum at room temperature. The precipitates were analyzed using wide angle X-ray diffraction (XRD) with a Rigaku rotating Co anode system, operating in continuous scanning mode at a voltage of 40 kV and a current of 160 mA. X-ray photoelectron spectroscopy (XPS) was also performed on samples using an AXIS-165 XPS system with an Al-K α (1400 eV) X-ray source with a resolution of 0.5 eV. The binding energies of the C 1s, O 1s and Sn 3d_{5/2} levels were detected and the C 1s (284.65 eV) level was taken as the standard for calibration. Atomic ratios of carbon to oxygen, carbon to tin and oxygen to tin (C/O, C/S, O/Sn) were determined from fits to the survey spectra. Citric acid and tri-ammonium citrate were used as reference specimens.

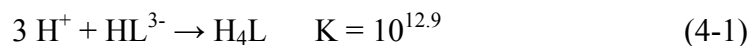
4.3 Results and discussion

4.3.1 Sn-citrate solution chemistry studies

To determine the distribution of various Sn(II)-citrate species in solution, it is necessary to know their stability constants. Two different sets of stability constants for SnHL⁻ were found in the literature, as shown in Table 4-1.

To determine which stability constants were applicable to the solutions in this work, calculations with data from both the literature and experiments were done and are described below.

From the stability constants for citric acid (Table 4-1), the following data can be obtained:



$$\Delta G^\circ = -RT \ln K = \Delta G_{f, \text{H}_4\text{L}}^\circ - \Delta G_{f, \text{HL}^{3-}}^\circ - 3 \Delta G_{f, \text{H}^+}^\circ$$

From the above equations and the free energy data in Table 4-2, the standard Gibbs free energy of formation for HL^{3-} can be calculated as $-1162.81 \text{ kJ}\cdot\text{mol}^{-1}$.

Table 4-1 Stability constants for Sn(II)-citrate complex ions and Sn(II)-hydroxyl species (“L” represents tetravalent citrate ligands).

Equilibrium	Log K	Ref.
$\text{H}^+ + \text{HL}^{3-} \rightarrow \text{H}_2\text{L}^{2-}$	5.69	(Martell and Smith, 1977)
$\text{H}^+ + \text{H}_2\text{L}^{2-} \rightarrow \text{H}_3\text{L}^-$	4.35	(Martell and Smith, 1977)
$\text{H}^+ + \text{H}_3\text{L}^- \rightarrow \text{H}_4\text{L}$	2.87	(Martell and Smith, 1977)
$\text{Sn}^{2+} + \text{HL}^{3-} \rightarrow \text{SnHL}^-$	19.5	(Survila et al., 2000)
	10.3	(Jean and Sinicki, 1981; Tselesh, 2008)
$\text{Sn}^{2+} + \text{H}_2\text{L}^{2-} \rightarrow \text{SnH}_2\text{L}$	7.4	(Jean and Sinicki, 1981; Tselesh, 2008)
$\text{Sn}^{2+} + \text{H}_3\text{L}^- \rightarrow \text{SnH}_3\text{L}^+$	5.5	(Jean and Sinicki, 1981; Tselesh, 2008)
$\text{Sn}^{2+} + \text{H}_2\text{O} \rightarrow \text{SnOH}^+ + \text{H}^+$	-3.8	(Seby et al., 2001)
$\text{Sn}^{2+} + \text{H}_2\text{O} \rightarrow \text{Sn}(\text{OH})_2 + \text{H}^+$	-7.8	(Seby et al., 2001)
$\text{Sn}^{2+} + \text{H}_2\text{O} \rightarrow \text{Sn}(\text{OH})_3^- + \text{H}^+$	-17.5	(Seby et al., 2001)
$\text{Sn}^{2+} + \text{H}_2\text{O} \rightarrow \text{Sn}_2(\text{OH})_2^{2+} + (\text{H}^+)^2$	-2.4	(Seby et al., 2001)
$\text{Sn}^{2+} + \text{H}_2\text{O} \rightarrow \text{Sn}_2(\text{OH})_3^+ + \text{H}^+$	-6.66	(Seby et al., 2001)
$\text{Sn}^{2+} + \text{H}_2\text{O} \rightarrow \text{Sn}_3(\text{OH})_4^{2+} + \text{H}^+$	-5.6	(Seby et al., 2001)

Table 4-2 Selected free energy data for the Sn(II)-citrate system at 298K

Species	ΔG_f° ($\text{kJ}\cdot\text{mol}^{-1}$)	Ref.
Citric acid (H_4L)	-1236.4	(Dean, 1999)
H^+ (aq.)	0	(Dean, 1999)
Sn^{2+} (aq.)	-27.2	(Dean, 1999)
Sn, white	0	(Dean, 1999)

Table 4-3 Composition of Sn-citrate solutions used in this study

	S1	S2	S3	S4
$\text{SnCl}_2\cdot 2\text{H}_2\text{O}$ (mol/L)	0.22	0.22	0.22	0.22
Tri-ammonium citrate (mol/L)	0.30	0.33	0.44	0.66

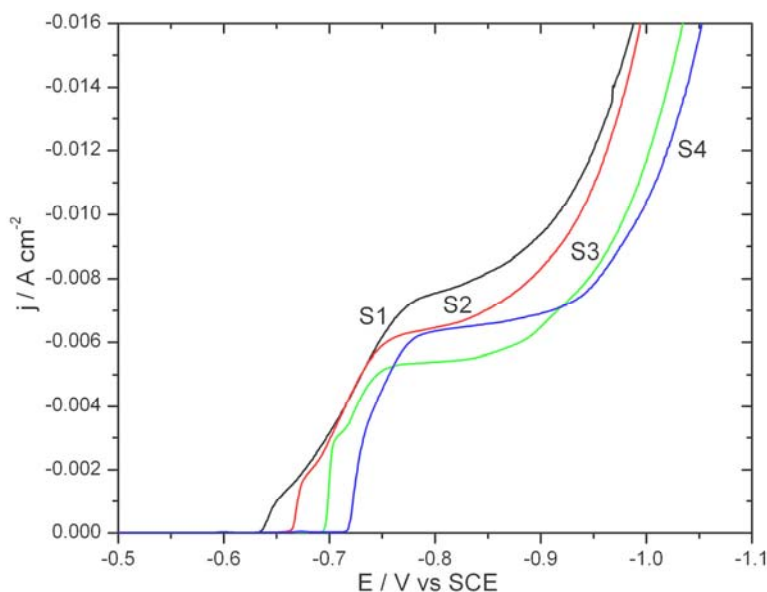


Fig. 4-1 Polarization curves for Sn-citrate solutions. In all solutions, the concentration of $\text{SnCl}_2 \cdot 2\text{H}_2\text{O}$ was kept at 0.22 mol/L, while the concentration of tri-ammonium citrate was varied as follows: S1, 0.30 mol/L; S2, 0.33 mol/L; S3, 0.44 mol/L; S4, 0.66 mol/L.

Speciation calculations were initially performed on a solution containing 0.22 mol/L SnCl_2 and 0.30 mol/L tri-ammonium citrate, which is labeled as S1 (Table 4-3). This particular solution was chosen because 0.30 mol/L of tri-ammonium citrate has been shown to be the minimum amount required to completely dissolve 0.22 mol/L SnCl_2 , as discussed in Chapter 3. The natural pH of solution S1 is 4.1. At this pH, all three ammonium ions should fully dissociate from the citrate ions and each citrate ion can carry up to four protons, thus forming H_4L , H_3L^- , H_2L^{2-} and HL^{3-} . Only H_3L^- , H_2L^{2-} and HL^{3-} are considered as ligand species with Sn^{2+} ions in solution. Survila et al. (2000) considered both SnHL^- and SnL^{2-} in their model for Sn(II)-citrate complexes. The difference is that they used citric acid instead of tri-ammonium citrate. One important consideration for tri-ammonium citrate is that the proton in the ternary hydroxyl group is difficult to dissociate at a pH of 4.1, so that SnHL^- was more likely to form in solution S1. To simplify the calculation, all Sn^{2+} ions were assumed to form the SnHL^- complex with the citrate, so that the concentration of SnHL^- would be 0.22 mol/L and the concentration of HL^{3-} would be 0.08 mol/L. From

the polarization measurements shown in Fig. 4-1, the reduction of SnHL⁻ started at about -0.64 V versus SCE (i.e., -0.398 V versus SHE, which is the standard hydrogen electrode). A further decrease in applied potential caused an almost linear increase in the current density, until about -0.75 V, where a plateau appeared which was the limiting current density for SnHL⁻ reduction in solution S1.

The reduction reaction for SnHL⁻ during the electrodeposition of Sn can be given as:



A potential of -0.398 V versus SHE, from the polarization measurements, was used as the reduction potential for reaction (4-2) in the following calculation. It follows from the Nernst equation that

$$E = E^\circ + \frac{RT}{nF} \ln \frac{[\text{SnHL}^-]}{[\text{HL}^{3-}]} = -0.398 \text{ V vs SHE}$$

The standard electrode potential E^o for reaction (4-2) can be calculated as -0.41 V vs SHE. The standard Gibbs free energy change for this reaction is therefore equal to:

$$\Delta G^\circ = -nFE^\circ = \Delta G_{f, \text{HL}^{3-}}^\circ + \Delta G_{f, \text{Sn}}^\circ - \Delta G_{f, \text{SnHL}^-}^\circ = 79.3 \text{ kJ}\cdot\text{mol}^{-1}$$

From the above equations and data shown in Table 2, the standard Gibbs free energy of formation for SnHL⁻ is -1242.11 kJ·mol⁻¹.

The SnHL⁻ complex forms according to,



The standard Gibbs free energy change for the formation of SnHL⁻ is,

$$\Delta G^\circ = -RT \ln K = \Delta G_{f, \text{SnHL}^-}^\circ - \Delta G_{f, \text{HL}^{3-}}^\circ - \Delta G_{f, \text{Sn}^{2+}}^\circ$$

Thus

$$K = e^{\frac{\Delta G^\circ}{-RT}} = 1.36 \times 10^9 \text{ and } \log K = 9.1.$$

Comparing this value with the data from the literature, the stability constant for SnHL⁻ from (Jean and Sinicki, 1981; Tselesh, 2008) (i.e., log K = 10.3) is much closer than the value from Survila (2000) (log K = 19.5) to our results and thus was used in the subsequent calculations.

Other than the formation of Sn(II)-citrate complexes, the hydrolysis of the Sn^{2+} ions was also taken into account and the available stability constants are listed in Table 4-1. In this study, the equilibrium concentrations of the citrate complexes and all other compounds were calculated with the aid of spreadsheet software (e.g., Microsoft Excel). To perform a calculation, the concentrations of all possible Sn(II)-citrate complexes and Sn^{2+} hydrolysis products were expressed as a function of the concentration of SnHL^- , Sn^{2+} and/or the pH of the solution. Then, mass balance equations for both Sn and citrate were set up, so that the concentration of SnHL^- could be calculated at a given pH. Subsequently, the concentrations of all the other species were calculated.

The two mass balance equations used during the calculations are:

$$C_{\text{citrate}} = [\text{H}_4\text{L}] + [\text{H}_3\text{L}^-] + [\text{H}_2\text{L}^{2-}] + [\text{HL}^{3-}] + [\text{SnH}_3\text{L}^+] + [\text{SnH}_2\text{L}] + [\text{SnHL}^-] \quad (4-4)$$

$$C_{\text{Sn(II)}} = [\text{SnH}_3\text{L}^+] + [\text{SnH}_2\text{L}] + [\text{SnHL}^-] + [\text{Sn}^{2+}] + [\text{SnOH}^+] + [\text{Sn}(\text{OH})_2] + [\text{Sn}(\text{OH})_3^-] + 2[\text{Sn}_2(\text{OH})_2^{2+}] + 2[\text{Sn}_2(\text{OH})_3^+] + 3[\text{Sn}_3(\text{OH})_4^{2+}] \quad (4-5)$$

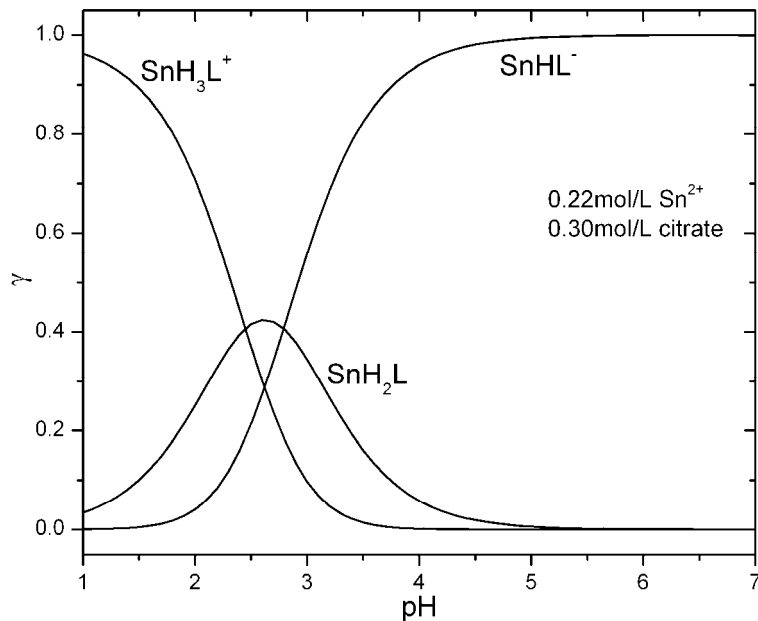


Fig. 4-2 Sn(II)-citrate speciation diagram as a function of pH for solution S1 (0.22 mol/L Sn^{2+} and 0.30 mol/L tri-ammonium citrate). γ is the molar percentage of Sn(II)-citrate complexes.

The distribution of Sn(II)-citrate complexes (SnH_3L^+ , SnH_2L and SnHL^-) in molar fraction as a function of pH for solution S1, is shown in Fig. 4-2. The concentration of Sn^{2+} ions is in the range of 10^{-3} to 10^{-9} mol/L and concentrations of all the Sn^{2+} hydrolysis products are in the range of 10^{-5} to 10^{-40} mol/L and they are not shown in the distribution diagram. It can be noted that at the solution natural pH of 4.1, the main species in solution S1 is SnHL^- , with a very small amount of SnH_2L . Hydrochloric acid was added to solution S1 to decrease the pH. During the pH adjustment, the solution remained clear until the pH reached about 3.3. When the pH was decreased to about 3.1, a small amount of precipitates started forming. Once the solution was stirred for about 30 seconds, more precipitates formed and eventually solution S1 became milky in appearance, with white precipitates settling out. During precipitation, the solution pH increased to about 3.3 and remained at that value. When the pH was lowered to 2.5, more precipitates formed; this was likely due to the formation of more SnH_2L based on Figure 4-2. As more HCl was added, the precipitates started to dissolve and the solution became almost clear at a pH of 1.1. This disappearance of precipitates can be explained by the dissolution of SnH_2L and the formation of SnH_3L^+ as the main Sn(II)-citrate complex (Fig. 4-2).

The same calculations were carried out for solutions S2, S3 and S4 (Table 4-3). For solutions S1, S2, S3 and S4, the concentration of $\text{SnCl}_2 \cdot 2\text{H}_2\text{O}$ was fixed at 0.22 mol/L, while the concentration of tri-ammonium citrate was varied from 0.30 mol/L to 0.66 mol/L. The concentrations of Sn(II)-citrate complexes (SnH_3L^+ , SnH_2L , SnHL^-) and citrate species (H_4L , H_3L^- , H_2L^{2-} , HL^{3-}) as a function of pH are shown in Fig. 4-3 a-d. There is almost no change in the distribution of the different Sn(II)-citrate complexes as the concentration of tri-ammonium citrate is increased from 0.30 mol/L to 0.66 mol/L, but the distribution of the citrate species changes. The peak positions of the curves for the four citrate species stayed the same for S1, S2, S3 and S4, but the height of each peak increased with increasing tri-ammonium citrate concentration.

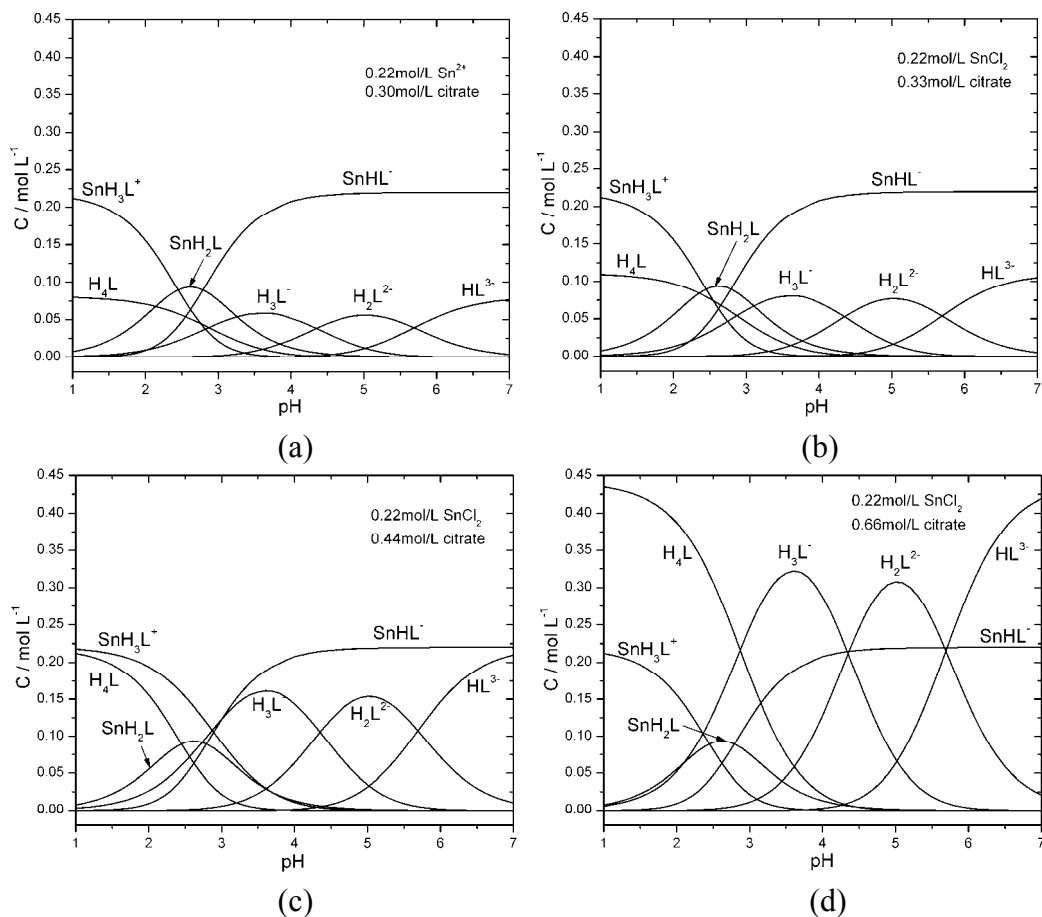


Fig. 4-3 Speciation diagrams as a function of pH for solutions S1 (a), S2 (b), S3 (c) and S4 (d). Note that all solutions contain 0.22 mol/L Sn²⁺, but different concentrations of tri-ammonium citrate: (a) 0.30 mol/L, (b) 0.33 mol/L, (c) 0.44 mol/L, and (d) 0.66 mol/L.

The standard electrode potentials (E°) for the reduction of Sn(II) to Sn⁰ from SnHL⁻, SnH₂L and SnH₃L⁺ calculated from Gibbs free energy data, were -0.69, -0.60 and -0.54 V vs SCE, respectively. These results show that SnH₃L⁺ is the easiest to reduce, followed by SnH₂L and then SnHL⁻ under standard conditions. To find out the effect of citrate species distribution on the reduction behavior of the Sn(II)-complexes, the reduction potentials (E) for SnHL⁻, SnH₂L and SnH₃L⁺ were calculated using the Nernst equation for solutions S1, S2, S3 and S4 and the results are shown in Figure 4-4a. In each solution, the reduction potentials for the three Sn(II)-citrate complexes were similar, although there is a slight increase from SnHL⁻ to SnH₂L and from SnH₂L to SnH₃L⁺. In addition, as

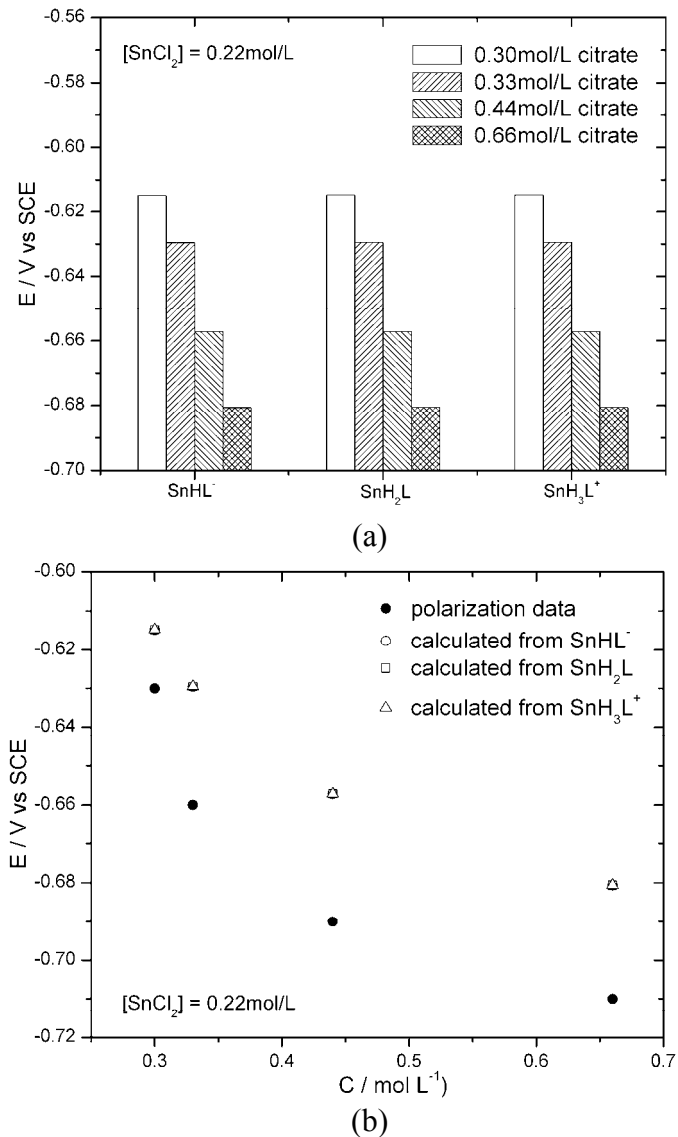


Fig. 4-4 (a) Calculated reduction potentials for SnHL^- , SnH_2L and SnH_3L^+ for solutions S1, S2, S3 and S4 at natural pH. (b) Comparison of calculated and experimental reduction potentials as a function of tri-ammonium citrate concentration.

the concentration of tri-ammonium citrate was increased from 0.30 mol/L to 0.66 mol/L, the reduction potentials for the Sn(II)-citrate complexes decreased from -0.61 V to about -0.68 V versus SCE. The calculated and experimental reduction potentials are shown in Fig. 4-4b; both follow the same trend. The values for each Sn(II)-citrate complex are so close that they overlap one another and thus only one data point is shown for each solution. The reduction potentials from the

polarization measurements are more negative than the calculated values, because during the polarization measurements the applied potential must cover the ohmic drop required to drive the ionic current in solution, as well as support the electrochemical reactions. Since the reduction potential for all three Sn(II)-citrate complexes are very close to one another, it is also quite possible that they would participate in the reduction reaction at the same time, and be reduced to Sn metal on the cathode.

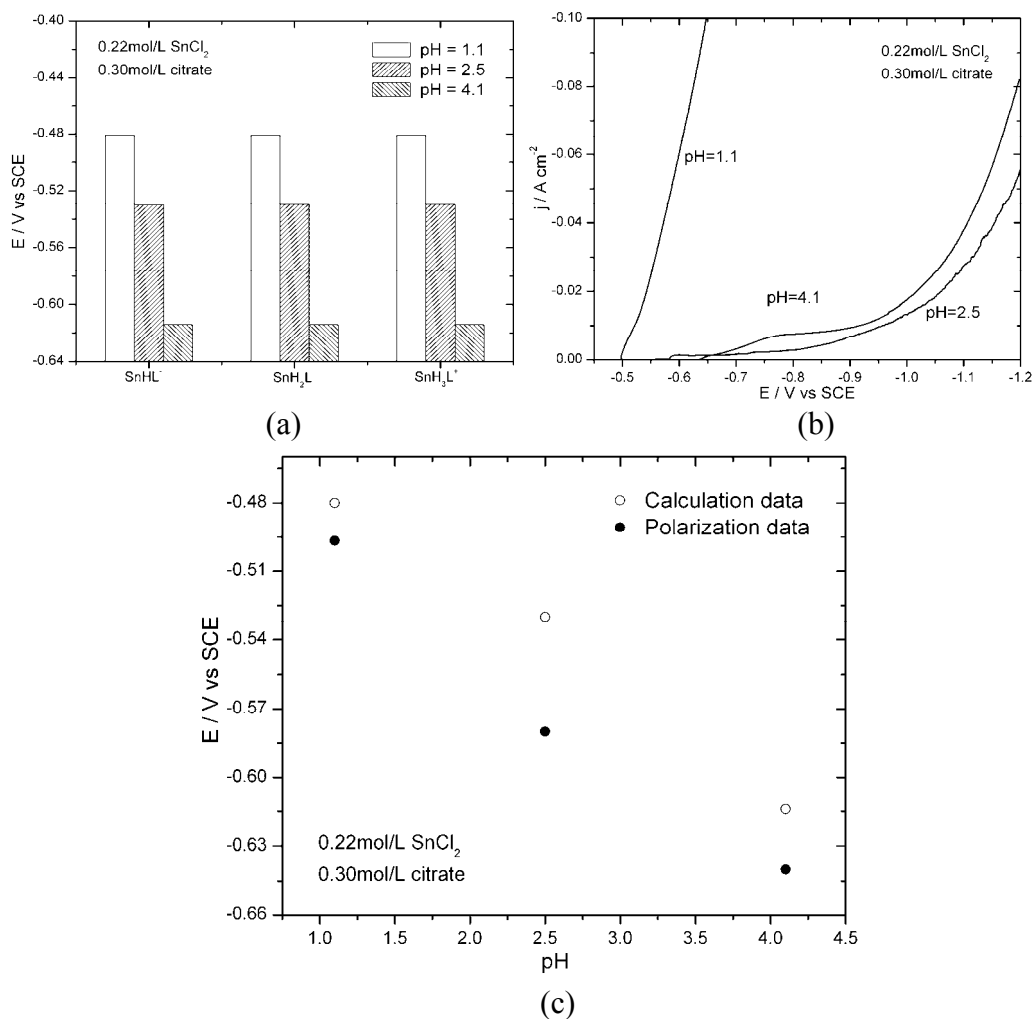


Fig. 4-5 (a) Calculated reduction potentials for SnHL^- , SnH_2L and SnH_3L^+ for solution S1 (0.22 mol/L Sn^{2+} and 0.30 mol/L tri-ammonium citrate) at pH 1.1, 2.5 and 4.1. (b) Polarization curves for solution S1 at pH 1.1, 2.5 and 4.1. (c) Comparison of calculated and experimental reduction potentials for solution S1 as a function of pH.

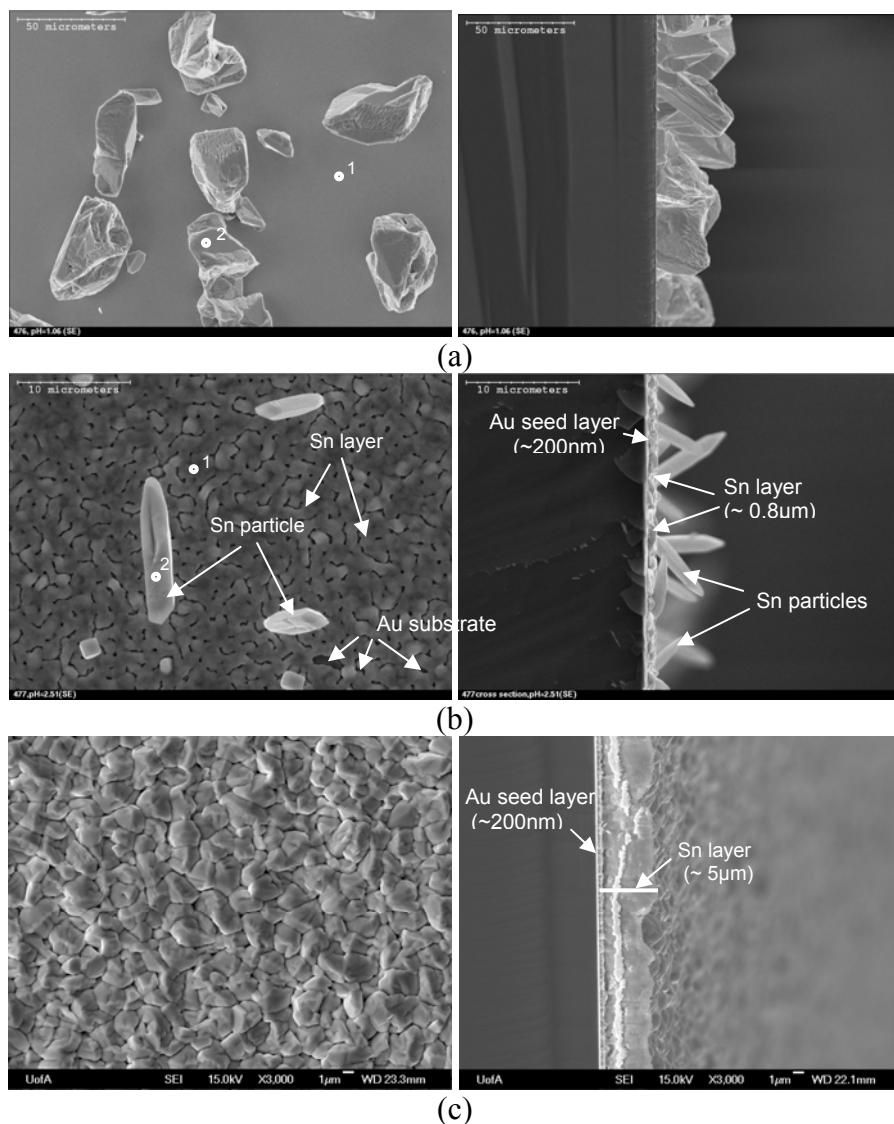


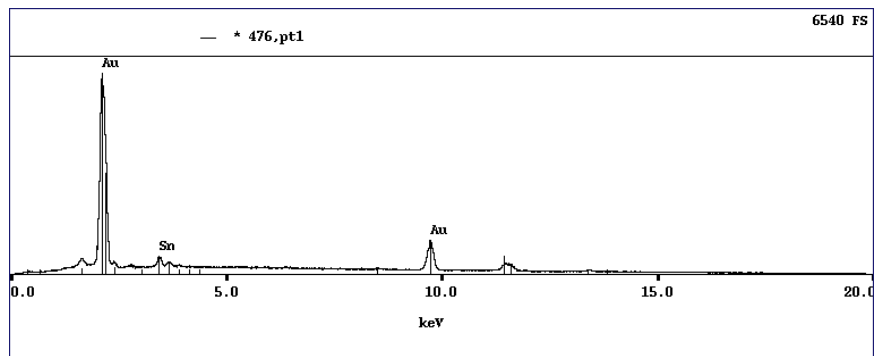
Fig. 4-6 SEM SE images (plan view and cross section) of Sn films electrodeposited from solution S1 (0.22 mol/L Sn^{2+} and 0.30 mol/L tri-ammonium citrate) at pH 1.1 (a), 2.5 (b) and 4.1 (c).

The same calculations for reduction potentials were also carried out for solution S1 at different pH values, and the results are shown in Fig. 4-5a. At each pH value, the reduction potentials for SnHL^- , SnH_2L and SnH_3L^+ were again similar to one another, with a very slight increase from SnHL^- to SnH_2L and then to SnH_3L^+ . As the pH was decreased from 4.1 to 2.5 and then to 1.1, the reduction potentials became less negative, moving from -0.615 V to -0.53 V and then to -

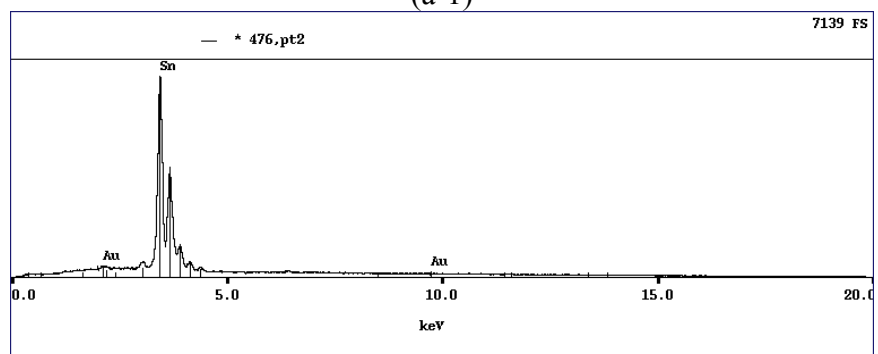
0.48 V versus SCE, which means that the Sn(II)-citrate complexes became easier to reduce at lower pH.

To verify the above calculations, polarization measurements were performed for solution S1 at pH 1.1, 2.5 and 4.1, and the results are shown in Fig. 4-5b. The reduction potential change as a function of pH showed a similar trend to the calculated results. The current density for solution S1, with a pH of 2.5, was very low, lower than the values for the other two solutions. This is due to the formation of a significant quantity of precipitates at a pH value of 2.5. In addition, both the Sn and citrate concentrations in the solution were much lower. The polarization curve for solution S1, with a pH of 1.1, showed an almost linear dependence, due to significant hydrogen evolution at this pH. For comparison, the calculated and experimental reduction potentials for different pH values are combined in Fig. 4-5c. The data follow the same trend, with the measured reduction potential being more negative for the reasons stated previously.

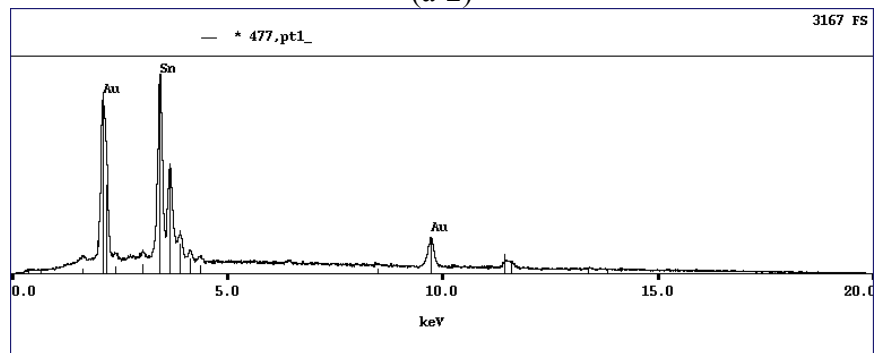
Electrodeposition of Sn from solution S1, with pH values of 1.1, 2.5 and 4.1, was carried out on Au-coated Si substrates. SEM secondary electron (SE) images for both plan views and cross sections of the as-deposited Sn films are shown in Fig. 4-6 a-c. Note that the magnification for Fig. 4-6a is 5 times lower than that for Fig. 4-6b and Fig. 4-6c. EDX point analysis at the positions identified in the plan view images of Fig. 4-6a and 4-6b is shown in Fig. 4-7a and 4-7b. As shown in Fig. 4-6a and Fig. 4-6b, when the pH is 1.1, Sn grows rapidly towards the anode producing large particles (35-40 μm in size after 30 minutes of plating). EDX point analyses from position 1 (smooth area) and position 2 (one of the large particles) in Fig. 4-6a are shown in Fig. 4-7a-1 and 4-7a-2. The EDX spectrum in Fig. 4-7a-1 is mostly Au with a small Sn peak. The Au is from the underlying seed layer and the Sn is from a thin continuous Sn layer ($\ll 1\mu\text{m}$ thick), which forms during the initial nucleation stage from the reduction of SnH_3L^+ , SnH_2L and SnHL^- . The larger particles are pure Sn (Fig. 4-7a-2). At pH 2.5, a thicker continuous Sn layer (about 0.8 μm thick) forms before isolated Sn particles grow preferentially (Fig. 4-7b-1 and 4-7b-2). The reason why the continuous Sn layer is thicker at pH 2.5 than at pH 1.1 is that the concentration of



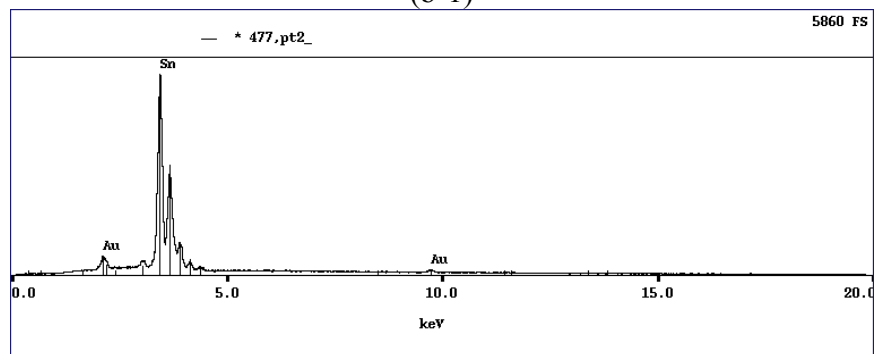
(a-1)



(a-2)



(b-1)



(b-2)

Fig. 4-7 EDX point analysis for Sn plated from solution S1 at pH 1.1 (a-1, a-2) and 2.5 (b-1, b-2).

SnHL^- is much higher at pH 2.5 than at pH 1.1. This is important because SnHL^- has a slower plating rate and is favored to form a continuous layer. Consequently, fewer and smaller Sn particles are formed at this pH. At the natural pH (solution S1), a dense Sn film forms with a thickness of about 5 μm . All three cross section samples were prepared by cleaving with a diamond pen. The cross section image in Fig. 4-6c was not perfectly edge-on, so some of the surface is visible.

As shown in Fig. 4-2, at a pH of 1.1, the main complex in the solution is SnH_3L^+ . With a positive charge, SnH_3L^+ will be easily attracted to cathode. In addition, as shown in Fig. 4-5a, SnH_3L^+ itself becomes easier to reduce when the pH is as low as 1.1 than at higher pH values and SnH_3L^+ is also easier to reduce than both SnH_2L and SnHL^- at higher pH values. All these reasons contribute to the high growth rate of Sn on the cathode. In contrast to SnH_3L^+ , the SnHL^- species (which forms at higher pH values) has a negative charge. The charge distribution within the polar complex ions must be aligned to facilitate attraction to the cathode, so that mass transfer will be slower and the deposited film should have sufficient time to densify.

4.3.2 Sn(II)-citrate precipitates identification

XRD and XPS were used in an attempt to identify the precipitates from solution S1, which formed at different pH values, and precipitates from solution S2, S3 and S4 when the pH was decreased. Both XRD and XPS analyses indicated that the precipitates had the same composition and structure. An XRD pattern, from precipitates which formed from solution S1 at a pH of 2.5, is shown in Fig. 4-8. The pattern is quite complex, with the strongest peak at $2\theta = 11.75^\circ$. The pattern does not match XRD patterns obtained for tri-ammonium citrate, citric acid, tin chloride dihydrate or tin oxide. We were unable to index the pattern.

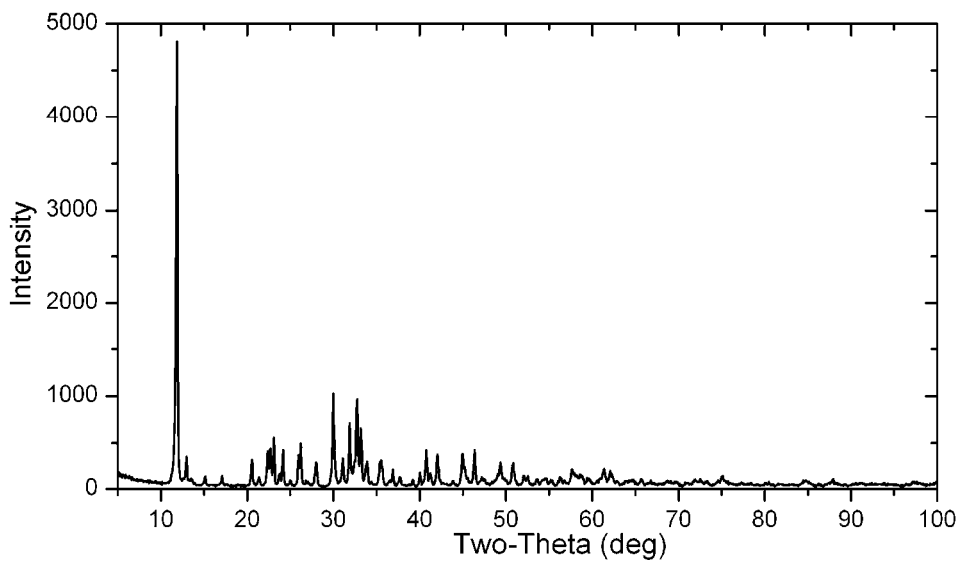


Fig. 4-8 XRD pattern for precipitates obtained from solution S1 at pH 2.5.

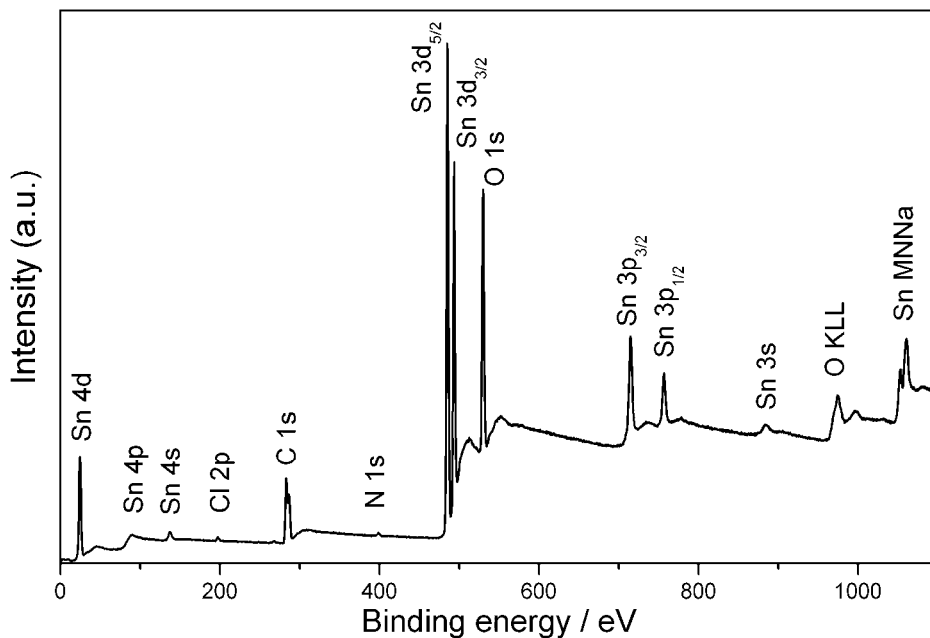


Fig. 4-9 XPS survey spectrum for precipitates obtained from solution S1 at pH 2.5.

Fig. 4-9 shows an XPS survey spectrum for the precipitates from solution S1 (pH = 2.5). Several elements, including Sn, C, O, Cl and N were detected. There was a small amount of N (about 0.7 at%) and Cl (about 0.5 at%) present in

the precipitates. XPS analysis was done on standard citric acid and tri-ammonium citrate samples for comparison. Similar N levels (about 0.2 at%) were detected in the citric acid specimen and similar Cl levels (about 0.3 at.%) were detected in the tri-ammonium citrate specimen, and may be due to contamination.

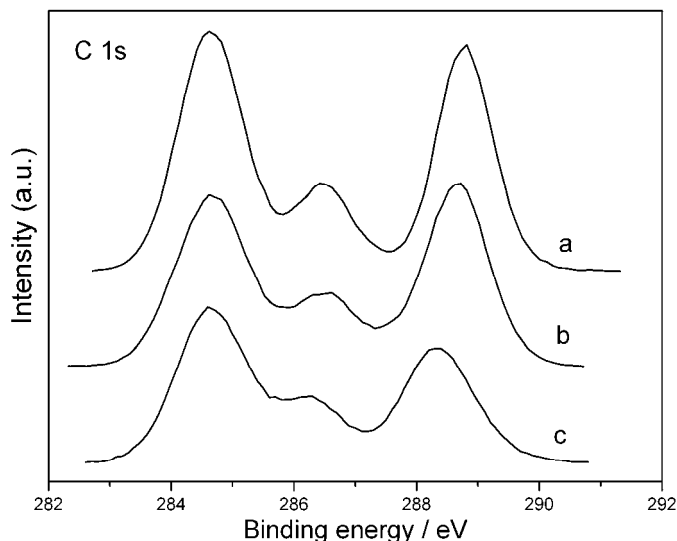


Fig. 4-10 XPS C 1s spectrum from: (a) citric acid, (b) tri-ammonium citrate and (c) precipitates obtained from solution S1 at pH 2.5.

Fig. 4-10 shows the C 1s XPS spectra for citric acid, tri-ammonium citrate and the Sn(II)-citrate solution precipitates. Three peaks were identified by peak fitting and these correspond to different surroundings for carbon, which match the number of C bond types in both citric acid and tri-ammonium citrate. The C 1s peaks at 284.65 eV (Table 4-4) are assigned to methyl carbons (Dennis et al., 1980; Kodolov et al., 1998; Tselesh, 2008), while the peaks at 286.4 eV (citric acid), 286.53 eV (tri-ammonium citrate) and 286.27 eV (Sn(II)-citrate precipitates) correspond to carbon bonded to carbonyl groups (Kodolov et al., 1998; Tselesh, 2008). The peaks at 288.78 eV (citric acid), 288.65 eV (tri-ammonium citrate) and 288.36 eV (Sn(II)-citrate precipitates) are attributed to carbon atoms of COO⁻ groups, which is also in agreement with the binding energy values reported for acetyl carbons (Dennis et al., 1980; Kodolov et al., 1998; Kall et al., 2001; Tselesh, 2008).

Table 4-4 Binding energies for main components of XPS C 1s, O 1s and Sn 3d_{5/2} peaks for citric acid, tri-ammonium citrate and precipitates obtained from solution S1 at pH 2.5

Binding energy (eV)							
XPS peak parameters	C 1s				O 1s		Sn 3d _{5/2}
Components	-C-C-	-C-OH	-COO	-COOM	-COOH	C-O-H	O-Sn-O
Citric acid	284.65	286.49	288.78		531.84	533.07	
Tri-ammonium citrate	284.65	286.53	288.65	531.77		533.03	
Sn-citrate precipitate	284.65	286.27	288.36	531.47			486.8

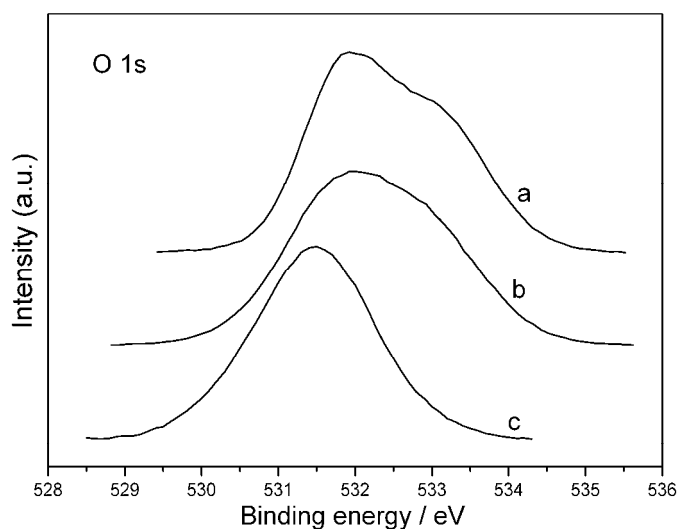


Fig. 4-11 XPS O 1s spectrum from: (a) citric acid, (b) tri-ammonium citrate and (c) precipitates obtained from solution S1 at pH 2.5.

Fig. 4-11 shows the O 1s XPS spectra for citric acid, tri-ammonium citrate and Sn(II)-citrate precipitates. Two peaks were deconvoluted for both citric acid and tri-ammonium citrate, and these also matched the number of O bonds in both reference specimens. The high binding energy for O 1s at 533.07 eV (citric acid) and 533.03 eV (tri-ammonium citrate) can be assigned to oxygen atoms in -C-OH

groups (Kodolov et al., 1998; Atzei et al., 2000), and the oxygen peaks at 531.84 eV (citric acid) and 531.77 eV (tri-ammonium citrate) can be assigned to -COO^- groups (Dennis et al., 1980; Kodolov et al., 1998; Atzei et al., 2000; Kall et al., 2001). It should be noted that the binding energies for O 1s in -COOH (531.84 eV) and -COO-M (531.77 eV) are very close. For the Sn(II)-citrate precipitates, the O 1s spectrum has only one peak with a binding energy of 531.47 eV, suggesting equivalent oxygen atoms and implying equivalency of the two Sn atoms to which they are bound. Comparison with the reference O 1s peaks in citric acid and tri-ammonium citrate indicates that the O 1s peak for the precipitates is associated with -COOH bonds and/or -COO-M bonds, with no C-O-H bonds. The O 1s binding energy for the Sn(II)-citrate precipitates was lower than that for citric acid and tri-ammonium citrate by 0.37 eV and 0.3 eV, respectively, which can be attributed to a decrease in the electron density of the carboxyl oxygen by an increase in the positive environment produced by Sn(II). To ensure reproducibility, two additional precipitation tests were carried out from solution S1 at pH 2.5, and the precipitates were subjected to the same XPS measurements. In all cases, similar XPS spectra were obtained.

The XPS Sn 3d core level spectrum, with a binding energy of 486.8 eV, from the precipitates is shown in Fig. 4-12. It is difficult to distinguish between O-Sn(II)-O and O-Sn(IV)-O since the positions of the Sn $3d_{5/2}$ peaks for Sn(II) and Sn(IV) oxy/hydroxy compounds partially overlap: 486.3 ± 0.6 eV (SnO) and 486.9 ± 0.6 eV (SnO₂) (Jimenez et al., 1995; Batzill and Diebold, 2005; Li et al., 2007; Tselesh, 2008). Considering that tri-ammonium citrate was not likely an oxidizing agent for stannous ions in solution, the Sn $3d_{5/2}$ line at 486.8 eV could indicate the presence of a Sn(II) compound and not a Sn(IV) compound. Quantitative analysis, based on the area estimated from the XPS C 1s, O 1s and Sn $3d_{5/2}$ spectra, was carried out. The atomic concentrations of C and O in citric acid and tri-ammonium citrate, and C, O and Sn in the Sn(II)-citrate precipitates are shown in Table 4-5. The relative concentrations of C/O for citric acid and tri-ammonium citrate are 1.23 and 1.11 respectively, which are higher than the ratio of 0.86 calculated from the chemical formulas of citric acid (C₆H₈O₇) and tri-

ammonium citrate ((NH₄)₃C₆H₅O₇). This indicates that some C contamination from air occurred and the calculated C concentrations are too high. The same effect would be expected for Sn(II)-citrate precipitates under the same working conditions, giving higher C/Sn relative concentrations than expected. Therefore, the actual C/Sn atomic ratio in the Sn(II)-citrate precipitates is lower than 3.86, e.g., 3, 2 or 1.

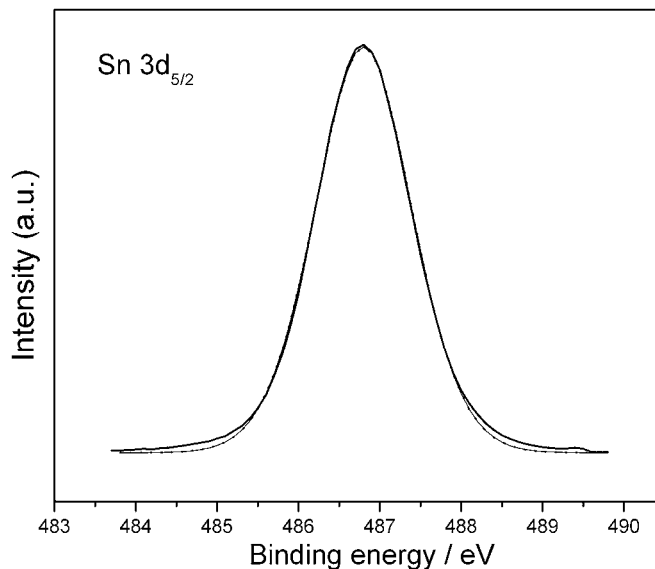


Fig. 4-12 XPS Sn3d core level spectrum for precipitates obtained from solution S1 at pH 2.5. The thick solid line is the experimental spectrum; the thin line is the fitted spectrum.

Table 4-5 Composition results for citric acid, tri-ammonium citrate and precipitates obtained from solution S1 at pH 2.5

Element	Atom concentration (%)			Atomic ratio		Atomic ratio	
	C	O	Sn	C/O (theoretical)	C/O (actual)	C/Sn	O/Sn
Citric acid	55.0	44.8		0.86	1.2		
Tri-ammonium citrate	51.1	46.1		0.86	1.1		
Sn-citrate precipitate	46.5	40.2	12.0	0.86	1.2	3.9	3.3

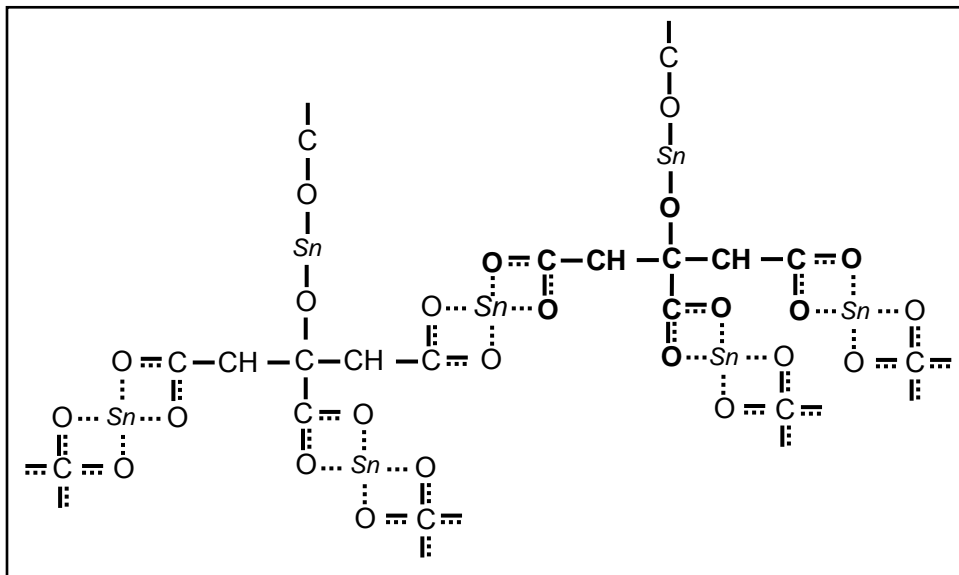


Fig. 4-13 Proposed structure of Sn(II)-citrate precipitate with a formula of Sn_2L (where L represents the tetravalent citrate ligand).

Taking into account that there are no C-O-H bonds for the O 1s spectrum for the precipitate (Fig. 4-11), the Sn_2L structure shown in Fig. 4-13 is proposed, with a C/Sn atomic ratio of 3. Each citrate molecule is combined with four stannous ions through O bonds, and connected with another four citrates. Each stannous ion is connected with two citrates through O bonds.

Thermodynamic calculations, based on the SnHL^- , SnH_2L and SnH_3L^+ stability constants proposed by Jean and Sinicki (1981), match the polarization measurements and electrodeposition experiments very well. In addition, precipitate formation from the Sn(II)-citrate solutions followed the predicted complex distribution diagrams. It is possible that the Sn(II)-citrate neutral molecule is Sn_2L and not SnH_2L based on an analysis of the XPS spectra obtained. The consumption of H^+ during precipitation is probably due to other side reactions.

4.4 Conclusions

The distribution of Sn(II)-citrate complexes presented in this chapter are useful for explaining the kinetics of Sn electrodeposition and the formation of

precipitates in the citrate solutions. The distribution of Sn(II)-citrate complexes changed with solution pH, with SnH_3L^+ as the main complex when the pH was lower than about 1.2 and SnHL^- as the main complex when the pH was higher than about 4. The distribution of Sn(II)-citrate complexes did not change as the tri-ammonium citrate concentration was changed, while the distribution of citrate species changed. The reduction potentials for the Sn(II)-citrate complexes were almost the same at a given solution composition and pH, so that reduction of all these species likely occurs simultaneously. The Sn(II)-citrate complexes were more difficult to reduce at higher tri-ammonium citrate concentrations, and were easier to reduce at lower solution pH. The SnHL^- species is favored for Sn plating due to its slower electroplating kinetics which results in smoother films. The precipitates that formed in the Sn-citrate solutions at low pH are proposed to be Sn_2L .

Chapter 5 Nucleation and film growth of Sn and Sn-Cu solders during electrodeposition¹

5.1 Introduction

Recently published studies on the electrodeposition of Sn and Sn-based alloys have mainly focused on new Sn alloying elements to achieve low melting temperatures and on the effect of the types and concentrations of additives and plating parameters. Only a few studies have focused on the initial stages of Sn and Sn-Cu alloy electrodeposition (Gomez et al., 1999; Torrent-Burgues et al., 2002; Wen and Szpunar, 2005; Correia et al., 2007). Electrodeposition can be carried out by controlling either the potential or current. In industrial coating preparations, the current step method, also known as the galvanostatic method, is mostly applied (Wen and Szpunar, 2005). The advantage of the current step method is that the thickness of the deposited films can be easily controlled according to the Faraday's Law. Wen and Szpunar (2005) studied the nucleation and growth of Sn on low carbon steel from sulfuric acid solutions with gelatin as an additive, and the current step method was used to study the potential-time behavior at different constant current densities. It was suggested that three-dimensional Sn crystallites formed preferentially on step edges initially, followed by fast coverage of neighboring sites with much smaller and densely packed crystallites about 150-180 nm in size.

The current transient technique, also known as chronoamperometry, is another technique which is commonly used to determine the nucleation mechanism. A potential step is applied from an initial potential at which the nucleation rate is negligible, to a fixed overpotential (Oskam et al., 1998). The

¹ Some of the results from this chapter have been published. Han, C., Liu, Q. and Ivey, D. G., Nucleation of Sn and Sn-Cu alloys on Pt during electrodeposition from Sn-citrate and Sn-Cu-citrate solutions, *Electrochimica Acta*, 54 (2009) 3419-3427.

formation of stable nuclei and their growth can be observed by monitoring the current. Information on the rate of nucleation, the density of nuclei and the mechanism of growth can be obtained from the shape of the resulting current-time transient plots (Oskam et al., 1998). Chronoamperometry has been used to study the nucleation mechanisms of different metals such as Sn, Cu, Ni and Co and alloys such as CdTe, CoFe and Bi₂Te₃ on different substrates (Gomez et al., 1999; Grujicic and Pesic, 2002; Torrent-Burgues et al., 2002; Grujicic and Pesic, 2006; Kelber et al., 2006; Kim and Duquette, 2006a; Richoux et al., 2007). Torrent-Burgues et al. (2002) and Gomez et al. (1999) studied the electrodeposition of Sn from sulfuric acid solutions on carbon substrates using chronoamperometric experiments and showed a linear dependence between current density and time, which they attributed to instantaneous nucleation followed by two or three-dimensional growth limited by diffusion. Whether the growth is two-dimensional or three-dimensional depends on the concentrations of the chemical species, the presence or absence of additives in solutions and the applied cathodic potential. Correia et al. (2007) studied the mechanism for Sn, Cu and Sn-Cu nucleation from pyrophosphate-based solutions using chronoamperometry with potentials varying from -0.56 to -0.64 V for Sn and Sn-Cu solutions, and from -0.30 to -0.34 V for Cu solutions. Their results suggested instantaneous nucleation (Correia et al., 2007). The Sn-Cu electrodeposition processes with a solution pH of 0.65 were classified as regular deposition, i.e., the deposit composition corresponded to the solution composition, and the Sn-Cu alloy was characterized as a solid solution (Correia et al., 2007).

Simple and “green” Sn-citrate and Sn-Cu-citrate solutions have been developed in Chapter 3. In this chapter, the initial stages (nucleation and growth) of Sn and Sn-Cu electrodeposition from citrate solutions on Pt are studied using both current step and chronoamperometric methods to obtain an understanding of Sn and Sn-Cu electrodeposition under controlled current and potential conditions. Information about the morphologies and phases of Sn-Cu films electrodeposited on Ni substrates under controlled current densities for different lengths of time

were obtained to better understand the mechanism of Sn-Cu film growth from Sn-Cu-citrate solution.

5.2 Experimental materials and procedures

The electrochemical experiments were carried out using a Gamry electrochemical system. Silicon wafers, metallized with sputter deposited TiW (25 nm) adhesion and Pt (200 nm) seed layers, were used as both the working and the counter electrodes, and a saturated calomel electrode (SCE) as the reference electrode. The electrodes were positioned vertically within the electrolyte. All the potentials reported in this chapter are against the saturated calomel electrode. Before each test, the Pt electrodes were cleaned ultrasonically for 2 minutes in acetone followed by ethanol and then rinsed with deionized water. During the galvanostatic (current step) experiments, seven constant current densities were applied between the working electrode and the counter electrode: 5, 10, 15, 25, 35, 50 and 75 mA/cm² for both the Sn-citrate and Sn-Cu-citrate solutions. Chronoamperometric experiments were performed from an initial potential at which no current flow was detected (-0.15 V for the Sn-citrate solution and -0.06 V for the Sn-Cu-citrate solution) to five constant potentials at -0.72, -0.9, -1.0, -1.1 and -1.5 V.

To study the film growth mechanism for Sn-Cu solders under controlled current, two types of substrates were used. One type was silicon wafer pieces, metallized with a 25 nm TiW adhesion layer and a 200 nm Au seed layer, which were used for electrodeposition on Au. The other type was a Ni layer (~12 μm thick) electrodeposited from a standard Watts Ni plating solution onto Au seed layers on silicon wafer pieces, which was utilized for Sn-Cu electrodeposition on Ni. Before plating, the silicon wafer pieces with the Au seed layer were cleaned ultrasonically for 2 minutes in acetone, followed by ethanol, and then rinsed with deionized water.

The chemicals used were tri-ammonium citrate ((NH₄)₃C₆H₅O₇, Alfa Aesar, 98%), SnCl₂·2H₂O (Fisher Scientific) and CuCl₂·2H₂O (Fisher Scientific).

Based on the results from Chapter 3, the Sn-citrate solution containing 0.3 mol/L tri-ammonium citrate and 0.22 mol/L SnCl_2 was used to study Sn nucleation, and the Sn-Cu solution containing 0.3 mol/L tri-ammonium citrate, 0.22 mol/L SnCl_2 and 0.003 mol/L CuCl_2 was used to study Sn-Cu nucleation and film growth. All solutions were prepared by dissolving tri-ammonium citrate in deionized water, followed by the dissolution of $\text{SnCl}_2 \cdot 2\text{H}_2\text{O}$ (Sn-citrate solution) and then $\text{CuCl}_2 \cdot 2\text{H}_2\text{O}$ dissolution (for the Sn-Cu-citrate solution only) in the citrate solution. The deionized water was obtained from an Aqua MAX™-ultra purification system.

Surface morphology was characterized by atomic force microscopy (MFP-3D, Asylum Research, Inc.) in tapping mode. The cantilever probes (OMCL-AC160TS-W2, Olympus) were made from Si with a resonant frequency between 277.3 and 314.0 kHz. Auger secondary electron images, Auger spectra and imaging analysis data were collected using a JEOL JAMP-9500F field emission Auger microprobe, operating at a primary electron beam energy of 15 keV and a probe current of about 6 nA. The sample was tilted about 30° away from the primary beam toward the axis of the electron analyzer. An auto-probe tracking system was used during imaging to eliminate drift due to instabilities in power, temperature, etc. The intensities in the image and line profile distributions were calculated from $(P-B)/B$ to remove edge effects, where P represents the peak intensity and B represents the background intensity. The images are presented on a scale where brighter areas correspond to higher intensity. A Hitachi H2700 scanning electron microscope (SEM) operating at 20 kV with a working distance of 17 mm was used to characterize the morphologies of Sn-Cu films after plated for different length of time in the study of Sn-Cu film growth mechanism. Phase analysis was performed using thin film X-ray diffraction (XRD) with a Rigaku rotating Co anode system, operating in continuous scanning mode at a voltage of 40 kV and a current of 160 mA.

5.3 Results and discussion

5.3.1 Current step (galvanostatic) method

The galvanostatic experiments were used to study the potential change with time. Fig. 5-1 shows potential-time transients on Pt for Sn-citrate solutions containing 0.22 mol/L $\text{SnCl}_2 \cdot 2\text{H}_2\text{O}$ and 0.3 mol/L $(\text{NH}_4)_3\text{C}_6\text{H}_5\text{O}_7$ at different current densities. Previous studies in Chapter 4 showed that the predominant species in this Sn-citrate solution at natural pH is SnHL^- (where L represents the tetravalent citrate ligand and citric acid can be represented as H_4L). All the curves' potentials go slightly towards the positive direction initially and then decrease. This initial increase in potential is likely due to the reduction of SnHL^- anions to Sn on the cathode surface, so that the cathode surface is depleted of the SnHL^- anions. Afterwards, a slight concentration overpotential is required to maintain the current density, so the potential drops (to a more negative direction). When the current density is low, e.g., 5, 10 and 15 mA/cm^2 , which are the average

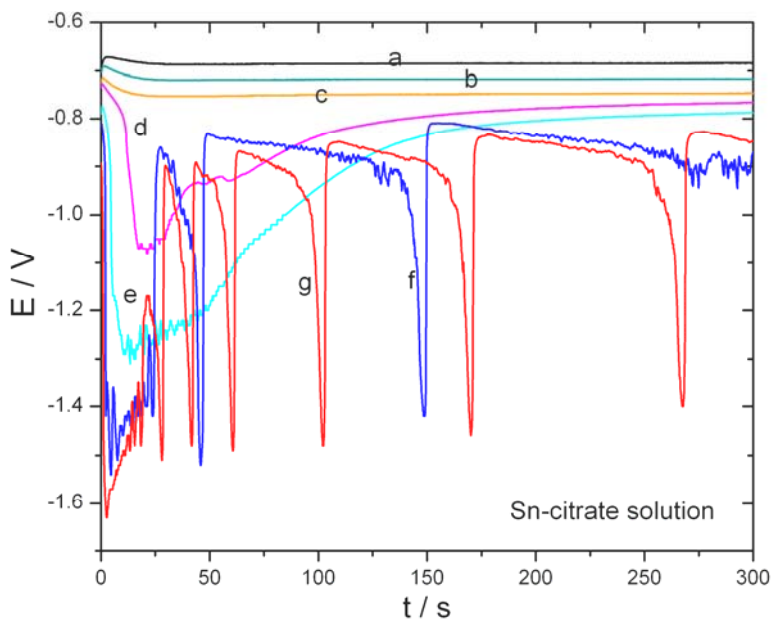


Fig. 5-1 Potential-time transients for plating from Sn-citrate solution (0.22 mol/L $\text{SnCl}_2 \cdot 2\text{H}_2\text{O}$ and 0.30 mol/L tri-ammonium citrate) on Pt at different current densities: (a) 5 mA/cm^2 ; (b) 10 mA/cm^2 ; (c) 15 mA/cm^2 ; (d) 25 mA/cm^2 ; (e) 35 mA/cm^2 ; (f) 50 mA/cm^2 ; (g) 75 mA/cm^2 .

current densities used in previous DC and PC plating work for Sn and Sn-Cu films to form dense and uniform films (Chapter 3), the potential drop is much less significant than that at high current densities (higher than 25 mA/cm²), which is because lower current densities require a smaller concentration overpotential. The potential remains almost constant afterwards. At higher current densities of 25 and 35 mA/cm², a potential drop appeared at about 11 s and 4.4 s, respectively; again likely due to concentration overpotential to maintain the current density. The higher the applied current density, the larger the overpotential required and the sooner the potential drops. The potential drops rapidly to about -1.07 V and -1.29 V at current densities of 25 and 35 mA/cm², respectively, until the diffusion of SnHL⁻ and H⁺ to the electrode surface is sufficient to maintain the applied current density and hydrogen evolution takes place. The generation of hydrogen bubbles at the electrode surface causes turbulence in the solution surrounding the growing Sn particles. This effectively results in a “mixing” action, which eliminates the depletion layer around the growing Sn particles. Therefore, Sn deposition proceeds more favorably and the potential is restored to a higher value. As deposition progresses, the potential increases due to the growth of Sn grains which increases the effective electrode surface area and, therefore, lowers the actual current density below its limiting value. Eventually the potential reaches a constant value and reactions are controlled by diffusion again.

When the current density is increased to 50 mA/cm² the potential oscillates for about 5 min during the total recording period of 10 min. (Fig. 5-1 only presents results for the first 5 min.) The frequency of the oscillation becomes progressively lower after the first drop. Such oscillations have been observed by other researchers (e.g., Wen and Szpunar, 2005). The oscillation of the potential is believed to be the result of repeated depletion and restoration of the concentration of SnHL⁻ ions (by hydrogen evolution). At an even higher current density of 75 mA/cm², the oscillation starts sooner and the frequency becomes lower over time, which is probably due to more significant hydrogen evolution at the higher current density and the increase in electrode surface area caused by faster Sn

growth. In fact, significant hydrogen evolution at current densities higher than 25 mA/cm² prevents Sn deposits from forming dense and uniform films.

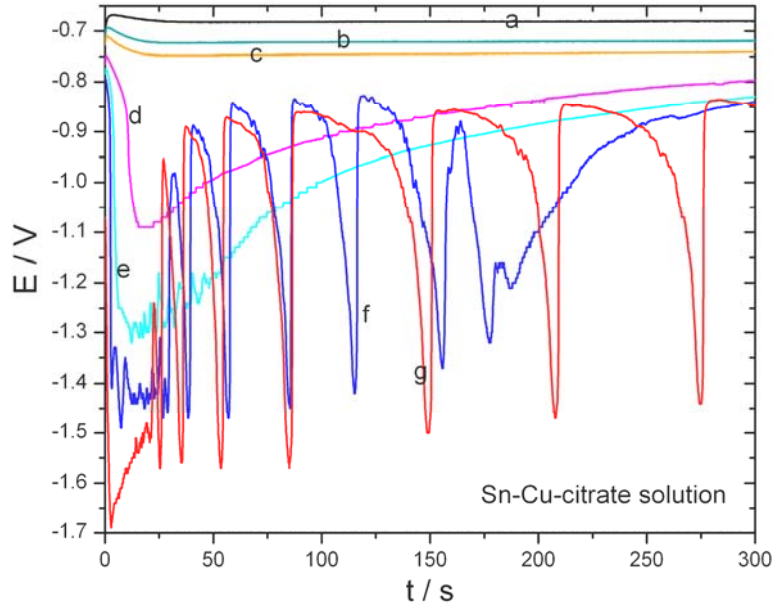


Fig. 5-2 Potential-time transients for plating from Sn-Cu-citrate solution (0.30 mol/L tri-ammonium citrate + 0.22 mol/L SnCl₂·2H₂O + 0.003 mol/L CuCl₂·2H₂O) on Pt at different current densities: (a) 5 mA/cm²; (b) 10 mA/cm²; (c) 15 mA/cm²; (d) 25 mA/cm²; (e) 35 mA/cm²; (f) 50 mA/cm²; (g) 75 mA/cm².

The same galvanostatic experiments were carried out for Sn-Cu-citrate solutions containing 0.22 mol/L SnCl₂·2H₂O, 0.003 mol/L CuCl₂·2H₂O and 0.3 mol/L (NH₄)₃C₆H₅O₇, and the results are shown in Fig. 5-2. As expected, at each applied current density the potential-time transient for Sn-Cu-citrate solution was very similar to that of the Sn-citrate solution, which is because the amount of Cu²⁺ ions added to the Sn-citrate solution is very small. There were slight differences in time and potential values at each peak for the Sn-citrate solution and Sn-Cu-citrate solution, which can be attributed to the co-deposition of Sn and Cu. It can also be seen that at the same current density, the frequency of the oscillation for the Sn-Cu-citrate solution is higher than that of the Sn-citrate solution, which means that the depletion of SnHL⁻ and Cu-citrate complex ions and their restoration by hydrogen evolution happens faster than for Sn alone. Again,

significant hydrogen evolution at current densities higher than 25 mA/cm² prevents Sn-Cu deposits from forming dense and uniform films.

The potential-time transients can be used to determine the diffusion coefficient using the Sand equation (Bard and Faulkner, 2001):

$$\frac{i\tau^{1/2}}{C_o^*} = \frac{nFAD^{1/2}\pi^{1/2}}{2} \quad (5-1)$$

where i is the applied current, τ is the transition time, C_o^* is the bulk ion concentration, n is the number of electrons consumed in the reaction, F is the Faraday's constant, A is the electrode surface area (the initial planar surface area of 0.64 cm² was used in calculation) and D is the diffusion coefficient.

The transition time is the time for the ionic concentrations at the electrode surface to drop to zero and the potential shifts rapidly toward more negative values after the application of a constant current. The transition time can be determined from potential-time transients at each known current i . When the current density is lower than 15 mA/cm², the potential drop is very small which makes it difficult to determine the transition time. Therefore only current densities higher than 15 mA/cm² were considered. The term $i\tau^{1/2} / C_o^*$ on the left hand side of Equation 5-1 is also known as the transition time constant and, for a well-behaved system, it is independent of i or C_o^* (Bard and Faulkner, 2001). The measured transition time, calculated transition time constant and diffusion coefficient are listed in Table 5-1. For both Sn-citrate and Sn-Cu-citrate solutions, the calculated transition time constant remains almost constant as expected for a mass-transfer controlled process. The diffusion coefficient calculated from Equation 5-1, for both the Sn-citrate solution and the Sn-Cu-citrate solution, was in the range of 3.7×10^{-6} to 4.8×10^{-6} cm²/s when the applied current density was between 25 and 75 mA/cm². These values are very close to that reported by Wen and Szpunar (2005) for a tin sulfate electrolyte with gelatin (3.9×10^{-6} cm²/s). For both the Sn-citrate solution and the Sn-Cu-citrate solution, the calculated diffusion coefficient at 25 mA/cm² is higher than at the other three current densities. This may be because the potential drop at 25 mA/cm² is not as sharp as

for the other three current densities, which results in uncertainties to the measured transition time. Excluding the result at 25 mA/cm², the average diffusion coefficient is about 3.8×10⁻⁶ cm²/s for Sn-citrate solution and 4.1×10⁻⁶ cm²/s for Sn-Cu-citrate solution.

Table 5-1 Calculated diffusion coefficients for reduction of ionic species from Sn-citrate and Sn-Cu-citrate solutions on Pt (calculated from Equation 5-1)

	$j / \text{mA cm}^{-2}$	τ / s	$i \times \tau^{1/2} \times C^{-1} / (\text{mA s}^{1/2} (\text{mM})^{-1})$	$D / \text{cm}^2 \text{s}^{-1}$
Sn-citrate solution	25	11	0.21	4.8×10 ⁻⁶
	35	4.4	0.21	3.8×10 ⁻⁶
	50	2.1	0.21	3.7×10 ⁻⁶
	75	1	0.22	4.0×10 ⁻⁶
Sn-Cu-citrate solution	25	10.9	0.24	4.7×10 ⁻⁶
	35	4.8	0.22	4.0×10 ⁻⁶
	50	2.5	0.23	4.3×10 ⁻⁶
	75	1.1	0.23	4.2×10 ⁻⁶

5.3.2 Chronoamperometry and nucleation modeling

In order to study the nucleation mechanism during the early stages of electrodeposition of Sn and Sn-0.7wt%Cu alloys and to determine the kinetic parameters, chronoamperometric experiments were carried out to obtain transient currents (Sahari et al., 2006). Fig. 5-3 shows a series of current-time transients for Sn electrodeposition with potentials ranging from -0.72 to -1.5 V. All the transient plots show an initial increase in cathodic current density followed by a gradual decrease over time. During each test, an initial potential at which no current flow was detected was applied followed by constant potentials at -0.72, -0.9, -1.0, -1.1 and -1.5 V. When the second potential is applied as a step perturbation, the reduction reactions on the electrode occur instantly, resulting in a high current density. These reduction reactions consume the reducing ionic species at the surface of the electrode and create a depletion zone where the concentrations of the ionic species are low at the electrode surface, but are progressively higher away from the surface (i.e., a concentration gradient). The diminishing

concentrations of the reducing ionic species in the depletion zone cause the current density to drop continuously. When diffusion of the reducing ionic species from the bulk solution to the depletion zone is just sufficient to permit continuous reduction, the current density will reach a constant value, as shown in Fig. 5-3. A constant current density indicates a diffusion-controlled process. It should be noted that Fig. 5-3 only shows electrodeposition up to 1.5s.

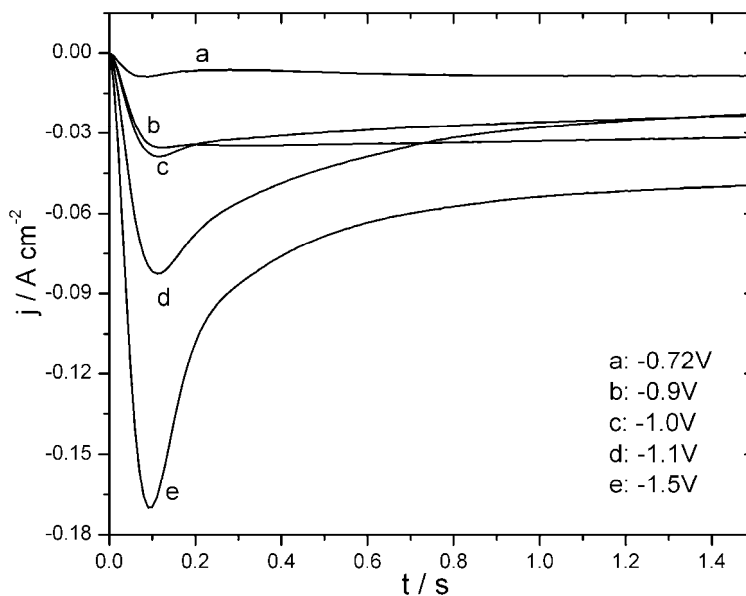


Fig. 5-3 Current-time transient curves for Sn electrodeposition on Pt at potentials ranging between -0.72 and -1.5 V.

Scharifker and Hills (1983) developed a theoretical model to analyze the current-time transient results of chronoamperometric experiments. In their models (Scharifker and Hills, 1983; Oskam et al., 1998), two limiting nucleation mechanisms, i.e., instantaneous nucleation and progressive nucleation, were considered. Instantaneous nucleation corresponds to immediate activation of all nucleation sites, so that the rate of further nuclei formation is negligible and nuclei growth is slow in the time frame of the experiments. For progressive nucleation, the rate of new nuclei formation is not negligible and the growth of nuclei is fast, which will produce different sizes of nuclei during nucleation.

The models for instantaneous and progressive nucleation, followed by three-dimensional diffusion-limited growth, are given by Equations 5-2 and 5-3 respectively (Scharifker and Hills, 1983; Oskam et al., 1998):

$$\frac{j^2}{j_{max}^2} = 1.9542 \left(\frac{t_{max}}{t} \right) \left[1 - \exp \left(-1.2564 \frac{t}{t_{max}} \right) \right]^2 \quad (5-2)$$

$$\frac{j^2}{j_{max}^2} = 1.2254 \left(\frac{t_{max}}{t} \right) \left[1 - \exp \left(-2.3367 \frac{t^2}{t_{max}^2} \right) \right]^2 \quad (5-3)$$

where j_{max} and t_{max} are the current and time coordinates of the current-time transient curve peak, respectively.

By representing the experimental chronoamperometric data in a non-dimensional plot $(j/j_{max})^2$ versus t/t_{max} and comparing these with the theoretical plots resulting from the above equations, instantaneous and progressive nucleation processes can be distinguished when the experimental current transient curve approaches either of the theoretical plots. In the following diagrams, the theoretical instantaneous and progressive nucleation processes will be represented by thick and thin solid lines, respectively.

Fig. 5-4 shows theoretical plots and experimental curves for Sn nucleation on Pt at potentials of -0.72, -1.1 and -1.5 V. It can be seen that at a potential of -1.1 V, the experimental curve matches the theoretical progressive nucleation plot very well, which suggests that the nucleation process for Sn on Pt surfaces at -1.1 V is progressive with diffusion controlled growth according to Fig. 5-3. On the other hand, the data for the experimental curves at potentials of -0.72 V and -1.5 V match the progressive nucleation mechanism up to about $t/t_{max} = 1.5$ with subsequent deviation. This type of deviation was also observed by others (Grujicic and Pesic, 2002; Grujicic and Pesic, 2006; Kim and Duquette, 2006; Richoux et al., 2007) who attributed the deviation to the reduction of hydrogen ions and hydrogen gas evolution. Our results indicate that the deviation occurred for both the low (-1.5 V) and high (-0.72 V) potentials, whereas no deviation was observed at the intermediate potential (-1.1 V). Clearly, hydrogen gas evolution

could not be the only mechanism. However, at this point an adequate explanation for the deviation at both low and high potentials is not available.

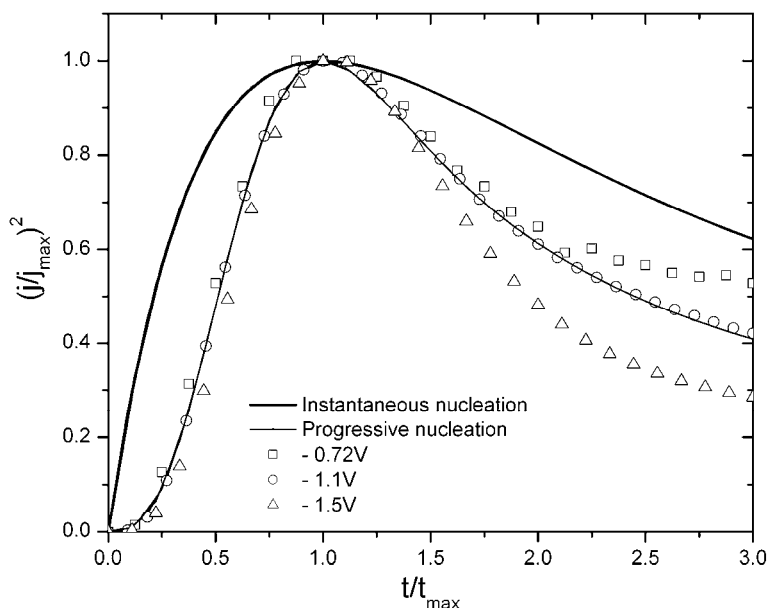


Fig. 5-4 Normalised $(j/j_{max})^2$ vs. t/t_{max} plots obtained from current-time transient curves in Fig. 3 at -0.72, -1.1 and -1.5 V. The thick and thin solid lines represent the theoretical models for instantaneous and progressive nucleation, respectively.

The same chronoamperometric experiments were applied to Sn-Cu alloy electrodeposition and the current-time transients plots are shown in Fig. 5-5. All the transient curves showed the same shape at each potential and followed the same potential trend as those for Sn electrodeposition (Fig. 5-3). At each potential, the peak current density during Sn-Cu electrodeposition is slightly higher than that of Sn electrodeposition. Theoretical plots and experimental curves for Sn-Cu nucleation at potentials of -0.72, -1.1 and -1.5 V are shown in Fig. 5-6. Very similar to Sn nucleation in Fig. 5-4, the experimental curve matches the theoretical progressive nucleation plot at a potential of -1.1 V, suggesting progressive nucleation of Sn-Cu on Pt at -1.1 V. Again, the experimental curves at both potentials of -0.72 V and -1.5 V match the progressive nucleation mechanism up to about $t/t_{max} = 1.3$ with deviation after that value.

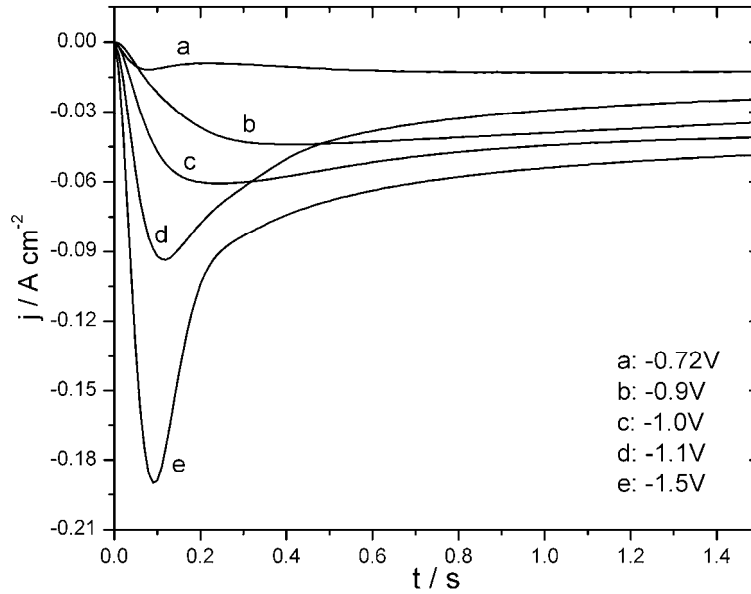


Fig. 5-5 Current-time transient curves for Sn-Cu alloy electrodeposition on Pt at potentials ranging between -0.72 and -1.5 V.

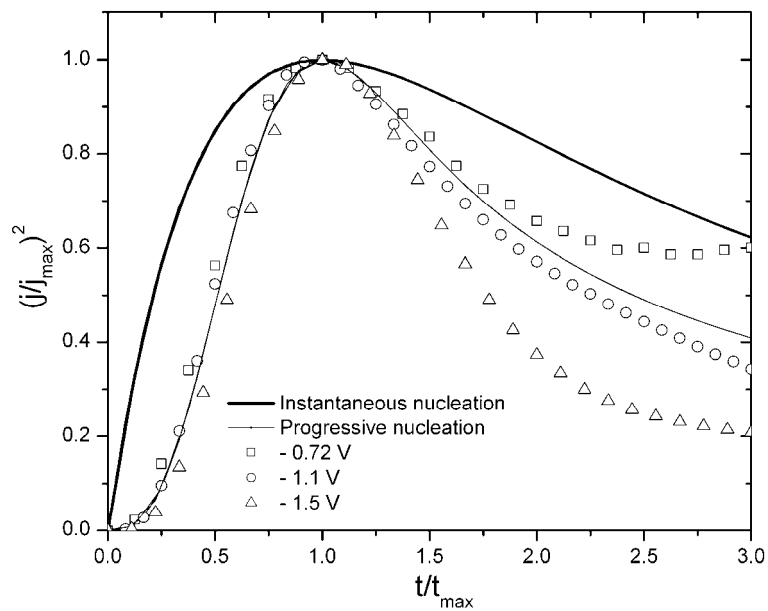


Fig. 5-6 Normalised $(j/j_{max})^2$ vs. t/t_{max} plots obtained from current-time transient curves in Fig. 5 at -0.72, -1.1 and -1.5 V. The thick and thin solid lines represent the theoretical models for instantaneous and progressive nucleation, respectively.

Verification of the nucleation and growth mechanisms can be obtained through determination of the diffusion coefficient and comparison with known

values. The diffusion coefficient for the metal-citrate complex ions, D , can be calculated from the product $j_{\max}^2 t_{\max}$ (Scharifker and Hills, 1983; Oskam et al., 1998; Richoux et al., 2007).

For instantaneous nucleation,

$$D = \frac{j_{\max}^2 t_{\max}}{0.1629(zFc)^2} \quad (5-4)$$

For progressive nucleation,

$$D = \frac{j_{\max}^2 t_{\max}}{0.2598(zFc)^2} \quad (5-5)$$

Since both the above modeling analysis and AFM analysis (presented in the next section) show progressive nucleation for both Sn and Sn-Cu on Pt, only progressive nucleation calculations were carried out using Equation 5-5. The results are shown in Table 5-2. When the applied potential is -0.72 V, the calculated diffusion coefficients are 1.3×10^{-8} and 2.3×10^{-8} cm²/s for the Sn-citrate solution and Sn-Cu-citrate solution, respectively. When the applied potential is more negative than -1.1 V, the diffusion coefficient is in the range of 1.6×10^{-6} to 6.9×10^{-6} cm²/s, which is more in line with the results calculated from the Sand equation. The diffusion coefficients are 1.6×10^{-6} and 5.6×10^{-6} cm²/s at -1.1 and -1.5 V for the Sn-citrate solution and 2.2×10^{-6} and 6.9×10^{-6} cm²/s for Sn-Cu-citrate solution.

Table 5-2 Diffusion coefficients for reduction of ionic species in Sn-citrate and Sn-Cu-citrate solutions on Pt (calculated from Equation 5-5).

Solution	E / V	$j_{\max} / \text{Acm}^{-2}$	t_{\max} / s	$D / \text{cm}^2\text{s}^{-1}$
Sn-citrate solution	-0.72	-0.009	0.08	1.3×10^{-8}
	-1.1	-0.082	0.11	1.6×10^{-6}
	-1.5	-0.17	0.09	5.6×10^{-6}
Sn-Cu-citrate solution	-0.72	-0.012	0.08	2.3×10^{-8}
	-1.1	-0.093	0.12	2.2×10^{-6}
	-1.5	-0.19	0.09	6.9×10^{-6}

5.3.3 Microstructure characterization of Sn and Sn-Cu nucleation

To verify the nucleation mechanisms obtained from the above theoretical models, the morphologies of the above Sn and Sn-Cu nuclei after plating at -0.72, -1.1 and -1.5 V for 0.2 s under potentiostatic conditions were characterized using the Auger microprobe initially, and the corresponding SE images are shown in Fig. 5-7 (Sn deposits) and Fig. 5-8 (Sn-Cu deposits). Considering that the time used for electrodeposition was very short, both the Sn and Sn-Cu deposits would be very thin. An SE image of the Pt seed layer was also taken for comparison. After plating at -0.72 V for 0.2 s, Sn nuclei were difficult to identify as the image (Fig. 5-7b) was very similar to that for the Pt seed layer (Fig. 5-7a). The Sn-Cu nuclei (Fig. 5-8b) became smoother with finer grain sizes compared with the Pt seed layer (Fig. 5-8a). As the applied potential became more negative, both Sn and Sn-Cu nuclei grew into larger particles. To obtain more details about individual grains, especially for deposits plated at -1.1 V and -1.5 V, AFM

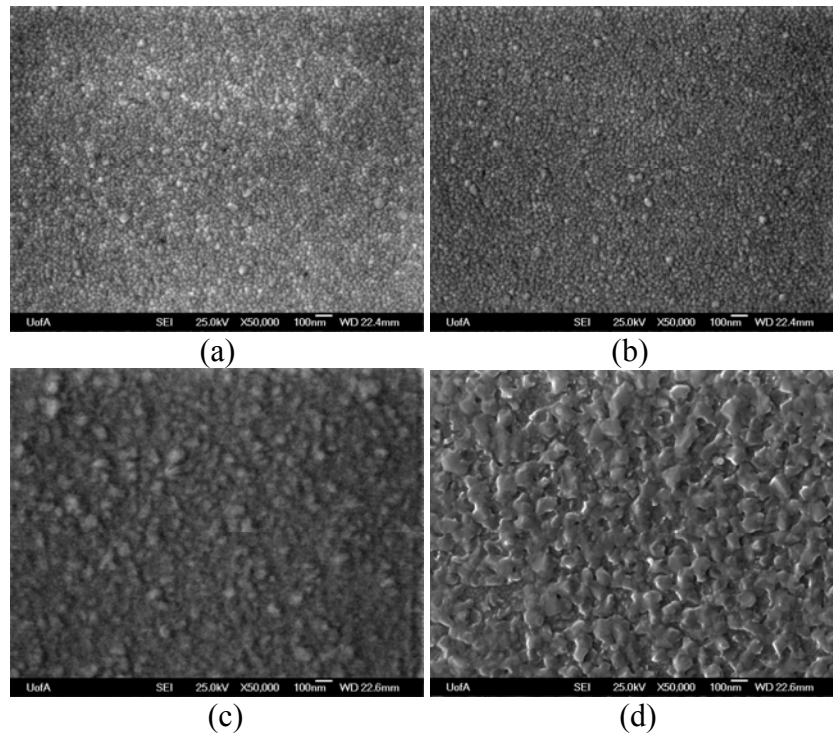


Fig. 5-7 Auger SE images for (a) Pt seed layer and Sn deposited under potentiostatic conditions of (b) -0.72 V, (c) -1.1 V and (d) -1.5 V for 0.2 seconds.

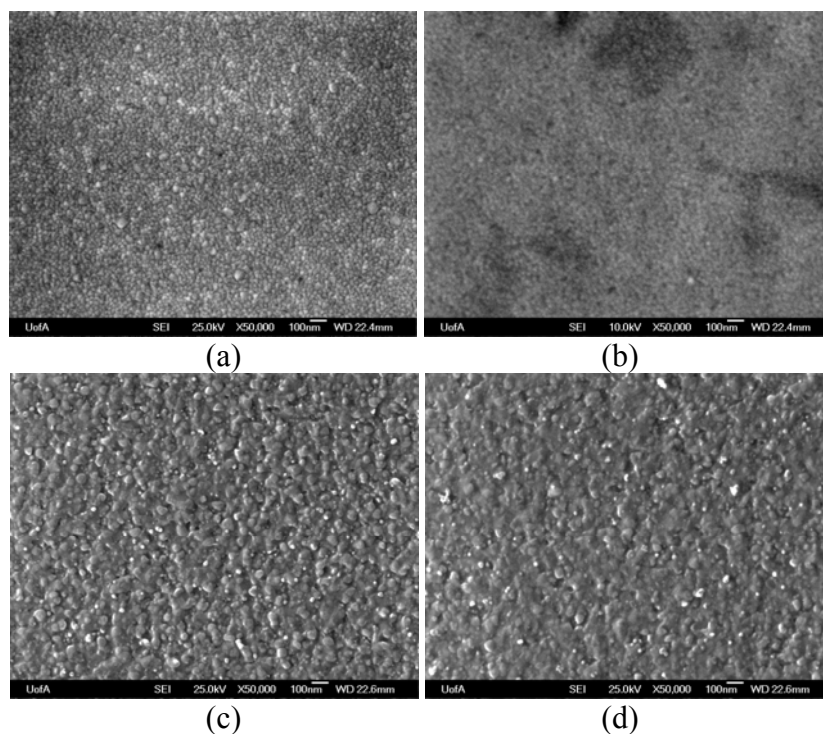


Fig. 5-8 Auger SE images for (a) Pt seed layer and Sn-Cu deposited under potentiostatic conditions of (b) -0.72 V, (c) -1.1 V and (d) -1.5 V for 0.2 seconds.

analyses were carried out for the above Sn (Fig. 5-7) and Sn-Cu (Fig. 5-8) deposits. Fig. 5-9 shows AFM images for the Pt seed layer and the Sn nuclei from an area of $1 \mu\text{m} \times 1 \mu\text{m}$. The large white particles in Fig. 5-9b are probably contaminants from the air. Comparing Fig. 5-9a and Fig. 5-9b, the surface morphologies for Pt and Sn electrodeposited at -0.72 V for 0.2 s appear to be similar. It is possible that the grain structure visible in Fig. 5-9b is still Pt and that no Sn has been deposited. However, Auger analysis (with a depth resolution of 3-5 nm) clearly shows the presence of Sn (Fig. 5-10a), perhaps suggesting that a thin, discontinuous layer of Sn has formed on the surface. XRD analysis (presented later in Fig. 5-13) for the same conditions shows very strong Pt peaks, which indicates that the amount of Sn deposited is very small. To separate Sn nuclei from the Pt seed layer and to identify their distribution, Auger imaging was carried out for both Sn and Pt for the same sample in Fig. 5-9b at areas inside the square as marked in Fig. 5-10b. The results are shown in Fig. 5-10c and d.

Element-rich areas are displayed in red and yellow colors. Comparison of Fig. 5-10c with Fig. 5-10d shows that Sn nuclei are evenly distributed above Pt (Fig. 5-9b). As the potential is increased, the Sn grain size increases. At a potential of -1.1 V, as shown in Fig. 5-9c, Sn grains have sizes ranging from about 40-80 nm, which indicates a progressive nucleation mechanism. At a potential of -1.5 V (Fig. 5-9d), Sn grains have sizes of about 80-100 nm and form Sn clusters with sizes of about 80-300 nm, which suggests a progressive nucleation mechanism as well.

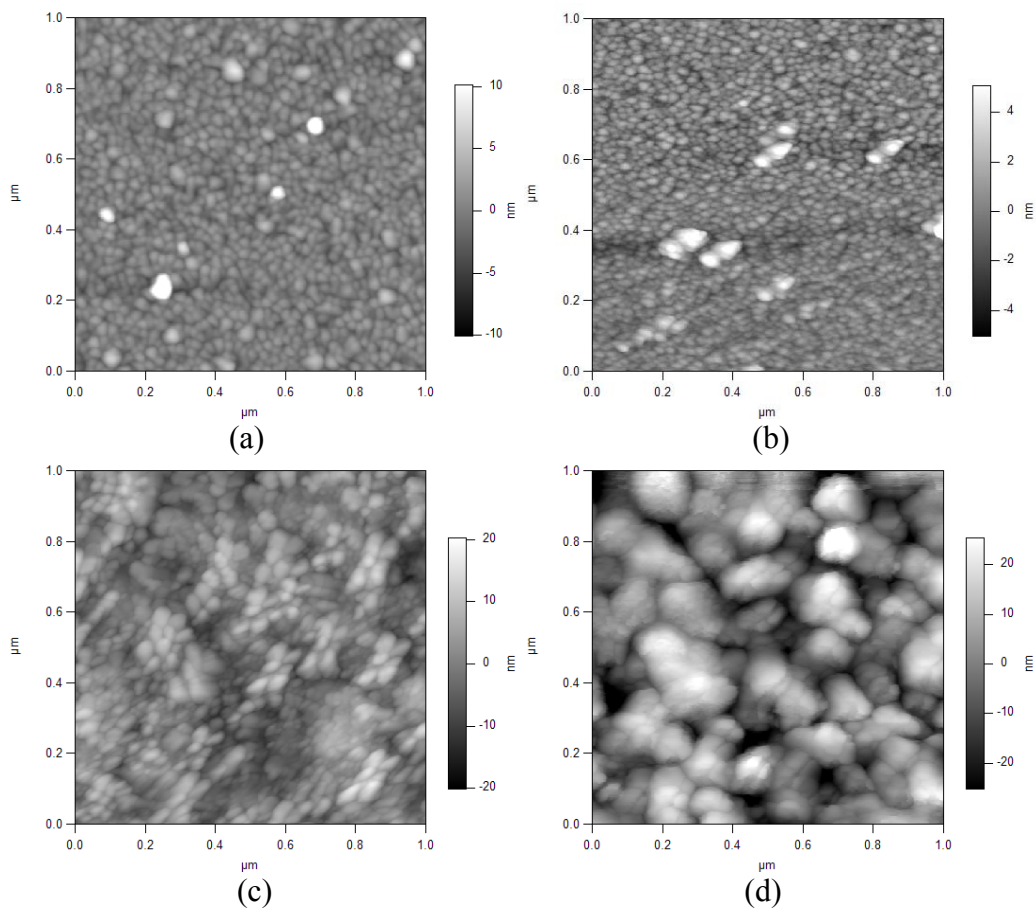


Fig. 5-9 AFM images for (a) Pt seed layer and Sn deposited under potentiostatic conditions of (b) -0.72 V, (c) -1.1 V and (d) -1.5 V for 0.2 seconds.

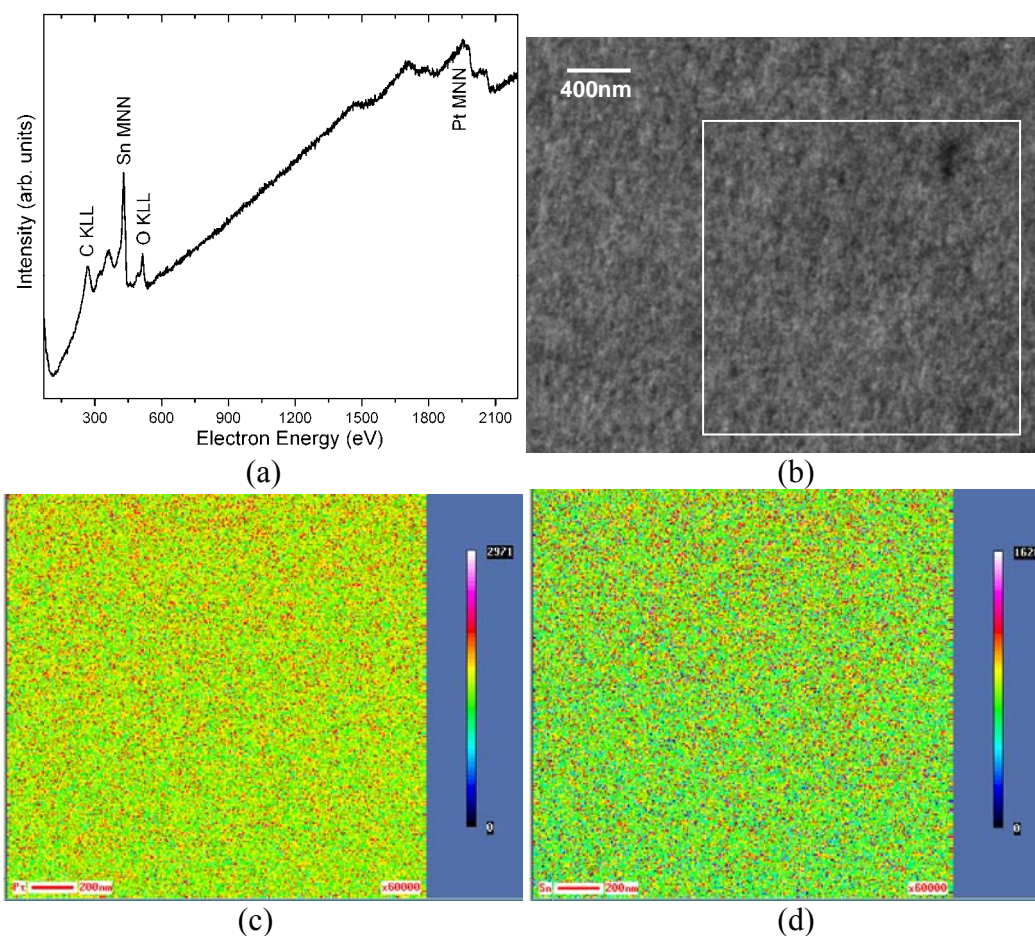


Fig. 5-10 (a) Auger spectra for Sn deposit on Pt at an applied potential of -0.72 V for 0.2 seconds. (b) Auger SE image for Sn nuclei deposited on Pt under potentiostatic conditions at -0.72 V for 0.2 seconds; the area in the square is the tested area for the imaging analysis. (c) Pt and (d) Sn Auger imaging analysis for Sn nuclei deposited on Pt under potentiostatic conditions at -0.72 V for 0.2 seconds.

The same AFM analysis was done for Sn-Cu deposits and the results are shown in Fig. 5-11, with Fig. 5-11a for the Pt seed layer and Fig. 5-11b-d for Sn-Cu deposits at potentials of -0.72 V, -1.1 V and -1.5 V, respectively. At a potential of -0.72 V (Fig. 5-11b), the morphology and grain size of the Sn-Cu deposits appear to be similar to those of Pt, likely for the same reasons given in the previous paragraph for Sn deposition. Auger analysis was carried to verify the presence of Sn and Cu, and the results are shown in Fig. 5-12a. Both Sn and Cu peaks were detected. To find out how Sn and Cu are distributed on Pt, Auger imaging was carried out at areas inside the square as marked in Fig. 5-12b and the

results are shown in Fig. 5-12 c-e. Both Sn and Cu are evenly distributed above Pt. It can be concluded that a thin, discontinuous Sn-Cu layer initially forms on the Pt. It is difficult to identify individual Sn-Cu nuclei from the Pt grains and, therefore, impossible to determine the individual grain sizes for Sn-Cu deposits. As the potential is increased to -1.1 V (Fig. 5-11c), the grain size becomes larger, ranging from 40 nm to 80 nm. The differences in size indicate a progressive nucleation mechanism as shown before. When the potential is -1.5 V (Fig. 5-11d), large grains with sizes of about 100 nm can be seen. In addition, nuclei as small as 30 nm continue to form, which suggests progressive nucleation.

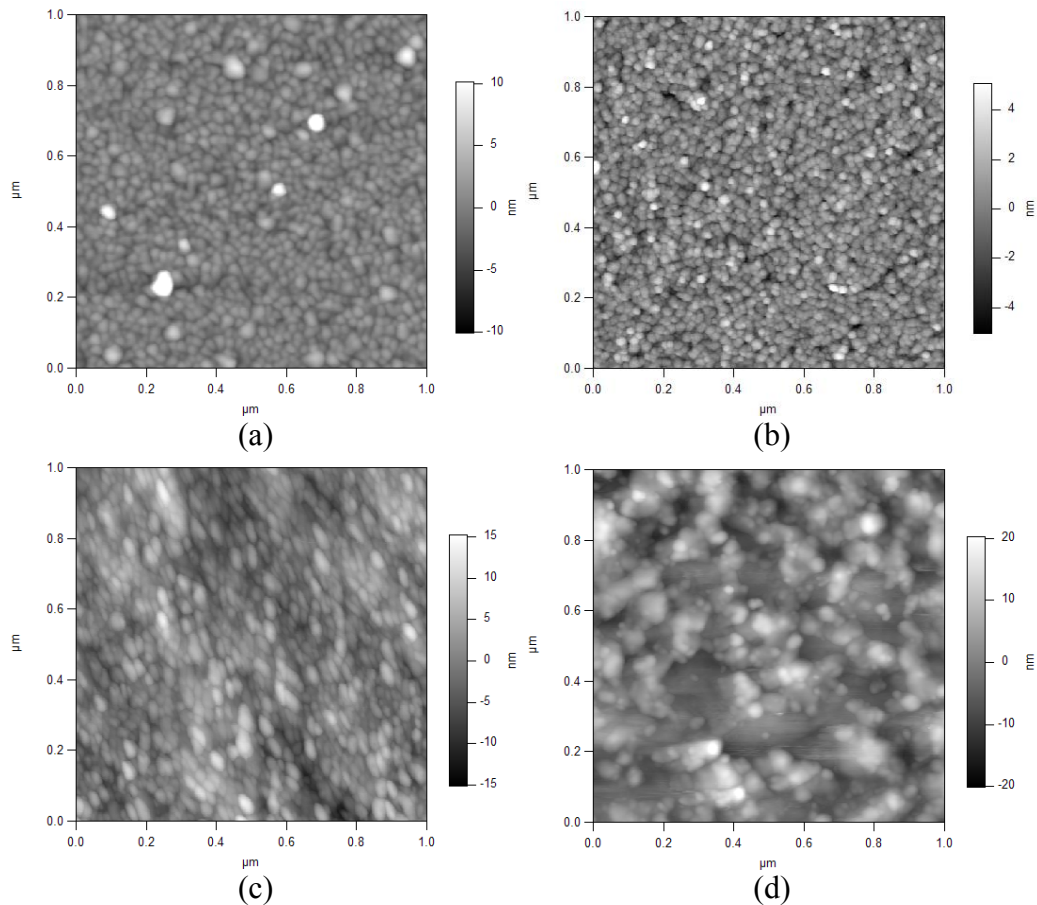


Fig. 5-11 AFM images for (a) Pt and Sn-Cu alloys deposited under potentiostatic conditions of (b) -0.72 V, (c) -1.1 V and (d) -1.5 V for 0.2 seconds.

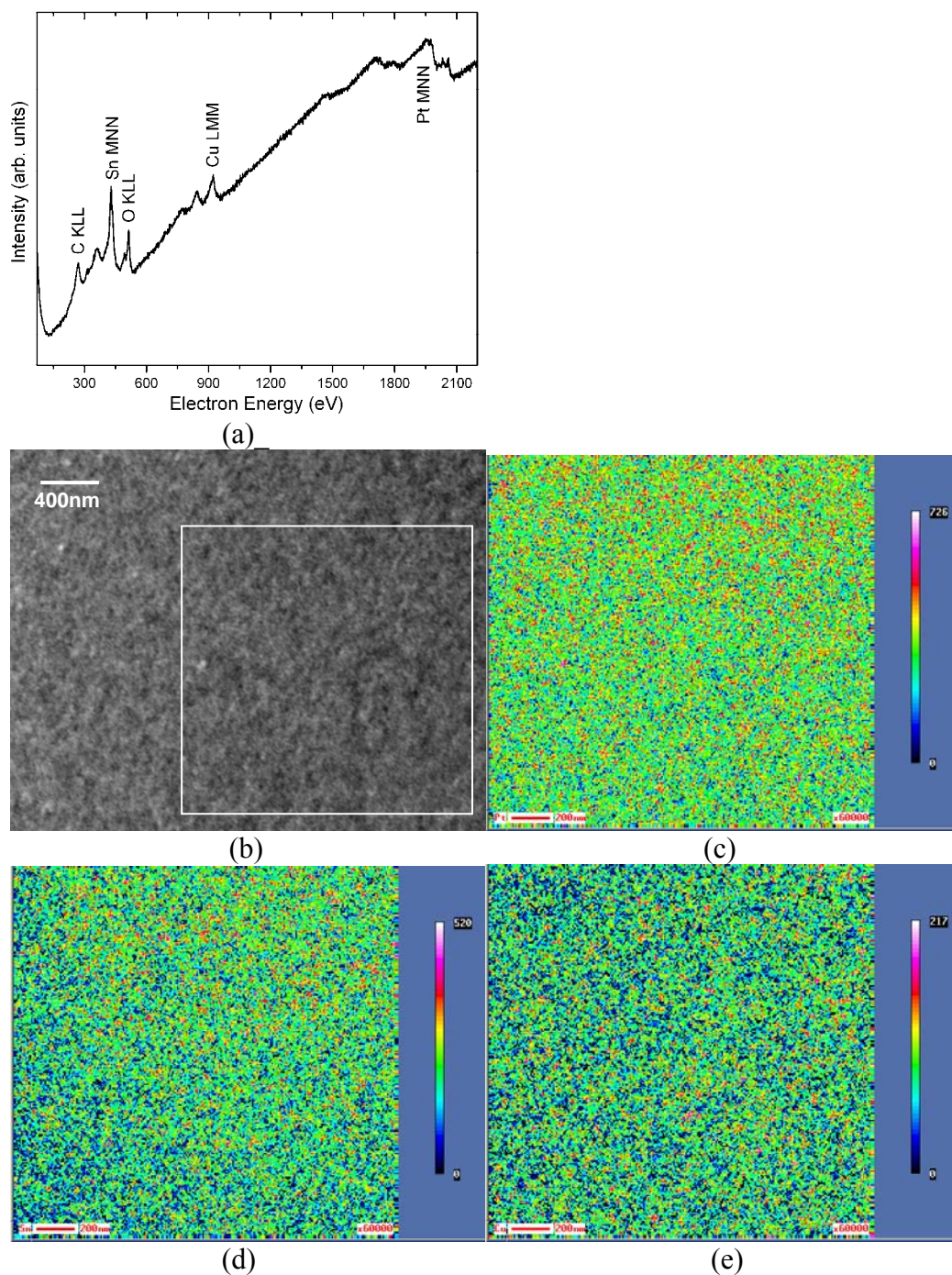


Fig. 5-12 (a) Auger spectra for Sn-Cu deposit on Pt at an applied potential of -0.72 V for 0.2 seconds. (b) Auger SE image for Sn-Cu nuclei deposited on Pt under potentiostatic conditions at -0.72 V for 0.2 seconds; the area in the square is the tested area for the imaging analysis. (c) Pt, (d) Sn and (e) Cu Auger imaging analysis for Sn-Cu alloys deposited on Pt under potentiostatic conditions at -0.72 V for 0.2 seconds.

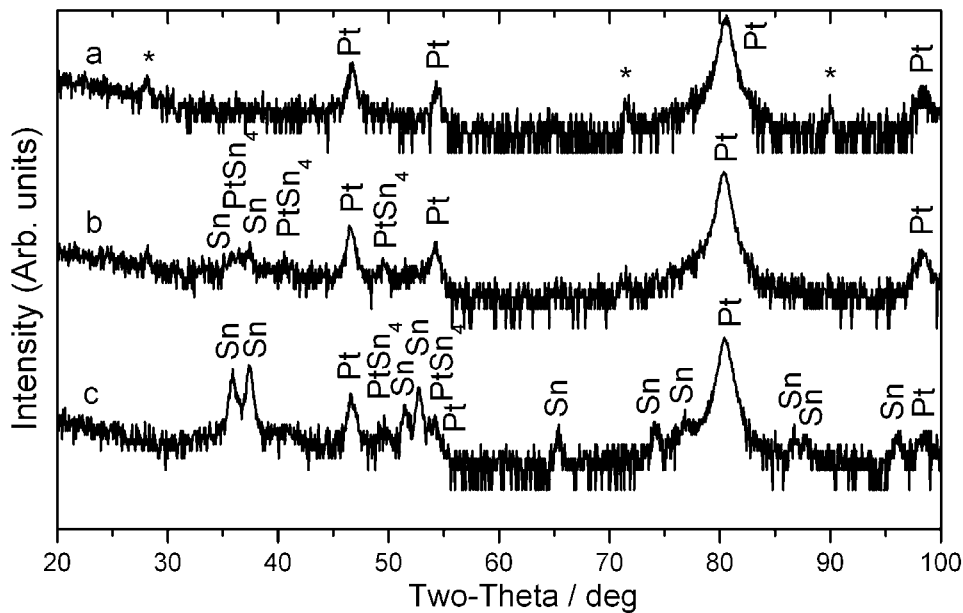


Fig. 5-13 XRD patterns of Sn electrodeposited on Pt at different potentials: (a) - 0.72 V, (b) -1.1 V, (c) -1.5 V plated for 0.2 seconds.

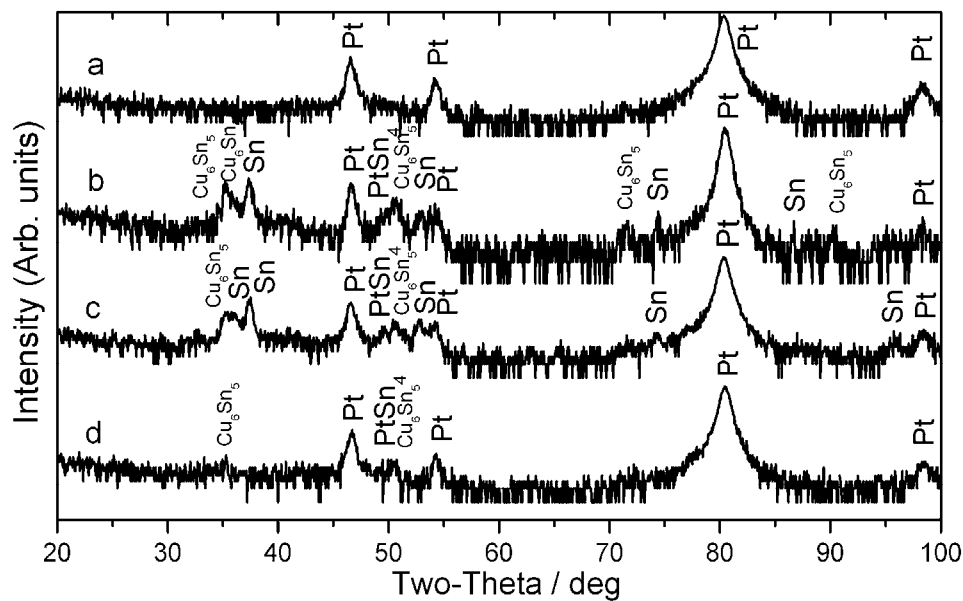


Fig. 5-14 XRD patterns of Sn-Cu alloys electrodeposited on Pt at different potentials: (a) -0.72 V, (b) -1.1 V, (c) -1.5 V plated for 0.2 seconds; (d) -0.72 V plated for 0.8 seconds.

To identify the phases formed in the initial stages of Sn and Sn-Cu electrodeposition, thin film X-ray diffraction was used and the results are shown

in Fig. 5-13 and Fig. 5-14. Since the plating time is only 0.2 s, the deposited layer is very thin and the signal from the Pt seed layer is very strong. Therefore, in both figures, the vertical axis is plotted on a log scale in order to better show the intensity of the weak peaks. As shown in Fig. 5-13a, at a potential of -0.72 V, Pt peaks were detected as well as three other weak peaks (marked with asterisks), which could not be indexed. They could be from a metastable Sn or Sn-Pt phase, which is not available in the database. At a potential of -1.1 V, Sn and PtSn₄ phases were detected in addition to Pt. At a potential of -1.5 V, both Sn and PtSn₄ were detected with Sn being more prevalent. During Sn nucleation, some Sn reacted with Pt to form PtSn₄. With a more negative applied potential, more Sn is deposited. During Sn-Cu nucleation, at a potential of -0.72 V, no Sn or Cu was detected by XRD, but both were detected by Auger analysis as shown in Fig. 5-10a. After plating for 0.8 s at the same potential, Cu₆Sn₅ and PtSn₄ were detected. At a potential of -1.1 V, besides Pt, Cu₆Sn₅ and PtSn₄, Sn was also detected. At a potential of -1.5 V, the same phases were detected with additional Sn relative to the other phases. Therefore, during Sn-Cu nucleation, Sn reacts with the Pt seed layer to form PtSn₄ and co-deposits with Cu to form Cu₆Sn₅. As the potential becomes more negative, Sn formation dominates. Auger quantitative analysis for the above Sn-Cu deposits show that Cu contents in the deposits are higher than the Cu composition in Sn-Cu-citrate solution. This is because Cu-citrate complexes are more noble than SnHL⁻ ions in citrate solutions, so that Cu reduction dominates initially, giving a higher Cu composition in the initial deposits.

5.3.4 Sn-Cu film growth mechanism

The Sn-Cu film growth mechanism was studied by electroplating Sn-Cu films for different lengths of time (from 1 s to 1800 s) at a current density of 10 mA/cm² and the corresponding SEM SE plain view images and some cross section images are shown in Fig. 5-15. Comparison of the plan view images shows that after plating for 1 s, fine isolated nuclei formed. XRD analysis (Fig. 5-16) for the same sample identified that these nuclei were Cu₆Sn₅ compounds.

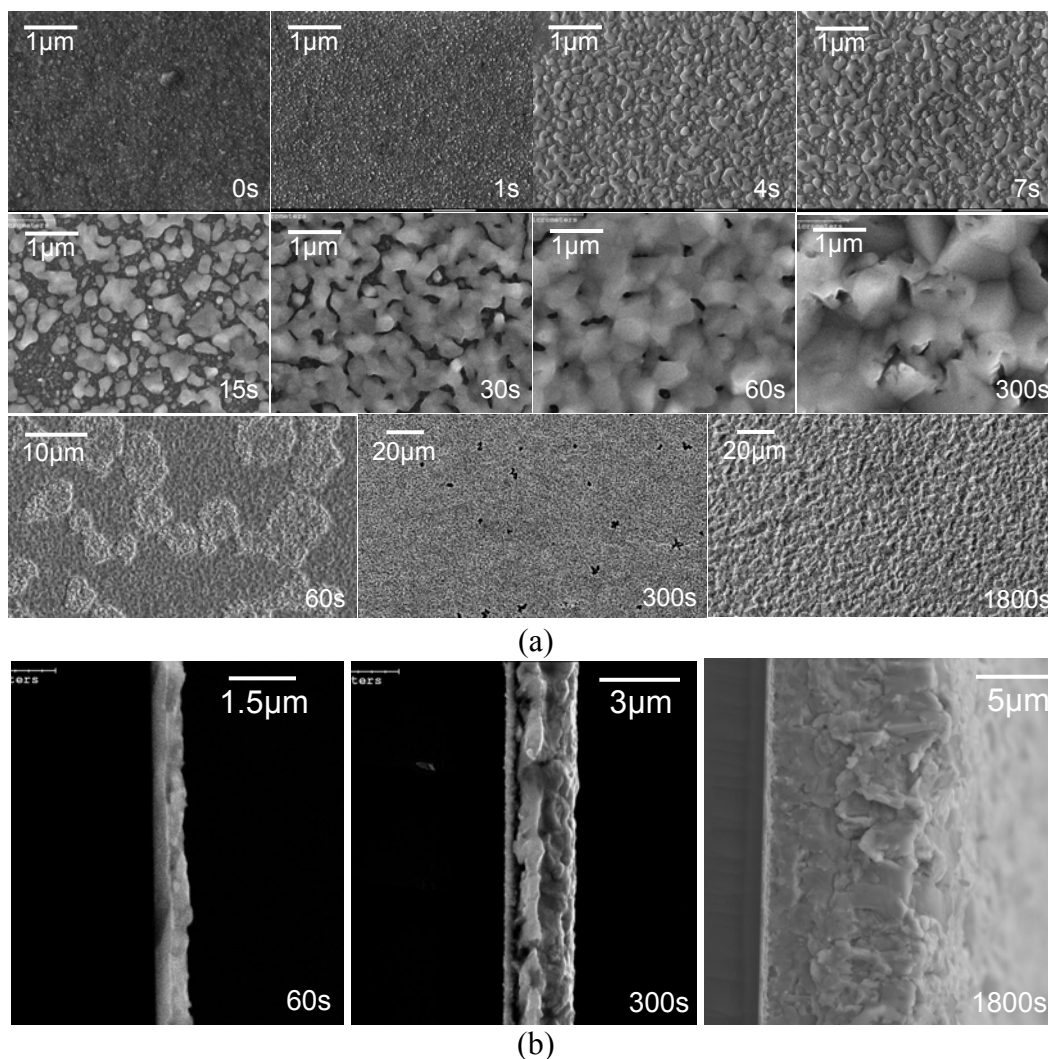


Fig. 5-15 SEM SE plan view (a) and cross section (b) images of Sn-Cu electrodeposited on Ni or Au seed layer for different lengths of time in solution containing 0.22 mol/L $\text{SnCl}_2 \cdot 2\text{H}_2\text{O}$, 0.003 mol/L $\text{CuCl}_2 \cdot 2\text{H}_2\text{O}$ and 0.30 mol/L tri-ammonium citrate. The current density is 10 mA/cm^2 .

After plating for 4 s, some fine isolated nuclei grew into 3D crystallites. As the plating continued, some of the 3D crystallites coalesced into elongated crystallites with continuous growth in the thickness direction, as can be seen from the images for deposits plated for 7 and 15 s. After plating for 30 s, a linked network structure formed. After plating for up to 300 s, a continuous deposit formed containing holes and channels. By filling these holes and channels, a continuous

and hole-free film was obtained after plating for 1800 s. It is worth noting that after plating for 300 s, EDX analysis of the hole regions (Fig. 5-15a) indicated that Ni was the main constituent (coming from the Ni substrate) with small amounts of Sn, which may be from the surrounding Sn-Cu film. Cross section images in Fig. 5-15b show that after plating for 60 s, the thickness of the as-deposited Sn-Cu film is about 0.3 μm . After plating for 300 s, the thickness is about 2 μm and after 1800 s, the thickness is about 10 μm . The Sn-Cu films continuously grew in the thickness direction, even before the holes (exposed substrate) were filled (plating for up to 300 s). There are three different thin film growth mechanisms (Ohring, 1992), as shown in Fig. 5-17. Based on the above description of the Sn-Cu film growing process, as well as analysis of thickness growth for the cross section samples, it can be concluded that part of the Ni substrate was not covered (exposed as holes) even when the Sn-Cu deposits grew to a certain thickness (2 μm after 300 s). Continued deposition filled the holes, eventually forming continuous Sn-Cu films, which matches the island (Volmer-Weber) growth mechanism.

To further understand the co-deposition of Sn and Cu during the initial stage of Sn-Cu electrodeposition under controlled current, Auger point analysis was carried out for Sn-Cu deposits plated on Ni substrate for 1s, 4s and 7s and the results are shown in Fig. 5-18. The positions where Auger point analysis was performed for each sample are marked by red numbers as shown in the Auger SE images (left) and the corresponding spectra are shown on right. It can be noticed that Sn, Cu and Ni were detected for all the positions tested in all three samples. Quantification analysis of the elements detected in each spectrum in all three samples shows that Cu content decreased as the detected particle size increased. Copper content in Sn-Cu deposits after plating for 1 s was estimated to be about 19-23 wt%, about 4 wt % after plating for 4 s and about 2 wt% after plating for 7 s. Copper reduction dominated initially, since Cu ions are more noble than Sn ions in citrate solutions, which gave a high Cu content at the beginning. Since the Cu concentration in the solution was only 0.003 mol/L, which is almost two orders of magnitude lower than the Sn concentration, Cu ions are depleted quickly

at the cathode surface and Sn reduction dominates afterwards. Therefore, as plating continued, more Sn was reduced, which caused grain growth, with a decrease in Cu content.

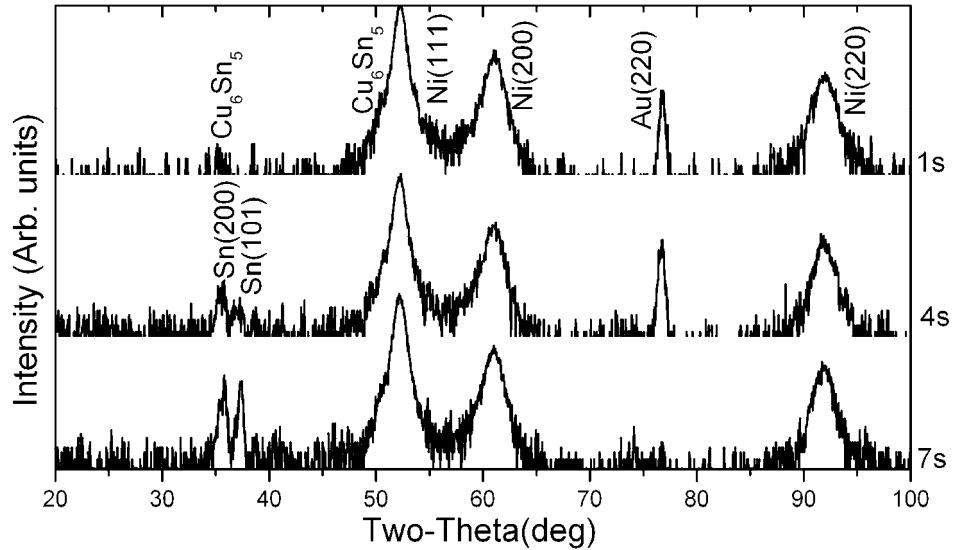


Fig. 5-16 XRD patterns for Sn-Cu electrodeposited onto Ni substrate for 1 s, 4 s and 7 s.

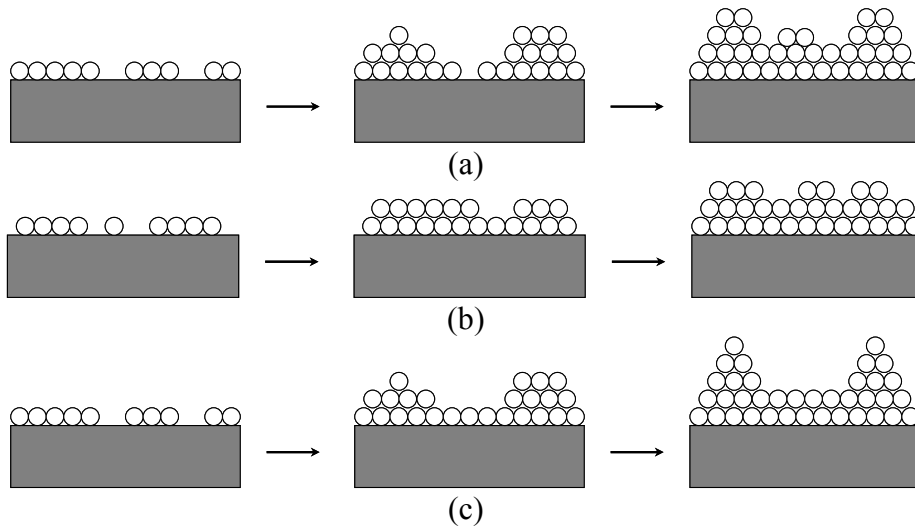


Fig. 5-17 Schematic illustration of three different film growth mechanisms (Ohring, 1992): (a) island (Volmer-Weber) growth mechanism, (b) layer growth (Frank-van der Merwe) mechanism and (c) mixed growth mechanism.

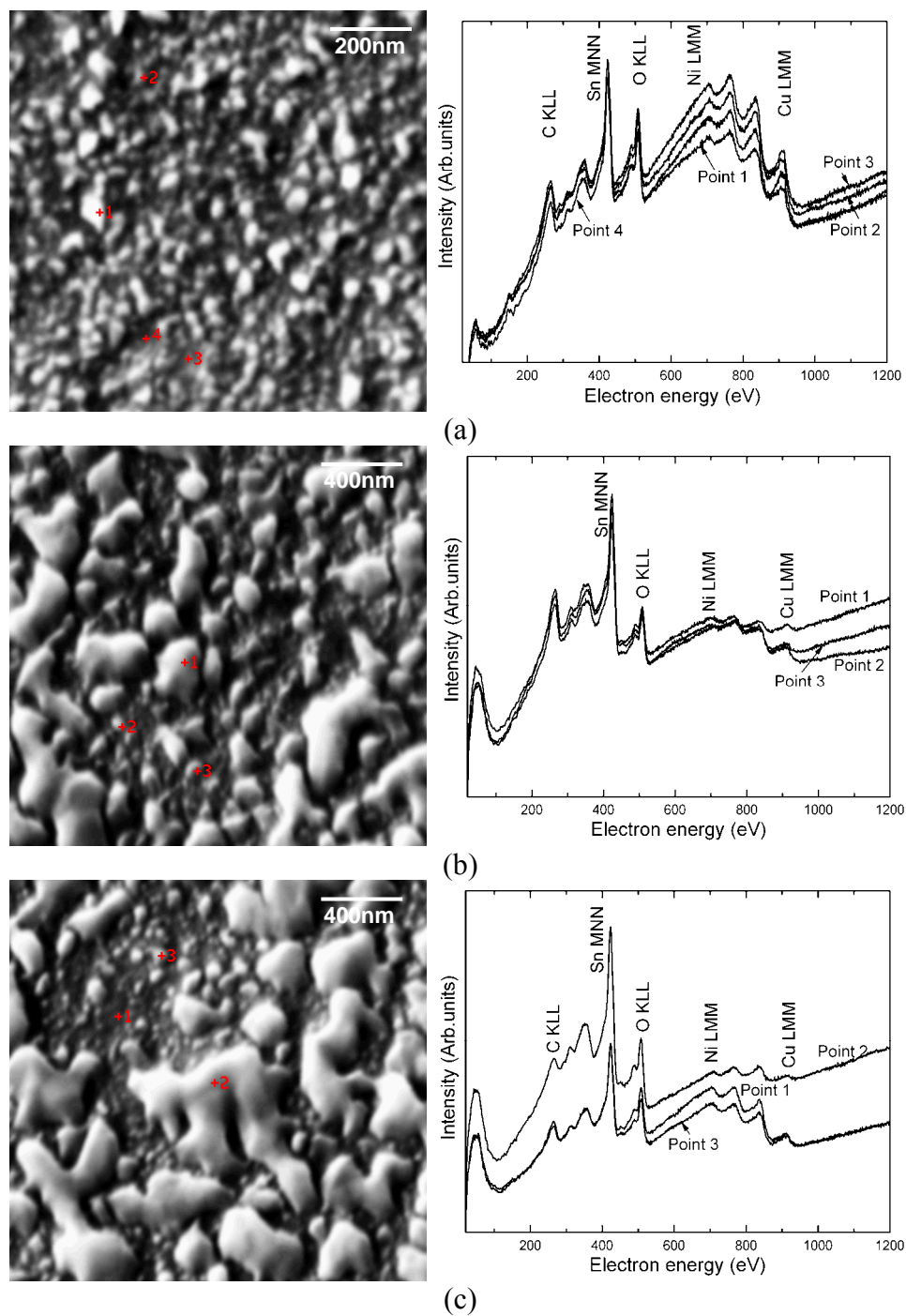


Fig. 5-18 Auger SE images (left) and Auger spectra point analysis (right) of Sn-Cu electrodeposited onto Ni substrates for: (a) 1 s, (b) 4 s and (c) 7 s.

To identify the phases formed in the initial stages of Sn-Cu electrodeposition under controlled current, thin film X-ray diffraction was utilized

and the results are shown in Fig. 5-16. A Ni layer electrodeposited on top of the Au seed layer on the silicon wafer piece was used as the substrate to prevent interdiffusion between the Au seed layer and deposited Sn, which can occur even at room temperature (Buene et al., 1980; Tang et al., 2008b). In the absence of a Ni layer, when short plating times (e.g., 1 s) were chosen to deposit Sn-Cu, only a small amount of Sn was plated, so the relative amount of Au was high. As such, most of the as-deposited Sn would react with the Au seed layer after nucleation to form Au-Sn intermetallic compounds. In Fig. 5-16, the vertical axis is plotted on a log scale in order to better show the intensity of the Sn-Cu phases. After plating for 1 s, other than the Ni and Au peaks from the substrate, only Cu_6Sn_5 peaks located at 35° and 51° were detected. All the Sn and Cu reduced from solution formed Cu_6Sn_5 after plating for 1 s. After plating for 4 s, besides Ni, Au and Cu_6Sn_5 , Sn was also detected. After plating for 7 s, the same phases were detected with additional Sn relative to the other phases. Therefore, during Sn-Cu electrodeposition under controlled current, Sn co-deposited with Cu to form Cu_6Sn_5 initially. As the plating continued, Sn reduction dominated.

5.4 Conclusions

Both current step (galvanostatic) and chronoamperometric methods were used to study the initial stages for Sn and Sn-Cu electrodeposition from Sn-citrate and Sn-Cu-citrate solutions on Pt. For both Sn-citrate and Sn-Cu-citrate solutions, when the controlled current density is lower than 15 mA/cm^2 , the potential remains almost constant. When current density is between 25 and 35 mA/cm^2 , the potential drops quickly to a value between -1.07 and -1.3 V, followed by a gradual increase and eventually reaches a constant value. When the current density is higher than 50 mA/cm^2 , potential oscillation happens due to repeated ion depletion and restoration by hydrogen evolution. The steady transition time constant indicates a diffusion controlled process. The average diffusion coefficient calculated from the Sand equation is about $3.8 \times 10^{-6} \text{ cm}^2/\text{s}$ for the Sn-citrate solution and $4.1 \times 10^{-6} \text{ cm}^2/\text{s}$ for the Sn-Cu-citrate solution.

Nucleation modeling from current-time transients at -0.72, -1.1 and -1.5 V and AFM analysis for samples deposited at -1.1 and -1.5 V show a progressive nucleation mechanism controlled by diffusion for the initial stages of both Sn and Sn-Cu electrodeposition. When the applied potential is -0.72 V, a thin layer of Sn or Sn-Cu is electrodeposited. The diffusion coefficient is 1.3×10^{-8} cm²/s for Sn electrodeposition and 2.3×10^{-8} cm²/s for Sn-Cu electrodeposition. When the applied potential is -1.1 V, nuclei range in size from 40 to 80 nm and the diffusion coefficient is 1.6×10^{-6} cm²/s for Sn electrodeposition and 2.2×10^{-6} cm²/s for Sn-Cu electrodeposition. When the applied potential is -1.5 V, nuclei ranging in size from 80 nm to 100 nm form clusters with sizes from 80 nm to 300 nm for Sn electrodeposition. For the Sn-Cu-citrate solution, nuclei as small as 30 nm continue to form. The diffusion coefficient is 5.6×10^{-6} cm²/s for Sn electrodeposition and 6.9×10^{-9} cm²/s for Sn-Cu electrodeposition. Tin reacts with the Pt seed layer to form PtSn₄ and co-deposits with Cu to form Cu₆Sn₅ during nucleation, with more Sn forming at higher applied potentials.

Under controlled current, Sn-Cu film growth follows the island (Volmer-Weber) growth mechanism. Tin co-deposits with Cu to form Cu₆Sn₅ initially. As plating continued, Sn formation dominates.

Chapter 6 Electrochemical composite deposition of Sn-Ag-Cu alloys

6.1 Introduction

Among all the Pb-free solders listed in Chapter 2, Sn-Ag-Cu solder is considered to be one of the most promising replacements for Pb-Sn solders, although the preferred composition is still the subject of debate (Wu et al., 2004; Anderson, 2007). By adding Ag into the Sn-Cu system, the melting temperature can be reduced from 227°C to about 217°C, which helps reduce the magnitude of thermal stresses during soldering and improve solder reliability (Puttlitz and Stalter, 2004). In addition, a well designed Sn-Ag-Cu solder can promote enhanced joint strength and creep and thermal fatigue resistance, and permit increased operating temperature for advanced electronic systems and devices (Zeng et al., 2002; Sharif et al., 2004; Wu et al., 2004; Anderson, 2007). The International Printed Circuit Association (IPC) has indicated Sn-3.0Ag-0.5Cu and Sn-3.9Ag-0.6Cu as two choices for electronics manufacturers; these compositions have also been recommended by the Japan Electronics and Information Technology Industries Association (JEITA) and the National Electronics Manufacturing Initiative (NEMI), respectively (Miller et al., 1994; Loomans and Fine, 2000; Moon et al., 2000; Wu et al., 2004). The JEITA also proposed a composition of Sn-3.5Ag-0.7Cu (Kim et al., 2002). Other eutectic Sn-Ag-Cu compositions such as Sn-3.5±0.3Ag-0.9±0.2Cu (Moon et al., 2000), Sn-4.7Ag-1.7Cu (Miller et al., 1994; Anderson et al., 1996), and Sn-3.5-0.9Cu (Loomans and Fine, 2000) have also been recommended by different researchers. In this study, Sn-3.5Ag-0.7Cu was chosen as the preferred composition.

Typical methods to produce Sn-Ag-Cu solder bumps on wafers include screen printing of solder pastes, evaporation of solder alloy through a perforated stencil and electrodeposition using a photoresist mask. Screen printing technology remains the main method because of its low cost to produce relatively large

volumes of solder bumps (Kim and Ritzdorf, 2003a, 2003b). However, as the density of patterns and the complexity of circuitry increases, the size of solder bumps decreases; thus, the limitation of this method becomes more serious. Electrodeposition is a preferred alternative technique in bumping applications because of its simplicity and compatibility with photolithography (Joseph and Phatak, 2008). Yet not much work has been done on the electrodeposition of eutectic and near eutectic Sn-Ag-Cu solder films.

The great difference in the standard reduction potentials between Ag/Ag^+ and Sn/Sn^{2+} , which is nearly about 0.94 V, makes it difficult to obtain Sn-Ag-Cu alloys from simple ionic solutions. One approach is to add suitable complexing agents which are able to bring the Ag and Sn deposition potentials closer. Most reported non-cyanide Sn-Ag-Cu plating baths are alkaline and based on pyrophosphate-iodide (Arai and Kaneko, 1997; Arai, 1999; Kim and Ritzdorf, 2003a), but are not compatible for photolithography as many photoresist systems depend upon alkaline media for the development. Others are strongly acidic, mainly sulphuric acid based, with thiourea and polyoxyethylene lauryl ether (POELE) as complexing agents (Fukuda et al., 2002; Fukuda et al., 2003; Ozga, 2006), and may corrode metal plates, as well promote the oxidation of Sn^{2+} to Sn^{4+} (Martyak and Seefeldt, 2004; Zhang et al., 2008). This oxidation makes the solution unstable and can cause the precipitation of Ag and Cu ions (Zhang et al., 2008). Thus, a Sn-Ag-Cu plating bath in a mild acidic pH range is desirable.

Joseph and Phatak (2008) developed a methanesulphonic acid based bath (pH adjusted to about 4) for Sn-Ag-Cu co-deposition. Thiourea was used as a chelating agent for both Ag^+ and Cu^{2+} ions and altered their deposition potentials to make it possible to co-deposit Sn, Ag, and Cu. Iso-octyl phenoxy polyethoxy ethanol (OPPE) was added as a non-ionic surfactant, which improved bath stability from a few hours to up to one week. As-deposited Sn-Ag-Cu films have an average composition of Sn-2.7Ag-0.9Cu when the current density is beyond 5 mA/cm^2 , and have grain sizes of 6-8 μm with a compact microstructure. Zhang et al. (2008) developed a weakly acidic bath (pH = 5.5) containing methylsulfonic acid salts, iodide salts, pyrophosphoric salts, hydroquinone, heliotropin (HT) and

triethanolamine (TEA). HT acted as a brightening agent, which increased the cathodic polarization and refined the deposited grains. TEA acted as a brightening promoter which decreased the cathodic polarization and densified the deposits. TEA was also a complexing agent for Cu ions. The as-deposited Sn-Ag-Cu films contained 5-10 wt% Ag and 0.5-2wt% Cu.

The second approach is by co-deposition during electroplating of particles suspended in a plating bath with the other metals, which is also referred to as electrochemical composite deposition. Silver particles instead of Ag salts can be used during co-deposition of Sn and Cu with no complexing agents required. Barkey et al. (2006) studied the deposition of Sn-Ag bumps from suspensions of Ag particles (spherical, 0.5-1 μm in size) with a pure Sn plating bath. The Sn-Ag deposits obtained either had very low Ag content (< 1 wt%) with low Ag particle concentration (< 4 g/L) or very high Ag content (25-72 wt% Ag) with high Ag particle concentration. When the Ag content was high, a mossy structure formed, and the deposits could not be melted. Fujiwara et al. (2003) reported their studies on the electrodeposition of near-eutectic Sn-Ag films from solutions containing SnSO_4 , $\text{K}_4\text{P}_2\text{O}_7$, AgNO_3 and polyethyleneglycol 6000. Ag nano-particles were confirmed to form spontaneously in the solution through UV-vis spectra analysis, and Sn-Ag deposits were obtained from Ag nano-particles suspensions. No reports have been found about Sn-Ag-Cu deposition from suspensions with Ag particles.

In Chapter 3, a simple and environmentally friendly Sn-Cu-citrate plating bath was developed to electrodeposit eutectic and near eutectic Sn-Cu solder films with a natural pH of about 4. In this study, Ag nano-particles are added into the Sn-Cu-citrate solution to deposit Sn-Ag-Cu solder films. Plating parameters such as current density, $\text{CuCl}_2 \cdot 2\text{H}_2\text{O}$ concentrations, Ag particle concentrations and agitation are studied to obtain eutectic and near eutectic Sn-Ag-Cu compositions. As one of the most popular anionic surfactants, sodium dodecyl sulfate (SDS) is used to help disperse the Ag nano-particles. The effect of SDS on Sn-Ag-Cu deposition is studied. In addition, differential scanning calorimetry (DSC) thermal

analysis is carried out to study the melting behavior for as-deposited Sn-Ag-Cu alloys.

6.2 Experimental materials and procedures

The Sn-Cu-citrate solutions were prepared by dissolving tri-ammonium citrate ($(\text{NH}_4)_3\text{C}_6\text{H}_5\text{O}_7$, Alfa Aesar, 98%) in deionized water and then dissolving $\text{SnCl}_2 \cdot 2\text{H}_2\text{O}$ (Fisher Scientific) and $\text{CuCl}_2 \cdot 2\text{H}_2\text{O}$ (Fisher Scientific) in the citrate solution. The deionized water was obtained from an Aqua MAX™-ultra purification system. Silver particles (Sigma-Aldrich, 100 nm in size) were added into the Sn-Cu-citrate solution after the solution was stabilized for about 1 hour. Ultrasonic dispersion (BRANSON 2510 Ultrasonic Cleaner) and two types of agitation, i.e., a magnetic stirrer (CORNING PC-220) and an overhead Caframo mechanical stirrer (Caframo BDC 3030 stirrer, 20-3000 rpm), were used to help disperse the Ag particles. Sodium dodecyl sulfate (Fisher Scientific) was dissolved in deionized water first, then mixed with stabilized Sn-Cu-citrate solution and Ag nano-particles.

Silicon wafer pieces, metallized with a 25 nm TiW adhesion layer and a 200 nm Au or Pt seed layer, were used as the cathode and anode for Sn-Ag-Cu deposition, respectively. TiW acts as an adhesion and barrier layer and Au as a seed layer for electroplating. The plating surface area was kept constant at 0.64 cm^2 . Before plating, both the Au and Pt electrodes were cleaned ultrasonically for 2 minutes in acetone followed by ethanol and then rinsed with deionized water. A Dynatronix DuPR 10-0.1-0.3 pulse plating power supply was used for Sn-Ag-Cu electrophoretic deposition, with a 2 ms forward on-time and 8 ms forward off-time based on previous work (Sun and Ivey, 1999; Olsen, 2005). No reverse pulse was used. The current densities were varied from 10 mA/cm^2 to 40 mA/cm^2 and all deposition was done at room temperature for 30 min.

The microstructure and composition of the Sn-Ag-Cu films were characterized using a Hitachi H2700 scanning electron microscope (SEM) equipped with an ultrathin window energy dispersive x-ray (EDX) spectrometer.

Deposit compositions were found by averaging measurements taken from at least three regions, each $400 \times 400 \mu\text{m}^2$ in size. Analysis was done at 20 kV with a working distance of 17 mm and a count rate of 2500-4000 counts/s. Phase analysis was performed using thin film X-ray diffraction (XRD) with a Rigaku rotating Co anode system, operating in continuous scanning mode at a voltage of 40 kV and a current of 160 mA. The thickness of the Sn-Cu films was measured using an Alpha-step 200 profilometer. The thickness was taken as the average of at least seven measurements. Thermal analysis of as-deposited Sn-Ag-Cu and Sn-Cu alloys was carried out using a NETZSCH STA 409PC Luxx differential scanning calorimetry (DSC) after peeling the deposits from the substrates. Sample temperature was raised from 40°C to 300°C at a rate of $10^\circ\text{C}/\text{min}$. All the measurements in the DSC were performed under an atmosphere of flowing N_2 .

6.3 Results and discussion

6.3.1 Effect of agitation

Two types of agitation were utilized to help disperse the Ag nano-particles during solution preparation and Sn-Ag-Cu solder film deposition, as shown in Fig. 6-1, with both top and side views. Fig. 6-1a shows magnetic stir bar agitation which was applied initially. The final volume of the plating bath was kept at 40 mL. The stirrer was located in the middle of the two electrodes and the stirring speed was set at 80 rpm. The effect of Ag particle concentration on Ag and Cu content in the deposits using the magnetic agitation was studied using EDX analysis and the results are shown in Fig. 6-2. As Ag particle concentration is increased from 0.8 g/L to 3 g/L, Cu content in the deposit stays almost the same (about 1.2 wt%), while there is a slight decrease for Ag content from about 1.5 wt% to about 0.9 wt%. Compared with the preferred Sn-Ag-Cu film composition, e.g., 3.5 wt% Ag and 0.7 wt% Cu, the Ag content in the above as-deposited Sn-Ag-Cu films is too low. The surface morphologies of the as-deposited Sn-Ag-Cu films are shown in Fig. 6-3. All the films were smooth, with protrusions on the surface, which are due to the reduction of Sn and Cu around Ag particles that

were adsorbed to the surface of the cathode and became active sites for deposition. In order to increase Ag content in deposits, many other experiments were carried out, including changing the Cu concentration and Ag particle concentration in solutions and adding additives such as gelatin and β -naphthol and SDS. EDX analysis showed that the Ag content in all the deposits were very low; Ag contents were even dropped to zero with the addition of gelatin and β -naphthol.

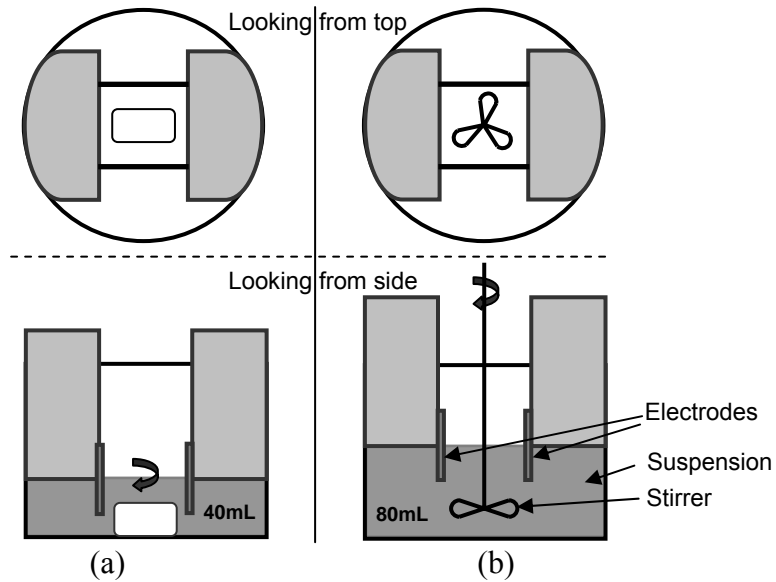


Fig. 6-1 Schematic illustration of plating set up for Sn-Ag-Cu electrochemical composite deposition: (a) magnetic agitation, 40mL suspension; (b) agitation from top, 80mL suspension.

Stronger agitation was another approach to increase Ag content in as-deposited Sn-Ag-Cu films. As shown in Fig. 6-1b, agitation using an overhead Caframo BDC 3030 stirrer was utilized. Once the agitation started, a vortex formed in the middle of the two electrodes, and the solution level around the two electrodes became much lower. In order to make sure there was enough solution to submerge the two electrodes with agitation, 80 mL of solution was used. The stirring speed was set at 600 rpm. The effect of this plating set up on Ag and Cu content, as a function of Ag particle concentration in solution at a current density of 10 mA/cm^2 , is shown in Fig. 6-4. Both Ag and Cu content increased to about 3

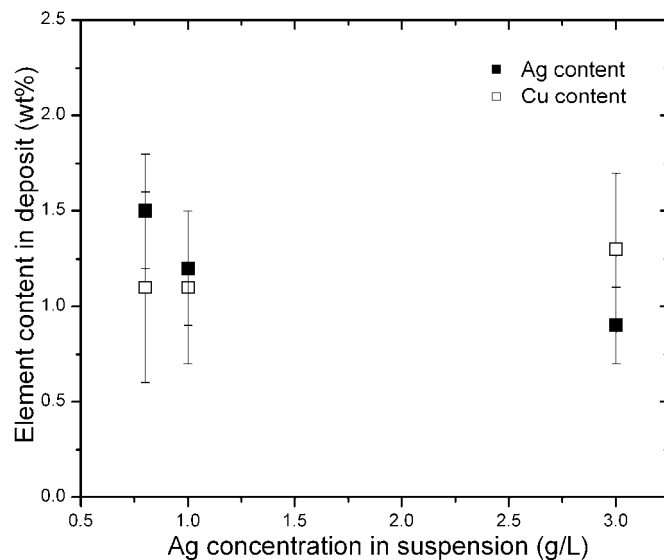


Fig. 6-2 Deposit Ag and Cu content as a function of Ag particle concentration in a 40 mL suspension. The concentrations of $\text{SnCl}_2 \cdot 2\text{H}_2\text{O}$, tri-ammonium citrate, and $\text{CuCl}_2 \cdot 2\text{H}_2\text{O}$ were fixed at 0.22 mol/L, 0.30 mol/L, and 0.001 mol/L. The current density was 10 mA/cm^2 . The suspension was agitated with a magnetic stir bar during electroplating.

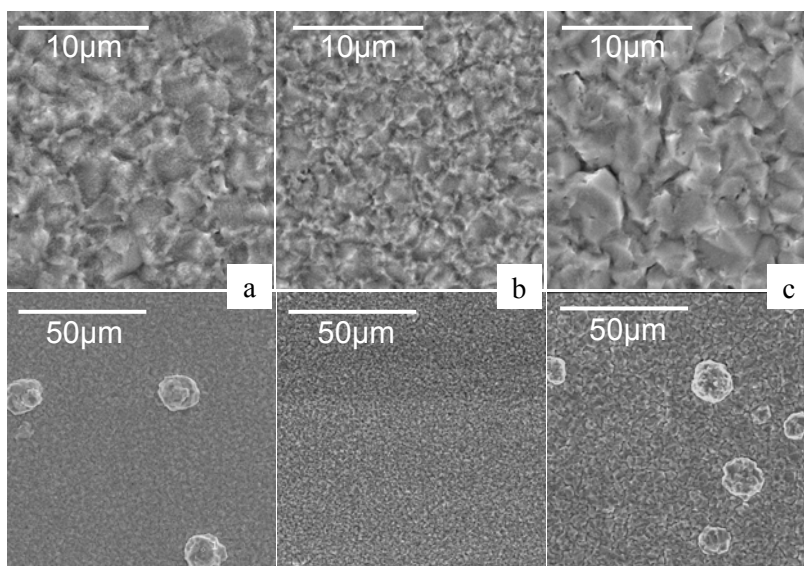


Fig. 6-3 SEM SE plan view images of Sn-Ag-Cu films deposited onto Au seed layers from 40 mL Sn-Cu-citrate suspensions with different Ag additions: (a) 0.8 g/L, (b) 1 g/L and (c) 3 g/L. The concentrations of $\text{SnCl}_2 \cdot 2\text{H}_2\text{O}$, tri-ammonium citrate, and $\text{CuCl}_2 \cdot 2\text{H}_2\text{O}$ were fixed at 0.22 mol/L, 0.30 mol/L, and 0.001 mol/L. The current density was 10 mA/cm^2 . The suspensions were agitated with a magnetic stir bar during electroplating.

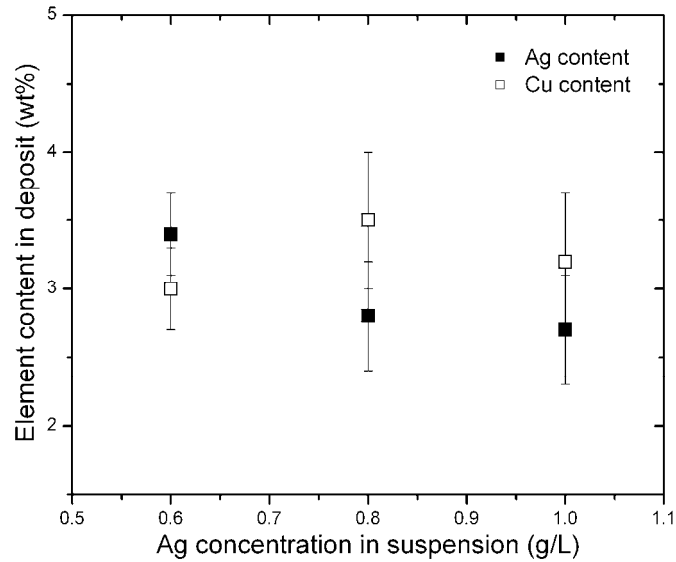


Fig. 6-4 Deposit Ag and Cu content as a function of Ag concentration in an 80 mL suspension. The concentrations of $\text{SnCl}_2 \cdot 2\text{H}_2\text{O}$, tri-ammonium citrate and $\text{CuCl}_2 \cdot 2\text{H}_2\text{O}$ were fixed at 0.22 mol/L, 0.30 mol/L, and 0.001 mol/L, respectively. The current density was 10 mA/cm^2 . The suspensions were agitated by an overhead mechanical stirrer during electroplating.

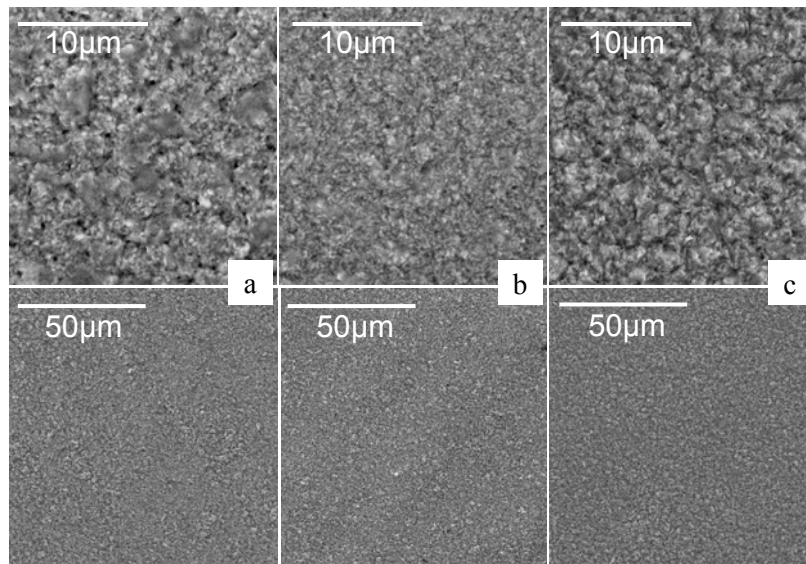


Fig. 6-5 SEM SE plan view images of Sn-Ag-Cu films deposited onto Au seed layers from 80 mL Sn-Cu-citrate suspensions with different Ag additions: (a) 0.6 g/L, (b) 0.8 g/L and (c) 1 g/L. The concentrations of $\text{SnCl}_2 \cdot 2\text{H}_2\text{O}$, tri-ammonium citrate, and $\text{CuCl}_2 \cdot 2\text{H}_2\text{O}$ were fixed at 0.22 mol/L, 0.30 mol/L, and 0.001 mol/L, respectively. The current density was 10 mA/cm^2 . The suspensions were agitated with an overhead mechanical stirrer during electroplating.

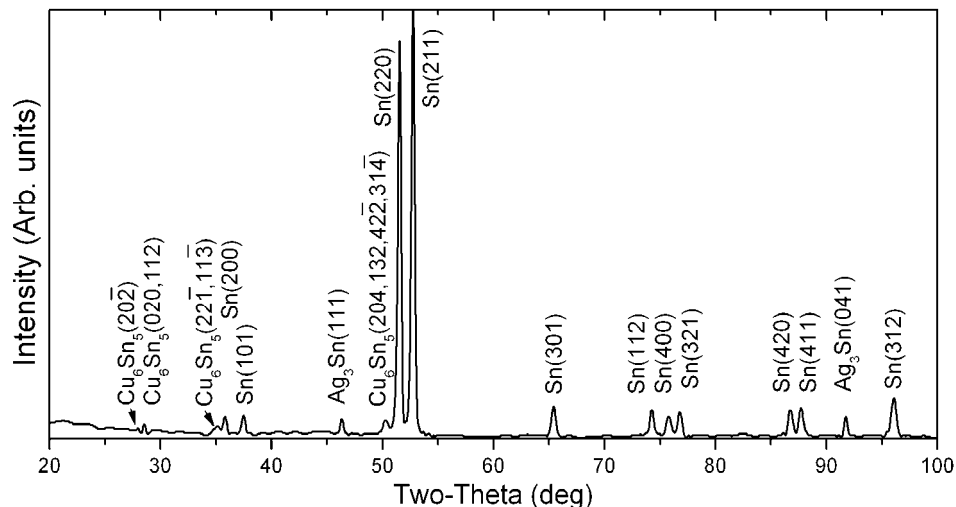


Fig. 6-6 XRD pattern of Sn-Cu-Ag film deposited onto an Au seed layer from a suspension containing 0.22 mol/L $\text{SnCl}_2 \cdot 2\text{H}_2\text{O}$, 0.30 mol/L triammonium citrate, 0.001 mol/L $\text{CuCl}_2 \cdot 2\text{H}_2\text{O}$, and 0.8 g/L Ag nanoparticles. The current density was 10 mA/cm^2 .

wt%, which was almost more than twice the previous Ag and Cu content. The Ag content was only 0.5 wt% below the desired Ag composition. As Ag particle concentration was increased from 0.005 mol/L to 0.009 mol/L, there was a slight decrease in Ag content in the deposits. SEM SE images of as-deposited Sn-Ag-Cu films were shown in Fig. 6-5. All the films were smooth and uniform. The morphologies of Sn-Ag-Cu films showed little change with changing Ag concentration. The plating set up shown in Fig. 6-1b was utilized in subsequent work for Sn-Ag-Cu deposition. XRD analysis of the as-deposited Sn-Ag-Cu film on the Au seed layer at a current density of 10 mA/cm^2 is shown in Fig. 6-6. Three phases were detected. The major phase was tetragonal Sn, with a small amount of Cu_6Sn_5 and Ag_3Sn intermetallic compounds.

6.3.2 Effect of current density

Although stronger agitation helped increase Ag content from about 1.5 wt% to about 3 wt%, which is very close to the desired Ag composition, the Cu content increased to about 3 wt% as well, which is too high based on the desired Cu composition (0.7 wt%). Previous work on Sn-Cu electrodeposition from Sn-

Cu-citrate solutions (Chapter 3) showed that Cu content in deposits decreased as the current density was increased. In order to decrease Cu content in as-deposited Sn-Ag-Cu films, current densities higher than 10 mA/cm² were applied. It was also noticed that Ag content in deposits increased as the CuCl₂·2H₂O concentration increased. In order to study the effect of CuCl₂·2H₂O concentration on Sn/Cu/Ag co-deposition, 0.002 and 0.003 mol/L CuCl₂·2H₂O additions were also studied. Fig. 6-7 shows Ag content in Sn-Ag-Cu deposits as a function of current density from suspensions with different CuCl₂·2H₂O concentrations. A small decrease in deposit Ag content appeared as current density was increased. Similar results were reported by Banovic et al. (1999) who observed that an increase in current density led to fewer nano-particles being incorporated in the metal deposit. According to Fig. 6-7, a higher CuCl₂·2H₂O concentration in solution gave higher Ag content in the deposits, which means the Cu²⁺ ions accelerated the co-deposition of Ag. Similar effects were reported by Takahashi et al. (1994) who showed that the addition of Fe group metal ions in a Zn bath increased the co-deposition of SiO₂ particles. As shown in Fig. 6-7, Sn-Ag-Cu films plated from suspensions containing 0.002 mol/L CuCl₂·2H₂O at 10 mA/cm², or plated from suspensions containing 0.003 mol/L CuCl₂·2H₂O at current densities higher than 30 mA/cm², have Ag content close to 3.5 wt%. Copper content in deposits as a function of current density from suspensions with different CuCl₂·2H₂O concentrations is shown in Fig. 6-8. For each CuCl₂·2H₂O concentration, deposit Cu content in Sn-Ag-Cu films decreased as current density increased. At each current density, a higher CuCl₂·2H₂O concentration gave higher Cu content in the deposit. However, at higher current densities, the differences became less pronounced. A composition of 0.7 wt% Cu was attainable from suspensions containing 0.001 mol/L CuCl₂·2H₂O at current densities higher than 30 mA/cm², or from suspensions containing 0.002 mol/L CuCl₂·2H₂O at a current density of 40 mA/cm². Combining the results from Fig. 6-7 and Fig. 6-8, it can be seen that while the deposit Ag content is more or less constant at about 3.5 wt%, deposit Cu content changed from 4.8 wt% (0.002 mol/L CuCl₂·2H₂O, 10 mA/cm²), to 3 wt% (0.003 mol/L CuCl₂·2H₂O, 30 mA/cm²) and 1.8 wt% (0.003

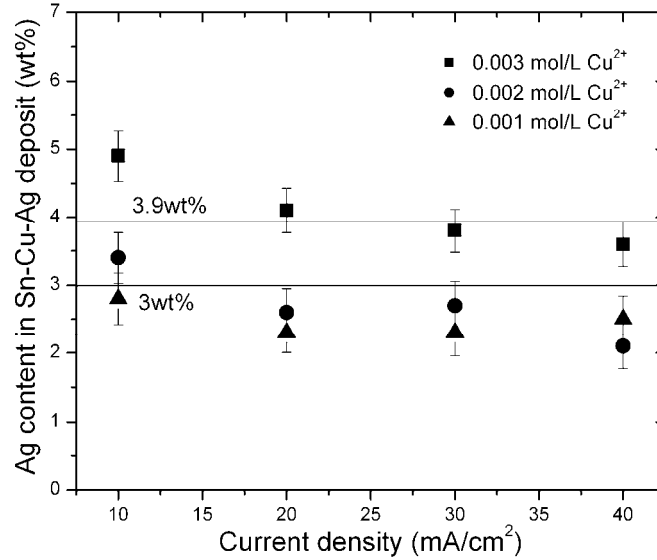


Fig. 6-7 Deposit Ag content as a function of current density in an 80 mL Sn-Cu-citrate + Ag suspension. The concentrations of $\text{SnCl}_2 \cdot 2\text{H}_2\text{O}$, triammonium citrate and Ag were fixed at 0.22 mol/L, 0.30 mol/L and 0.8 g/L, respectively. Ag content in the area between the two solid horizontal lines are acceptable for Sn-Ag-Cu solders based on criteria from the literature.

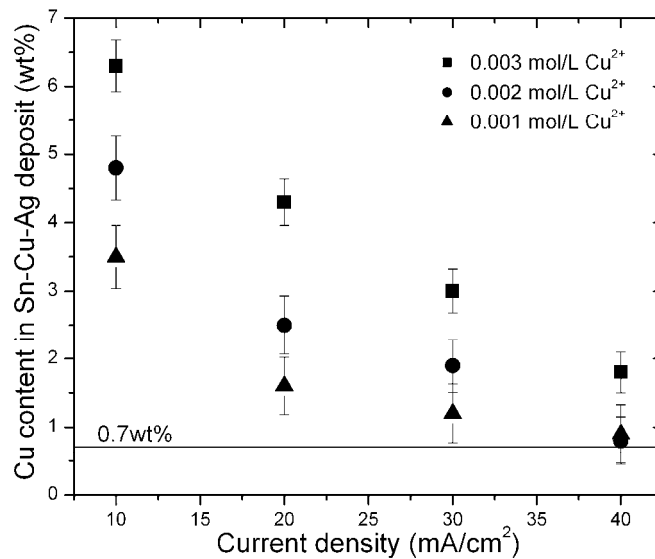
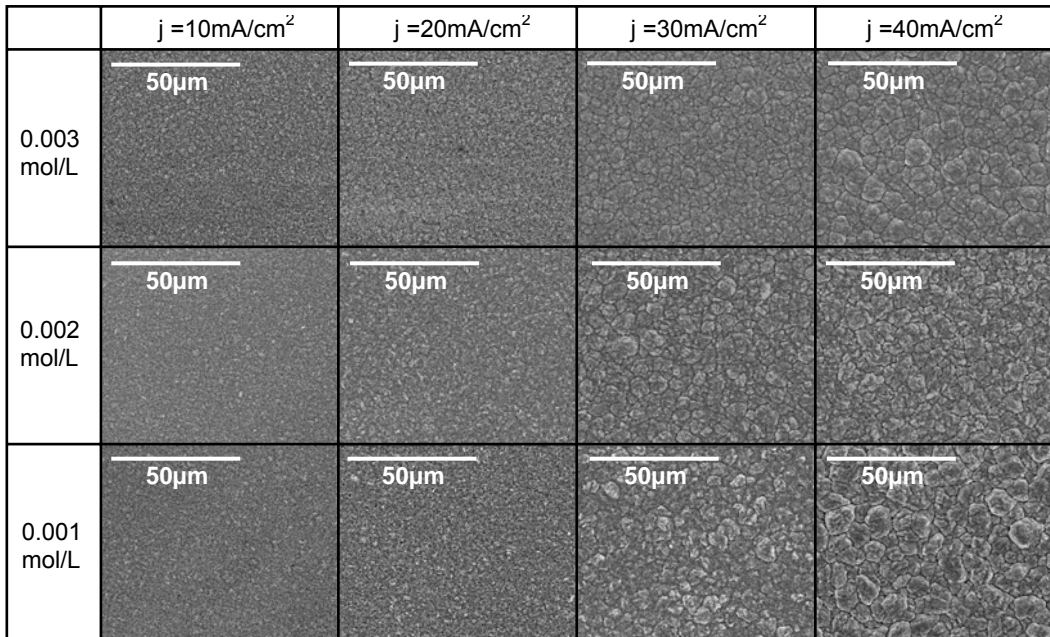
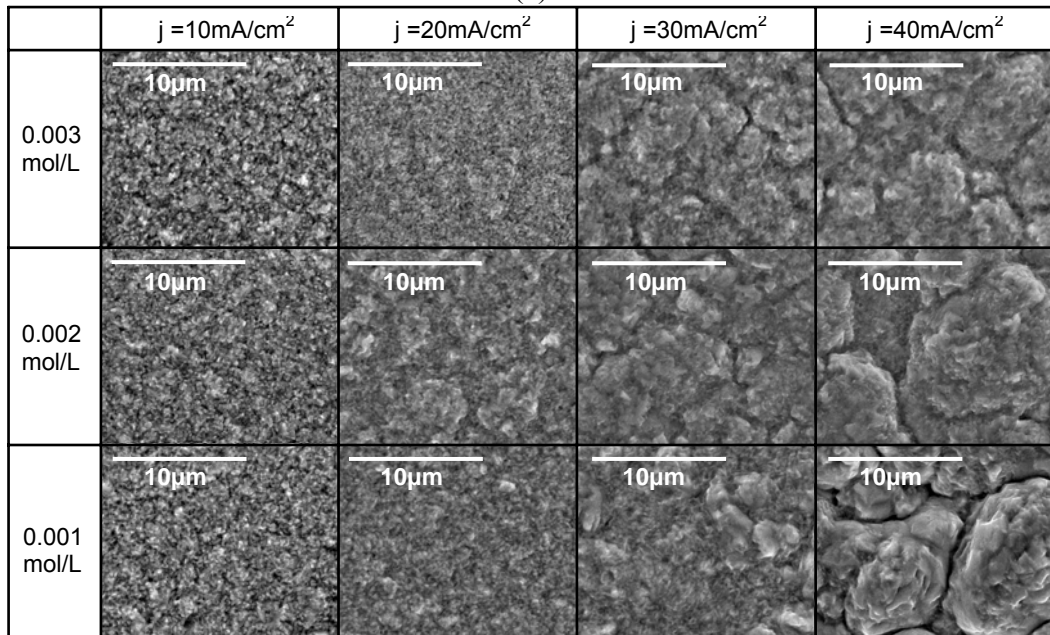


Fig. 6-8 Deposit Cu content as a function of current density in an 80 mL Sn-Cu-citrate + Ag suspension. The concentrations of $\text{SnCl}_2 \cdot 2\text{H}_2\text{O}$, triammonium citrate and Ag were fixed at 0.22 mol/L, 0.30 mol/L, and 0.8 g/L, respectively. The solid horizontal line represents the eutectic composition of Sn-Cu solder.

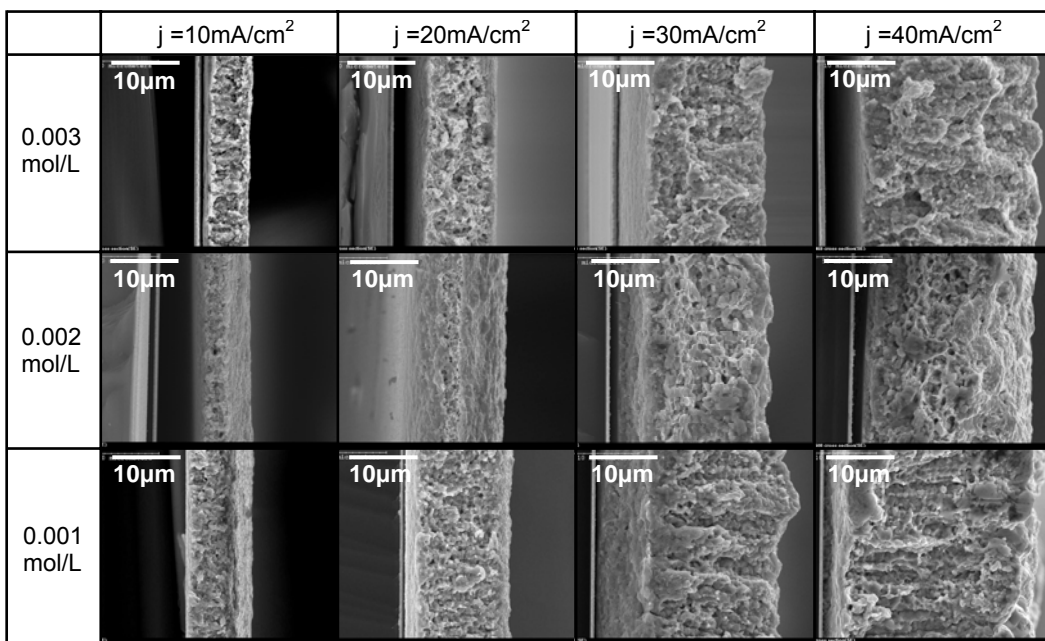
mol/L $\text{CuCl}_2 \cdot 2\text{H}_2\text{O}$, 40 mA/cm^2). The Cu content is higher than the desired Cu composition. When the deposit Cu content is about 0.7 wt%, deposit Ag content is about 2.1 wt% ($0.002 \text{ mol/L CuCl}_2 \cdot 2\text{H}_2\text{O}$, 40 mA/cm^2), 2.3 wt% ($0.001 \text{ mol/L CuCl}_2 \cdot 2\text{H}_2\text{O}$, 30 mA/cm^2) and 2.5 wt% ($0.001 \text{ mol/L CuCl}_2 \cdot 2\text{H}_2\text{O}$, 40 mA/cm^2), which are lower than the desired Ag composition.



(a)



(b)



(c)

Fig. 6-9 SEM SE images of Sn-Ag-Cu films deposited onto Au seed layers from 80 mL Sn-Cu-citrate + Ag suspensions under different current densities: (a) low magnification plan view images, (b) high magnification plan view images and (c) cross section images. The concentrations of $\text{SnCl}_2 \cdot 2\text{H}_2\text{O}$, tri-ammonium citrate and Ag were fixed at 0.22 mol/L, 0.30 mol/L, and 0.8 g/L, respectively.

Fig. 6-9 shows plan view and cross section images of Sn-Ag-Cu films plated at different current densities from suspensions with different $\text{CuCl}_2 \cdot 2\text{H}_2\text{O}$ concentrations. All the Sn-Ag-Cu films are uniform and dense. At each current density, $\text{CuCl}_2 \cdot 2\text{H}_2\text{O}$ concentration had little effect on Sn-Ag-Cu film surface morphology. When the current densities were higher than 30 mA/cm^2 , deposit agglomeration started to occur and Sn-Ag-Cu surface morphology became rougher. Fig. 6-9c shows SEM SE images of cross sections of the as-deposited Sn-Ag-Cu films. Sn-Ag-Cu films became thicker as current density increased. A profilometer was used to measure the thickness of the Sn-Ag-Cu films and the results are shown in Fig. 6-10. For each $\text{CuCl}_2 \cdot 2\text{H}_2\text{O}$ concentration, the Sn-Ag-Cu film plating rate increased with increasing current density following a linear relationship. At each current density, a lower $\text{CuCl}_2 \cdot 2\text{H}_2\text{O}$ concentration gave a higher plating rate. According to Fig. 6-7, lower Ag content in the deposits was obtained with a lower $\text{CuCl}_2 \cdot 2\text{H}_2\text{O}$ concentration in suspension, which means

fewer Ag particles were co-deposited into the Sn-Ag-Cu films. Therefore, at each current density, a lower $\text{CuCl}_2 \cdot 2\text{H}_2\text{O}$ concentration likely causes less energy to be used to move the Ag particles, and therefore more energy is used to plate Sn ions, giving a higher plating rate. The effect of $\text{CuCl}_2 \cdot 2\text{H}_2\text{O}$ concentration on the plating rate was more pronounced at higher current densities. The effect of current density on Ag co-deposition was much less significant. The plating rate for Sn-Ag-Cu films is as high as $67 \mu\text{m/hr}$ from suspensions containing 0.001 mol/L $\text{CuCl}_2 \cdot 2\text{H}_2\text{O}$ at a current density of 40 mA/cm^2 , with a deposit composition of 0.7 wt\% Cu and 2.5 wt\% Ag .

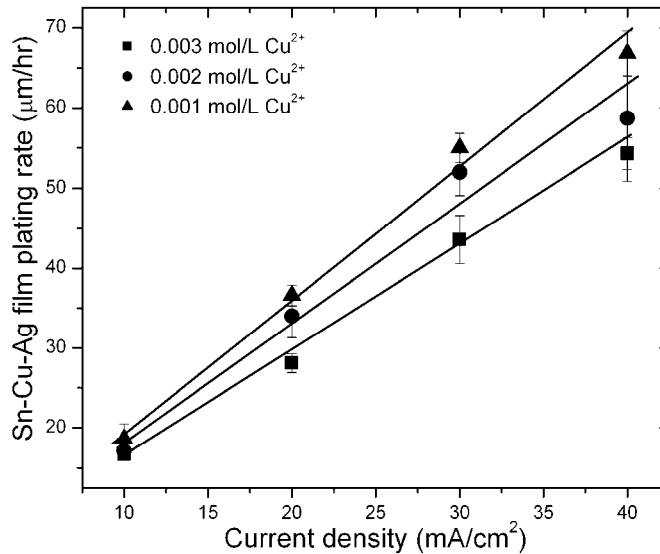


Fig. 6-10 Sn-Ag-Cu film plating rate as a function of current density from a suspension containing different $\text{CuCl}_2 \cdot 2\text{H}_2\text{O}$ concentrations. The concentrations of $\text{SnCl}_2 \cdot 2\text{H}_2\text{O}$, tri-ammonium citrate and Ag were fixed at 0.22 mol/L , 0.30 mol/L , and 0.8 g/L , respectively.

To better understand the effect of Ag nano-particles on Sn and Cu reduction, Cu content in both Sn-Ag-Cu films and Sn-Cu films plated from Sn-Cu-citrate suspensions with Ag nano-particles and Sn-Cu-citrate solutions containing different $\text{CuCl}_2 \cdot 2\text{H}_2\text{O}$ concentrations under the same plating conditions was analyzed and the results are shown in Fig. 6-11a. All the solid points represent Cu content in Sn-Ag-Cu films, while all the open points indicate Cu content in Sn-Cu films. By adding Ag nano-particles into the Sn-Cu-citrate

solution, deposit Cu content increased, which means the addition of Ag nanoparticles accelerated Cu deposition. Fig. 6-11b shows the differences in deposit Cu content between Sn-Ag-Cu films and Sn-Cu films as a function of current density. After adding Ag particles, more Cu was reduced from suspensions

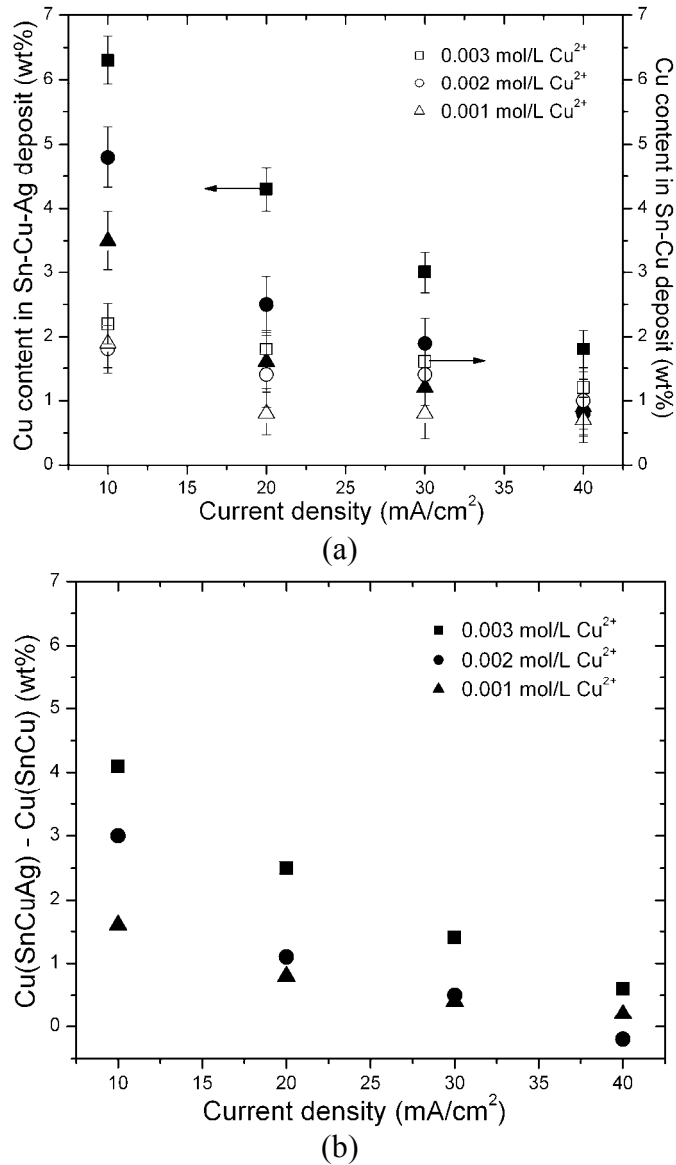


Fig. 6-11 (a) Deposit Cu content as a function of current density for both Sn-Ag-Cu films and Sn-Cu films plated under the same conditions. The concentrations of SnCl₂·2H₂O, tri-ammonium citrate and Ag were fixed at 0.22 mol/L, 0.30 mol/L, and 0.8 g/L, respectively. (b) Differences in Cu content between Sn-Ag-Cu films and Sn-Cu films as a function of current density.

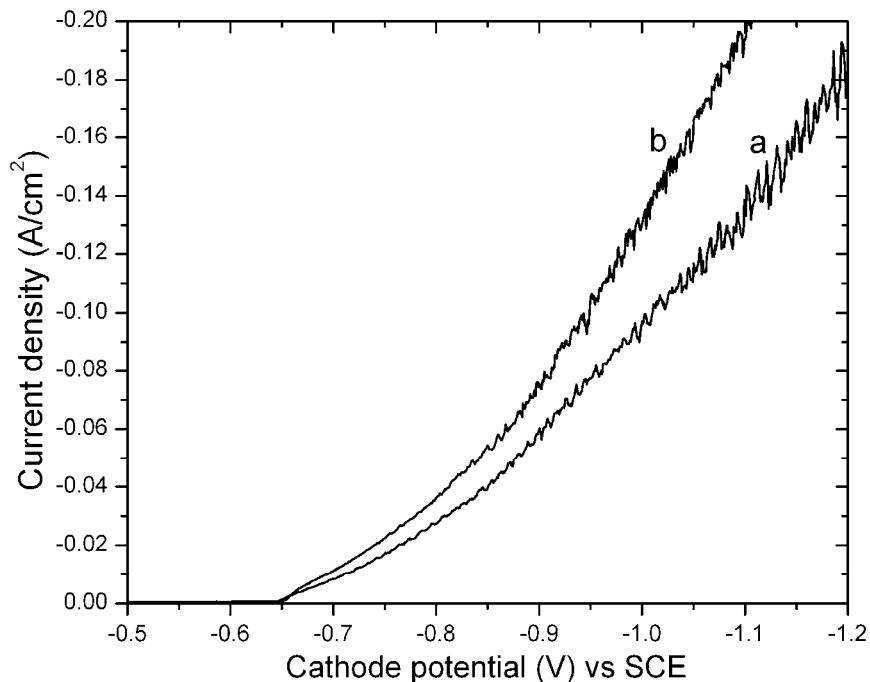


Fig. 6-12 Polarization curves for (a) Sn-Cu-citrate solution (0.22 mol/L SnCl₂·2H₂O + 0.003 mol/L CuCl₂·2H₂O + 0.30 mol/L tri-ammonium citrate) and (b) Sn-Cu-citrate suspension with Ag nano-particles (0.22 mol/L SnCl₂·2H₂O 0.003 mol/L CuCl₂·2H₂O + 0.30 mol/L tri-ammonium citrate + 0.8 g/L Ag. The stirring speed was 600 rpm.

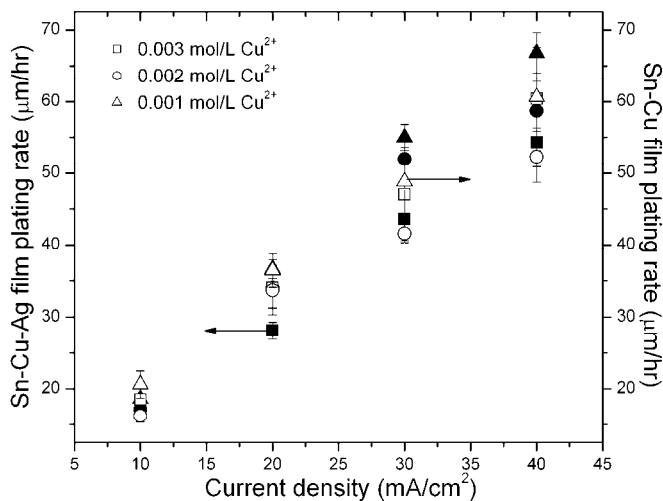


Fig. 6-13 Sn-Ag-Cu and Sn-Cu film plating rate as a function of current density from baths containing different CuCl₂·2H₂O concentrations. The concentrations of SnCl₂·2H₂O, tri-ammonium citrate and Ag were fixed at 0.22 mol/L, 0.30 mol/L, and 0.8 g/L, respectively.

containing higher $\text{CuCl}_2 \cdot 2\text{H}_2\text{O}$ concentrations. At higher current density, this difference became much less pronounced. Polarization measurements for both the Sn-Cu-citrate solution and the Sn-Cu-citrate suspension with Ag nano-particles were carried out and the results are shown in Fig. 6-12. A higher current density was obtained for the same cathode potential when Ag nano-particles were present. Similar changes in polarization curves have been reported by other researchers after particles were suspended in solution, such as Al_2O_3 particles in a CuSO_4 solution and a $\text{KAu}(\text{CN})_2$ solution (Buelens et al., 1983), Cr particles in a NiSO_4 solution (Watson and Walters, 1991), SiC particles in a NiSO_4 solution (Watson, 1993), and Si particles in a FeCl_2 solution (Hovestad et al., 1997). An increase in current density was reported as depolarization which means a decrease in the magnitude of the cathodic potential (less negative) at a fixed applied current (Hovestad and Janssen, 1995; Conway, 2005). Therefore, the addition of Ag nano-particles into Sn-Cu-citrate solutions decreased the cathodic potential, which made both Sn and Cu ions easier to reduce. Since Cu-citrate complex ions were easier to reduce than Sn-citrate complex ions, as discussed in Chapter 3, the decrease in cathodic potential made Cu-citrate complex ions even easier to reduce than Sn-citrate complex ions, giving a higher Cu content in the Sn-Ag-Cu films. With higher $\text{CuCl}_2 \cdot 2\text{H}_2\text{O}$ concentration, more Cu ions were available to be reduced, which gave even higher Cu contents. When the deposition current density increased, Cu ions were depleted at the cathode more quickly due to their low concentration compared with Sn, so more Sn ions were reduced instead and the difference in Cu content became less pronounced. It was also noticed that with the addition of Ag nano-particles, plating rates decreased slightly (Fig. 6-13).

In order to investigate the reactions between Ag nano-particles and Sn ions and Cu ions in citrate suspensions, the same amount of Ag particles was added to a Sn-citrate solution and a Cu-citrate solution with the same ion concentrations (0.22 mol/L Sn^{2+} or Cu^{2+} ions and 0.3 mol/L tri-ammonium citrate), respectively. Electrodeposition was carried out from these two suspensions and SEM images (at low and high magnifications) of the as deposited films are shown in Fig. 6-14. Morphologies of both films were very different from

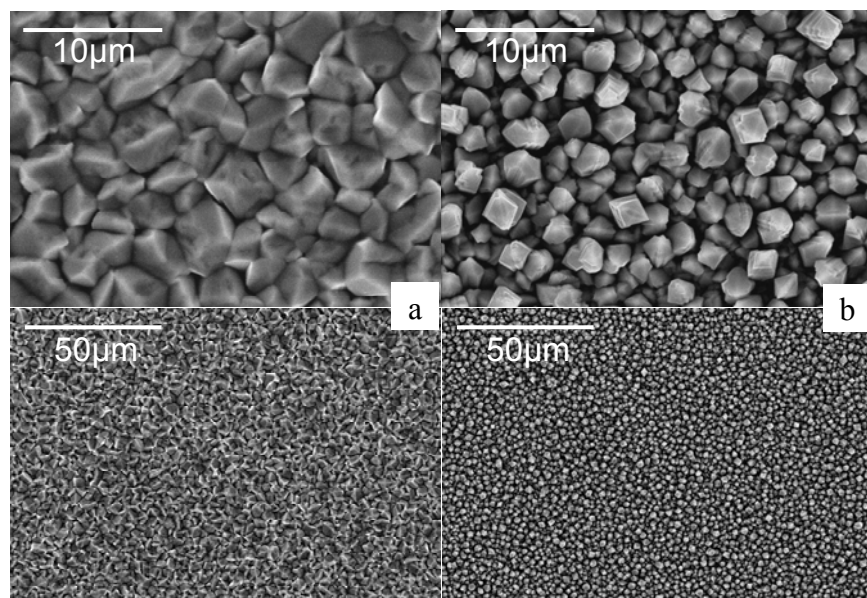


Fig. 6-14 SEM SE plan view images of films deposited onto Au seed layers from (a) Sn-citrate solution + Ag particles and (b) Cu-citrate solution + Ag particles. The concentrations of tri-ammonium citrate and Ag were fixed at 0.30 mol/L and 0.8 g/L, respectively. The concentrations of $\text{SnCl}_2 \cdot 2\text{H}_2\text{O}$ and $\text{CuCl}_2 \cdot 2\text{H}_2\text{O}$ were both 0.22 mol/L.

previous Sn-Ag-Cu films. EDX analysis showed that no Ag was detected in either film. Therefore, the Ag nano-particles were not able to co-deposit with either Sn or Cu from the Sn-citrate suspension or Cu-citrate suspension. Previously (Fig. 6-11a), it was shown that when 0.001- 0.003 mol/L of $\text{CuCl}_2 \cdot 2\text{H}_2\text{O}$ was present in the above Sn-citrate suspension, Ag nano-particles were able to co-deposit into the films with a composition of 3-5 wt% Ag. The Ag nano-particles were able to co-deposit with the Cu ions from citrate suspensions, when the Cu ion concentration was low but not at higher concentrations. The Ag nano-particles, however, were unable to co-deposit with the Sn ions. Different particle incorporation rates have been reported for different types of baths (Hovestad and Janssen, 1995; Conway, 2005). Brandes and Goldthorpe (1967) studied the co-deposition of Al_2O_3 particles from different plating baths and reported that Al_2O_3 particles were able to co-deposit in Cu and Ni baths, but not in a Cr bath. Takahashi et al. (1994) studied the incorporation of SiO_2 particles in Zn-Co, Zn-Ni and Zn-Fe plating baths and found that SiO_2 content increased with increasing

Fe group metal salt concentration. The reason why Ag nano-particles are able to deposit in the Sn-Cu-citrate bath but not the Cu-citrate bath may be due to the differences in $\text{CuCl}_2 \cdot 2\text{H}_2\text{O}$ concentration. The effects of metal ions concentration on particle surface charge were studied by different researchers. Lee and Wan (1988) investigated zeta potentials of $\alpha\text{-Al}_2\text{O}_3$ in a dilute Cu sulfate bath (less than 0.1 mol/L) and determined that $\alpha\text{-Al}_2\text{O}_3$ had a positive surface charge when the concentration of CuSO_4 was between 0.053 mol/L and 0.08 mol/L. Hayashi et al. (1993) studied the co-deposition of $\alpha\text{-Al}_2\text{O}_3$ particles from a more concentrated Cu sulfate bath (0.5 mol/L) and observed that the surface charge of $\alpha\text{-Al}_2\text{O}_3$ was negative, due to strong anion adsorption. The same phenomenon may happen for the Ag nano-particles in Cu-citrate baths. It is possible that in concentrated Cu-citrate baths, Ag nano-particles carry a negative surface charge, while in dilute Cu-citrate baths, Ag nano-particles carry a positive surface charge. Therefore, in the concentrated Cu-citrate bath (0.22 mol/L), negatively charged Ag nano-particles were inhibited from co-deposition due to the repulsive forces from species having the same charge as the negatively charged cathode. In the Sn-Cu-citrate bath, the Cu ion concentration was much more dilute (0.001-0.003 mol/L), so that positively charged Ag nano-particles were attracted to the cathode to be co-deposited. With a higher $\text{CuCl}_2 \cdot 2\text{H}_2\text{O}$ concentration in the bath (0.003 mol/L), but still a low $\text{CuCl}_2 \cdot 2\text{H}_2\text{O}$ concentration relative to the Cu-citrate bath, more Ag nano-particles were able to carry a positive charge, giving a higher Ag content (Fig. 6-7).

6.3.3 Effect of SDS

The above research work showed that both Cu and Ag content in Sn-Ag-Cu films increased or decreased with an increase or decrease of $\text{CuCl}_2 \cdot 2\text{H}_2\text{O}$ concentration. In addition, both Cu and Ag content decreased as current density increased. This behaviour made it difficult to obtain the desired eutectic Ag (3.5 wt%) and Cu (0.7 wt%) compositions in the deposits, by changing current density and $\text{CuCl}_2 \cdot 2\text{H}_2\text{O}$ concentration. In order to decouple the co-deposition of Ag

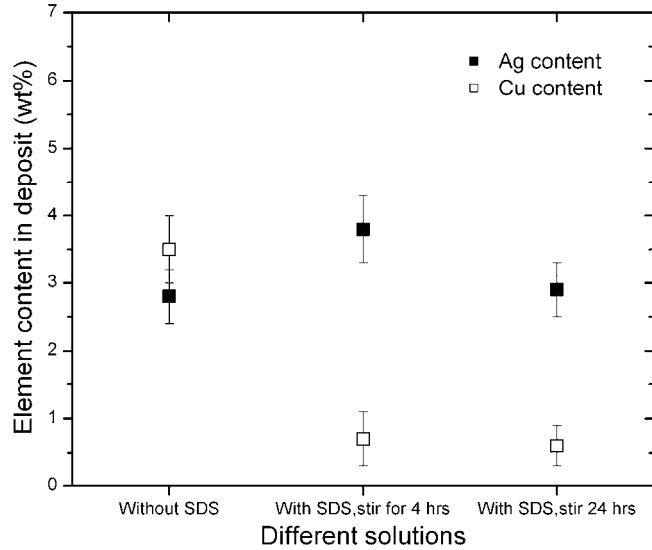


Fig. 6-15 Deposit Ag and Cu content from suspensions without and with SDS and with different stirring times. The concentrations of $\text{SnCl}_2 \cdot 2\text{H}_2\text{O}$, tri-ammonium citrate, $\text{CuCl}_2 \cdot 2\text{H}_2\text{O}$, Ag, and SDS were fixed at 0.22 mol/L, 0.30 mol/L, 0.001 mol/L, 0.8 g/L, and 0.1 g/L, respectively. The current density was 10 mA/cm^2 .

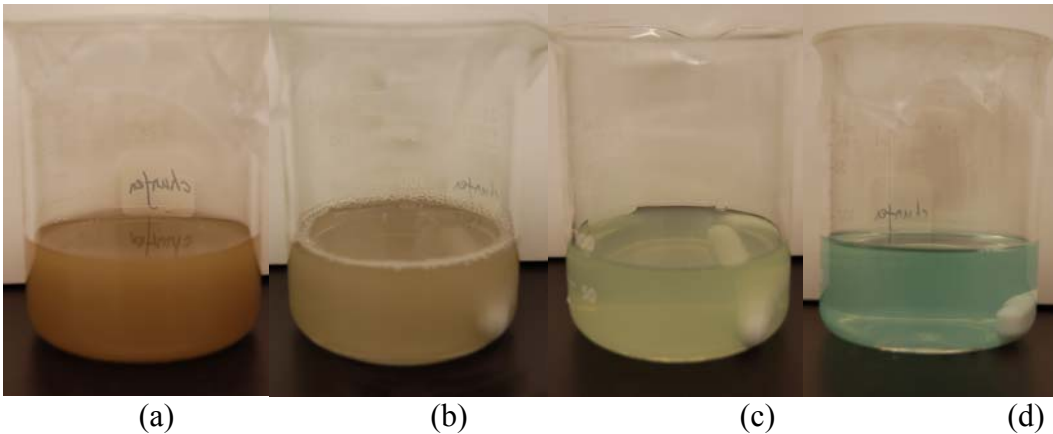


Fig. 6-16 Solutions after stirring for different times: (a) Sn-Cu-citrate + Ag, stirred for 1 hour; (b) Sn-Cu-citrate + Ag + SDS, stirred for 1 hour; (c) Sn-Cu-citrate + Ag + SDS, stirred for 4 hrs; (d) Sn-Cu-citrate + Ag + SDS, stirred for 24 hrs.

nano-particles with Cu ions, and to achieve the desired eutectic Sn-Ag-Cu film composition, sodium dodecyl sulfate (SDS) was used and its effects on Sn-Ag-Cu film composition were studied. Fig. 6-15 shows deposit Cu and Ag content in Sn-Ag-Cu films from suspensions without and with SDS additions, plated at a current

density of 10 mA/cm². Without SDS, the Cu content was about 3.5wt% and Ag content was about 2.8 wt%. After adding SDS and stirring the solution for 4 hours, Ag content increased to about 3.8 wt%, while Cu content decreased to about 0.7 wt%, which was lower than the Cu content in Sn-Cu films from Sn-Cu-citrate solutions (Fig. 6-11a). The addition of SDS and extended agitation accelerated Ag deposition slightly and made Cu ions more difficult to reduce. It was also noticed that after the suspension was stirred for 24 hours, the suspension became almost clear, as shown in Fig. 6-16. EDX analysis for the as-deposited Sn-Ag-Cu film deposited from the suspension with SDS stirred for 24 hours showed that Ag content decreased to about 2.9 wt%, while Cu content was about 0.6 wt% (Fig. 6-15). The changes in Sn-Cu-citrate suspension with Ag nano-particles after SDS was added and after the suspension was stirred for different lengths of time is shown in Fig. 6-16. Without SDS, the Sn-Cu-citrate suspension with Ag nano-particles was cloudy with a light brown color. After SDS was added and the suspension was stirred for 1 hour, the suspension became less cloudy and had an olive green color. After stirring for 4 hours, the suspension became light green. After stirring for 24 hours, the suspension had a blue color and was clear. The Sn-Cu-citrate solution without any Ag nano-particles was also blue in color and clear. Therefore, the SDS had the desired effect of dispersing any agglomerated Ag particles.

Fig. 6-17 shows SEM SE images of the Sn-Ag-Cu films studied in Fig. 6-15. With the addition of SDS and after the suspension was stirred for 4 hours, as deposited Sn-Ag-Cu films became less smooth. After stirring for 24 hours, cubic shape particles formed and no Cu was detected in these grains.

The effects of CuCl₂·2H₂O and Ag concentration on deposit Cu and Ag content from suspensions with SDS addition and after stirring for 24 hours, were studied and the results are shown in Fig. 6-18. As Ag particle concentration in suspension increased, Ag content in the deposit increased. However, there was little effect on Cu content. As CuCl₂·2H₂O concentration in the suspension increased from 0.001 mol/L to 0.003 mol/L, both Cu and Ag content in the deposits increased. SEM SE images of Sn-Ag-Cu films deposited from these

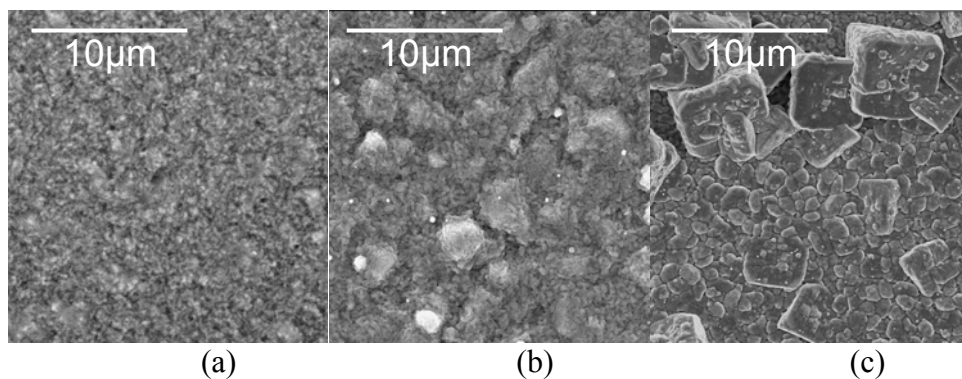


Fig. 6-17 SEM SE plan view images of Sn-Ag-Cu films deposited onto Au seed layers from 80mL suspensions: (a) Sn-Cu-citrate + Ag, stirred for 1 hour; (b) Sn-Cu-citrate + Ag + SDS, stirred for 4 hrs; (c) Sn-Cu-citrate + Ag + SDS, stirred for 24 hrs. The concentrations of $\text{SnCl}_2 \cdot 2\text{H}_2\text{O}$, tri-ammonium citrate, $\text{CuCl}_2 \cdot 2\text{H}_2\text{O}$, Ag, and SDS were fixed at 0.22 mol/L, 0.30 mol/L, 0.001 mol/L, 0.8 g/L, and 0.1g/L, respectively. The current density was 10 mA/cm^2 .

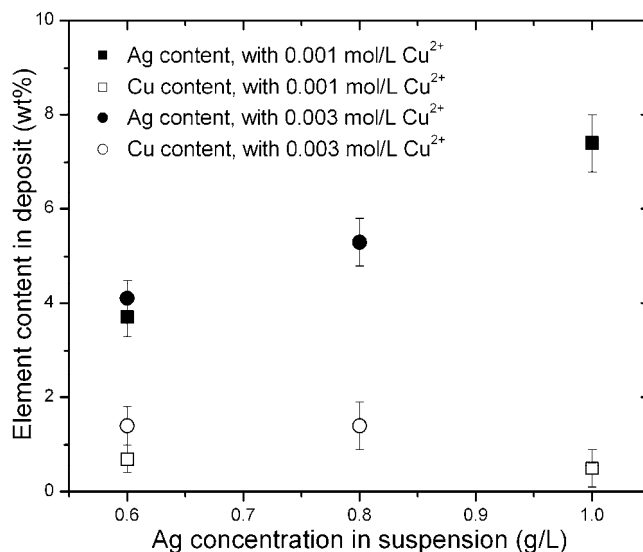


Fig. 6-18 Deposit Ag and Cu content as a function of Ag concentration in 80 mL Sn-Cu-citrate + Ag + SDS suspensions. The concentrations of $\text{SnCl}_2 \cdot 2\text{H}_2\text{O}$, tri-ammonium citrate, and SDS were fixed at 0.22 mol/L, 0.30 mol/L, and 0.1g/L, respectively. The suspensions were stirred for 24hrs. The current density was 10 mA/cm^2 .

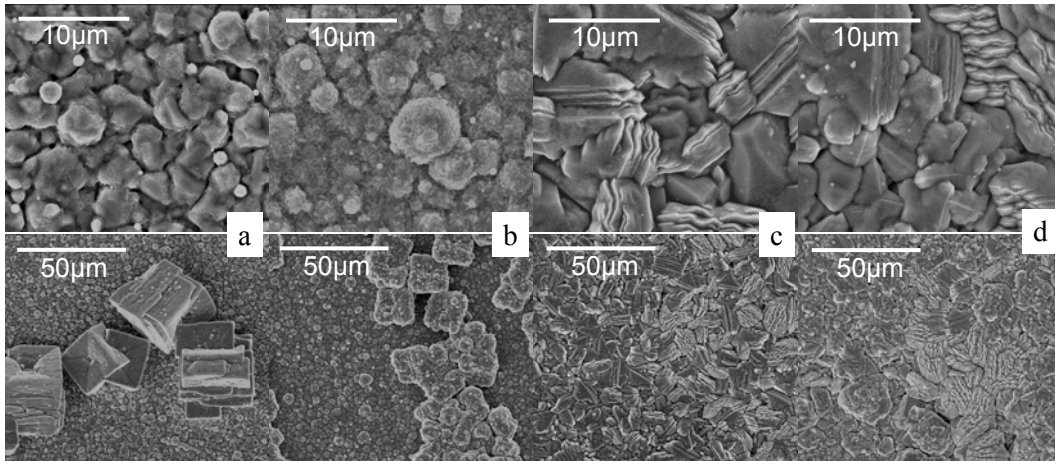


Fig. 6-19 SEM SE plan view images of Sn-Ag-Cu films deposited onto Au seed layers from 80 mL Sn-Cu-citrate + Ag + SDS suspensions: (a) 0.001 mol/L $\text{CuCl}_2 \cdot 2\text{H}_2\text{O}$ + 0.6 g/L Ag; (b) 0.001 mol/L $\text{CuCl}_2 \cdot 2\text{H}_2\text{O}$ + 1 g/L Ag; (c) 0.003 mol/L $\text{CuCl}_2 \cdot 2\text{H}_2\text{O}$ + 0.6 g/L Ag; (d) 0.003 mol/L $\text{CuCl}_2 \cdot 2\text{H}_2\text{O}$ + 0.8 g/L mol/L Ag. The concentrations of $\text{SnCl}_2 \cdot 2\text{H}_2\text{O}$, tri-ammonium citrate, and SDS were fixed at 0.22 mol/L, 0.30 mol/L, and 0.1g/L, respectively. The suspensions were stirred for 24 hrs. The current density was 10 mA/cm².

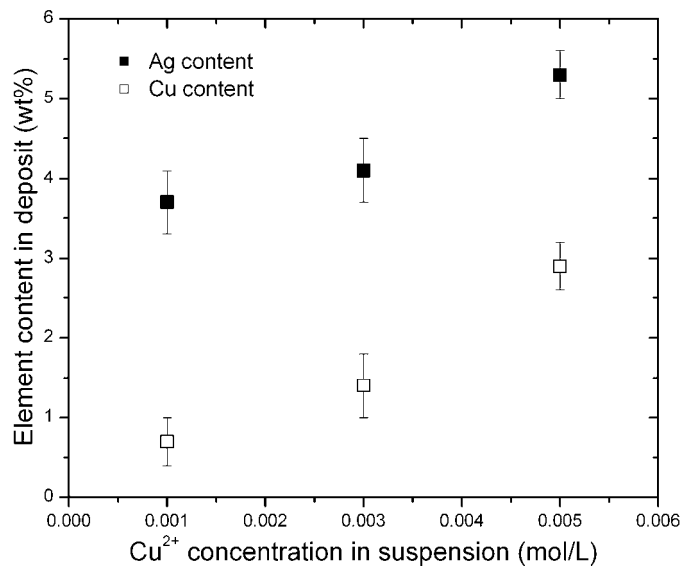


Fig. 6-20 Deposit Ag and Cu content as a function of $\text{CuCl}_2 \cdot 2\text{H}_2\text{O}$ concentration in 80 mL Sn-Cu-citrate + Ag + SDS suspensions. The concentrations of $\text{SnCl}_2 \cdot 2\text{H}_2\text{O}$, tri-ammonium citrate, Ag, and SDS were fixed at 0.22 mol/L, 0.30 mol/L, 0.6 g/L, and 0.1g/L, respectively. The suspensions were stirred for 24 hrs. The current density was 10 mA/cm².

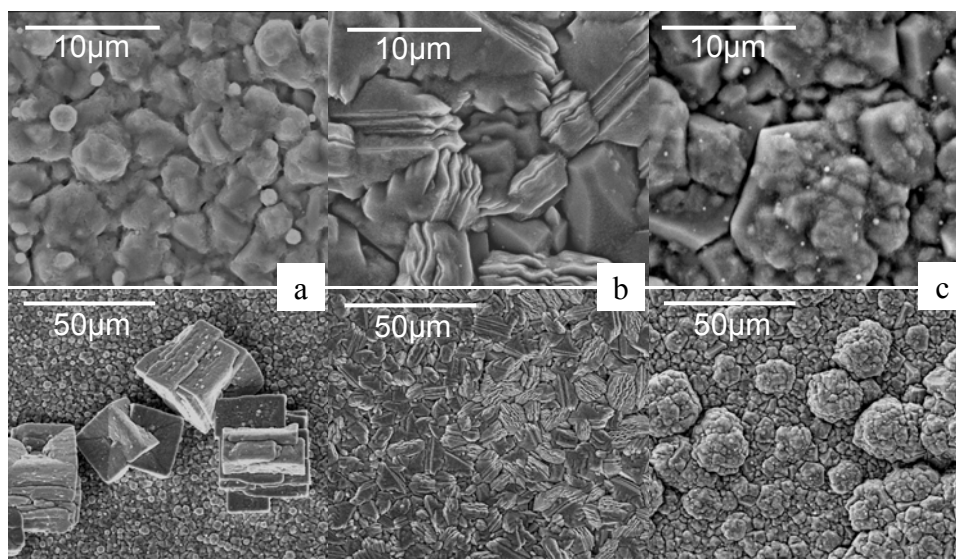


Fig. 6-21 SEM SE plan view images of Sn-Ag-Cu films deposited onto Au seed layers from 80 mL Sn-Cu-citrate + Ag + SDS suspensions with different $\text{CuCl}_2 \cdot 2\text{H}_2\text{O}$ concentrations: (a) 0.001 mol/L; (b) 0.003 mol/L; (c) 0.005 mol/L. The concentrations of $\text{SnCl}_2 \cdot 2\text{H}_2\text{O}$, triammonium citrate, Ag; and SDS were fixed at 0.22 mol/L, 0.30 mol/L, 0.6 g/L; and 0.1 g/L, respectively. The suspensions were stirred for 24 hrs. The current density was 10 mA/cm^2 .

suspensions are shown in Fig. 6-19. When the Cu concentration is as low as 0.001 mol/L (Fig. 6-19a and b), a discontinuous layer of grains (no Cu detected) was formed on the surface. Higher Ag concentrations in the solution (Fig. 6-19b) gave irregular cubic shaped deposits. When the $\text{CuCl}_2 \cdot 2\text{H}_2\text{O}$ concentration was 0.003 mol/L (Fig. 6-19c and d), no such layer was found and deposits formed larger size clusters. To further confirm the effect of $\text{CuCl}_2 \cdot 2\text{H}_2\text{O}$ concentration on deposit Cu and Ag contents, more experiments were carried out and the results are shown in Fig. 6-20. Both Cu and Ag content increased as $\text{CuCl}_2 \cdot 2\text{H}_2\text{O}$ concentration in suspension increased. Compared to Fig. 6-7 and Fig. 6-8, the addition of SDS and stirring for 24 hours resulted in lower Cu content in as-deposited Sn-Ag-Cu films. The amount decreased from 3.5-6.3 wt% to 0.7-1.4 wt% with 0.001-0.003 mol/L $\text{CuCl}_2 \cdot 2\text{H}_2\text{O}$ addition, while no significant change was found for the Ag content. The addition of SDS did not significantly affect Ag co-deposition, but made Cu ions more difficult to reduce. When $\text{CuCl}_2 \cdot 2\text{H}_2\text{O}$ concentration was increased, the Ag content increased, which means that the Cu ions still had similar effects on the

Ag particle surface charge as for Sn-Ag-Cu baths without SDS. SEM images for as-deposited Sn-Ag-Cu films are shown in Fig. 6-21. As with Fig. 6-19, as $\text{CuCl}_2 \cdot 2\text{H}_2\text{O}$ concentration was increased, cubic shaped Sn-Ag particles disappeared and large, agglomerated clusters formed.

6.3.4 DSC thermal analysis

DSC thermal analysis was carried out to study the melting behavior of as-deposited Sn-Ag-Cu alloys. Fig. 6-22 shows a comparison of DSC curves of an as-deposited Sn-Ag-Cu alloy on a Au seed layer (curve a), an as-deposited Sn-Cu alloy on a Au seed layer (curve b) and an as-deposited Sn-Cu alloy on Ni substrate (curve c). The Sn-1.1Cu solder alloy was prepared using Sn-Cu-citrate solutions developed in Chapter 3. Only one endothermic peak was observed in both curve (a) and curve (b). This peak is due to the heat of fusion of the alloy. The temperature corresponding to the start of melting, i.e., the solidus temperature of the alloy, was about 203.7°C for the Sn-4.9Ag-1.1Cu deposit, which is about

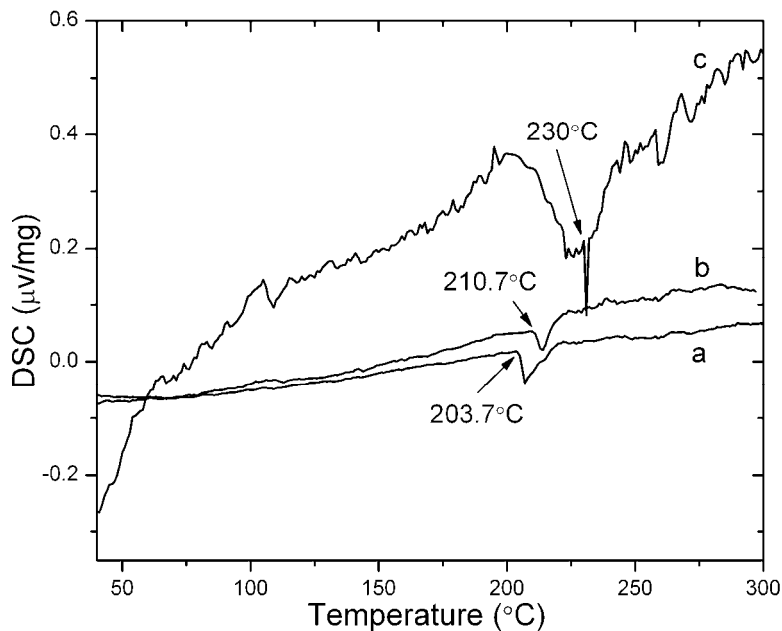


Fig. 6-22 Comparison of DSC curves of as-deposited Sn-Ag-Cu films on Au seed layers and as-deposited Sn-Cu alloys on Au seed layers and Ni substrates. (a) Sn-4.9Ag-1.1Cu/Au; (b) Sn-1.1Cu/Au; (c) Sn-1.1Cu/Ni.

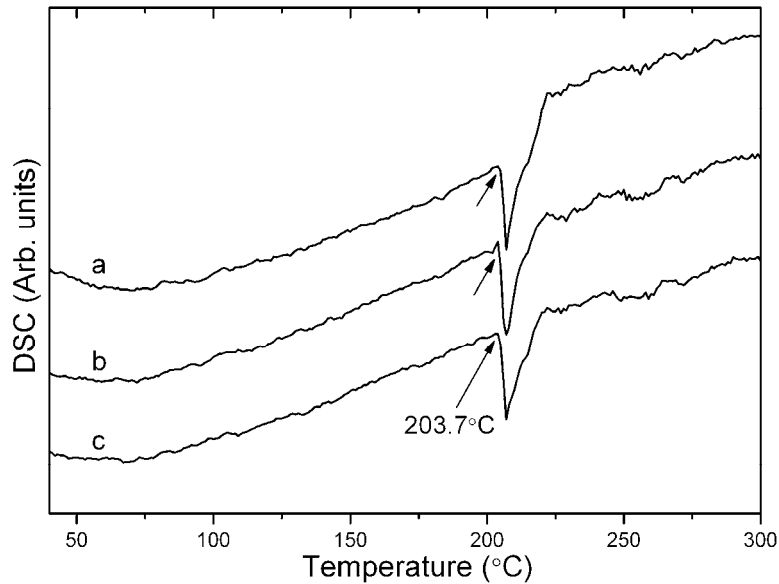


Fig. 6-23 DSC curves of as-deposited Sn-Ag-Cu films on Au seed layers with various compositions. (a) Sn-3.3Ag-1.1Cu; (b) Sn-3.6Ag-1.4Cu; (c) Sn-4.9Ag-1.4 Cu.

13°C lower than the reported eutectic Sn-Ag-Cu melting temperature (217°C), and about 210.7°C for Sn-1.1Cu deposits which is about 16°C lower than the eutectic Sn-0.7Cu melting temperature (227°C). One possible reason is that for both, Sn is the main phase. The Au seed layer (200 nm) can alloy with Sn which decreases the melting point of both alloys. In order to confirm the effect of Au seed layer, DSC analysis for a Sn-1.1Cu alloy on a Ni seed layer (2.5 μm thick) was carried out (Fig. 6-22c). The slow decrease before the sharp peak indicates reaction between the Sn-1.1Cu deposit and the Ni substrate to form intermetallic compounds. A sharp peak starts at about 230°C corresponding to the solidus temperature, which is much higher than the solidus temperature for the Sn-1.1Cu alloy on the Au seed layer.

Fig. 6-23 shows DSC curves for as-deposited Sn-Ag-Cu alloys, with various compositions, on Au seed layers. All three Sn-Ag-Cu alloys showed the same solidus temperature, about 203.7°C. The temperature of 203.7°C is lower than the eutectic temperature of Sn-Ag-Cu alloy reported, which is due to the alloying effect of the Au seed layer. The same situation that Sn-Ag-Cu alloys with

various compositions showed the same solidus temperature was also reported by Arai and Kaneko (1997).

6.4 Conclusions

Eutectic and near eutectic Sn-Ag-Cu solder films were attainable from Sn-Cu-citrate suspensions with Ag nano-particles. Deposit Ag and Cu contents decreased with increasing current density, or decreasing $\text{CuCl}_2 \cdot 2\text{H}_2\text{O}$ concentration. When deposit Ag content is about 3.5 wt%, deposit Cu content is 1.8-4.8 wt%. When deposit Cu content is about 0.7 wt%, deposit Ag content is 2.1-2.5 wt%. The plating rate for Sn-Ag-Cu films can reach as high as 67 $\mu\text{m/hr}$ with a deposit composition of 0.7 wt% Cu and 2.5 wt% Ag. By adding Ag nano-particles into the Sn-Cu-citrate solutions, Cu content increased and film plating rate decreased slightly. Copper content in Sn-Ag-Cu films increased more with higher $\text{CuCl}_2 \cdot 2\text{H}_2\text{O}$ concentration compared with the Cu content in Sn-Cu films with similar $\text{CuCl}_2 \cdot 2\text{H}_2\text{O}$ concentrations.

The addition of sodium dodecyl sulfate (SDS) helped disperse the Ag nano-particles. With the addition of SDS, a Sn-3.8 wt% Ag-0.7 wt% Cu near-eutectic composition was attainable. It was also noticed that increased stirring for Sn-Cu-citrate suspensions, with Ag nano-particles and SDS, resulted in clearer suspensions and lower deposit Cu content. Copper was distributed unevenly in Sn-Ag-Cu films and a discontinuous layer of Sn-Ag cubic shaped grains formed on the surface.

The as-deposited Sn-Ag-Cu solder films with various compositions on Au seed layer have a solidus temperature of about 203.7°C, which is lower than the eutectic temperature of 217°C. The as-deposited Sn-Cu solder films on Au seed layer have a solidus temperature of about 210.7°C, which is lower than the eutectic temperature of 227°C. The same Sn-Cu solder films on Ni substrates have a much higher solidus temperature of about 230°C. One possible reason is the Au seed layer alloys with the Sn which decreases the melting temperature.

Chapter 7 Interfacial reactions between Pb-free Sn-based solders and substrates

7.1 Introduction

During soldering, interdiffusion and reactions between the molten solder and conductor metals occur. The substrate metal dissolves into the molten solder and simultaneously the active constituents in the solder combine with the substrate metal to form IMCs at the solder/substrate interface (Shangguan, 2005). The completion of the formation of IMCs is so called solder joint interconnection. As discussed in Chapter 2, the formation of a thin, continuous and uniform IMCs layer is necessary for good bonding (Abteu and Selvaduray, 2000; Kim et al., 2003). However, due to their inherent brittle nature and tendency to generate structural defects because of the microstructural mismatch between solder and metallization, IMC layers that are too thick (caused by excessive interfacial reactions during soldering operation or in use) are sensitive to stress and sometimes provide sites for the initiation and propagation of cracks (Kim et al., 2005; Laurila et al., 2005). This may lead to poor joint strength and degrade the long term reliability of solder joints (Laurila et al., 2005; Shangguan, 2005; Ipser et al., 2007). Moreover, the IMCs layer will become thicker during thermal aging due to solid state diffusion (Yu et al., 2008). Therefore, it is important to study the formation and growth of IMCs layers during high temperature reflow and aging.

Many studies have been performed on the interfacial reaction and growth mechanism of IMCs between Pb-free solders and Cu and/or Ni during reflow and/or aging, which have been reviewed in Chapter 2. In the Sn-Cu system, Cu_3Sn and Cu_6Sn_5 are the two IMCs formed at the Sn/Cu interface. For the Sn-Ni system, three intermetallic phases, i.e., Ni_3Sn , Ni_3Sn_2 , and Ni_3Sn_4 , are stable at temperatures below 300°C, and only the Ni_3Sn_4 phase is frequently found in the Sn/Ni couples (Marinkovic and Simic, 1982; Chen et al., 1998; Chen et al., 2003).

When a small amount of Cu was added to a Sn-rich solder to form a Cu-bearing solder, such as Sn-Cu and Sn-Ag-Cu solders, ternary IMCs consisting of Sn, Cu and Ni formed after reacting with Ni substrate. It was also found that as Cu concentration in the solder increased, the IMCs formed at the solder/Ni interface changed from $(\text{Ni,Cu})_3\text{Sn}_4$ phase to $(\text{Cu,Ni})_6\text{Sn}_5$ phase (Chen et al., 2002; Ho et al., 2002; Luo et al., 2005; Ho et al., 2007). In the Sn-Ag system, only orthorhombic Ag_3Sn exists as an IMC. Large Ag_3Sn intermetallic plates ($>30 \mu\text{m}$ in length) were reported to form at the Sn-Ag-Cu solder/substrate interface (Kang et al., 2003; Kim et al., 2003; Kang et al., 2005). These were believed to be harmful to the mechanical properties of the solder joints by inducing brittle fracture or providing crack initiation sites (Lee et al., 2002; Kim et al., 2003; Anderson, 2007). Higher populations of large Ag_3Sn plates were found in Sn-Ag-Cu solders with higher Ag content (Kang et al., 2003; Kim et al., 2003).

The objective of this chapter is to investigate interfacial reactions between Pb-free, Sn-based solders (Sn-Cu and Sn-Ag-Cu solder films) and substrates (Cu and Ni) during reflow and aging. Most solders used to study interfacial reactions previously were from commercial solder pastes and solder balls, or pure metals assembled with specific compositions. In this study, near eutectic Sn-Cu solder films (Sn-1.1Cu) were electrodeposited from Sn-Cu-citrate solutions developed in Chapter 3 and near eutectic Sn-Ag-Cu solder films (Sn-3.6Ag-1.8Cu) were deposited from Sn-Cu-citrate suspensions with Ag nano-particles developed in Chapter 6. Both the solder (Sn-Cu, Sn-Cu-Ag) and substrate (Cu, Ni) layers are thick enough to provide a sufficient supply of material for reactions during reflow and aging. For Pb-free solders, reflow processing requires temperatures at least 30°C higher than the melting point (Dariavach et al., 2006). The melting points of Sn-0.7Cu and Sn-3.8Ag-0.7Cu are in the range of $221\text{--}227^\circ\text{C}$, so that 260°C was chosen as the reflow temperature. Compared to Pb-Sn solder, the higher reflow temperature plus the higher Sn content for both the Sn-Cu and Sn-Ag-Cu solders increase the potential for IMC growth and substrate dissolution at the solder/substrate interface (Dariavach et al., 2006). Microstructural characterization was carried out for Sn-Cu and Sn-Ag-Cu solder films on both Cu

and Ni substrates after reflowing and aging for different lengths of time to better understand the formation and growth of IMCs layers in Sn-Cu/Cu, Sn-Cu/Ni, Sn-Ag-Cu/Cu, and Sn-Ag-Cu/Ni systems.

7.2 Experimental materials and procedures

The Sn-Cu-citrate solutions were prepared by dissolving 0.30 mol/L tri-ammonium citrate ((NH₄)₃C₆H₅O₇, Alfa Aesar, 98%) in deionized water and then dissolving 0.22 mol/L SnCl₂·2H₂O (Fisher Scientific) and 0.003 mol/L CuCl₂·2H₂O (Fisher Scientific) in the citrate solution (Chapter 3). The deionized water was obtained from an Aqua MAX™-ultra purification system. Silver particles (Sigma-Aldrich, 100 nm in size) were added to the above Sn-Cu-citrate solution to a concentration of 0.8 g/L after the solution was stabilized for about 1 hour. Ultrasonic dispersion (BRANSON 2510 Ultrasonic Cleaner) and overhead mechanical agitation (Caframo BDC 3030 stirrer, 20-3000 rpm) were used to help disperse the Ag particles.

Silicon wafer pieces, metallized with a 25 nm TiW adhesion layer and a 200 nm Au seed layer, were used for deposition on Au. A Ni layer (~6 μm thick) electroplated from a standard Watts Ni plating solution onto Au was utilized for deposition on Ni. Two different kinds of Cu materials were used for deposition on Cu. At the beginning of the work, sectioned Cu sheet (~2 mm thick) was used as the Cu substrate for Sn-Cu electrodeposition on Cu, which is noted in the figure captions for the specific samples. Before plating, Cu pieces from the sectioned Cu sheet were cleaned and any surface oxide layers were removed by treating in a CuCl₂ + H₂SO₄ solution for about 20 seconds, followed by rinsing with deionized water. A low speed diamond saw (Model 650, South Bay Technology, Inc.) was used to cut the Sn-Cu/Cu samples into pieces with the desired size to make cross section samples. In order to simplify the process of making cross section samples, cleaving was used instead of cutting. Copper layers (~6 μm thick) were electrodeposited from a Cu-citrate solution (containing 0.30 mol/L tri-ammonium citrate and 0.22 mol/L CuCl₂·2H₂O) onto Au metallized Si wafer pieces. Silicon

wafer pieces, metallized with a 25 nm TiW adhesion layer and a 200 nm Pt seed layer, were used as anodes. Before plating, both Au and Pt seed layers were cleaned ultrasonically for 2 minutes in acetone followed by cleaning in ethanol and then rinsing with deionized water.

A Dynatronix DuPR 10-0.1-0.3 pulse plating power supply was used to PC plate Sn-Cu, Sn-Ag-Cu, and Cu, with a 2 ms forward on-time and 8 ms forward off-time, and to DC plate the Ni. All the Sn-Cu solder films were plated at a current density of 10 mA/cm² for 20 min without agitation and Sn-Ag-Cu solder films were plated at a current density of 40 mA/cm² for 8 min with a stirring speed of 600 rpm. Copper was plated at a current density of 10 mA/cm² for 30 min without agitation. All electrodeposition of Sn-Cu, Sn-Ag-Cu and Cu was done at room temperature. Nickel was plated at a current density of 50 mA/cm² for 10 min. The temperature was kept at 50°C and the stirring speed was set at 80 rpm using a magnetic stirrer and hot plate (CORNING PC-220).

A RC2400 Bio-Rad alloying furnace was used to reflow and age Sn-Cu and Sn-Ag-Cu samples. The reflow process was done in a forming gas (95 vol% N₂ + 5 vol% H₂) atmosphere with a heating rate of 400°C/min and a cooling rate of 100°C/min. The as-deposited samples were reflowed at 260°C for 30-90 s. The aging treatment was carried out for reflowed samples by keeping the temperature at 125°C, which is a typical aging temperature used in literature (Lee et al., 2002; Pang et al., 2004; Fix et al., 2005), for 24, 48 and 72 hrs in the same forming gas atmosphere.

The microstructure and composition of the Sn-Ag-Cu films were characterized using a Hitachi H2700 scanning electron microscope (SEM) equipped with an ultrathin window energy dispersive x-ray (EDX) spectrometer. Deposit compositions were found by averaging measurements taken from at least three regions, each 400×400 μm² in size. Analysis was done at 20 kV with a working distance of 17 mm and a count rate of 2500-4000 counts/s. A JEOL JAMP-9500F field emission Auger microprobe, operating at a primary electron beam energy of 15 keV and a probe current of about 6 nA, was also used to collect Auger spectra and take SE images at high magnification. Samples were

tilted about 30° away from the primary beam toward the axis of the electron analyzer. Cross section samples were made by cleaving using a diamond pen or cutting using a diamond saw. After sectioning, the samples were mounted with epoxy resin, then ground with SiC papers (240, 320, 400, 600, 1200 and 4000 grit) in sequence in cold water and finally polished with a 0.05 µm diameter Al₂O₃ particle suspension. Phase analysis was performed using thin film XRD with a Rigaku rotating Co anode system, operating in continuous scanning mode at a voltage of 40 kV and a current of 160 mA. The samples were scanned from 20° to 100° at a rate of 3°/min. Transmission electron microscopy using a JEOL 2010 TEM, operated at 200 kV, was used to identify Sn, Cu and Ag IMCs. Two different methods were used to prepare TEM samples. Cross section samples were prepared by mechanical dimpling (Fischione Model 150) followed by sputtering. After dimpling to a central thickness of about 20 µm, a sample was sputtered using an ion mill (Fischione, Model 1010) operating at 5 kV and 0.5 mA per gun with an initial angle (ion beam to the surface) of 10°. Near completion, the operation voltage was decreased to 3.5 kV, the current was kept the same, and the angle was decreased to 6°. The sample was liquid nitrogen cooled during sputtering to reduce preferential sputtering effects and to prevent specimen heating. The whole ion milling process took about 3-4 hours. An extraction method was also used to prepare TEM sample. A reflowed Sn-Ag-Cu sample was dipped in an etching solution (2%HCl + 5%HNO₃ + 93%CH₃OH) for 5 seconds to expose IMCs particles and then was coated with evaporated carbon. The carbon coating on the surface of the sample was sectioned in pieces (~1 mm x 1 mm) using a scalpel. The sample was immersed in a similar, but more concentrated etching solution (4%HCl + 10%HNO₃ + 86%CH₃OH), so that the matrix under the carbon would dissolve and release the carbon pieces. Carbon pieces, with extracted IMCs, were captured with carbon coated Cu grids, which were rinsed with ethanol and allowed to dry.

7.3 Results and discussion

7.3.1 Interfacial reactions between Sn-Cu solder and Cu and Ni substrates during reflow and aging

7.3.1.1 Sn-Cu solder and Cu substrate

Near eutectic Sn-Cu (1.1 wt% Cu) solder films were electrodeposited onto Cu substrates. After reflow at 260°C for 90s, the entire sample surface was covered with melted solder that had resolidified. Fig. 7-1a (low magnification) and b (high magnification) show SEM BSE cross section images of the Sn-Cu/Cu after reflow and resolidification. The low contact angle shown in Fig. 7-1a indicates that the Sn-Cu solder has good wettability to the Cu substrate. At high magnification (Fig. 7-1b), two continuous layers were observed at the interface between the Cu and Sn-Cu solder. In order to further study the interfacial layers, an etching solution (2%HCl + 5%HNO₃ + 93%CH₃OH) was used to selectively etch the Sn matrix away, and the corresponding SEM BSE cross section image of the reflowed Sn-Cu/Cu sample after etching for 5 seconds is shown in Fig. 7-1c. There are two continuous layers of IMCs formed between the Cu substrate and the Sn-Cu solder. One layer is very thin and is adjacent to the Cu substrate; it possesses a darker color and has a composition of 62 wt% Cu (~75 at% Cu)

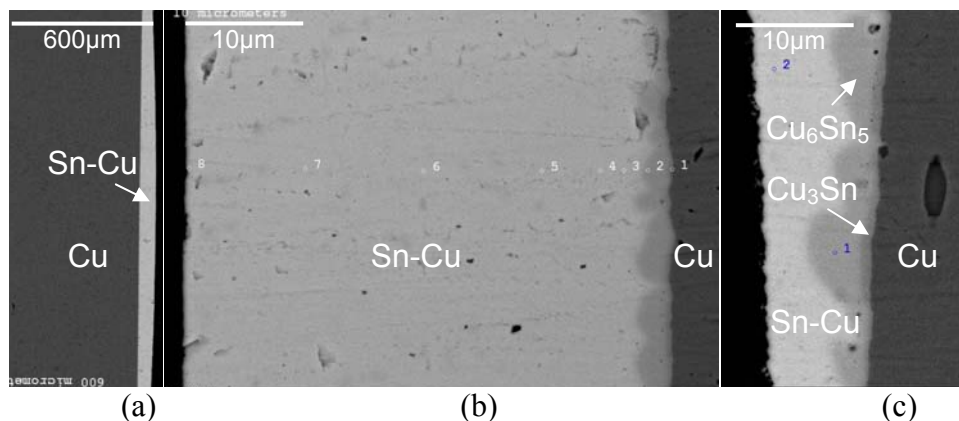


Fig. 7-1 SEM BSE cross section images of Sn-Cu films electrodeposited onto Cu substrate (from sectioned Cu sheet) after reflow at 260°C for 90 s: (a) Sn-Cu/Cu, low magnification; (b) Sn-Cu/Cu, higher magnification,; (c) Sn-Cu/Cu after etching most of the solder layer.

which is close to Cu_3Sn . The other layer is thicker and between the Cu_3Sn layer and the Sn-Cu solder. It is characterized by a brighter color and has a composition of 40 wt% Cu (55 at% Cu) which is close to Cu_6Sn_5 .

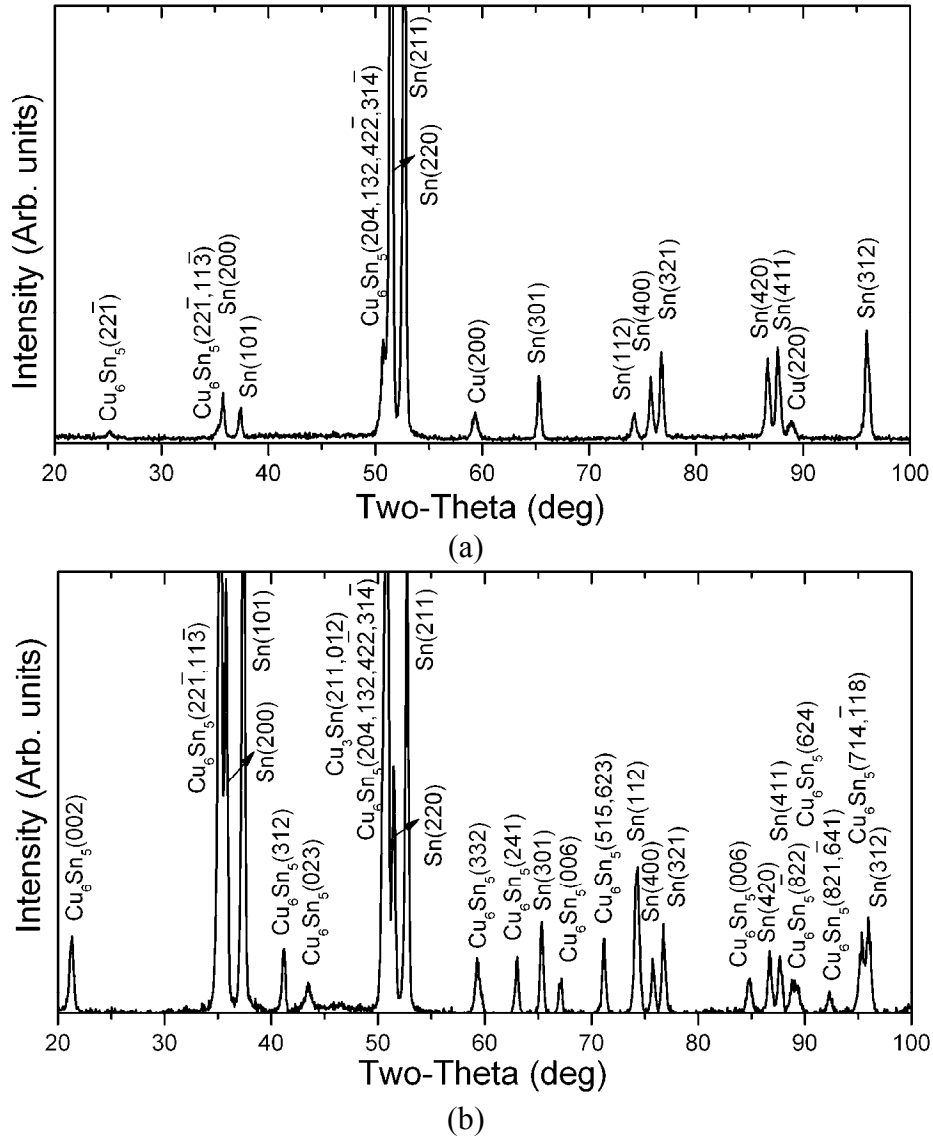


Fig. 7-2 XRD patterns of Sn-Cu films electrodeposited onto Cu substrate (from sectioned Cu sheet): (a) as-deposited, (b) after reflow at 260°C for 90 s.

XRD analysis was carried out to verify the phases in the Sn-Cu/Cu system before and after reflow and the results are shown in Fig. 7-2. Before reflow (Fig. 7-2a), three different phases were detected. Copper peaks at 59.3° and 88.9° were

from the Cu substrate. The main phase in the Sn-Cu deposit was Sn with a small amount of Cu_6Sn_5 . After reflow (Fig. 7-2b), the Cu_6Sn_5 peaks increased in intensity and additional Cu_6Sn_5 peaks were detected, indicating that more Cu_6Sn_5 formed during reflow. In addition, a Cu_3Sn peak was detected at about 50.8° . In order to study the effect of reflow on Cu distribution along the cross section, EDX point analysis at the positions shown in Fig. 7-1b was performed and the results are shown in Fig. 7-3. Compared to the EDX analysis results before reflow, which are marked as open points in Fig. 7-3, the Cu content at the interface increased dramatically after reflow (marked as solid points). This is due to the dissolution of Cu into the molten Sn-Cu solder and the formation of Cu_6Sn_5 and Cu_3Sn IMCs during reflow. Copper content further away from the interface increased as well, which is due to the diffusion of Cu in the liquid Sn phase during reflow.

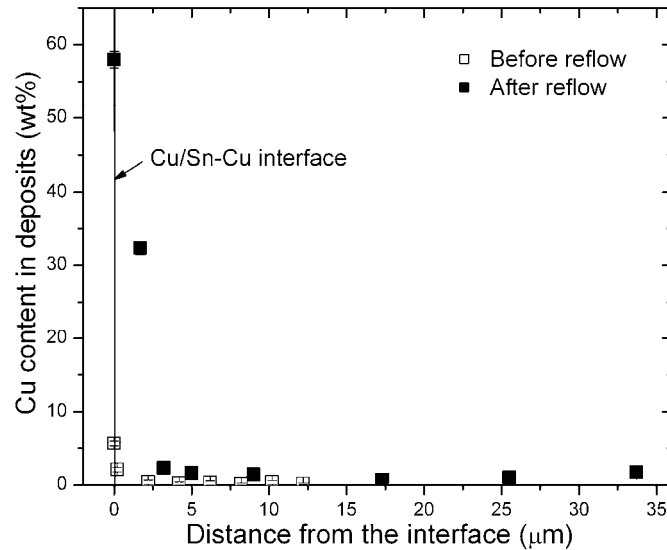


Fig. 7-3 Deposit Cu distribution in Sn-Cu films electrodeposited onto Cu substrate (from sectioned Cu sheet) along the cross section before and after reflow at 260°C for 90 s.

To further understand interdiffusion and reactions at Sn-Cu/Cu interface during reflow, half of the surface of a Cu coated Si wafer piece was coated with evaporated C to serve as a marker, prior to Sn-Cu electrodeposition. A schematic illustration is shown in Fig. 7-4a. After the Sn-Cu solder film was electrodeposited onto the partially C coated Cu, the whole sample was reflowed at

260°C for 30 s. SEM BSE cross section images for the reflowed sample taken at position I (with C marker) and II (without C marker) as indicated in Fig. 7-4a are shown in Fig. 7-4b and c. No intermetallic layer was found in Fig. 7-4b, which means that C was an effective and inert marker. The interface between the Sn-Cu solder and Cu at position I is marked as the original interface. In Fig. 7-4c, continuous bilayers of Cu_6Sn_5 and Cu_3Sn are present at the Sn-Cu/Cu interface without C as a barrier layer. In addition, comparison of Fig. 7-4b and Fig. 7-4c shows that after reflow at 260°C for 30 s, the Cu layer became thinner which means that Cu was consumed during reflow.

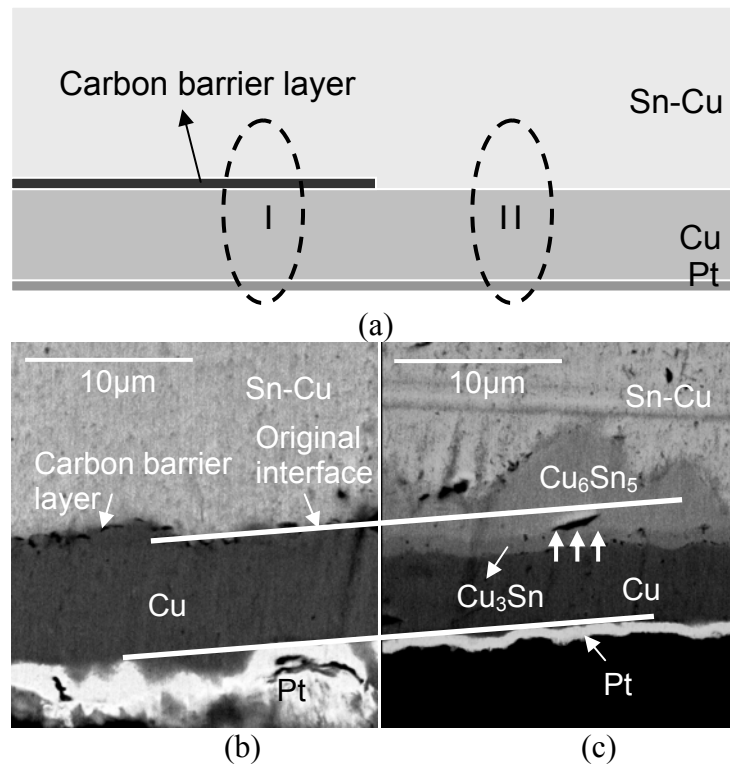


Fig. 7-4 (a) Schematic illustration of sample structure for Sn-Cu/Cu reflow analysis; (b) SEM BSE image of Sn-Cu/Cu after reflow at 260°C for 30 s at spot I in Fig. 7-4a with a carbon barrier layer; (c) SEM BSE image of Sn-0.7wt%Cu/Cu sample after reflow at 260°C for 30 s at spot II as in Fig. 7-4a without a carbon barrier layer.

A schematic illustration for the formation of the Cu_3Sn and Cu_6Sn_5 bilayer at the Sn-Cu/Cu interface during reflow is shown in Fig. 7-5. Cu_6Sn_5 is generally believed to be the first phase to form at the liquid Sn and solid Cu interface when

reflow occurs at temperatures below 260°C (Laurila et al., 2005). During the initial stages of reaction, Cu dissolves rapidly into the molten Sn and forms Cu₆Sn₅ crystallites quickly at the Sn-Cu/Cu interface, according to Reaction 7-1. These crystallites were observed by Gegliano et al. when hot Cu was dipped into molten Sn for 1 s in the temperature range from 240°C to 300°C (Gagliano et al., 2002) and they grew into a continuous layer.

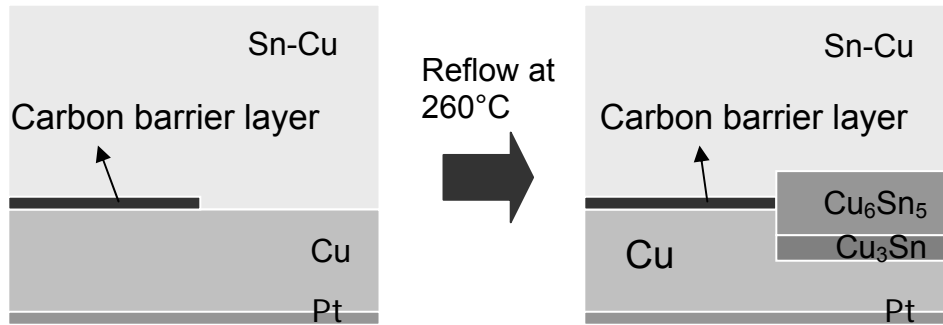


Fig. 7-5 Schematic illustration of the formation of Cu₃Sn and Cu₆Sn₅ bilayer at the Sn-Cu/Cu interface during reflow.

The Cu₃Sn layer is located between the Cu substrate and the Cu₆Sn₅ layer. The Cu atoms at the Cu/Cu₆Sn₅ interface react with Cu₆Sn₅ to form Cu₃Sn, according to Reaction 7-2 (below).



After a continuous Cu₃Sn layer forms, Cu atoms continuously diffuse through the formed Cu₃Sn layer and to the Cu₆Sn₅ layer and react with Cu₆Sn₅ to form more Cu₃Sn at the Cu/Cu₆Sn₅ interface through the consumption of some of the Cu₆Sn₅.

In order to study the growth of IMCs at Sn-Cu/Cu interface, reflowed Sn-Cu/Cu samples (260°C, 30s) were aged at 125°C for 0, 24, 48 and 72 hours, and corresponding SEM BSE cross section images are shown in Fig. 7-6. A continuous bilayer of Cu₃Sn and Cu₆Sn₅ was found in all four samples with a maximum thickness of about 3 μm. The thickness of Cu₃Sn layer increased as aging time increased, which is due to continuous diffusion of Cu from the Cu

substrate to the $\text{Cu}_3\text{Sn}/\text{Cu}_6\text{Sn}_5$ interface and continuous reaction between diffused Cu and Cu_6Sn_5 :



where $[\text{Cu}]$ represents the diffusing atom in the reaction region.

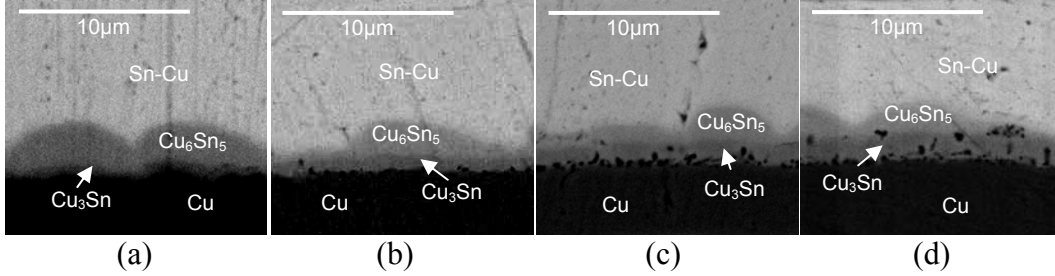


Fig. 7-6 SEM BSE cross section images of Sn-0.7wt%Cu films electrodeposited onto Cu substrate after reflow and aging: (a) reflowed at 260°C for 30 s, no aging; (b) reflowed at 260°C for 30 s and aged at 125°C for 24 hrs; (c) reflowed at 260°C for 30 s and aged at 125°C for 48 hrs; (d) reflowed at 260°C for 30 s and aged at 125°C for 72 hrs.

The Cu_6Sn_5 layer has a morphology that is scallop-shaped and highly non-planar, which makes it difficult to determine the exact thickness of the Cu_6Sn_5 layer in each sample. The maximum thickness of the Cu_6Sn_5 layer decreases as aging time is increased, which is due to the consumption of Cu_6Sn_5 to form Cu_3Sn according to Equation 7-3. It is also possible that some Cu diffuses all the way to the $\text{Cu}_6\text{Sn}_5/\text{Sn}$ interface to react with Sn to form more Cu_6Sn_5 :



When the Cu_6Sn_5 consumption rate (Equation 7-3) is faster than the Cu_6Sn_5 formation rate (Equation 7-4), the final thickness of the Cu_6Sn_5 layer will decrease. A schematic illustration of the diffusion mechanism for the growth of IMCs layers in reflowed Sn-Cu/Cu during aging is shown in Fig. 7-7.

During the aging process, solid state Sn-Cu/Cu IMC growth is diffusion controlled and can be expressed using the following simple equation (Tu et al., 1992):

$$X(t) - X_0 = \sqrt{4Dt} \quad (7-5)$$

where $X(t)$ is the IMC thickness after aging for time t , X_0 is the initial thickness after reflow and D is the diffusion coefficient, which is related to the growth rate of the Sn-Cu/Cu IMC layer.

Equation 7-5 can be used to calculate the diffusion coefficient D when both $X(t)$ and X_0 are known. Unlike the Cu_6Sn_5 layer, Cu_3Sn layer in each sample is quite planar. The thickness of the Cu_3Sn layer in Fig. 7-6 was determined by averaging measurements, taken from at least 10 locations, using IMAGE J software. A plot of Cu_3Sn thickness as a function of the square root of aging time at 125°C is shown in Fig. 7-8. The linear correlation coefficient, R^2 , was 0.9998. A D value of $2.25 \times 10^{-14} \text{ cm}^2/\text{s}$ was determined.

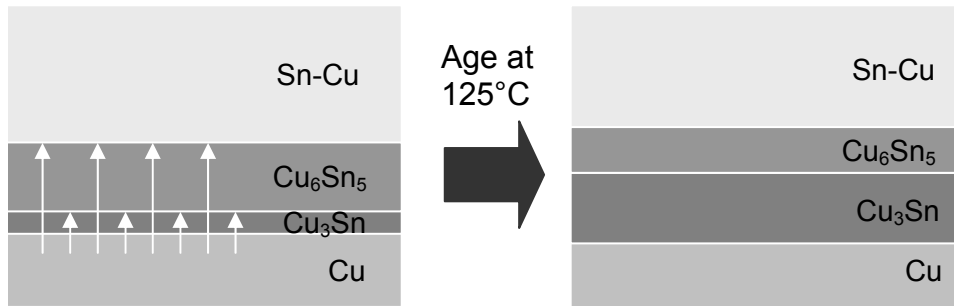


Fig. 7-7 Schematic illustration of the diffusion mechanism for the growth of IMCs layers in reflowed Sn-Cu/Cu during aging.

Fine Kirkendall voids were observed not only at $\text{Cu}/\text{Cu}_3\text{Sn}$ interface, but also inside the Cu_3Sn layer and at the $\text{Cu}_3\text{Sn}/\text{Cu}_6\text{Sn}_5$ interface in aged Sn-0.7wt%Cu/Cu samples, as shown in Fig. 7-6b-d. These result from the rapid diffusion of Cu from the Cu layer and through the Cu_3Sn layer. Previous work has shown that both Cu and Sn are mobile within Cu_3Sn , although the diffusion rate of Cu is greater than that of Sn (three times greater at 200°C) (Laurila et al., 2005; Ho et al., 2007). Kirkendall voids were also reported to form between electrodeposited Cu and eutectic Pb-Sn after reflow at 220°C and aging at 100 - 150°C (Zeng et al., 2005), as well as for Ni-doped Sn-Ag (Wang et al., 2008) and pure Sn (Laurila et al., 2005). Fig. 7-6b-d shows that as aging time increases, the density of the voids (i.e., the number of voids) at the interface increases. The

coalescence of these voids could cause the separation of the Cu_3Sn layer from the Cu substrate, a potential reliability threat.

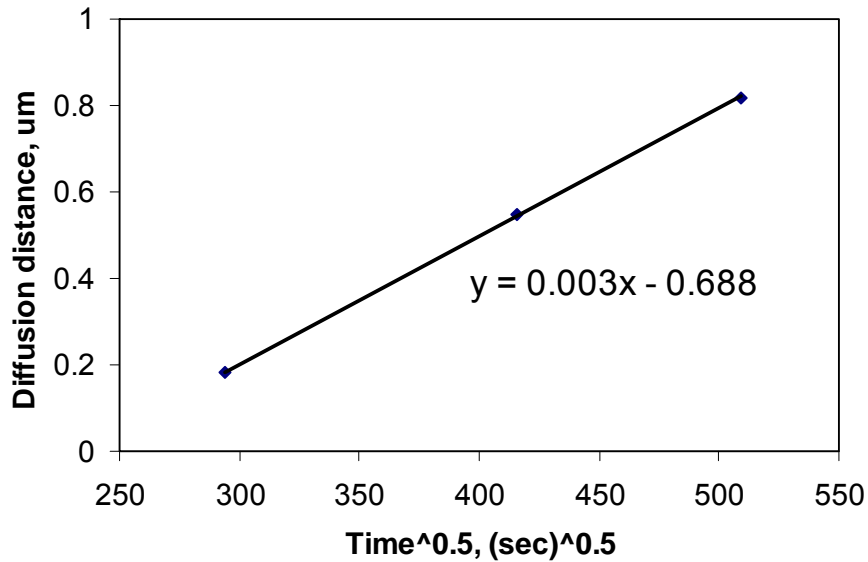


Fig. 7-8 Plot of Cu_3Sn thickness in Sn-Cu/Cu as a function of square root of aging time at 125°C .

7.3.1.2 Sn-Cu solder and Ni substrate

Near eutectic Sn-Cu solder films with the same composition as above were electrodeposited onto Ni to study interfacial reactions between Sn-Cu solders and Ni during reflow and aging. During reflow at 260°C , molten Sn-Cu spread out quickly and covered the whole sample surface with some differences in thickness at different positions. A low magnification SEM BSE cross section image after reflow is shown in Fig. 7-9a. The contact angle between Sn-Cu solder and Ni substrate is very low, indicating good wettability of Sn-Cu on Ni. The higher magnification image shown in Fig. 7-9b was taken from an area where the solder thickness was about $3\ \mu\text{m}$ and needle-like grains developed. In order to better reveal the microstructure at the interface, an etching solution (2% HCl + 5% HNO_3 + 93% CH_3OH) was used to selectively etch the Sn matrix away and the corresponding SEM BSE image for the sample etched for 5 s is shown in Fig. 7-9c. Three different types of morphologies were observed: a continuous planar layer at the Ni interface (point 3 in Fig. 7-9c); long, thin needles (point 4 in Fig. 7-

9c); and large, polygonal crystals (point 1 and 2 in Fig. 7-9c). Similar morphologies were reported by Bader et al. (1995) when the Sn-Ni system was reflowed at 240-400°C. They found out that large quantities of Ni_3Sn_4 needles were present after reflowing at 240°C for only 7 s. The first large Ni_3Sn_4 crystals appeared after 30 s and their numbers increased rapidly with continuous reflow. Bader et al. believed that coarsening of Ni_3Sn_4 needles into large crystals took place.

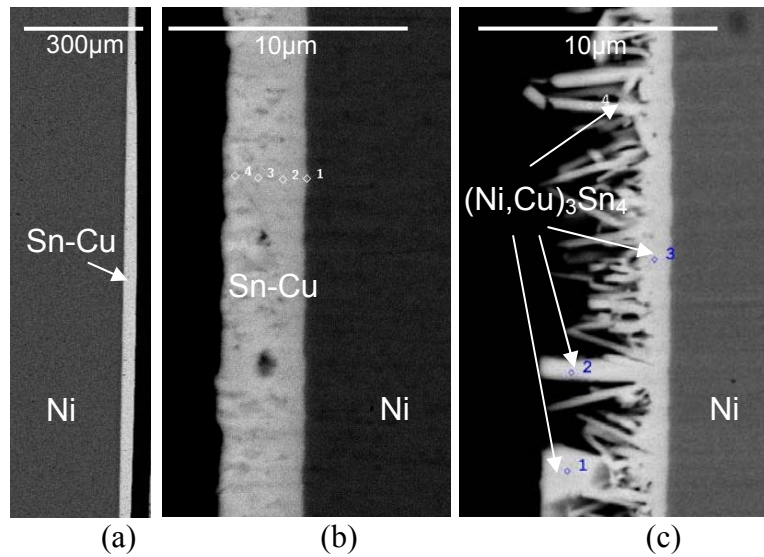


Fig. 7-9 SEM BSE cross section images of Sn-Cu films electrodeposited onto Ni substrate, after reflow at 260°C for 90 s: (a) at low magnification; (b) at higher magnification; (c) etched.

To find out the compositions of the three different morphologies, EDX point analysis was performed at position 1-4 in Fig. 7-9c and the results are shown in Table 1. All four positions have very similar Sn, Cu and Ni contents, with a 1-3 wt% difference in Sn and Cu content and a 1-6 wt% difference in Ni content. The continuous planar layer at the Ni interface (point 3 in Fig. 7-9c) has the highest Ni content (28 wt%) and lowest Cu content (3 wt%). The large, polygonal crystal at position 1 in Fig. 7-9c has the lowest Ni content (22 wt%) and highest Cu content (6 wt%), which may be because the position is further away from the interface. The compositions at all four positions are in agreement with a $(\text{Ni,Cu})_3\text{Sn}_4$ structure. Needles and crystals with similar morphologies were

also found at the reflowed Sn-Ag-Cu/Ni interface and were identified as $(\text{Ni,Cu})_3\text{Sn}_4$ by TEM analysis, which will be presented later in this section. To better show the morphologies of IMCs in reflowed Sn-0.7wt%Cu/Ni, an Auger microprobe with high spatial resolution was used to take high magnification SE plan view images for the above reflowed and etched Sn-Cu/Ni sample and the result is shown in Fig. 7-10a. Very similar long, thin needles and large, polygonal crystals to those shown in Fig. 7-9c were observed. Auger spectra collected at positions 1-5 as marked in Fig. 7-10a are shown in Fig. 7-10b. Sn, Cu, and Ni were detected at all 5 positions, and quantitative analysis gave a composition range of 69-72 wt% Sn, 4-6 wt% Cu and 24-27 wt% Ni.

Table 7-1 EDX point analysis results for Sn, Cu, Ni at positions marked in Fig. 7-9c

	Sn content		Cu content		Ni content	
	wt%	at%	wt%	at%	wt%	at%
Position 1	72	56	6	9	22	35
Position 2	72	56	4	5	24	39
Position 3	69	53	3	3	28	44
Position 4	71	55	4	5	25	40

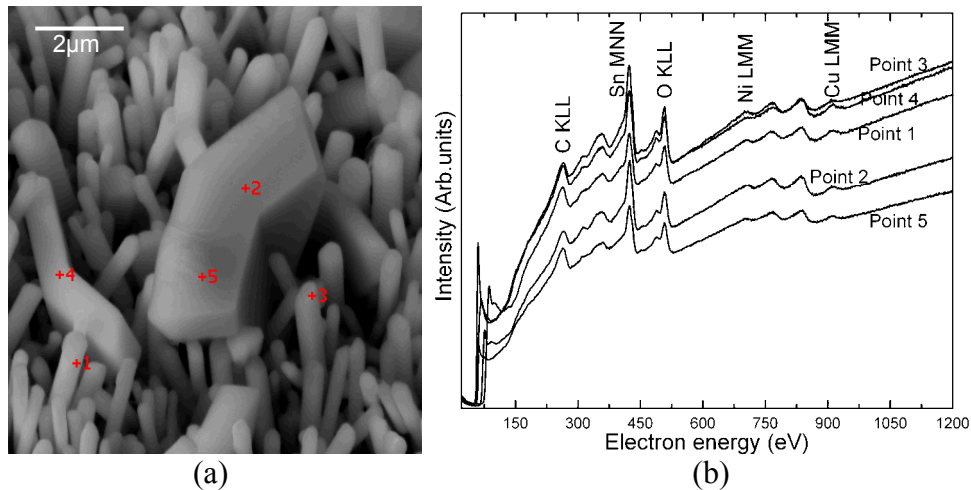
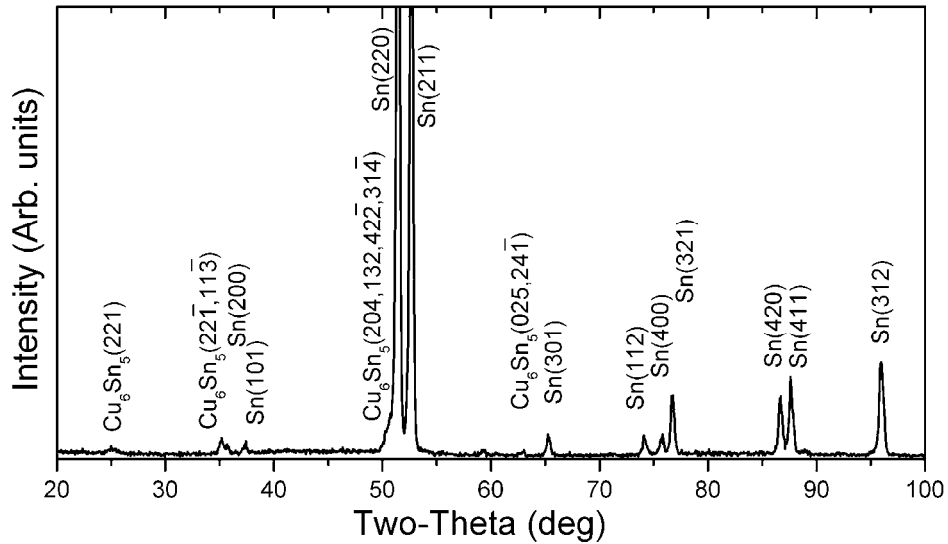
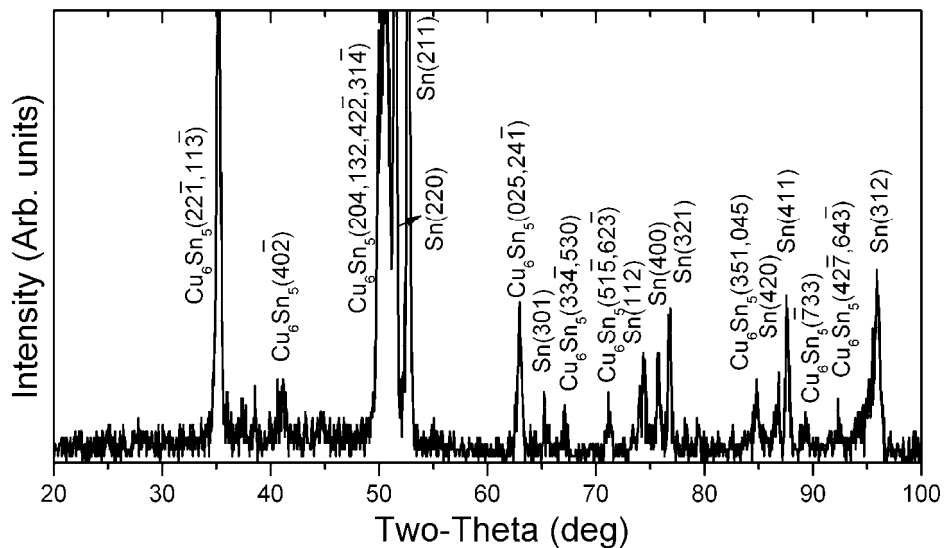


Fig. 7-10 (a) Auger SE plan view image of Sn-Cu films electrodeposited onto Ni substrate after reflow at 260°C for 30 s and etching; (b) Auger point analysis at points 1 to 5 in (a).

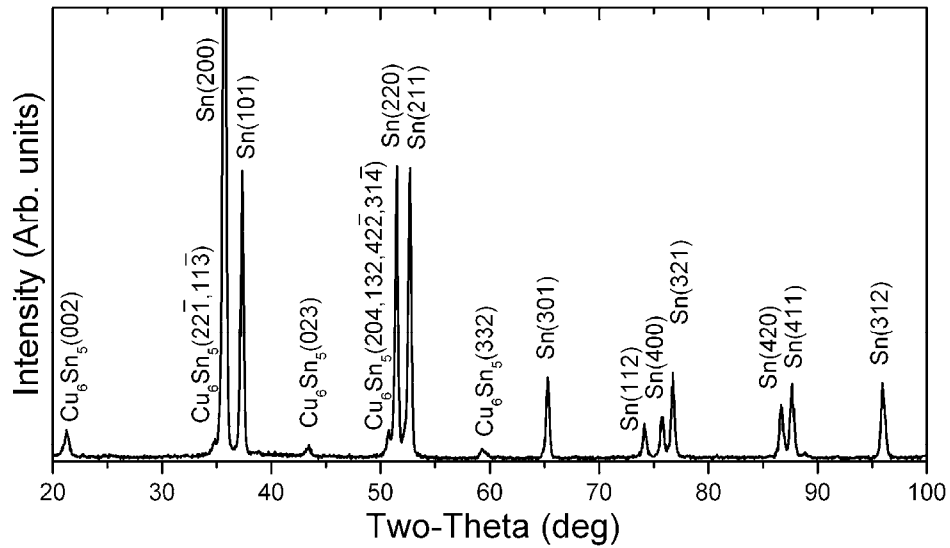
In order to study phase changes in Sn-Cu/Ni before and after reflow, XRD analysis was carried out for as-deposited Sn-Cu/Ni, as-deposited Sn-Cu/Ni after etching, Sn-Cu/Ni after reflow and Sn-Cu/Ni after reflow and etching, and the results are shown in Fig. 7-11a-d. In as-deposited Sn-Cu/Ni (Fig. 7-11a), two phases were detected, with Sn as the main phase and a small amount of the Cu_6Sn_5 phase. After etching (2% HCl + 5% HNO_3 + 93% CH_3OH), Cu_6Sn_5 peaks at 35.2° , 50.5° and 62.9° became much more intense, with additional Cu_6Sn_5 peaks detected (Fig. 7-11b). This is because the Sn matrix was selectively etched away leaving the Cu_6Sn_5 phase. The morphology of Sn-Cu/Ni after etching is



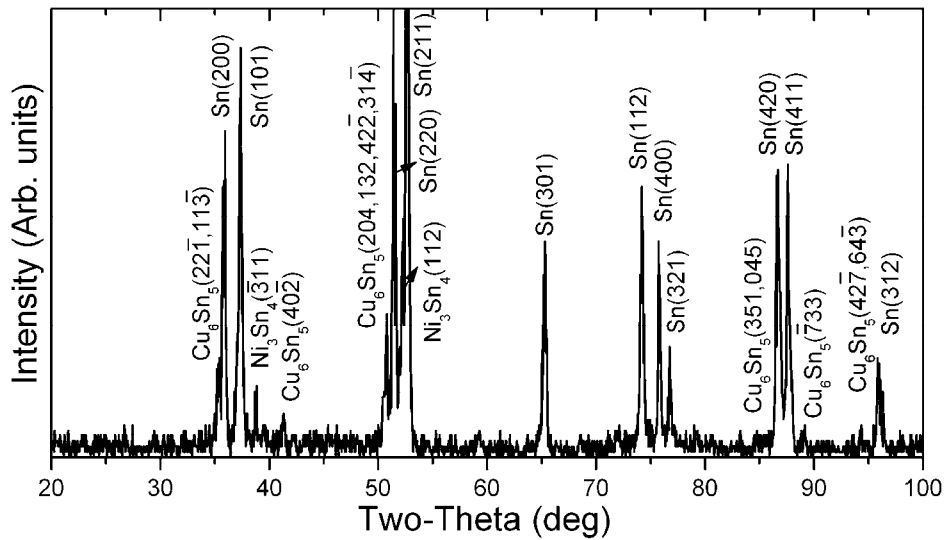
(a)



(b)



(c)



(d)

Fig. 7-11 XRD patterns of Sn-Cu films electrodeposited onto Ni substrate: (a) as-deposited; (b) as-deposited and etched; (c) after reflow at 260°C for 30 s; (d) after reflow at 260°C for 30 s and etched.

shown in Fig. 7-12a. Two different morphologies indicated as numbers 1 and 2 were observed. Auger spectra collected from positions 1 and 2 in Fig. 7-12a are shown in Fig. 7-12b. Grains at position 2 were identified as pure Sn, while particles at position 1 contained Sn and Cu and were identified as Cu_6Sn_5 . The Auger results agree with the XRD results. After reflow at 260°C for 30s (Fig. 7-11c), the most intense Sn peak changed from Sn (220) to Sn (200). The Cu_6Sn_5

peaks at 21.2° and 43.4° disappeared and additional Cu_6Sn_5 peaks at 41.3° and 94.9° were detected. In order to obtain IMC phase information at the interface, the reflowed Sn-Cu was etched using the same etching solution as above for 25 s to remove most of the remaining solder and reveal the interface. The XRD results are shown in Fig. 7-11d. Comparing Fig. 7-11c with Fig. 7-11d, after etching, the Cu_6Sn_5 peaks became much stronger at 35.2° and 50° and four additional Cu_6Sn_5 peaks were detected. This is due to the same reason as explained above for etched Sn-Cu/Cu. In addition, Ni_3Sn_4 was detected, and is referred to as $(\text{Ni,Cu})_3\text{Sn}_4$ because of Cu dissolution in the phase.

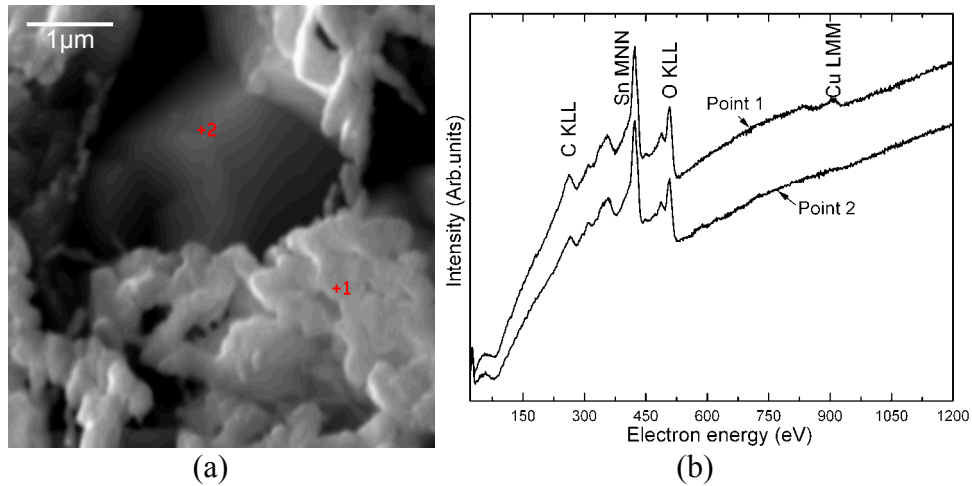


Fig. 7-12 (a) Auger SE plan view image of Sn-Cu film electrodeposited onto Ni substrate after etching; (b) Auger point analysis of points 1 and 2 in (a) after etching.

To study the effect of reflow on Cu and Ni distribution along the cross section of Sn-Cu/Ni, EDX point analysis at positions marked in Fig. 7-9b was carried out, and the results are shown in Fig. 7-13 and Fig. 7-14. Before reflow, the Cu concentration was quite uniform across the thickness (~ 0.7 wt% Cu), except at the Sn-Cu/Ni interface where the Cu content was as high as about 5.7 wt%. The reason for this has been discussed previously in Chapter 3. After reflow at 260°C for 30 s, the Cu content was about 3 wt% to at least $3 \mu\text{m}$ from the Ni/solder interface, which is due to the dissolution of Cu into the Ni_3Sn_4 IMC which formed at the interface. A high Ni content was found deep into the solder

layer after reflow, due to the formation of Ni_3Sn_4 IMCs and the dissolution of Ni in Cu_6Sn_5 (Fig. 7-14).

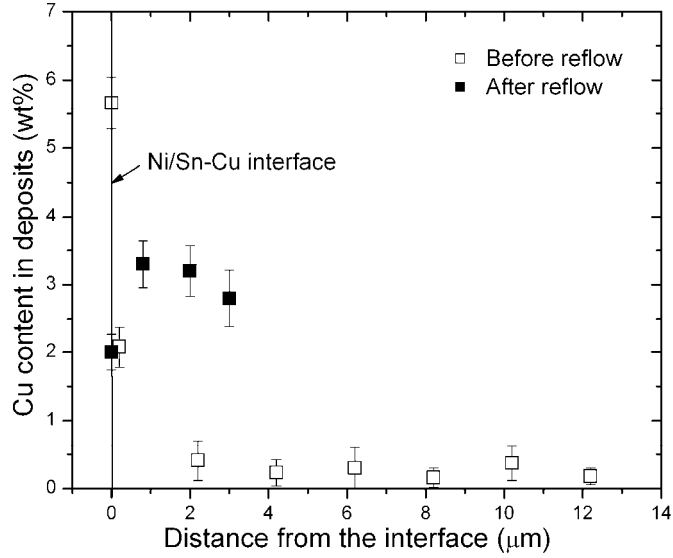


Fig. 7-13 Deposit Cu distribution in Sn-Cu films electrodeposited onto Ni substrate along the cross section before and after reflow at 260°C for 30 s.

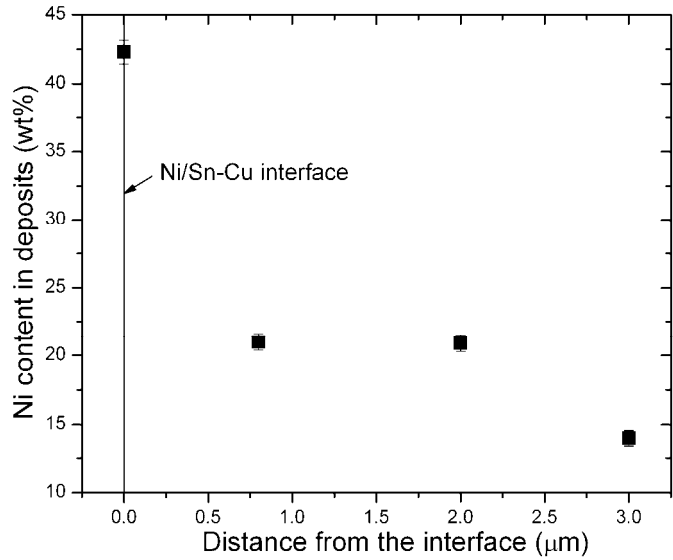


Fig. 7-14 Ni distribution in Sn-Cu films electrodeposited onto Ni substrate along the cross section after reflow at 260°C for 30 s.

The results presented above suggest that during reflow at 260°C, Ni dissolved into the liquid solder until the solder was saturated with Ni. Ni₃Sn₄ nucleation started at the solder/Ni interface and formed a continuous planar layer, from where Ni₃Sn₄ needles grew. With continuous reflow, coalescence of Ni₃Sn₄ needles took place forming large crystals. Meanwhile, Cu at the solder/Ni interface dissolved into Ni₃Sn₄ to form (Ni,Cu)₃Sn₄ and diffused towards the solder surface due to the concentration gradient. Nickel diffused into the Sn-Cu solder and dissolved into the existing Cu₆Sn₅ particles to form (Cu,Ni)₆Sn₅.

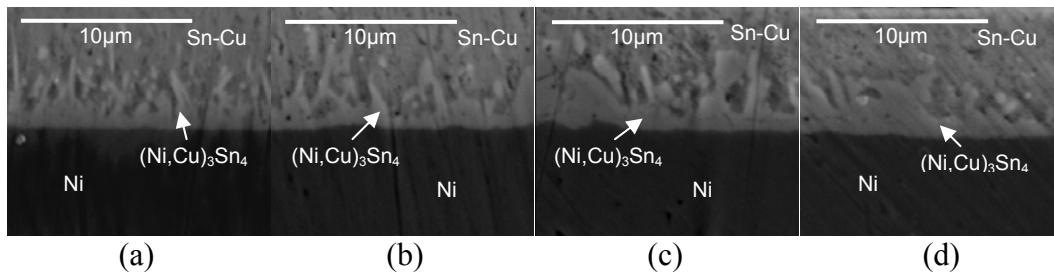


Fig. 7-15 SEM BSE cross section images of Sn-Cu films electrodeposited onto Ni substrate after reflow and aging: (a) reflowed at 260°C for 30 s; (b) reflowed at 260°C for 30 s and aged at 125°C for 24 hrs; (c) reflowed at 260°C for 30 s and aged at 125°C for 48 hrs; (d) reflowed at 260°C for 30 s and aged at 125°C for 72 hrs.

Similar aging experiments as for reflowed Sn-Cu/Cu were carried out for reflowed Sn-Cu/Ni and corresponding SEM BSE cross section images are shown in Fig. 7-15. In all four samples, the areas between the Sn-Cu solder and Ni substrate were characterized by a brighter color which was identified as (Ni,Cu)₃Sn₄. As the aging time was increased, the number of (Ni,Cu)₃Sn₄ needles decreased and the size of the polygonal (Ni,Cu)₃Sn₄ crystals increased, which means that coalescence of (Ni,Cu)₃Sn₄ needles into larger (Ni,Cu)₃Sn₄ crystals occurred during aging. The thickness of the (Ni,Cu)₃Sn₄ layer stayed almost the same after aging for up to 48 hrs and decreased after aging for 72 hrs. This may be due to the formation of a linked network structure of (Ni,Cu)₃Sn₄.

Comparison of Fig. 7-6 and Fig. 7-15 shows that two different types of IMCs structures formed between Sn-Cu/Cu and Sn-Cu/Ni after reflow at 260°C

for 30 s. In addition, no Kirkendall voids formed at the Sn-Cu/Ni interface even after aging at 125°C for up to 72 hrs.

7.3.2 Interfacial reactions between Sn-Ag-Cu solder and Cu and Ni substrates during reflow and aging

7.3.2.1 Sn-Ag-Cu solders and Cu substrate

Sn-3.6Ag-1.8Cu solder films (Chapter 6, Fig. 6-9) were electrodeposited onto Cu. After etching the as-deposited Sn-Ag-Cu solder films for 5 s, small, bright contrast particles showed up in the SEM BSE plan view images (Fig. 7-16a). These particles contained high amounts of Ag, as determined from EDX

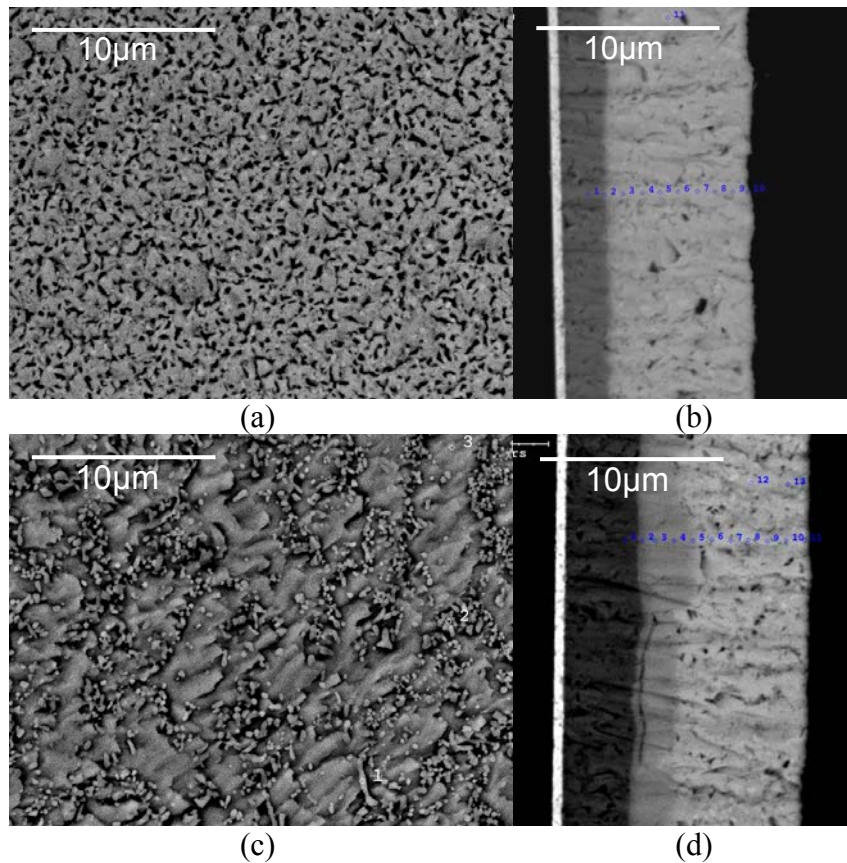


Fig. 7-16 SEM BSE images of Sn-Ag-Cu films deposited onto Cu substrate: (a) plan view, after etching; (b) cross section, (c) plan view, after reflow at 260°C for 30 s and etching; (d) cross section, after reflow at 260°C for 30 s and before etching.

analysis, and were identified as Ag_3Sn within the Sn matrix. The same high Ag content particles were also found in polished Sn-Ag-Cu/Cu cross section samples, even without etching (Fig. 7-16b). The Ag_3Sn particles were evenly distributed within the solder films. After reflow at 260°C for 30 s, elongated Ag_3Sn particles formed, such as point 1 marked in Fig 7-16c. At position 2 in Fig. 7-16c, Sn, Ag and Cu were detected by EDX point analysis. Since only Ag_3Sn and Cu_6Sn_5 were detected by XRD analysis (Fig. 7-17), it was assumed that the small particles at position 2 in Fig. 7-16c were mixtures of Ag_3Sn and Cu_6Sn_5 particles. The rest of the areas, with the same morphology as position 3 in Fig. 7-16c, were identified as pure Sn by EDX point analysis. A cross section image for Sn-Ag-Cu/Cu after reflow (Fig. 7-16d) shows a continuous bilayer of Cu_3Sn (very thin) and Cu_6Sn_5 (thick) between the Cu substrate and the solder. Within the solder, Ag_3Sn white particles were found in some areas and depleted in others. The long scratch between the Cu_3Sn layer and the Cu_6Sn_5 layer and along the Cu substrate is from polishing.

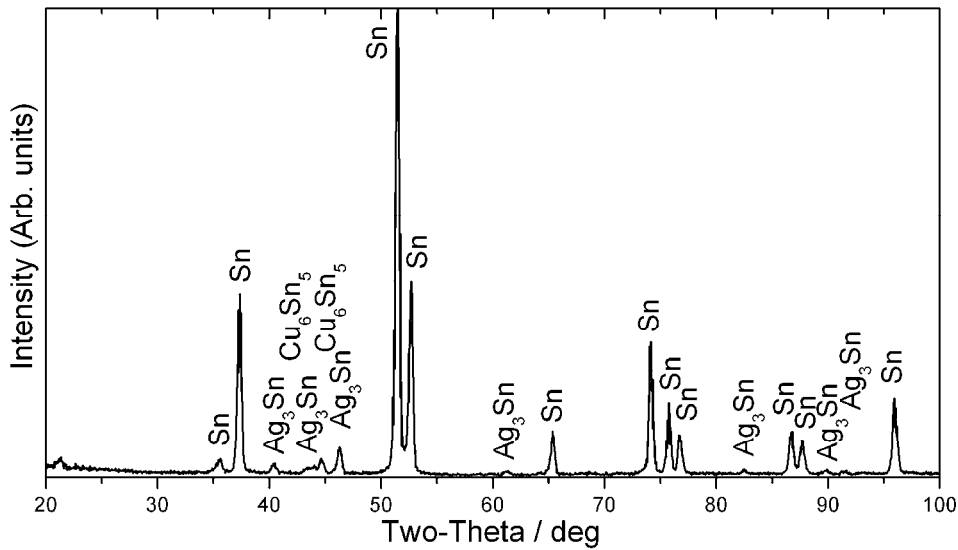


Fig. 7-17 XRD pattern of Sn-Ag-Cu film after reflow at 260°C for 30 s.

Three phases were detected by XRD analysis for Sn-Ag-Cu/Cu after reflow, as shown in Fig. 7-17. The main phase is Sn, with small amounts of Cu_6Sn_5 and Ag_3Sn . The reason only small amounts of Cu_6Sn_5 phase were detected

and no Cu_3Sn was detected is because after reflow the sample thickness became non-uniform due to wetting reactions between the solder and the Cu substrate. During XRD analysis, the X-ray beam happened to be directed at a thicker region and was not able to penetrate to the Cu_6Sn_5 and Cu_3Sn intermetallic layers at the interface. The same situation happened for the Ni_3Sn_4 IMC phase in Sn-Cu/Ni after reflow (Fig. 7-11c and d).

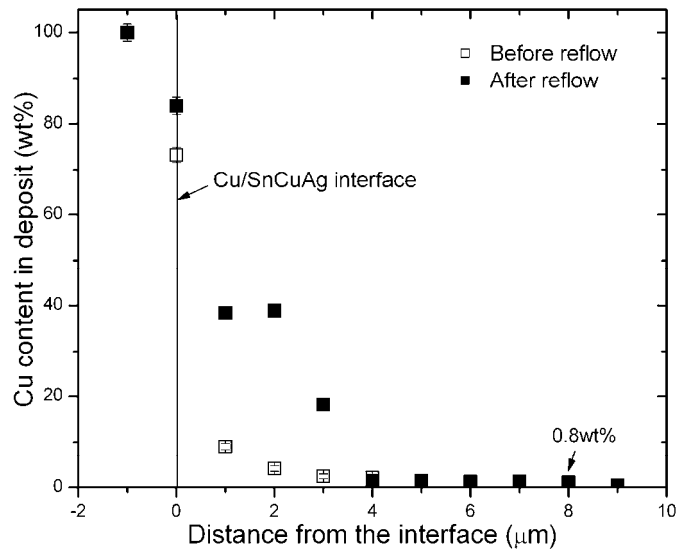


Fig. 7-18 Deposit Cu distribution through thickness for Sn-Ag-Cu films deposited onto Cu substrate before and after reflow at 260°C for 30 s. The analysis points are indicated in Figure 7-16b.

EDX point analysis along the Sn-Ag-Cu/Cu cross section at the positions marked in Fig. 7-16b and Fig. 7-16d were carried out to study the effects of reflow on the Cu (Fig. 7-18) and Ag (Fig. 7-19) distribution. As for the Sn-Cu/Cu sample discussed before, Cu content at Sn-Ag-Cu/Cu interface increased dramatically after reflow, which is due to the formation of Cu_3Sn and Cu_6Sn_5 IMCs. Before reflow Ag was distributed randomly in the Sn-Ag-Cu solder film, with an average composition of about 3.6 wt%. After reflow, in some regions no Ag was detected, while other areas were enriched with Ag_3Sn particles, which grew in size. An SEM BSE cross section image of Sn-Ag-Cu/Cu after reflow and etching is shown in Fig. 7-20. As with the Sn-Cu/Cu samples, a uniform thin layer of Cu_3Sn formed adjacent to the Cu substrate and Cu_6Sn_5 formed as a layer

between Cu_3Sn and the Sn-Ag-Cu solder with a scallop-shape morphology. The difference is that after reflow at 260°C for 30 s, a thinner Cu_3Sn layer formed in Sn-Ag-Cu/Cu than the one that formed in Sn-Cu/Cu. It appears that the addition of Ag into Sn-Cu solders inhibits the formation of Cu_3Sn layer during reflow.

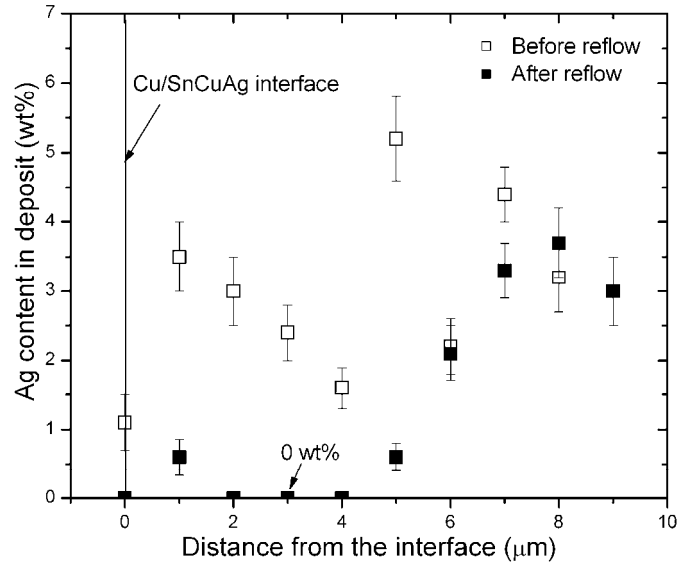


Fig. 7-19 Deposit Ag distribution through thickness for Sn-Ag-Cu films deposited onto Cu substrate before and after reflow at 260°C for 30 s. The analysis points are indicated in Figure 7-16d.

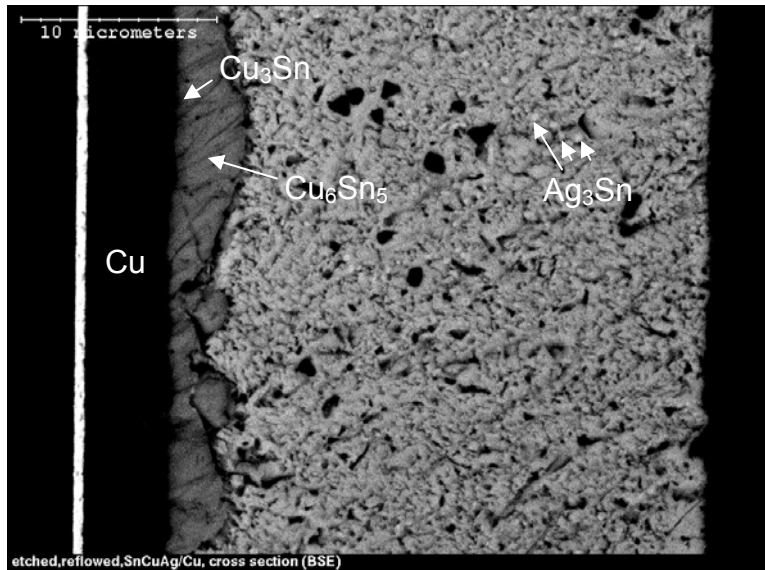


Fig. 7-20 SEM BSE cross section image of Sn-Ag-Cu film deposited onto Cu substrate after reflow at 260°C for 30 s and etching.

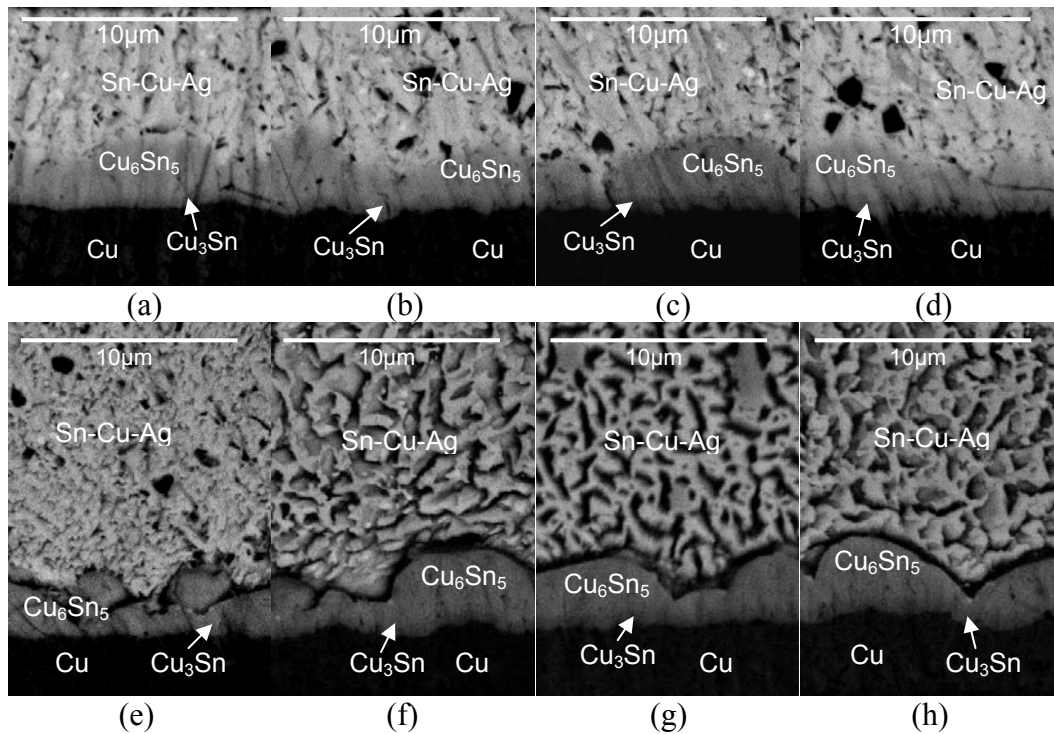


Fig. 7-21 SEM BSE cross section images of Sn-Ag-Cu films deposited onto Cu substrate after reflow and aging: (a) reflowed at 260°C for 30 s; (b) reflowed at 260°C for 30 s and aged at 125°C for 24 hrs; (c) reflowed at 260°C for 30 s and aged at 125°C for 48 hrs; (d) reflowed at 260°C for 30 s and aged at 125°C for 72 hrs. (e)-(f) are SEM BSE images of samples (a)-(d) after etching.

To study the aging behavior, Sn-Ag-Cu/Cu samples were reflowed at 260°C for 30 s first and then aged at 125°C for different lengths of time. Corresponding SEM BSE cross section images are shown in Fig. 7-21, both without and with etching. As for the Sn-Cu/Cu samples, after aging for up to 72 hrs, the thickness of the entire IMC layer did not change much. The Cu_3Sn layer became thicker as aging time increased, which is due to the continuous diffusion of Cu from the Cu substrate to the $\text{Cu}_3\text{Sn}/\text{Cu}_6\text{Sn}_5$ interface to react with Cu_6Sn_5 and form Cu_3Sn (Equation 7-3 - as discussed previously). The decrease in Cu_6Sn_5 thickness can be explained in the same way as for Sn-Cu/Cu samples. The thicknesses of the Cu_3Sn layers in samples after aging for 0, 20, 48, and 72 hrs were determined by averaging measurements taken from at least 10 locations using IMAGE J software, and a plot of Cu_3Sn layer diffusion distance as a

function of the square root of aging time at 125°C is shown in Fig. 7-22. The linear correlation coefficient, R^2 , was 0.9884. According to Equation 7-5, the diffusion coefficient D was determined as $3.6 \times 10^{-15} \text{ cm}^2/\text{s}$, which is almost one order of magnitude smaller than that D value for Sn-Cu/Cu after aging. Therefore, the addition of Ag into Sn-Cu not only inhibited the formation of Cu_3Sn during reflow (formation of a thinner Cu_3Sn IMC), but also slowed down the growth of the Cu_3Sn layer during aging (smaller diffusion coefficient), which should improve the reliability of the solder joint.

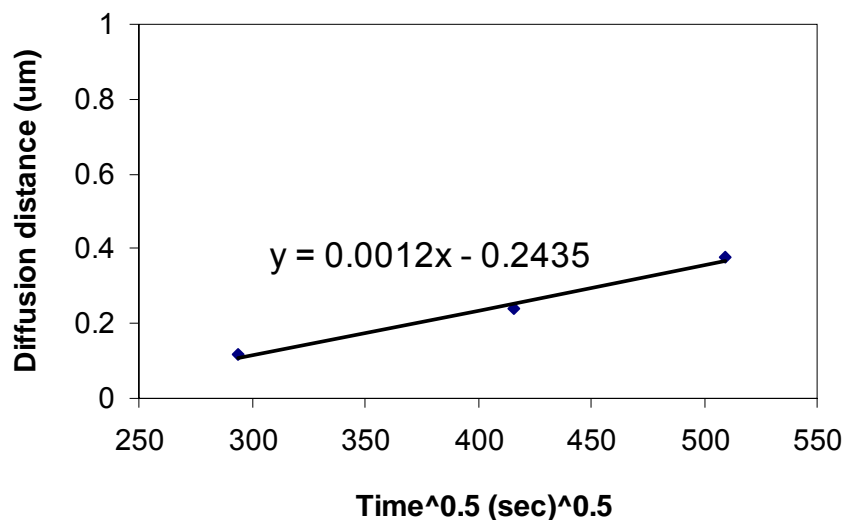


Fig. 7-22 Plot of Cu_3Sn layer diffusion distance in Sn-Ag-Cu/Cu as a function of the square root of aging time at 125°C.

7.3.2.2 Sn-Ag-Cu solders and Ni substrate

The same Sn-3.6Ag-1.8Cu solder films as used for the previous section were electrodeposited onto Ni substrates to study the interactions between Sn-Ag-Cu solders and Ni during reflow and aging. SEM SE plan view images of the Sn-Ag-Cu/Ni samples after reflow at 230°C for 30 s and etching for 5 s are shown in Fig. 7-23a. Higher magnification images at location I and II in Fig. 7-23a are also shown in Fig. 7-23b and c. Two different types of morphologies were observed: elongated particles and larger round plates. The small circular particles are actually elongated particles in perpendicular or near perpendicular orientations.

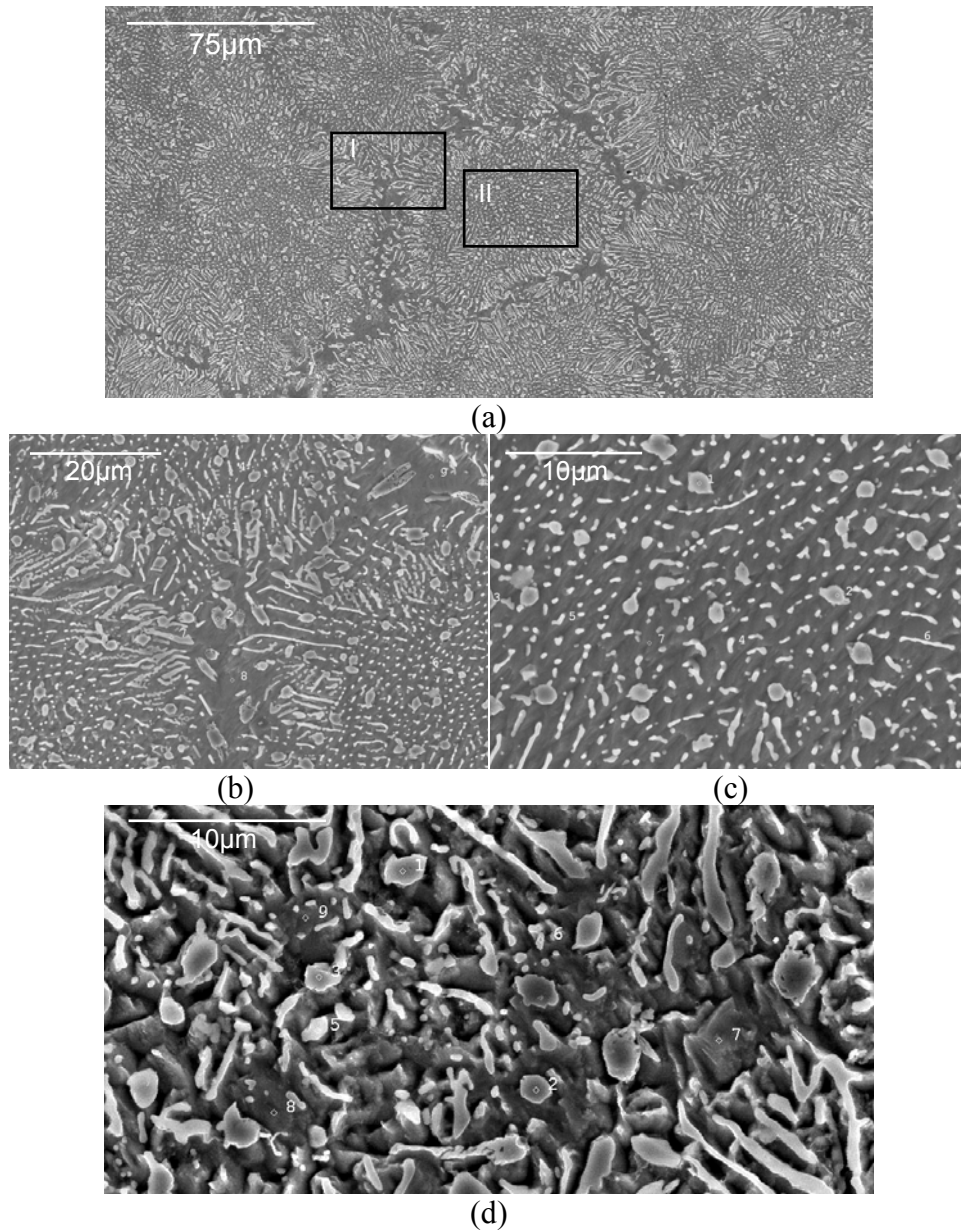


Fig. 7-23 SEM SE plan view images of Sn-Ag-Cu films deposited onto Ni substrate: (a) after reflowing at 230°C for 30 s and etching; (b) higher magnification at location I in (a); (c) higher magnification image at location II in (a); (d) after reflowing at 260°C for 30 s and etching.

Similar morphologies were also observed for Sn-Ag-Cu/Ni after reflow at 260°C for 30 s (Fig. 7-23d). EDX point analysis showed that the elongated particles had high Ag content (as high as 24 wt% or 26 at%), similar to the particles in Fig. 7-16c, and were identified as Ag_3Sn IMCs within the Sn matrix. Similar elongated particles were also observed by TEM analysis, as shown in Fig. 7-24a and c.

Selected area diffraction (SAD) patterns obtained from region 1 in both Fig. 7-24a and Fig. 7-24c are shown in Fig. 7-24b and Fig. 7-24d, respectively. Indexing of the patterns is also shown in Fig. 7-24b and Fig. 7-24d. The elongated particles in both Fig. 7-24a and Fig. 7-24c were identified as Ag_3Sn . These particles precipitate from the molten solder. The round plate particles were about 200 nm in diameter. EDX point analysis showed that these particles contained Sn, Cu and Ni. The Cu content was as high as 23 wt% (32 at%) and the Ni content was as high as 12 wt% (20 at%). Particles (region 1 in Fig. 7-25) with similar round plate morphologies and similar size were also observed in the TEM. An SAD pattern

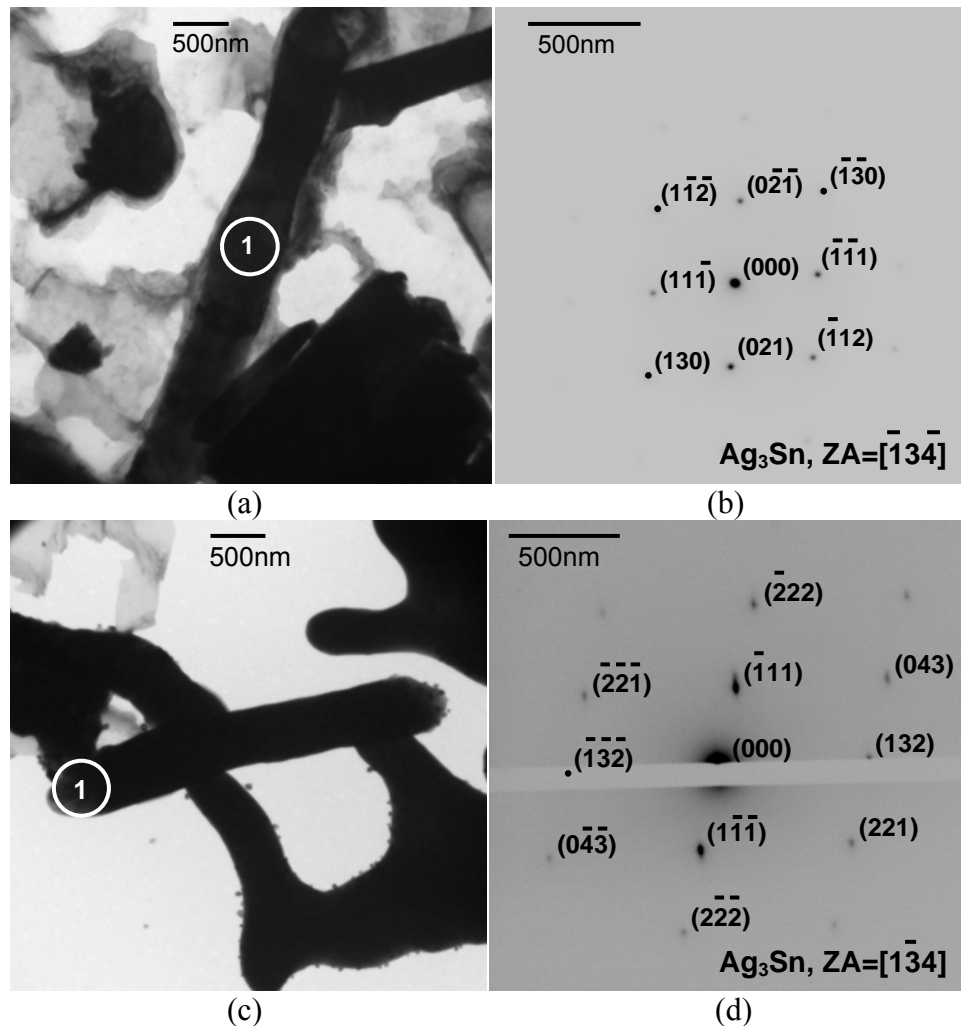


Fig. 7-24 (a), (c) TEM image of Sn-Ag-Cu/Ni sample after reflow at 260°C for 30 s; (b) TEM selected area diffraction (SAD) pattern from region 1 in (a); (d) TEM SAD pattern from region 1 in (c).

from region 1 in Fig. 7-25a was obtained and both the pattern and the solution are shown in Fig. 7-25b. The particle was identified as $(\text{Cu,Ni})_6\text{Sn}_5$. The dark background in Fig. 7-23a was identified as pure Sn by EDX point analysis. When the reflow temperature was increased from 230°C to 260°C, the morphologies of the IMCs looked the same, with an increase in particle densities, as more IMC particles formed at higher temperature.

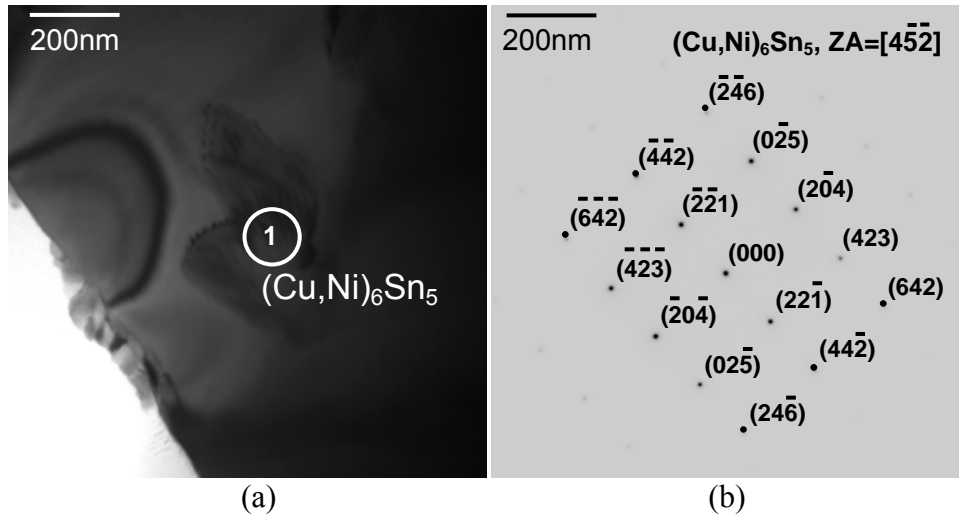


Fig. 7-25 (a) TEM image of Sn-Ag-Cu/Ni sample after reflow at 260°C for 30 s (b) TEM SAD pattern from region 1 in (a).

Fig. 7-26 shows SEM BSE cross section images of Sn-Ag-Cu/Ni after reflow at 260°C for 30 s without (Fig. 7-26a) and with etching (Fig. 7-26b). Similar to the reflowed Sn-Ag-Cu/Cu samples, the small bright particles (position 12 in Fig. 7-26a for example) were identified as Ag_3Sn , and are marked in both Fig. 7-26a and b. Large Cu_6Sn_5 particles, with significant amounts of Ni dissolution, are located at position 11 in Fig. 7-26a and position 5 in Fig. 7-26b, and are specified as $(\text{Cu,Ni})_6\text{Sn}_5$ since Ni substitutes for Cu. To better verify the phase distribution at the Sn-Ag-Cu/Ni interface after reflow, a TEM cross section sample was prepared. A TEM cross section image from the Sn-Ag-Cu/Ni interface of a sample after reflow at 260°C for 30 s is shown in Fig. 7-27a. Only Ni was detected at positions 1 and 2, while Ni, Cu and Sn were detected at positions 3 and 4 with similar compositions using EDX analysis in the TEM. An

SAD ring pattern from the Ni layer (positions 1) in Fig. 7-27a was obtained and is shown in Fig. 7-27b. An SAD pattern from position 3 in Fig. 7-27a was obtained and is shown in Fig. 7-27c. The pattern was indexed as Ni_3Sn_4 . Since Cu was also present in this phase and Ni and Cu are mutually soluble, the phase adjacent to the Ni layer was identified as $(\text{Ni,Cu})_3\text{Sn}_4$.

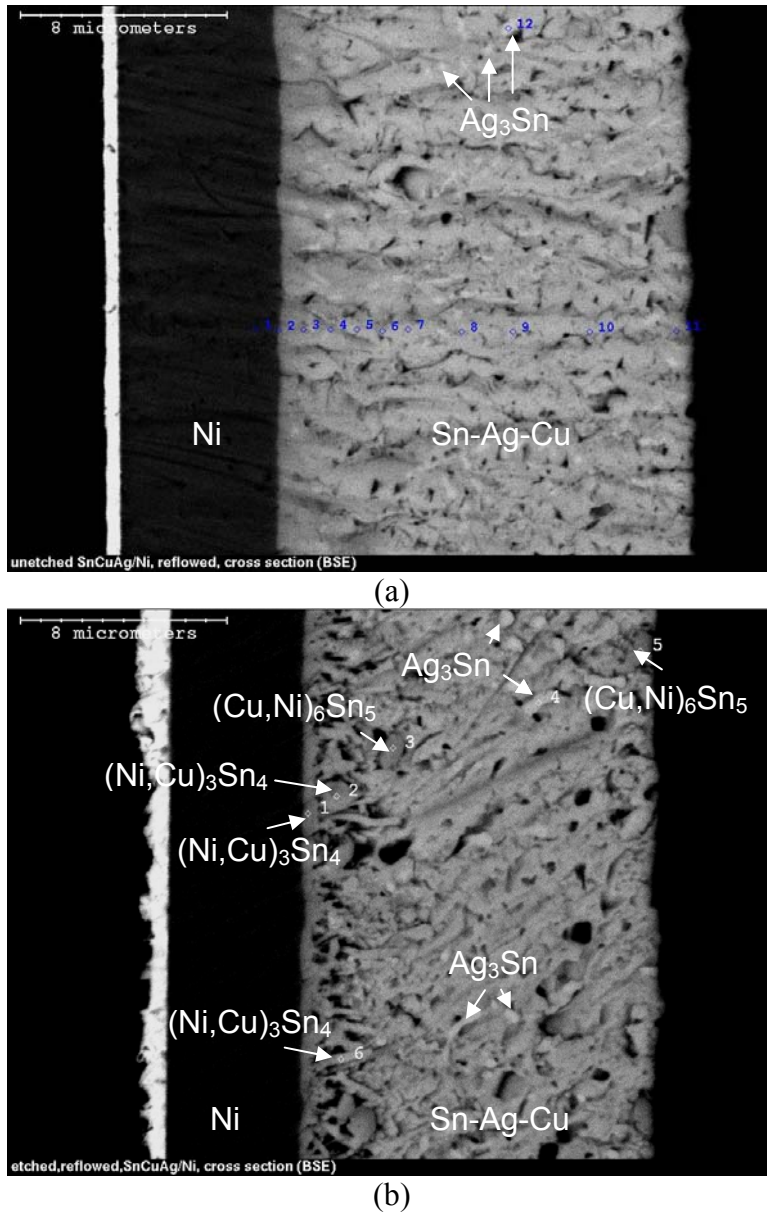


Fig. 7-26 SEM BSE cross section images of Sn-Ag-Cu film deposited onto Ni substrate: a) after reflow at 260°C for 30 s, without etching; b) after etching for 5 s.

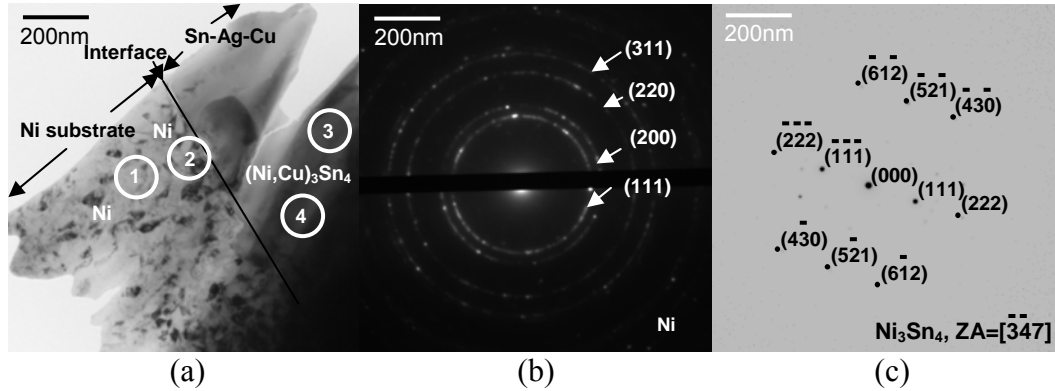


Fig. 7-27 (a) TEM cross section image of Sn-Ag-Cu/Ni interface after reflow at 260°C for 30 s; (b) TEM SAD pattern from region 1 in (a); (c) TEM SAD pattern from region 3 in (a).

After etching for 5 s, three different morphologies at the Sn-Ag-Cu/Ni interface were observed: a continuous planar layer at the Ni interface (position 1 in Fig. 7-26b); long, thin needles (position 6 in Fig. 7-26b) and large, polygonal crystals (position 2 in Fig. 7-26b), which are very similar to the interface structure of the reflowed and etched Sn-Cu/Ni sample shown in Fig. 7-9c. EDX point analysis at these positions gave a composition of about 60 at%Sn, 30 at%Ni and 10 at%Cu. The continuous planar layer adjacent to the Ni layer, which corresponds to the same location as position 4 in Fig. 7-30a, can be identified as $(\text{Ni,Cu})_3\text{Sn}_4$. Grains in both long, thin needle shape and polygonal crystal shape were observed by TEM and the corresponding images are shown in Fig. 7-28a and c. EDX analysis in the TEM showed similar compositions for positions 1 and 2 in Fig. 7-28a and position 1 in Fig. 7-28c. Fig. 7-28b shows an SAD pattern taken from position 1 in Fig. 7-28a and the pattern was identified as Ni_3Sn_4 ; position 2 in Fig. 7-28a and position 1 in Fig. 7-28c were also identified as Ni_3Sn_4 . Therefore, both the long, thin needles and the polygonal crystals that formed at the Sn-Ag-Cu/Ni interface after reflow are $(\text{Ni,Cu})_3\text{Sn}_4$. Comparison of Fig. 7-9c and Fig. 7-26b shows that both the continuous planar layer and the layer of needles and crystals are much thinner in reflowed Sn-Ag-Cu/Ni than in reflowed Sn-Cu/Ni, which means the addition of Ag inhibited the formation of $(\text{Ni,Cu})_3\text{Sn}_4$ for reflowing at 260°C.

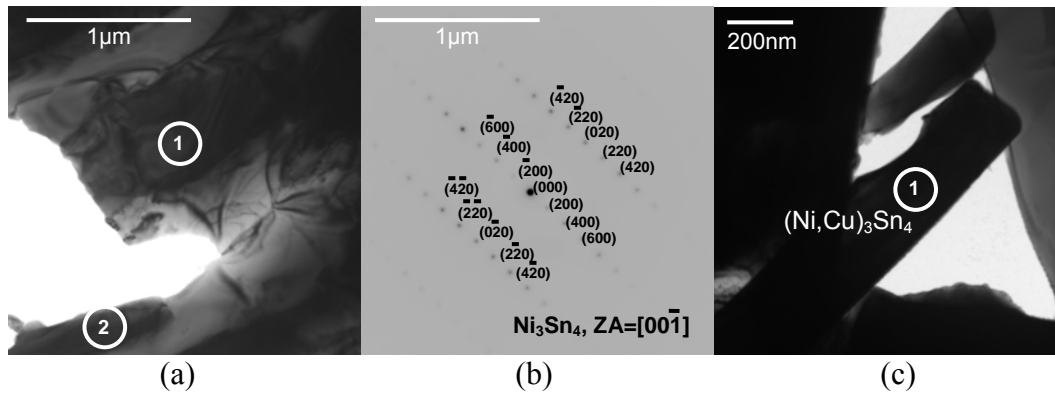


Fig. 7-28 (a) TEM image of Sn-Ag-Cu/Ni sample after reflow at 260°C for 30 s; (b) TEM SAD pattern from region 1 in (a); (c) TEM image of $(\text{Ni,Cu})_3\text{Sn}_4$ particle in Sn-Ag-Cu/Ni sample after reflow at 260°C for 30 s.

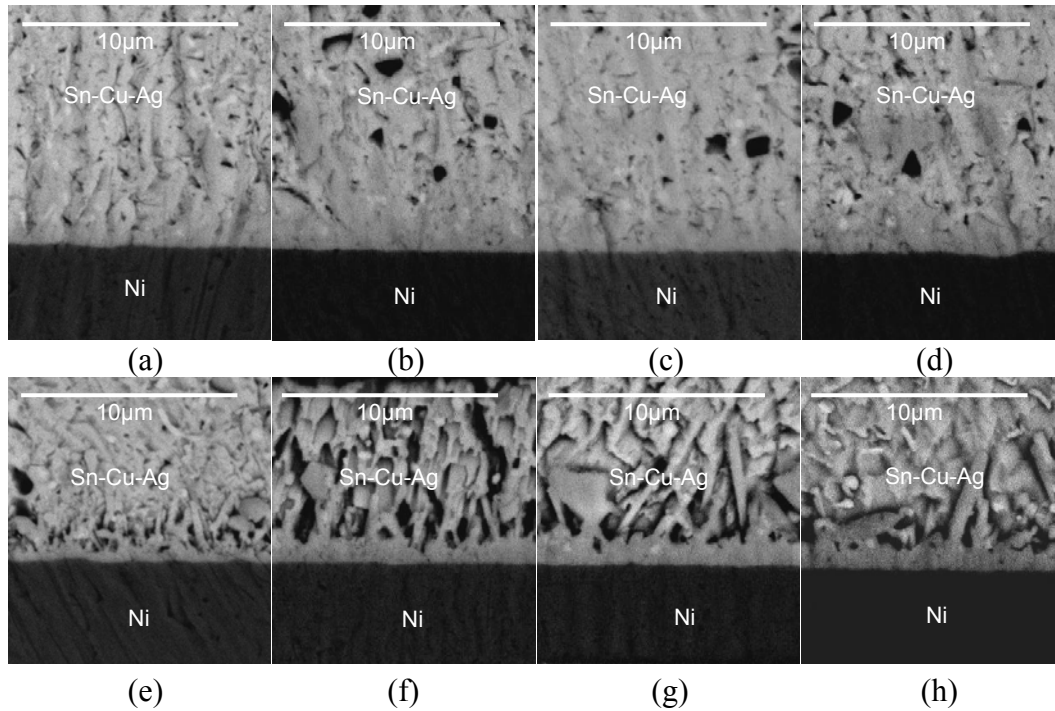


Fig. 7-29 SEM BSE cross section images of Sn-Ag-Cu films deposited onto Ni substrate after reflow and aging: (a) reflowed at 260°C for 30 s; (b) reflowed at 260°C for 30 s and aged at 125°C for 24 hrs; (c) reflowed at 260°C for 30 s and aged at 125°C for 48 hrs; (d) reflowed at 260°C for 30 s and aged at 125°C for 72 hrs. (e)-(f) are SEM BSE images of sample (a)-(d) after etching.

After reflow at 260°C for 30 s, the Sn-Ag-Cu/Ni samples were aged at 125°C for different lengths of time to study the effect of aging on IMC growth.

Fig. 7-29 shows SEM BSE cross section images of reflowed Sn-Ag-Cu/Ni after aging for 0, 24, 48 and 72 hrs without etching (Fig. 7-29a-d) and with etching (Fig. 7-29e-h). As shown in the images without etching, as aging time was increased, the size of the Ag_3Sn particles increased. This is due to the Ostwald ripening of Ag_3Sn . To better show the interfacial structures between Sn-Ag-Cu and Ni substrate, all the aged samples were etched for 5 s. After aging for 24 hrs, the continuous planar layer adjacent to the Ni became thicker, while after aging for 48 hrs and 72 hrs the thickness of the continuous planar layer did not change much. In addition, the amount of long, thin needles between the continuous planar layer and solder decreased and the size of the polygonal crystals increased. This indicates that during aging, thin needles and polygonal crystals coalesced to form larger needles and crystals.

7.4 Conclusions

Interfacial reactions between Sn-1.1Cu and Sn-3.6Ag-1.8Cu solder films and Cu or Ni layers, after reflow and aging, have been studied. Since Sn is the main constituent in both Pb-free solders, the reactions between Sn and the Ni or Cu layers were the main processes during reflow and aging.

When Cu is used as the seed layer, a continuous bilayer of Cu_3Sn (thin, planar) and Cu_6Sn_5 (thick, scallop-like) formed between the Cu and the solder after reflow at 260°C for both solders. It is generally believed that during reflow, Cu dissolves rapidly into the molten Sn, saturating the Sn. Cu_6Sn_5 then starts to nucleate and grow into a continuous layer. Continuous diffusion of Cu to the Cu_6Sn_5 layer makes the reaction between Cu and Cu_6Sn_5 possible leading to the formation of Cu_3Sn . The Cu_3Sn layer at the Sn-Ag-Cu/Cu interface is thinner than that at the Sn-Cu/Cu interface, indicating that the presence of Ag inhibited the formation of Cu_3Sn during reflow. After aging at 125°C , the thickness of the Cu_3Sn layer increased as aging time increased for both Sn-Cu/Cu and Sn-Ag-Cu/Cu. Calculated diffusion coefficients of Cu through the Cu_3Sn layer were $2.25 \times 10^{-14} \text{ cm}^2/\text{s}$ and $3.6 \times 10^{-15} \text{ cm}^2/\text{s}$, respectively. The lower diffusion

coefficient for Sn-Ag-Cu/Cu compared with that for Sn-Cu/Cu indicates that the addition of Ag slowed down the growth of the Cu_3Sn layer during aging at 125°C . The growth of the Cu_3Sn layer is due to the continuous diffusion of Cu through Cu_3Sn layer into Cu_6Sn_5 . The diffused Cu atoms react with Cu_6Sn_5 to form Cu_3Sn at the $\text{Cu}_3\text{Sn}/\text{Cu}_6\text{Sn}_5$ interface. Since the maximum thickness of the Cu_6Sn_5 layer decreased as the aging time increased, Cu_6Sn_5 is consumed to form Cu_3Sn . Some Cu may have diffused all the way to $\text{Cu}_6\text{Sn}_5/\text{Sn}$ interface to react with Sn to form additional Cu_6Sn_5 . The rate of Cu_6Sn_5 consumption is faster than the rate of Cu_6Sn_5 formation.

When Ni is used as the seed layer, $(\text{Ni,Cu})_3\text{Sn}_4$ IMCs with three different morphologies formed at the solder/Ni interface after reflow at 260°C for both Sn-1.1Cu and Sn-3.6Ag-1.8Cu solders: a continuous planar layer adjacent to the Ni; long and thin needles; and large, polygonal crystals. Both the continuous planar layer and the layer of needles and crystals are much thinner in reflowed Sn-Ag-Cu/Ni than in reflowed Sn-Cu/Ni, which means the addition of Ag inhibited the formation of $(\text{Ni,Cu})_3\text{Sn}_4$ when reflowed at 260°C . Both Ag_3Sn and Cu_6Sn_5 particles were evenly distributed in the solder after electrodeposition and became discontinuously distributed after reflow, with an increase in the sizes of some particles due to coarsening of both Ag_3Sn and Cu_6Sn_5 . Nickel atoms that had diffused into the solder dissolved into Cu_6Sn_5 and formed $(\text{Cu,Ni})_6\text{Sn}_5$. After aging at 125°C for different lengths of time, the continuous planar $(\text{Ni,Cu})_3\text{Sn}_4$ layer became thicker, while the entire $(\text{Ni,Cu})_3\text{Sn}_4$ IMC layer did not change much for either Sn-1.1Cu or Sn-3.6Ag-1.8Cu solders. The amount of the long, thin needles and polygonal crystals between the continuous planar layer and solder decreased and they increased in size during aging. As such, the thin needles and polygonal crystals coarsened to form large needles and crystals. Ag_3Sn particles continuously elongated and coarsened during aging and formed longer or larger Ag_3Sn particles. Nickel continuously diffused into the solder layer and dissolved into the $(\text{Cu,Ni})_6\text{Sn}_5$ particles. In addition, the $(\text{Cu,Ni})_6\text{Sn}_5$ particles coarsened and formed larger and higher Ni content $(\text{Cu,Ni})_6\text{Sn}_5$ particles.

Chapter 8 Conclusions and recommendations

8.1 Conclusions of the current work

Due to the toxicity of Pb, which can cause serious environment and healthy issues, many investigations have been performed to study different kinds of Pb-free solders as alternatives. In this work, the studies have focused on four main parts: (1) To develop simple and green plating baths for Sn and Sn-Cu solder film deposition, and to understand the effect of solution chemistry on Sn electrodeposition kinetics. (2) To study the nucleation and film growth mechanisms during Sn and Sn-Cu electrodeposition from the developed solutions. (3) To optimize plating conditions to obtain eutectic and near eutectic Sn-Cu and Sn-Ag-Cu solder films from citrate plating baths. (4) To study the interfacial reactions of as-deposited Sn-Cu or Sn-Ag-Cu solders with Cu or Ni substrates during reflow and aging.

8.1.1 Solution chemistry studies for Sn-citrate solutions

Sn-citrate solutions containing $\text{SnCl}_2 \cdot 2\text{H}_2\text{O}$ and tri-ammonium citrate have been studied. 0.30 mol/L (72.4 g/L) tri-ammonium citrate was found to be the minimum amount to completely dissolve 0.22 mol/L (50 g/L) $\text{SnCl}_2 \cdot 2\text{H}_2\text{O}$ without forming precipitates. Sn-citrate solutions containing 0.22 mol/L (50 g/L) $\text{SnCl}_2 \cdot 2\text{H}_2\text{O}$ and tri-ammonium citrate with a concentration higher than 0.30 mol/L (72.4 g/L) remained transparent and colorless for more than 3 months. The addition of $\text{CuCl}_2 \cdot 2\text{H}_2\text{O}$ caused the solutions to change color upon aging, producing rough and discontinuous films when the solutions were used for electroplating. The higher the tri-ammonium citrate concentration, the sooner the color change. Therefore, for Sn-Cu deposition, the optimal concentration of tri-ammonium citrate was 0.30 mol/L (72.4 g/L), which was the lowest tri-

ammonium citrate concentration needed to completely dissolve the 0.22 mol/L (50 g/L) tin salt.

Speciation calculations were performed on Sn-citrate solutions containing 0.22 mol/L (50 g/L) $\text{SnCl}_2 \cdot 2\text{H}_2\text{O}$ and different amounts of tri-ammonium citrate (0.30-0.66 mol/L) as a function of solution pH. All Sn^{2+} ions formed Sn-citrate complexes such as SnH_3L^+ , SnH_2L or SnHL^- , with excess citrate species present as H_4L , H_3L^- , H_2L^{2-} and HL^{3-} in the solution (here “L” represents the tetravalent citrate ligand). The distribution of the Sn(II)-citrate complexes changed with solution pH, with SnH_3L^+ as the main complex at pH below about 1.2 and SnHL^- above about 4. The addition of excessive ammonium citrate did not change the relative distribution of the Sn(II)-citrate complexes. The reduction potentials for the Sn(II)-citrate complexes in different electroplating solutions were almost the same at a given solution composition and pH, although the standard electrode potentials of these species differed substantially. The calculated reduction potential values indicated that the Sn(II)-citrate complexes were more difficult to reduce in solutions with higher tri-ammonium citrate concentrations and were easier to reduce in solutions with lower solution pH. The SnHL^- species were favored for Sn plating compared to SnH_3L^+ species due to its slower electroplating kinetics which resulted in smoother films. The precipitates formed at low pH from the Sn-citrate solutions were characterized using compositional and structural analysis and are proposed to be Sn_2L .

8.1.2 Nucleation and film growth mechanism studies for Sn and Sn-Cu from citrate solutions

The galvanostatic (current step) study showed that the potential-time transient at each applied current density was very similar for the Sn-citrate and Sn-Cu-citrate solutions. This was because the amount of Cu^{2+} ions in the Sn-Cu-citrate solution was very small. In all the galvanostatic experiments, the potentials were observed to initially move slightly towards the positive direction before dropping. The initial rise in potential was probably due to the reduction of SnHL^-

anions. The subsequent potential drop was caused by the depletion of the SnHL^- anions, requiring a concentration overpotential to maintain the current density. At current densities higher than 25 mA/cm^2 , the potential drop was much more significant. This was because higher current densities required higher concentration overpotentials. When the current density was between 25 and 35 mA/cm^2 , the potential dropped quickly and then was followed by a gradual increase. This gradual increase was due to hydrogen evolution which provided a mixing action, reducing the thickness of the depletion layer around the growing Sn or Sn-Cu particles. When the current density was higher than 50 mA/cm^2 , potential oscillation happened due to repeated SnHL^- ion depletion and restoration by hydrogen evolution. For the Sn-Cu-citrate solution, the depletion of SnHL^- and Cu-citrate complex ions and their restoration by hydrogen evolution happened faster than for Sn alone, and is attributed to a higher oscillation frequency. Significant hydrogen evolution at current densities higher than 25 mA/cm^2 prevented both Sn and Sn-Cu deposits from forming dense and uniform films. The steady state transition time constant indicated a diffusion controlled process. The average diffusion coefficient calculated from the Sand equation was about $3.8 \times 10^{-6} \text{ cm}^2/\text{s}$ for the Sn-citrate solution and $4.1 \times 10^{-6} \text{ cm}^2/\text{s}$ for the Sn-Cu-citrate solution.

In the chronoamperometric studies, all the current-time transients for both Sn and Sn-Cu electrodeposition showed an initial increase in cathodic current density followed by a gradual decrease over time. The increase in current density was due to the perturbation from the application of the constant potential and reactions occurring instantly on the electrode, resulting in a high current density. The decrease in current density afterward was due to the consumption of the reducing ionic species at the electrode surface during the reduction reaction, forming a concentration gradient between the electrode surface and the bulk solution. When the diffusion of the reducing ionic species from the bulk solution to the electrode surface was just sufficient to permit continuous reduction, the current density reached a constant value, indicating a diffusion-controlled process. Nucleation modeling from current-time transients at -0.72, -1.1, and -1.5 V and

surface morphology characterization for samples deposited at -1.1 and -1.5 V showed a progressive nucleation mechanism controlled by diffusion for the initial stages of both Sn and Sn-Cu electrodeposition. At an applied potential of -0.72 V, the diffusion coefficient was 1.3×10^{-8} cm²/s for Sn electrodeposition and 2.3×10^{-8} cm²/s for Sn-Cu electrodeposition. At an applied potential of -1.1 V, the diffusion coefficient was 1.6×10^{-6} cm²/s for Sn electrodeposition and 2.2×10^{-6} cm²/s for Sn-Cu electrodeposition. At an applied potential of -1.5 V, the diffusion coefficient was 5.6×10^{-6} cm²/s for Sn electrodeposition and 6.9×10^{-6} cm²/s for Sn-Cu electrodeposition. Tin reacted with the Pt seed layer to form PtSn₄ and co-deposited with Cu to form Cu₆Sn₅ during nucleation, with more Sn being deposited at higher applied potentials.

Sn-Cu films were electrodeposited for different lengths of time (1-1800 s) under controlled current conditions to study the mechanism of Sn-Cu film growth from Sn-Cu-citrate solutions. The results indicated that Sn-Cu film growth from Sn-Cu-citrate solutions followed an island (Volmer-Weber) growth mechanism. Tin co-deposited with Cu to form Cu₆Sn₅ initially. As plating continued, Sn deposition became dominant.

8.1.3 Deposition of Sn, Sn-Cu and Sn-Ag-Cu solder films from citrate plating baths

8.1.3.1 Sn electrodeposition

As a starting point for investigations on Sn-Cu and Sn-Ag-Cu deposition, Sn electrodeposition from Sn-citrate solutions was carried out initially. Dense and uniform Sn films were attainable from solutions containing 0.22 mol/L (50 g/L) SnCl₂·2H₂O and 0.30-0.82 mol/L (72.4-200 g/L) tri-ammonium citrate at an average current density of 5 mA/cm². The observed plating rate under these conditions was 8-10 μm/hr. As current density was increased, the plating rate increased but the Sn deposit surface became rougher.

8.1.3.2 Sn-Cu deposition

Two different types of solutions have been developed and optimized to deposit eutectic and near eutectic Sn-Cu alloys. One type of solution contained $\text{SnCl}_2 \cdot 2\text{H}_2\text{O}$ (fixed at 0.22 mol/L) and $\text{CuCl}_2 \cdot 2\text{H}_2\text{O}$ with tri-ammonium citrate as the only additive. The Cu content in deposits increased as the $\text{CuCl}_2 \cdot 2\text{H}_2\text{O}$ concentration was increased, and Sn-Cu deposits became rougher and less dense with higher $\text{CuCl}_2 \cdot 2\text{H}_2\text{O}$ concentration. Eutectic and near-eutectic Sn-Cu films were achievable from solutions containing 0.22 mol/L (50 g/L) $\text{SnCl}_2 \cdot 2\text{H}_2\text{O}$, 0.30 mol/L (72.4g/L) tri-ammonium citrate, and 0.003 mol/L (0.533 g/L) $\text{CuCl}_2 \cdot 2\text{H}_2\text{O}$ at current densities of 10-12.5 mA/cm². In this Sn-Cu-citrate solution, copper remained more noble than Sn so that Cu reduction dominated initially. This caused Cu enrichment at the Sn-Cu deposit/substrate interface. Since Cu concentration in the solution was almost two orders of magnitude lower than that of Sn, Cu levels depleted rapidly and Sn reduction soon became dominant. The developed Sn-Cu-citrate solution was stable for at least 77 days. The Cu^{2+} ions in the Cu(II)-citrate complexes became easier to reduce with aging while Sn-citrate was stable, resulting in a slight increase in the Cu content in the deposited Sn-Cu films.

For both PC and DC electrodeposition from the above Sn-Cu-citrate solution, Cu content in Sn-Cu deposits decreased and plating rate increased as current density was increased. PC plating gave slightly higher Cu content in the deposits but lower plating rates than DC plating. The co-deposition of Sn and Cu from the Sn-Cu-citrate solutions formed two phases, i.e., Sn as the major phase with small amounts of Cu_6Sn_5 .

Agitation increased the limiting current density and allowed higher current densities to be utilized, resulting in higher plating rates. With agitation, Cu content in the deposits decreased much more slowly as current density was increased. Eutectic Sn-Cu deposits are attainable from Sn-Cu-citrate solutions containing 0.001 mol/L (0.27 g/L) $\text{CuCl}_2 \cdot 2\text{H}_2\text{O}$, 0.22 mol/L (50 g/L) $\text{SnCl}_2 \cdot 2\text{H}_2\text{O}$, and 0.30 mol/L (72.4 g/L) tri-ammonium citrate at current densities of 20-40 mA/cm² and a stirring speed of 600 rpm.

The addition of gelatin and β -naphthol to the Sn-Cu-citrate solutions gave rougher and less dense Sn-Cu films at a current density of 15 mA/cm². When the current density was set at 25 mA/cm², Sn whiskers were detected. The difference in Cu content in Sn-Cu deposits was insignificant with and without the addition of gelatin (0-2 g/L) and β -naphthol (0-1 g/L).

Another type of Sn-Cu plating bath contained SnCl₂·2H₂O and triammonium citrate with suspended Cu particles, along with sodium metaphosphate as a dispersant. The addition of 0.48 g/L dispersant helped improve deposit surface morphology, uniformity, and plating rate. With 0.2 g/L of Cu particles, Sn-Cu deposits with 1.1±0.3 wt% Cu were attainable at a current density of 10 mA/cm².

8.1.3.3 Sn-Ag-Cu deposition

Silver nano-particles were added to Sn-Cu-citrate solutions to deposit Sn-Ag-Cu solder films. By adding Ag nano-particles, the Cu content in deposits increased and film plating rate decreased slightly. The Cu content in the Sn-Ag-Cu films increased more with increased CuCl₂·2H₂O concentration in solution compared with Sn-Cu films deposited from Sn-Cu solutions with the same CuCl₂·2H₂O concentration. Deposit Ag and Cu contents decreased with increasing current density, or decreasing CuCl₂·2H₂O concentration in solution. The addition of sodium dodecyl sulfate (SDS) decoupled Ag and Cu co-deposition, leading to near eutectic Sn-3.8Ag-0.7Cu deposit.

As-deposited Sn-Ag-Cu solder films with various compositions on Au seed layers had a solidus temperature of about 203.7°C, which is lower than the eutectic temperature of 217°C. As-deposited Sn-Cu solder films on Au seed layers had a solidus temperature of about 210.7°C, which was lower than the eutectic temperature of 227°C. The same Sn-Cu solder films on Ni substrates had a much higher solidus temperature of about 230°C. One possible reason was the Au seed layer alloyed with the solder, which decreased the eutectic temperature.

8.1.4 Interfacial reactions between Sn-Cu and Sn-Ag-Cu solders and Cu and Ni substrates during reflow and aging

8.1.4.1 Interfacial reactions between solders and Cu substrate

When Cu was used as the substrate, a continuous bilayer of Cu_3Sn and Cu_6Sn_5 formed between the Cu substrate and the solder (for both Sn-Cu and Sn-Ag-Cu deposits) after reflow at 260°C . During reflow, Cu reacted with molten Sn to form Cu_6Sn_5 and grew into a continuous layer at the interface. Copper atoms at the Cu/ Cu_6Sn_5 interface reacted with Cu_6Sn_5 to form Cu_3Sn . The thickness of the Cu_3Sn layer at the Sn-Ag-Cu/Cu interface was thinner than that at the Sn-Cu/Cu interface. This can be attributed to the presence of Ag, inhibiting the formation of Cu_3Sn during reflow.

After aging at 125°C , the thickness of the Cu_3Sn layer increased as aging time increased for both Sn-Cu/Cu and Sn-Ag-Cu/Cu, with a calculated diffusion coefficient of $2.25 \times 10^{-14} \text{ cm}^2/\text{s}$ and $3.6 \times 10^{-15} \text{ cm}^2/\text{s}$ for Cu diffusing through Cu_3Sn layer, respectively. The lower diffusion coefficient for Sn-Ag-Cu/Cu than that for Sn-Cu/Cu indicated that the addition of Ag slowed down the growth of Cu_3Sn layer during aging. The continuous growth of the Cu_3Sn layer during aging was due to the continuous diffusion of Cu through the Cu_3Sn layer to Cu_6Sn_5 . The diffused Cu atoms reacted with Cu_6Sn_5 and formed Cu_3Sn at the $\text{Cu}_3\text{Sn}/\text{Cu}_6\text{Sn}_5$ interface. The maximum thickness of the Cu_6Sn_5 layer decreased during aging, which was due to the continuous consumption of Cu_6Sn_5 to form Cu_3Sn . It was also possible that Cu diffused all the way to the $\text{Cu}_6\text{Sn}_5/\text{Sn}$ interface and reacted with Sn to form more Cu_6Sn_5 . The speed of Cu_6Sn_5 consumption was faster than the speed of Cu_6Sn_5 formation, which caused a decrease in Cu_6Sn_5 thickness.

8.1.4.2 Interfacial reactions between solders and Ni substrate

When Ni was used as the substrate, $(\text{Ni,Cu})_3\text{Sn}_4$ IMCs with three different types of morphologies formed at the solder/Ni interface after reflow at 260°C for both Sn-Cu and Sn-Ag-Cu solders. A continuous planar layer formed adjacent to the Ni substrate. Needles (long and thin) and crystals (large and polygonal)

formed above the planar layer. Both the continuous planar layer and the layer of needles and crystals were much thinner in reflowed Sn-Ag-Cu/Ni than in reflowed Sn-Cu/Ni. This indicated that the addition of Ag inhibited the formation of $(\text{Ni,Cu})_3\text{Sn}_4$ during reflow. Both Ag_3Sn and Cu_6Sn_5 particles were evenly distributed in the solders after electrodeposition and became discontinuously distributed after reflow. The size of some particles increased after reflow due to the coarsening of Ag_3Sn and Cu_6Sn_5 . Nickel diffused into the solder and dissolved into Cu_6Sn_5 to form $(\text{Cu,Ni})_6\text{Sn}_5$.

After aging at 125°C , the continuous planar $(\text{Ni,Cu})_3\text{Sn}_4$ layer became thicker, while the thickness of the $(\text{Ni,Cu})_3\text{Sn}_4$ IMC layer did not change for either Sn-Cu or Sn-Ag-Cu solders. The amount of needles and crystals between the continuous planar layer and solder decreased and their sizes increased during aging. These observations indicated that needles and crystals coarsened and formed larger needles and crystals. Ag_3Sn particles continuously elongated and coarsened during aging and formed longer or larger Ag_3Sn particles. Nickel continuously diffused and dissolved into the $(\text{Cu,Ni})_6\text{Sn}_5$ particles. The $(\text{Cu,Ni})_6\text{Sn}_5$ particles coarsened, resulting in larger particles with more Ni.

8.2 Original contribution highlights

The original contributions for this work can be summarized as follows:

- (1) Electrodeposition of Sn-Cu solder alloys from Sn-Cu-citrate solution using tri-ammonium citrate as the only additive;
- (2) Electrochemical composite deposition of Sn-Cu alloys from Sn-citrate + Cu particle suspensions;
- (3) Electrochemical composite deposition of Sn-Ag-Cu alloy from Sn-Cu-citrate + Ag nano-particle suspensions;
- (4) Sn-citrate solution chemistry studies through reduction potential calculations and polarization measurements, and identification of Sn-citrate precipitates as Sn_2L ;

(5) Nucleation and film growth mechanism study of Sn and Sn-Cu films from citrate solutions.

8.3 Recommendations for future work

8.3.1 Other plating parameters

8.3.1.1 Pulse plating conditions

For all the PC plating in this research work, a 2 ms ON and 8 ms OFF pulsed current was applied based on previous studies in the group. Other on-time and off-time should be tested to study their effects on deposit microstructure and composition.

8.3.1.2 $\text{SnCl}_2 \cdot 2\text{H}_2\text{O}$ concentration

In the Sn, Sn-Cu, and Sn-Ag-Cu deposition work, the concentration of $\text{SnCl}_2 \cdot 2\text{H}_2\text{O}$ was fixed at 0.22 mol/L (50 g/L) and the concentrations of tri-ammonium citrate, $\text{CuCl}_2 \cdot 2\text{H}_2\text{O}$, and Ag nano-particles were varied. It is worthwhile to test other $\text{SnCl}_2 \cdot 2\text{H}_2\text{O}$ concentrations to examine their influence on solution stability, plating rate, Cu content in deposit, Ag content in deposit, and microstructure of as-deposited Sn-Cu, Sn-Ag-Cu films.

8.3.2 Speciation calculation for Cu-citrate solution

In Chapter 4, Sn-citrate solution chemistry studies were done to better understand the formation and distribution of different Sn(II)-citrate complexes and their roles in Sn electrodeposition. Similar solution chemistry studies can be done for Cu-citrate solutions, although the structures of Cu-citrate complexes reported in literature are much more complicated. Several different possible Cu(II)-citrate complexes and different stability constants for the same type of

Cu(II)-citrate complex are reported in literature. More reliable data needs to be collected.

8.3.3 Reactions between Ag nano-particles and other species in suspensions

For Sn-Ag-Cu electrochemical composite deposition, in order to better understand the reactions between Ag nano-particles and Sn(II)-citrate complexing species and Cu(II)-citrate complexing species, further investigations are needed. Suspensions could include Sn-citrate solutions (different concentrations) + Ag nano-particles, Cu-citrate solutions (different concentrations) + Ag nano-particles, Sn-Cu-citrate solutions (different concentrations) + Ag nano-particles, Ag nano-particles suspended in water, Ag nano-particles suspended in CuCl₂-water solutions, and Ag nano-particles suspended in SnCl₂-water solutions. Investigations include surface charge measurement and composition and microstructure characterization of deposits from the suspensions. Current results showed that SDS was helpful to obtain eutectic Sn-Ag-Cu films. In order to better understand the effect of SDS on Sn-Ag-Cu deposition, more studies need to be done to determine the reactions occur between SDS and other species in Sn-Cu-citrate solutions + Ag nano-particles. Polarization tests could be carried out for suspensions without and with SDS, and with different concentrations of SnCl₂·2H₂O, CuCl₂·2H₂O, Ag, and SDS, to find the effect of SDS during deposition. Other electrochemical methods can be applied to study the initial stages of Sn-Ag-Cu deposition without and with SDS, to find out the effect of SDS on Sn-Ag-Cu nucleation and film growth.

8.3.4 Sn-Ag deposition using AgNO₃ as Ag source

The feasibility of depositing Sn-Ag alloys from solutions containing AgNO₃, tri-ammonium citrate, and SnCl₂·2H₂O has been tried. More time is needed to completely dissolve AgNO₃ in citrate solutions than in water. Once the

Ag-citrate solution (AgNO_3 dissolved in the tri-ammonium citrate solution) is mixed with the Sn-citrate solution ($\text{SnCl}_2 \cdot 2\text{H}_2\text{O}$ dissolved in tri-ammonium citrate solution), black precipitates start to form and the suspension color quickly became black. Electrochemical composite deposition was performed from this suspension onto Au seed layers at a current density of 10 mA/cm^2 for 30 min. The deposited film was black in color and easily detached from the substrate. SEM SE plan view and cross section images of the deposited film are shown in Fig. 8-1. The plan view image shows that the deposit is smooth with many protrusions at the surface, which are due to the reduction of Sn around the precipitates that were adsorbed to the surface of the cathode and became active sites for deposition. These protrusions make the surface very rough and cause the black appearance of the deposits. The cross section image shows that the smoother layer adjacent to the substrate is about $4 \mu\text{m}$ thick. EDX point analysis was carried out at positions marked in both images. Fig. 8-2 shows the EDX point analysis at position 1 in Fig. 8-1a and position 2 in Fig. 8-1b. The Ag content is about 27 wt% for the smooth area (position 1), about 30 wt% for the small protrusions (position 2), and about 37 wt% for the larger protrusion (position 3). The Ag content from the cross section is lower, about 17 wt% at position 1 and 22 wt% at position 2. The differences in Ag content at different positions for both the plan view and cross section samples may be due to the roughness of the sample surface. Although Ag is not evenly distributed on the deposit Sn-Ag film, the Ag content is much higher than that achieved with Sn-Ag-Cu films deposited from Sn-Cu-citrate suspensions with Ag nano-particles in Chapter 6, which means Ag is more readily deposited from this type of solution. By changing the plating conditions, such as the concentration of AgNO_3 , $\text{SnCl}_2 \cdot 2\text{H}_2\text{O}$, and tri-ammonium citrate, the current density, on-off time, agitation conditions, and additives, it may be possible to obtain uniform eutectic Sn-Ag alloys. This approach may also be used to develop Sn-Ag-Cu plating baths by adding a CuCl_2 or $\text{Cu}(\text{NO}_3)_2$ salt.

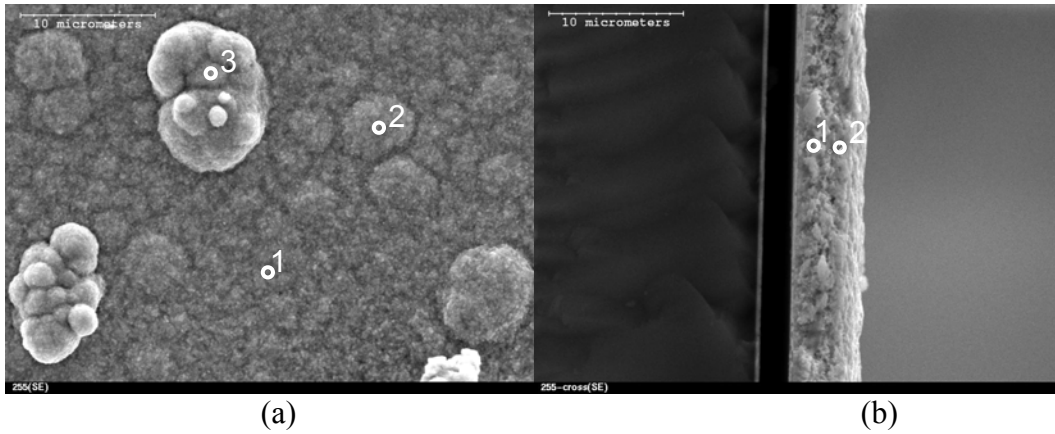


Fig. 8-1 SEM SE (a) plan view and (b) cross section images of Sn-Ag films deposited onto Au seed layer from plating baths containing 0.22 mol/L $\text{SnCl}_2 \cdot 2\text{H}_2\text{O}$, 0.01 mol/L AgNO_3 , and 0.30 mol/L tri-ammonium citrate. The current density is 10 mA/cm^2 and the plating time is 30 min.

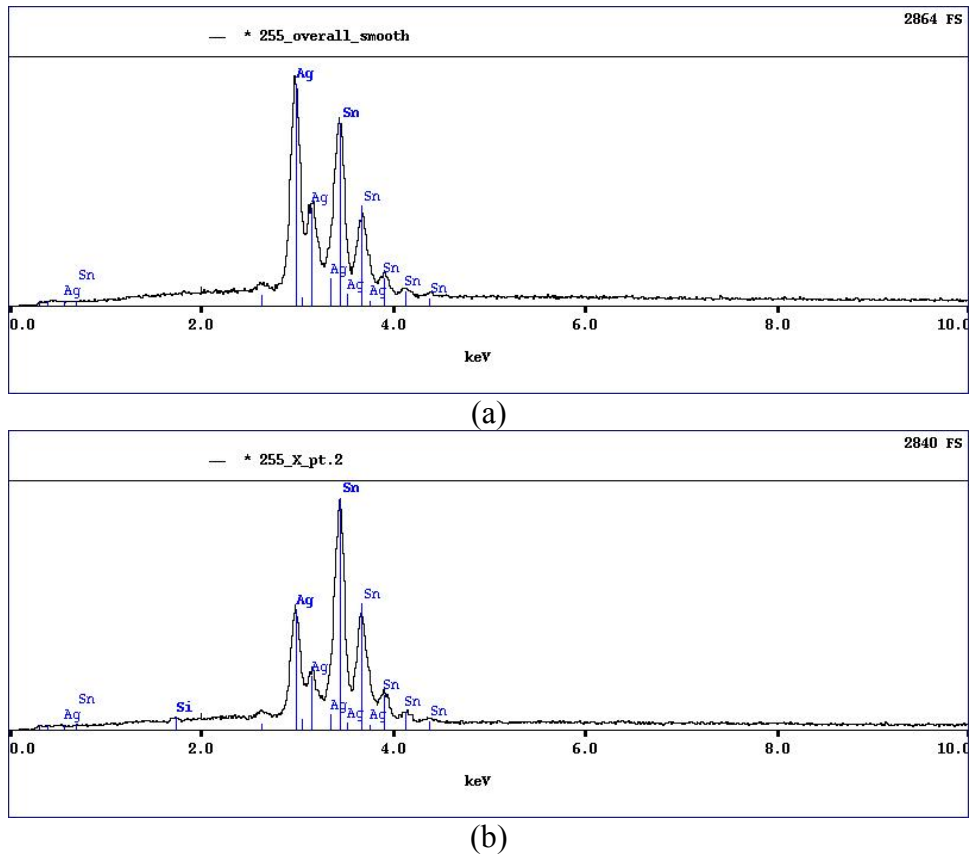


Fig. 8-2 EDX point analysis for Sn-Ag deposits at (a) position 1 in Fig. 8-1a and (b) position 2 in Fig. 8-1b.

8.3.5 Mechanical properties of Pb-free solder joints

As mentioned in Chapter 2, solders must meet the expected level of mechanical performance, because solder joints are often subjected to mechanical loading during manufacturing and service. Good fatigue resistance and shear strength are crucial to solder joint reliability and have been studied using different test methods. The ball shear test is the most common method to evaluate the strength of solder ball attachments. The test method is simple and convenient to implement, yet the experimental details such as shear speed have not been standardized. Kim and Jung (2005) investigated the effect of important shear test parameters, such as shear height and shear speed, on the evaluation of solder joint integrity using a global bond tester (Dage-4000s, Richardson Electronic Ltd.) under various conditions. A global bond tester (PTR-1000, Rhesca Co. Ltd.) was used by Yoon et al. (2005) to study the shear strength between Sn-0.7Cu solder balls and Au/Ni/Cu. It was also used to investigate the effect of microstructure variation in solder joints on the joint strength and failure mode of the test specimens (Kim and Jung, 2005). Kar et al. (2007) carried out shear tests for both the Sn-3.5Ag-0.5Cu/Cu and Pb-63Sn/Cu solder joints using a specially designed jig mounted on a tensile testing machine (Honsfield, H10K-S, 10kN capacity). Zhu et al. (2007) conducted tensile tests and creep tests using a self-built tester to study the effect of temperature and strain rate on tensile and creep properties of Sn-3Ag-0.5Cu solders, in which Sn-Ag-Cu solders were machined and sliced into dog-bone-shaped specimens for tensile and creep tests. Appropriate testing methods need to be found and standardized to study the mechanical properties of solder joints.

References

Abteu, M. and Selvaduray, G., Lead-free solders in microelectronics, *Materials Science and Engineering R*, 27 (2000) 95-141.

Alam, M. O., Chan, Y. C. and Tu, K. N., Effect of 0.5 wt% Cu addition in Sn-3.5%Ag solder on the dissolution rate of Cu metallization, *Journal of Applied Physics*, 94 (2003) 7904-7909.

Anderson, I. E., Yost, F. G., Smith, J. F., Miller, C. M. and Terpstra, R. L., Pb-free Sn-Ag-Cu ternary eutectic solder, US Patent 5,527,628 (1996).

Anderson, I. E., Development of Sn-Ag-Cu and Sn-Ag-Cu-X alloys for Pb-free electronic solder applications, *Journal of Materials Science: Materials in Electronics*, 18 (2007) 55-76.

Arai, S. and Kaneko, N., Electrodeposition of Sn-Ag-Cu alloys, *Denki Kagaku*, 65 (1997) 1102-1106.

Arai, S., Tin-silver alloy plating bath and process for producing plated object using the plating bath, US Patent 5,948,235 (1999).

Aravinda, C. L., Muralidharan, V. S. and Mayanna, S. M., Electrodeposition and dissolution of Co-W alloy films, *Journal of Applied Electrochemistry*, 30 (2000) 601-606.

Atzei, D., Sadun, C. and Pandolfi, L., X-ray photoelectron spectra of complexes with 1-(D-3-mercapto-2-methylpropionyl)-L-proline and Ni(II), Cd(II) and Cu(I): synthesis and LAXS study of Cu(I) derivative, *Spectrochimica Acta Part A: Molecular and Biomolecular Spectroscopy*, 56 (2000) 531-540.

Bader, S., Gust, W. and Hieber, H., Rapid formation of intermetallic compounds interdiffusion in the Cu-Sn and Ni-Sn systems, *Metallurgica et Materialia*, 43 (1995) 329-337.

Baker, H., *Alloy Phase Diagrams (ASM Handbook, Volume 3)*, ASM International, Ohio (1992).

Banovic, S. W., Barmak, K. and Marder, A. R., Characterization of single and discretely-stepped electro-composite coatings of nickel-alumina, *Journal of Materials Science*, 34 (1999) 3203-3211.

Bard, A. J. and Faulkner, L. R., *Electrochemical Methods: Fundamentals and Applications*, Wiley, New York (2001).

Barkey, D. P., Wu, Q., Keigler, A. and Liu, Z., Electrodeposition of silver particles with tin for fabrication of lead-free solder bumps, *ECS Transactions*, 1 (2006) 43-51.

Batzill, M. and Diebold, U., The surface and materials science of tin oxide, *Progress in Surface Science*, 79 (2005) 47-154.

Bonhote, C. and Landolt, D., Microstructure of Ni-Cu multilayers electrodeposited from a citrate electrolyte, *Electrochimica Acta*, 42 (1997) 2407-2417.

Bradley, P. E. and Landolt, D., Pulse-plating of copper-cobalt alloys, *Electrochimica Acta*, 45 (1999) 1077-1087.

Brandes, E. A. and Goldthorpe, D., *Metallurgia*, 76 (1967) 195.

Broggi, R. L., Oliveira, G. M. D., Barbosa, L. L., Pallone, E. M. J. A. and Carlos, I. A., Study of an alkaline bath for tin deposition in the presence of sorbitol and physical and morphological characterization of tin film, *Journal of Applied Electrochemistry*, 36 (2006) 403-409.

Buelens, C., Celis, J. P. and Roos, J. R., Electrochemical aspects of the codeposition of gold and copper with inert particles, *Journal of Applied Electrochemistry*, 13 (1983) 541-548.

Buene, L., Falkenberg-Arell, H. and Tafto, J., A study of evaporated gold-tin films using transmission electron microscopy, *Thin Solid Films*, 65 (1980) 247-257.

Bunshah, R. F., *Handbook of Deposition Technologies for Films and Coatings: Science, Technology, and Applications*, Noyes Publications, New Jersey (1994).

Carlos, I. A., Souza, C. A. C., Pallone, E. M. J. A., Francisco, R. H. P., Cardoso, V. and Lima-Neto, B. S., Effect of tartrate on the morphological characteristics of the copper-tin electrodeposits from a noncyanide acid bath, *Journal of Applied Electrochemistry*, 30 (2000) 987-994.

Cavallotti, P. L., Sirtori, V. and Zangari, G., Electrodeposition bath, US Patent 5,783,059 (1998).

Chada, S., Fournelle, R. A., Laub, W. and Shanguan, D., Copper substrate dissolution in eutectic Sn-Ag solder and its effect on microstructure, *Journal of Electronic Materials*, 29 (2000) 1214-1221.

- Chandrasekar, M. S. and Pushpavanam, M., Pulse and pulse reverse plating - Conceptual, advantages and applications, *Electrochimica Acta*, 53 (2008) 3313-3322.
- Chang, J. H., Hsu, F. Y., Liao, M. J. and Huang, C. A., A study of direct- and pulse-current chromium electroplating on rotating cylinder electrode (RCE), *Applied Surface Science*, 253 (2007) 6829–6834.
- Chen, C. S., Wan, C. C. and Wang, Y. Y., Effect of agitation on tin-lead alloy deposition in a methane sulfonate system, *Plating and Surface Finishing*, 88 (2001) 86-89.
- Chen, H. Y., Chen, C., WU, P. W., Shieh, J. M., Cheng, S. S. and Hensen, K., Effect of polyethylene glycol additives on pulse electroplating of SnAg solder, *Journal of Electronic Materials*, 37 (2008) 224-230.
- Chen, S. W., Chen, C. M. and Liu, W. C., Electric current effects upon the Sn/Cu and Sn/Ni interfacial reactions, *Journal of Electronic Materials*, 27 (1998) 1193-1198.
- Chen, S. W. and Yen, Y. W., Interfacial reactions in Ag-Sn/Cu couples, *Journal of Electronic Materials*, 28 (1999) 1203-1208.
- Chen, S. W., Wu, S. H. and Lee, S. W., Interfacial reactions in the Sn-(Cu)/Ni, Sn-(Ni)/Cu, and Sn/(Cu,Ni) system, *Journal of Electronic Materials*, 32 (2003) 1188-1194.
- Chen, W. T., Ho, C. E. and Kao, C. R., Effect of Cu concentration on the interfacial reactions between Ni and Sn-Cu solders, *Journal of Materials Research*, 17 (2002) 263-266.
- Cherkaoui, M., Chassaing, E. and Quang, K. V., Pulse plating on Ni-Cu alloys, *Surface and Coatings Technology*, 34 (1988) 243-252.
- Chin, D. and Zhang, H., A study of pulse plating of Chromium, *Electrochimica Acta*, 31 (1986) 299-306.
- Chin, D. and Balamurugan, D., An experimental study of metal distribution in pulse plating, *Electrochimica Acta*, 37 (1992) 1927-1934.
- Commander, J. H. and V. Panecasio, Bright Tin electrodeposition composition, US Patent 5,061,351 (1991).
- Conway, B. E., *Modern Aspects of Electrochemistry (No.38)*, Dordrecht: Springer, (2005).

Correia, A. N., Facanha, M. X. and Lima-Neto, P. d., Cu-Sn coatings obtained from pyrophosphate-based electrolytes, *Surface and Coatings Technology*, 201 (2007) 7216-7221.

Dariavach, N., Callahan, P., Liang, J. and Fournelle, R., Intermetallic growth kinetics for Sn-Ag, Sn-Cu, and Sn-Ag-Cu lead-free solders on Cu, Ni, and Fe-42Ni substrates, *Journal of Electronic Materials*, 35 (2006) 1581-1592.

Datta, M., Osaka, T. and Schultze, J. W., *Microelectronic Packaging (Volume 3)*, CRC Press, Boca Raton (2005).

Dean, J. A., *Lange's Handbook of Chemistry*, McGraw-Hill, (1999).

Dennis, A. M., Howard, R. A., Kadish, K. M., Bear, J. L., Brace, J. and Winograd, N., X-ray photoelectron-spectra of some dirhodium carboxylate complexes, *Inorganica Chimica Acta - Letters*, 44 (1980) 139-141.

Devaraj, G., Guruviah, S. and Seshadri, S. K., Pulse plating, *Materials Chemistry and Physics*, 25 (1990) 439-461.

Dohle, G. R., Callahan, J. J., Martin, K. P. and Drabik, T. J., A new bonding technique for microwave devices, *IEEE Transactions on Components, Packaging, and Manufacturing Technology - Part B*, 19 (1996) 57-63.

Elbourne, R. G. P. and Buchanan, G. S., A potentiometric study of complexes of Tin with some carboxylic acids, *Journal of Inorganic and Nuclear Chemistry*, 32 (1970) 3559-3567.

Evans, J. W., Kwon, D. and Evans, J. Y., *A Guide to Lead-free Solders: Physical Metallurgy and Reliability*, Springer-Verlag London Limited, London (2007).

Fix, A. R., Lopez, G. A., Brauer, I., Nuchter, W. and Mittemeijer, E. J., Microstructural development of Sn-Ag-Cu solder joints, *Journal of Electronic Materials*, 34 (2005) 137-142.

Fujiwara, Y., Enomoto, H., Nagao, T. and Hoshika, H., Composit plating of Sn-Ag alloys for Pb-free soldering, *Surface and Coatings Technology*, 169-170 (2003) 100-103.

Fukuda, M., Imayoshi, K. and Matsumoto, Y., Effect of polyoxyethylenelaurylether on electrodeposition of Pb-free Sn-Bi alloy, *Electrochimica Acta*, 47 (2001) 459-464.

Fukuda, M., Imayoshi, K. and Matsumoto, Y., Effect of thiourea and polyoxyethylene lauryl ether on electrodeposition of Sn-Ag-Cu alloy as a Pb-free solder, *Journal of The Electrochemical Society*, 149 (2002) 244-249.

- Fukuda, M., Imayoshi, K. and Matsumoto, Y., Effect of adsorption of polyoxyethylene laurylether on electrodeposition of Pb-free Sn alloys, *Surface and Coatings Technology*, 169-170 (2003) 128-131.
- Gagliano, R. A. and Fine, M. E., Growth of Cu_6Sn_5 phase scallops and whiskers in liquid tin-solid copper reaction couples, *Journal of the Minerals, Metals and Materials Society*, 53 (2001) 33-38.
- Gagliano, R. A., Ghosh, G. and Fine, M. E., Nucleation kinetics of Cu_6Sn_5 by reaction of molten tin with a copper substrate, *Journal of Electronic Materials*, 31 (2002) 1195-1202.
- Galdkiene, O. and Mockus, Z., Cathodic process in copper-tin deposition from sulphate solutions, *Journal of Applied Electrochemistry*, 24 (1994) 1009-1012.
- Ghaemi, M. and L. Binder, Effects of direct and pulse current on electrodeposition of manganese dioxide, *Journal of Power Sources*, 111 (2002) 248-254.
- Ghosh, S. K., Grover, A. K., Dey, G. K. and Totlani, M. K., Nanocrystalline Ni-Cu alloy plating by pulse electrolysis, *Surface and Coatings Technology*, 126 (2000) 48-63.
- Gillman, H. D., Fernandes, B. and Wikiel, K., Metal alloy sulfate electroplating baths, US Patent 6,562,220 B2 (2003).
- Gomez, E., Gaus, E., Sanz, F. and Valles, E., Tin electrodeposition on carbon electrodes from nuclei to microcrystallites, *Journal of Electroanalytical Chemistry*, 465 (1999) 63-71.
- Gomez, E., Llorente, A. and Valles, E., Obtention and characterisation of cobalt + copper electrodeposits from a citrate bath, *Journal of Electroanalytical Chemistry*, 495 (2000) 19-26.
- Green, T. A., Russell, A. E. and Roy, S., The development of a stable citrate electrolyte for the electrodeposition of copper-nickel alloys, *Journal of The Electrochemical Society*, 145 (1998) 875-881.
- Grujicic, D. and Pesic, B., Electrodeposition of copper: the nucleation mechanisms, *Electrochimica Acta*, 47 (2002) 2901-2912.
- Grujicic, D. and Pesic, B., Electrochemical and AFM study of nickel nucleation mechanisms on vitreous carbon from ammonium sulfate solutions, *Electrochimica Acta*, 51 (2006) 2678-2690.

Harper, C. A., *Electronic Materials and Processes Handbook (3rd Edition)*, McGraw-Hill, New York (2004).

Hayashi, H., Izumi, S. and Tari, I., Codeposition of alpha-alumina particles from acid copper sulfate bath, *Journal of The Electrochemical Society*, 140 (1993).

He, A., Liu, Q. and G.Ivey, D., Electrodeposition of tin: a simple approach, *Journal of Materials Science: Materials in Electronics*, 19 (2008) 553-562.

Hess, R. H. and Taft, R., The electrodeposition of tin from solutions of Its complex Salts, *Transactions of the Kansas Academy of Science*, 41 (1938) 171-173.

Ho, C. E., Tsai, R. Y., Lin, Y. L. and Kao, C. R., Effect of Cu concentration on the reactions between Sn-Ag-Cu solders and Ni, *Journal of Electronic Materials*, 31 (2002) 584-590.

Ho, C. E., Yang, S. C. and Kao, C. R., Interfacial reaction issues for lead-free electronic solders, *Journal of Materials Science: Materials in Electronics*, 18 (2007) 155-174.

Hodes, G., *Electrochemistry of Nanomaterials*, Wiley-VCH, Weinheim (2001).

Honma, H., Plating technology for electronics packaging, *Electrochimica Acta*, 47 (2001) 75-84.

Hou, K., Hwu, W., Ke, S. and Ger, M., Ni-P-SiC composite produced by pulse and direct current plating, *Materials Chemistry and Physics*, 100 (2006) 54-59.

Hovestad, A. and Janssen, L. J. J., Electrochemical codeposition of inert particles in a metallic matrix, *Journal of Applied Electrochemistry*, 25 (1995) 519-527.

Hovestad, A., Ansink, R. and Janssen, L. J. J., Iron deposition from a FeCl₂ solution containing suspended silicon particles, *Journal of Applied Electrochemistry*, 27 (1997) 756-761.

Humpston, G. and Jacobson, D. M., *Principles of Soldering*, ASM International, Ohio (2004).

Hwang, C. W., Kim, K. S. and Suganuma, K., Interfaces in lead-free soldering, *Journal of Electronic Materials*, 32 (2003) 1249-1256.

Ibl, N., Some theoretical aspects of pulse electrolysis, *Surface Technology*, 10 (1980) 81-104.

Igarashi, S., Fujisawa, Y. and Igarashi, T., Method for stabilizing tin or tin alloy electroplating baths, US Patent 4,163,700 (1979).

IPC, IPC-SPVC-WP-006, Round Robin testing and analysis of lead-free alloys: Tin, Silver, Copper- a white paper report by the lead-free technical subcommittee of the IPC solder products value council, (2003)

Ipser, H., Flandorfer, H., Luef, C., Schmetterer, C. and Saeed, U., Thermodynamics and phase diagrams of lead-free solder materials, *Journal of Materials Science: Materials in Electronics*, 18 (2007) 3-17.

Islam, M. N. and Chan, Y. C., Interfacial reactions of Sn-Cu solder with Ni/Au surface finish on Cu pad during reflow and aging in ball grid array packages, *Materials Science and Engineering B*, 117 (2005) 246-253.

Jawitz, M. W., *Printed Circuit Board Materials Handbook*, McGraw-Hill, (1997).

Jean, J. and C. Sinicki, Comptes Rendus des Seances de l'Academie des Sciences, Serie 2: Mecanique-Physique, Chimie, Sciences de l'Univers, Sciences de la Terre (in French), *C.R. Acad. Sci.II*, 292 (1981) 793.

Jimenez, V., Fernandez, A., Espinos, J. P. and Gonzalez-Elipe, A. R., Interface effects for metal oxide thin films deposited on another metal oxide: SnO deposited on SiO₂, *Surface Science*, 350 (1995) 123-135.

Joseph, S. and Phatak, G. J., Effect of surfactant on the bath stability and electrodeposition of Sn-Ag-Cu films, *Surface and Coatings Technology*, 202 (2008) 3023-3028.

Kall, P., Grins, J., Fahlman, M. and Soderlind, F., Synthesis, structure determination and X-ray photoelectron spectroscopy characterisation of a novel polymeric silver(I) nicotinic acid complex, H[Ag(py-3-CO₂)(2)], *Polyhedron*, 20 (2001) 2747-2753.

Kanani, N., *Electroplating: Basic Principles, Processes and Practice*, Elsevier Ltd., Oxford (2004).

Kang, S. K., Rai, R. S. and Purushothaman, S., Interfacial reactions during soldering with lead-tin eutectic and lead (Pb)-free, tin-rich solders, *Journal of Electronic Materials*, 25 (1996) 1113-1120.

Kang, S. K., Shih, D. Y., Donald, N. Y., Henderson, W., Gosselin, T., Sarkhel, A., Goldsmith, N. Y. C., Puttlitz, K. J. and Choi, W. K., Ag₃Sn plate formation in the solidification of near-ternary eutectic Sn-Ag-Cu, *Journal of the Minerals, Metals and Materials Society*, 55 (2003) 61-65.

Kang, S. K., Lauro, P. A., Shih, D.-Y., Henderson, D. W. and Puttlitz, K. J., Microstructure and mechanical properties of lead-free solders and solder joints

used in microelectronic applications, *IBM Journal of Research and Development*, 49 (2005) 607-620.

Kar, A., Ghosh, M., Ray, A. K. and Chosh, R. N., Effect of copper addition on the microstructure and mechanical properties of lead free solder alloy, *Materials Science and Engineering A*, 459 (2007) 69-74.

Kelber, J., Rudenja, S. and Bjelkevig, C., Electrodeposition of copper on Ru(0001) in sulfuric acid solution: Growth kinetics and nucleation behavior, *Electrochimica Acta*, 51 (2006) 3086-3090.

Kim, B. and Ritzdorf, T., Electrochemically deposited tin-silver-copper ternary solder alloys, *Journal of The Electrochemical Society*, 150 (2003a) 53-60.

Kim, B. and Ritzdorf, T., Electrodeposition of near-eutectic SnAg solders for wafer-level packaging, *Journal of The Electrochemical Society*, 150 (2003b) 577-584.

Kim, D. G. and Jung, S. B., Microstructure and mechanical properties of Sn-0.7Cu flip chip solder bumps using stencil printing method, *Materials Transactions*, 46 (2005) 2366-2371.

Kim, D. G., Kim, J. W. and S.B.Jung, Effect of aging conditions on interfacial reaction and mechanical joint strength between Sn-3.0Ag-0.5Cu solder and Ni-P UBM, *Materials Science and Engineering B*, 121 (2005) 204-210.

Kim, H. K., Liou, H. K. and Tu, K. N., Three-dimensional morphology of a very rough interface formed in the soldering reaction between eutectic SnPb and Cu, *Applied Physics Letters*, 66 (1995) 2337-2339.

Kim, J. H., Jeong, S. W., Kim, H. D. and Lee, H. M., Morphological transition of interfacial Ni₃Sn₄ grains at the Sn-3.5Ag/Ni joint, *Journal of Electronic Materials*, 32 (2003) 1228-1234.

Kim, J. W. and Jung, S. B., Characterization of the shear test method with low melting point In-48Sn solder joints, *Materials Science and Engineering A*, 397 (2005) 145-152.

Kim, K. S., Huh, S. H. and Suganuma, K., Effects of cooling speed on microstructure and tensile properties of Sn-Ag-Cu alloys, *Materials Science and Engineering A*, 333 (2002) 106-114.

Kim, K. S., Huh, S. H. and Suganuma, K., Effects of intermetallic compounds on properties of Sn-Ag-Cu lead-free soldered joints, *Journal of Alloys and Compounds*, 352 (2003) 226-236.

Kim, P. G., Jang, J. W., Lee, T. Y. and Tu, K. N., Interfacial reaction and wetting behavior in eutectic SnPb solder on Ni/Ti thin films and Ni foils, *Journal of Applied Physics*, 86 (1999) 6746-6751.

Kim, S. J. and Duquette, D. J., Nucleation characteristics of directly electrodeposited copper on TiN, *Journal of The Electrochemical Society*, 153 (2006a) 673-676.

Kim, S. J. and Duquette, D. J., Effect of chemical composition on adhesion of directly electrodeposited copper film on TiN, *Journal of The Electrochemical Society*, 153 (2006b) 417-421.

Kim, W. and Weil, R., Pulse plating effects in nickel electrodeposition, *Surface and Coatings Technology*, 38 (1989) 289-298.

Kivilahti, J. K., The chemical modeling of electronic materials and interconnections, *Journal of the Minerals, Metals and Materials Society*, 54 (2002) 52-57.

Kodolov, V. I., Tchirkova, E. I., Bystrova, S. G., Shabanova, I. N., Popova, O. V. and S. N. Babushkina, X-ray photoelectron spectroscopic investigation of metallorganic complexes, *Journal of Electron Spectroscopy and Related Phenomena*, 88 (1998) 977-982.

Kuwako, F., Method for producing multi-layer printed wiring boards having blind vias, US Patent 6,107,003 (2000).

Laurila, T., Vuorinen, V. and Kivilahti, J. K., Interfacial reactions between lead-free solders and common base materials, *Materials Science and Engineering R*, 49 (2005) 1-60.

Lee, C. C. and Wan, C. C., A study of the composite electrodeposition of copper with alumina powder, *Journal of The Electrochemical Society*, 135 (1988) 1930-1933.

Lee, T. Y., Choi, W. J., Tu, K. N., Jang, J. W., Kuo, S. M., Lin, J. K., Frear, D. R., Zeng, K. and Kivilahti, J. K., Morphology, kinetics, and thermodynamics of solid-state aging of eutectic SnPb and Pb-free solders (Sn-3.5Ag, Sn-3.8Ag-0.7Cu and Sn-0.7Cu) on Cu, *Journal of Materials Research*, 17 (2002) 291-301.

Li, C. L., Yang, Z. W., Wu, S. and Lei, Z. Q., Chloromethyl polystyrene supported dendritic Sn complexes, preparation and catalytic Baeyer-Villiger oxidation, *Reactive and Functional Polymers*, 67 (2007) 53-59.

Loomans, M. E. and Fine, M. E., Tin-Silver-Copper eutectic temperature and composition, *Metallurgical and Materials Transactions A*, 31 (2000) 1155-1162.

Lowenheim, F. A., *Modern Electroplating*, John Wiley and Sons, New York (1974).

Lugscheider, E., Bobzin, K. and Lake, M. K., Deposition of solder for micro-joining on M.E.M.S. components by means of magnetron sputtering, *Surface and Coatings Technology*, 142-144 (2001) 813-816.

Lugscheider, E., Bobzin, K. and Erdle, A., Solder deposition for transient liquid phase (TLP)-bonding by MSIP-PVD process, *Surface and Coatings Technology*, 174-175 (2003) 704-707.

Luo, W. C., Ho, C. E., Tsai, J. Y., Lin, Y. L. and Kao, C. R., Solid-state reactions between Ni and Sn-Ag-Cu solders with different Cu concentrations, *Materials Science and Engineering A*, 396 (2005) 385-391.

Maissel, L. I. and Glang, R., *Handbook of Thin Film Technology*, McGraw-Hill Book Company, New York (1970).

Makino, T. and Maeda, A., Electroplating bath containing citric acid or citrate for Tin or Tin alloy plating, US Patent 5,118,394 (1992).

Marinkovic, Z. and Simic, V., Room temperature interactions in Ni/metal thin film couples, *Thin Solid Films*, 98 (1982) 95-100.

Marlot, A., Kern, P. and Landolt, D., Pulse plating of Ni-Mo alloys from Ni-rich electrolytes, *Electrochimica Acta*, 48 (2002) 29-36.

Martell, A. E. and Smith, R. M., *Critical Stability Constants, Volume 3: Other Organic Ligands*, Plenum press, New York and London (1977).

Martyak, N. M. and Seefeldt, R., Additive-effects during plating in acid tin methanesulfonate electrolytes, *Electrochimica Acta*, 49 (2004) 4303-4311.

Miller, C. M., Anderson, I. E. and Smith, J. F., A viable tin-lead solder substitute: Sn-Ag-Cu, *Journal of Electronic Materials*, 23 (1994) 595-601.

Moon, K. W., Boettinger, W. J., Kattner, U. R., Biancaniello, F. S. and Handwerker, C. A., Experimental and thermodynamic assessment of Sn-Ag-Cu solder alloys, *Journal of Electronic Materials*, 29 (2000) 1122-1136.

Nakanishi, T., Ozaki, M., Nam, H., Yokoshima, T. and Osaka, T., Pulsed electrodeposition of nanocrystalline CoNiFe soft magnetic thin films, *Journal of The Electrochemical Society*, 148 (2001) C627-C634.

Neveu, B., Lallemand, F., Poupon, G. and Mekhalif, Z., Electrodeposition of Pb-free Sn alloys in pulsed current, *Applied Surface Science*, 252 (2006) 3561-3573.

Ohring, M., *The Materials Science of Thin Films*, Academic Press, Inc, Boston (1992).

Olsen, K. P., *Pulsed Current Electrodeposition of Sn and Sn-Cu films*, University of Alberta (2005).

Opaskar, V. C. and Capper, L. D., Plating bath and method for electroplating tin-zinc alloys, US Patent 6,436,269 B1 (2002).

Oskam, G., Long, J. G., Natarajan, A. and Searson, P. C., Electrochemical deposition of metals onto silicon, *Journal of Physics D*, 31 (1998) 1927-1949.

Ozga, P., Electrodeposition of Sn-Ag and Sn-Ag-Cu alloys from thiourea aqueous solutions, *Archives of Metallurgy and Materials*, 51 (2006) 413-421.

Pang, J. H. L., L. Xu, Shi, X. Q., Zhou, W. and Ngoh, S. L., Intermetallic growth studies on Sn-Ag-Cu lead-free solder joints, *Journal of Electronic Materials*, 33 (2004) 1219-1226.

Pauleau, Y., *Chemical Physics of Thin Film Deposition Processes for Micro- and Nano- Technologies*, Kluwer Academic Publishers, Dordrecht (1999).

Pittroff, W., Reiche, T., Barnikow, J., Klein, A., Merkel, U., Vogel, K. and Würfl, J., Au-Sn solder bumps with tungsten silicide based barrier metallization schemes, *Applied Physics Letters*, 67 (1995) 2367-2369.

Popov, K. I., Pavlovic, M. G., Pavlovic, L. J., Cekerevac, M. I. and Removic, G. Z., Electrode surface coarsening in pulsating overpotential copper electrodeposition, *Surface and Coatings Technology*, 34 (1988) 355-363.

Puttlitz, K. J. and Stalter, K. A., *Handbook of Lead-free Solder Technology for Microelectronic Assemblies*, Marcel Dekker, Inc., New York (2004).

Rehim, S. S., Refaey, S. A., Schwitzgebel, G., Taha, F. and Saleh, M. B., Electrodeposition of Sn-Co alloys from gluconate baths, *Journal of Applied Electrochemistry*, 26 (1996) 413-418.

Richoux, V., Diliberto, S., Boulanger, C. and Lecuire, J. M., Pulsed electrodeposition of bismuth telluride films: influence of pulse parameters over nucleation and morphology, *Electrochimica Acta*, 52 (2007) 3053-3060.

Rode, S., Henninot, C., Vallieres, C. and M. Matlosz, Complexation chemistry in copper plating from citrate baths, *Journal of The Electrochemical Society*, 151 (2004) 405-411.

Sahari, A., Azizi, A., Schmerber, G., Abes, M., Bucher, J. P. and Dinia, A., Electrochemical nucleation and growth of Co and CoFe alloys on Pt/Si substrates, *Catalysis Today*, 113 (2006) 257-262.

Schaefer, M., Fournelle, R. A. and Liang, J., Theory for intermetallic phase growth between Cu and liquid Sn-Pb solder based on grain boundary diffusion control, *Journal of Electronic Materials*, 27 (1998) 1167-1176.

Scharifker, B. and Hills, G., Theoretical and Experimental studies of Multiple nucleation, *Electrochimica Acta*, 28 (1983) 879-889.

Seby, F., Potin-Gautier, M., Giffaut, E. and Donard, O. F. X., A critical review of thermodynamic data for inorganic tin species, *Geochimica Et Cosmochimica Acta*, 65 (2001) 3041-3053.

Seshan, K., *Handbook of Thin-film Deposition Processes and Techniques - Principles, Methods, Equipment and Application (2nd Edition)*, William Andrew Publishing/Noyes Publications, New York (2002).

Shangguan, D., *Lead-free Solder: Interconnect Reliability*, ASM International, Ohio (2005).

Sharif, A., Islam, M. N. and Chan, Y. C., Interfacial reactions of BGA Sn-3.5%Ag-0.5%Cu and Sn-3.5%Ag solders during high-temperature aging with Ni/Au metallization, *Materials Science and Engineering B*, 113 (2004) 184-189.

Subramania, A., Priya, A. R. S. and V.S. Muralidharan, Electrocatalytic cobalt-molybdenum alloy deposits, *International Journal of Hydrogen Energy*, 32 (2007) 2843-2847.

Suganuma, K., Advances in lead-free electronics soldering, *Current Opinion in Solid State and Materials Science*, 5 (2001) 55-64.

Suganuma, K., *Lead-free Soldering in Electronics - Science, Technology, and Environmental Impact*, Marcel Dekker, Inc., New York (2004).

Sun, P., Andersson, C., Wei, X., Cheng, Z., Shangguan, D. and Liu, J., High temperature aging study of intermetallic compound formation of Sn-3.5Ag and Sn-4.0Ag-0.5Cu solders on electroless Ni(P) metallization, *Journal of Alloys and Compounds*, 425 (2006) 191-199.

Sun, W. and Ivey, D. G., Development of an electroplating solution for codepositing Au-Sn alloys, *Materials Science and Engineering B*, 65 (1999) 111-122.

Survila, A., Mockus, Z. and Kanapeckaite, S., Kinetics of Sn and Co codeposition in citrate solutions, *Electrochimica Acta*, 46 (2000) 571-577.

Survila, A., Mockus, Z., Jusienas, R. and Jasulaitiene, V., Electrodeposition of Sn and Co coatings from citrate solutions, *Journal of Applied Electrochemistry*, 31 (2001) 1109-1116.

Takahashi, A., Miyoshi, Y. and Hada, T., Effect of SiO₂ colloid on the electrodeposition of zinc-iron group metal alloy composites, *Journal of The Electrochemical Society*, 141 (1994) 954-957.

Talbot, J. B., Electrocodeposition of nanocomposite films, *Plating and Surface Finishing*, 91 (2004) 60-65.

Tan, A. C., *Tin and Solder Plating in the Semiconductor Industry*, Chapman & Hall, London (1993).

Tan, Y. J. and Lim, K. Y., Understanding and improving the uniformity of electrodeposition, *Surface and Coatings Technology*, 167 (2003) 255-262.

Tang, W., He, A., Liu, Q. and Ivey, D. G., Fabrication and microstructures of sequentially electroplated Sn-rich Au-Sn alloy solders, *Journal of Electronic Materials*, 37 (2008a) 837-844.

Tang, W., He, A., Liu, Q. and Ivey, D. G., Room temperature interfacial reactions in electrodeposited Au/Sn couples, *Acta Materialia*, 56 (2008b) 5818-5827.

Tikhonov, A. S. and Kurolap, N. S., Study of reactions of complex formation of bivalent tin ions with citric acid ions, *Trudy Voronezh. Univ.*, 42 (1956) 61-62.

Toben, M. P., Marchtell, D. C., Brown, N. D. and Doyle, C. A., Electrolyte and Tin-silver electroplating process, US Patent 6,210,556 B1 (2001).

Tomlinson, W. J. and Rhodes, H. G., Kinetics of intermetallic compound growth between nickel, electroless Ni-P, electroless Ni-B and tin at 453 to 493K, *Journal of Materials Science*, 22 (1987) 1769-1772.

Torrent-Burgues, J., Gaus, E. and Sanz, F., Initial stages of tin electrodeposition from sulfate baths in the presence of gluconate, *Journal of Applied Electrochemistry*, 32 (2002) 225-230.

Tselesh, A. S., Anodic behaviour of tin in citrate solutions: The IR and XPS study on the composition of the passive layer, *Thin Solid Films*, 516 (2008) 6253-6260.

Tsuji, K., Obata, K., Takeuchi, T., Mawafune, H. and Nishikawa, T., Plating bath and process for depositing alloy containing tin and copper, US Patent 6,607,653 B1 (2003).

- Tu, K. N., *Acta Metallurgica*, 21 (1973) 347.
- Tu, K. N. and Thompson, R. D., Kinetics of interfacial reaction on Bimetallic Cu-Sn thin films, *Acta Metallurgica*, 30 (1982) 947-952.
- Tu, K. N., Mayer, J. W. and Feldman, L. C., *Electronic Thin Film Science for Electrical Engineers and Materials Scientists*, Macmillan, New York (1992).
- Tu, K. N., Cu/Sn interfacial reactions: thin-film case versus bulk case, *Materials Chemistry and Physics*, 46 (1996) 217-223.
- Tu, K. N., Lee, T. Y., Jang, J. W., Li, L., Frear, D. R., Zeng, K. and Kivilahti, J. K., Wetting reaction versus solid state aging of eutectic SnPb on Cu, *Journal of Applied Physics*, 89 (2001) 4843-4849.
- Tu, K. N. and Zeng, K., Tin-lead (SnPb) solder reaction in flip chip technology, *Materials Science and Engineering R*, 34 (2001) 1-58.
- Tu, K. N., Gusak, A. M. and Li, M., Physics and materials challenges for lead-free solders, *Journal of Applied Physics*, 93 (2003) 1335-1353.
- Wang, C. H. and Chen, S. W., Sn-0.7wt.%Cu/Ni interfacial reactions at 250°C, *Acta Materialia*, 54 (2006) 247-253.
- Wang, Y. W., Lin, Y. W. and Kao, C. R., Kirkendall voids formation in the reaction between Ni-doped SnAg lead-free solders and different Cu substrates, *Microelectronics Reliability*, 49 (2009) 248-252.
- Watanabe, T., *Nano-plating: Microstructure Control Theory of Plated Film and Data Base of Plated Film Microstructure*, Elsevier, (2004).
- Watson, S. W. and Walters, R. P., The effect of chromium particles on nickel electrodeposition, *Journal of The Electrochemical Society*, 138 (1991) 3633-3642.
- Watson, S. W., Electrochemical study of SiC particle occlusion during nickel electrodeposition, *Journal of The Electrochemical Society*, 140 (1993) 2235-2238.
- Wen, S. and Szpunar, J. A., Nucleation and growth of tin on low carbon steel, *Electrochimica Acta*, 50 (2005) 2393-2399.
- Wu, C. M. L., Yu, D. Q., Law, C. M. T. and Wang, L., Properties of lead-free solder alloys with rare earth element additions, *Materials Science and Engineering R*, 44 (2004) 1-44.
- Yanada, I., Tsujimoto, M., Okada, T., Oka, T. and Tsubokura, H., Tin-copper alloy electroplating bath, US Patent 6,508,927 B2 (2003).

- Yeh, P. Y., Song, J. M. and Lin, K. L., Dissolution behavior of Cu and Ag substrates in molten solders, *Journal of Electronic Materials*, 35 (2006) 978-987.
- Yen, Y. W., Chou, W. T., Tseng, Y., Lee, C. and C.L. Hsu, Investigation of dissolution behavior of metallic substrates and intermetallic compound in molten lead-free solders, *Journal of Electronic Materials*, 37 (2008) 73-83.
- Yoon, J. W., Kim, S. W. and Jung, S. B., Interfacial reaction and mechanical properties of eutectic Sn-0.7Cu/Ni BGA solder joints during isothermal long-term aging, *Journal of Alloys and Compounds*, 391 (2005) 82-89.
- Yoon, J. W. and Jung, S. B., High temperature reliability and interfacial reaction of eutectic Sn-0.7Cu/Ni solder joints during isothermal aging, *Microelectronics Reliability*, 46 (2006) 905-914.
- Yoon, J. W., Kim, S. W. and Jung, S. B., Effects of reflow and cooling conditions on interfacial reaction and IMC morphology of Sn-Cu/Ni solder joint, *Journal of Alloys and Compounds*, 415 (2006) 56-61.
- Yu, C., Lu, H. and Li, S., Effect of Zn addition on the formation and growth of intermetallic compound at Sn-3.5wt%Ag/Cu interface, *Journal of Alloys and Compounds*, 460 (2008) 594-598.
- Yu, D. Q. and L. Wang, The growth and roughness evolution of intermetallic compounds of Sn-Ag-Cu/Cu interface during soldering reaction, *Journal of Alloys and Compounds*, 458 (2008) 542-547.
- Zeng, K. and Tu, K. N., Six cases of reliability study of Pb-free solder joints in electronic packaging technology, *Materials Science and Engineering R*, 38 (2002) 55-105.
- Zeng, K., Vuorinen, V. and Kivilahti, J. K., Interfacial reactions between lead-free SnAgCu solder and Ni(P) surface finish on printed circuit boards, *IEEE Transactions on Electronics Packaging Manufacturing*, 25 (2002) 162-167.
- Zeng, K., Stierman, R., Chiu, T., Edwards, D., Ano, K. and Tu, K. N., Kirkendall void formation in eutectic SnPb solder joints on bare Cu and its effect on joint reliability, *Journal of Applied Physics*, 97 (2005) 024508.
- Zhang, J., An, M., Chang, L. and Liu, G., Effect of triethanolamine and heliotropin on cathodic polarization of weakly acidic baths and properties of Sn-Ag-Cu alloy electrodeposits, *Electrochimica Acta*, 53 (2008) 2637-2643.
- Zhu, F., Zhang, H., Guan, R. and Liu, S., Effects of temperature and strain rate on mechanical property of Sn96.5Ag3Cu0.5, *Journal of Alloys and Compounds*, 438 (2007) 100-105.